GEOTECHNICAL ENGINEERING

LUNAR SURFACE ENGINEERING PROPERTIES EXPERIMENT DEFINITION

FINAL REPORT: VOLUME II OF IV
MECHANICS OF ROLLING SPHERE-SOIL SLOPE INTERACTION

by

H. J. HOVLAND
J. K. MITCHELL

PREPARED FOR GEORGE C. MARSHALL SPACE FLIGHT CENTER
HUNTSVILLE, ALABAMA, UNDER NASA CONTRACT NAS 8-21432

JULY 1971

SPACE SCIENCES LABORATORY

UNIVERSITY OF CALIFORNIA · BERKELEY

Space Sciences Laboratory
University of California
Berkeley, California 94720

LUNAR SURFACE ENGINEERING PROPERTIES EXPERIMENT DEFINITION

FINAL REPORT: VOLUME II OF IV

MECHANICS OF ROLLING SPHERE-SOIL SLOPE INTERACTION

by

H. J. Hovland and J. K. Mitchell

Prepared for George C. Marshall Space Flight Center,
Huntsville, Alabama, under
NASA Contract Number NAS 8-21432.

Control Number DCN 1-X-80-00058 S1 (IF)

July 1971

Space Sciences Laboratory Series 11 Issue 49

This report was prepared by the University of California, Berkeley, under Contract Number NAS 8-21432, Lunar Surface Engineering Properties Experiment Definition, for the George C. Marshall Space Flight Center of the National Aeronautics and Space Administration. This work was administered under the technical direction of the Space Sciences Laboratory of the George C. Marshall Space Flight Center.

Assistance in the experimental work described in Chapters 4 and 6 of this volume was provided by the Waterways Experiment Station in accordance with NASA Defense Purchase Request (DPR) H-58504A from the Marshall Space Flight Center.

PREFACE

This report presents the results of studies conducted during the period July 19, 1969 — July 19, 1970, under NASA Research Contract NAS 8-21432, "Lunar Surface Engineering Properties Experiment Definition." This study was sponsored by the Lunar Exploration Office, NASA Headquarters, and was under the technical cognizance of Dr. N. C. Costes, Space Science Laboratory, George C. Marshall Space Flight Center.

The report reflects the combined effort of five faculty investigators, a research engineer, a project manager, and eight graduate research assistants, representing several engineering and scientific disciplines pertinent to the study of lunar surface material properties. James K. Mitchell, Professor of Civil Engineering, served as Principal Investigator and was responsible for those phases of the work concerned with problems relating to the engineering properties of lunar soils and lunar soil mechanics. Co-investigators were William N. Houston, Assistant Professor of Civil Engineering, who was concerned with problems relating to the engineering properties of lunar soils; Richard E. Goodman, Associate Professor of Geological Engineering, who was concerned with the engineering geology and rock mechanics aspects of the lunar surface; Paul A. Witherspoon, Professor of Geological Engineering, who was concerned with fluid conductivity of lunar surface materials in general; Franklin C. Hurlbut, Professor of Aeronautical Science, who was concerned with experimental studies on fluid conductivity of lunar surface materials; and D. Roger Willis, Associate Professor of Aeronautical Science, who conducted theoretical studies on fluid conductivity of lunar surface materials. Dr. Karel Drozd, Assistant Research Engineer, performed laboratory tests and analyses pertinent to the development of a borehole jack for determination of the in situ characteristics of lunar soils and rocks; he also helped in the design of the borehole jack. H. Turan Durgunoglu, H. John Hovland, Laith I. Namiq, Parabaronen Raghuraman, James B. Thompson, Donald D. Treadwell, C. Robert Jih, Suphon Chirapuntu, and Tran K. Van served as Graduate Research Assistants and carried out many of the studies leading to the results presented in this

report. Ted S. Vinson, Research Engineer, served as project manager until May 1970, and contributed to studies concerned with lunar soil stabilization. H. John Hovland served as project manager after May 1970, and contributed to studies concerned with soil property evaluation from lunar boulder tracks.

Ultimate objectives of this project were:

1) Assessment of lunar soil and rock property data using information obtained from Lunar Orbiter, Surveyor, and Apollo missions.

2) Recommendation of both simple and sophisticated in situ testing techniques that would allow determination of engineering properties of lunar surface materials.

3) Determination of the influence of variations in lunar surface conditions on the performance parameters of a lunar roving vehicle.

4) Development of simple means for determining the fluid conductivity properties of lunar surface materials.

5) Development of stabilization techniques for use in loose, unconsolidated lunar surface materials to improve the performance of such materials in lunar engineering application.

The scope of specific studies conducted in satisfaction of these objectives is indicated by the following list of contents from the Detailed Final Report which is presented in four volumes. The names of the investigators associated with each phase of the work are indicated.

VOLUME I

MECHANICS, PROPERTIES, AND STABILIZATION OF LUNAR SOILS

VOLUME II

MECHANICS OF ROLLING SPHERE-SOIL SLOPE INTERACTION
H. J. Hovland and J. K. Mitchell

VOLUME III

BOREHOLE PROBES

VOLUME IV

FLUID CONDUCTIVITY OF LUNAR SURFACE MATERIALS

VOLUME II

CONTENTS

VOLUME II (Cont'd)

VOLUME II (Cont'd) Page

LIST OF FIGURES

Figure | Page

Figure | Page

Figure

Page

Figure | Page

VOLUME II

Mechanics of Rolling Sphere — Soil Slope Interaction

Chapter 1. INTRODUCTION

This report presents the results of studies related to rolling-sphere (rolling boulder) soil-slope interaction. It describes all work done on this phenomenon during the last 2 years at Space Sciences Laboratory, University of California. This work was also presented as a Ph.D. dissertation by H. John Hovland to the University of California.

The motivation for investigating the relationship between soil properties and the track left by a rolling sphere was provided by the observation of boulder tracks on the surface of the moon in Lunar Orbiter photographs. A typical lunar boulder track is shown in Figure 1-1.

It was soon recognized that a relationship must exist between the size and the track of the boulder, and that this relationship would include both soil and boulder properties. Hence, some lunar boulders were studied (Filice, 1967; Nordmeyer and Mason, 1967; Moore and Martin, 1967; Eggleston et al., 1968) in an effort to determine the static bearing capacity of lunar surface soil. We have been investigating in more detail the possibilities for deducing soil strength parameters from the boulder tracks.

A summary of the work done by our group on the study of lunar boulder tracks during the year 1967-68 was presented in the final report for Contract NSR 05-003-189 (Mitchell et al., 1969). In that report, several methods for analyzing boulder-track data were considered, each subject to limitations and giving somewhat different results. It was recommended that boulder-track phenomena be further studied, and it was noted also that if variability of the lunar surface is to be determined, it is important to use the same method of analysis throughout.

Studies during 1968-69 consisted of reviewing Orbiter photography for locating suitable boulder tracks for analysis, study of site geology for selected boulder tracks, and static analysis of the boulder tracks

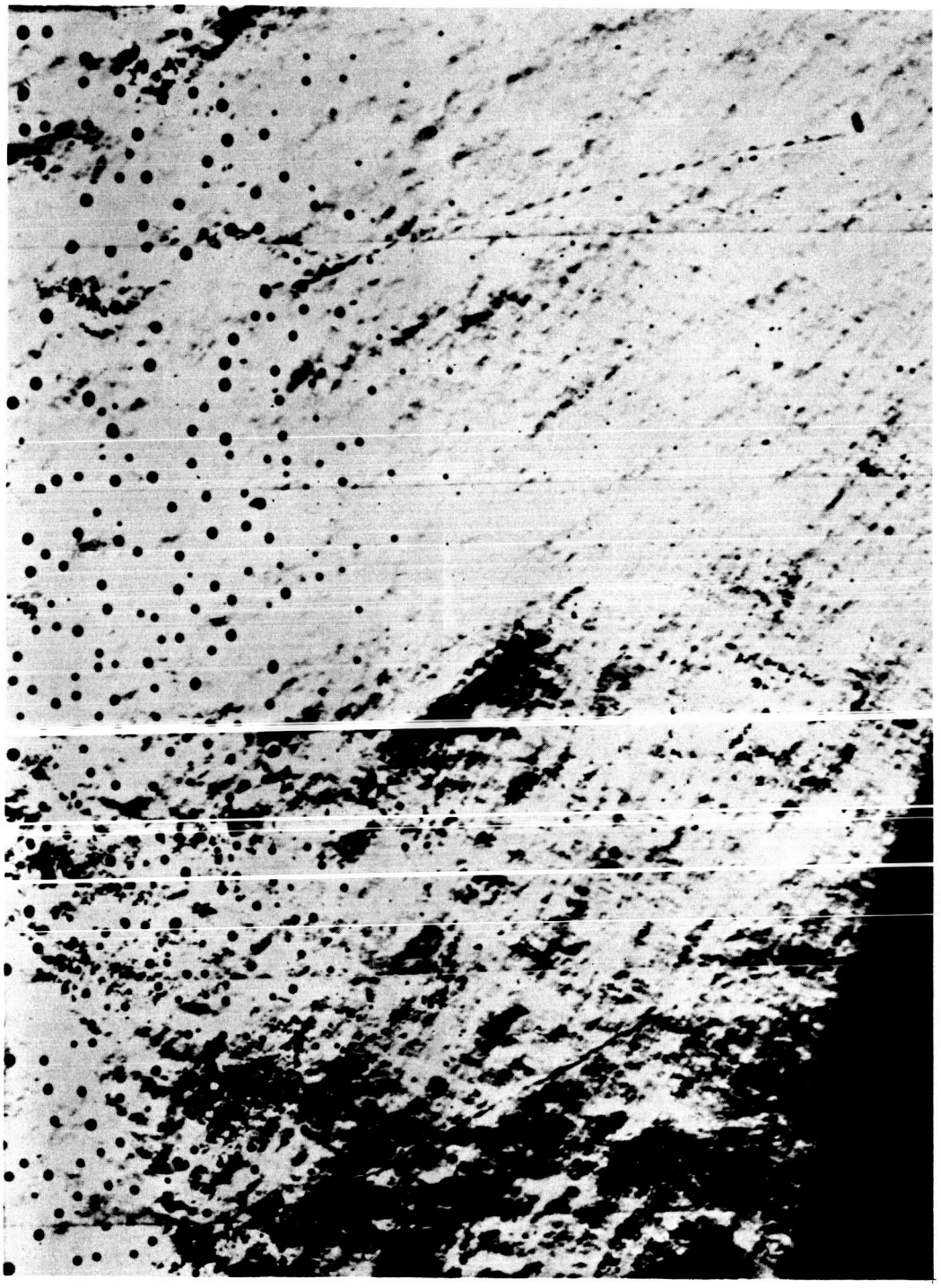

Fig. 1-1. Typical boulder tracks.

(North rim of Gassendi, Lunar Orbiter V, Frame 179,
scale: 1 cm = 143 m)

using bearing capacity theory. These investigations were reported in detail by Hovland and Mitchell (1970). The results suggested a variability of lunar soils. Possible causes of such variability were considered. It was also recognized that the theory used neglected the dynamic aspect of the problem. It was recommended that an improved theory or method be developed. The pertinent results and conclusions from this work are presented in Chapter 2.

The research for this report has consisted of an in-depth investigation of the fundamental nature of the rolling sphere-soil slope interaction phenomenon. Specific objectives of this research were:

1. To develop an understanding of the soil deformation mode under the action of a rolling sphere.
2. To develop an improved theory or method, based on the actual soil failure mechanism, which would provide a remote reconnaissance technique for study of soil conditions using boulder track observations.

The rolling sphere-soil slope interaction phenomenon was studied systematically to meet the stated objectives. The failure mechanism investigated using models and by testing an instrumented spherical wheel. The model studies are reported in Chapter 3. The instrumented spherical wheel was specifically designed to measure contact pressure, but it also provided much information on the failure mechanism, as reported in Chapter 4. Based on an understanding of the failure mechanism, theory was modified and developed as reported in Chapter 5. Further tests were conducted to study the dynamic aspects of the problem and the combined effect of several parameters. These tests included rolling some two hundred spheres down sand slopes. Films were taken of the rolling spheres, and the tracks were measured. This experimental work as reported in Chapter 6 provides the basis for comparison with theory.

Implications of the results and reevaluation of the lunar boulder tracks analyzed using the proposed method are discussed in Chapter 7.

Chapter 2. ANALYSIS OF LUNAR BOULDER TRACKS

Among the conspicuous and interesting features on the lunar surface are large boulders and the tracks they left as they rolled down slopes. These features were observed early on photographs provided by lunar orbiters. The tracks appear to be of three different types; i.e., (1) continuous tracks suggestive of a spherical boulder rolling uniformly down the slope, (2) segmented tracks suggestive of bouncing, and (3) relatively short tracks suggestive of plowing.

At the outset of this investigation sixty-nine boulder tracks from nineteen different locations on the moon, as shown in Figure 2-1, were analyzed. These locations include upland, maria, and perhaps intermediate terrain. Only tracks that appeared continuous (implying a relatively spherical boulder and uniform rolling) were selected.

A complete report including consideration of the geology of boulder track locations and detailed discussion of the implications of the results was presented previously (Hovland and Mitchell, 1970). A summary of this study is given here.

METHOD OF ANALYSIS

Geometrical Relations of Sphere and Track

A boulder rolling down a slope where the soil fails in general shear would leave a track with a raised rim, (Figure 2-2). Such rims have been observed on many lunar boulder tracks. For the purpose of the present analysis, preliminary theory can be developed for a somewhat more idealized situation, assuming a sphere-track geometry as shown on Figure 2-3.

From Figure 2-3 it may be seen that the track depth will be given by

$$z = r(1 - \cos\theta) = r\left(1 - \cos\left[\sin^{-1}\frac{w}{D}\right]\right), \qquad (2\text{-}1)$$

where

$D = 2r$, or the sphere diameter, and w is the track width

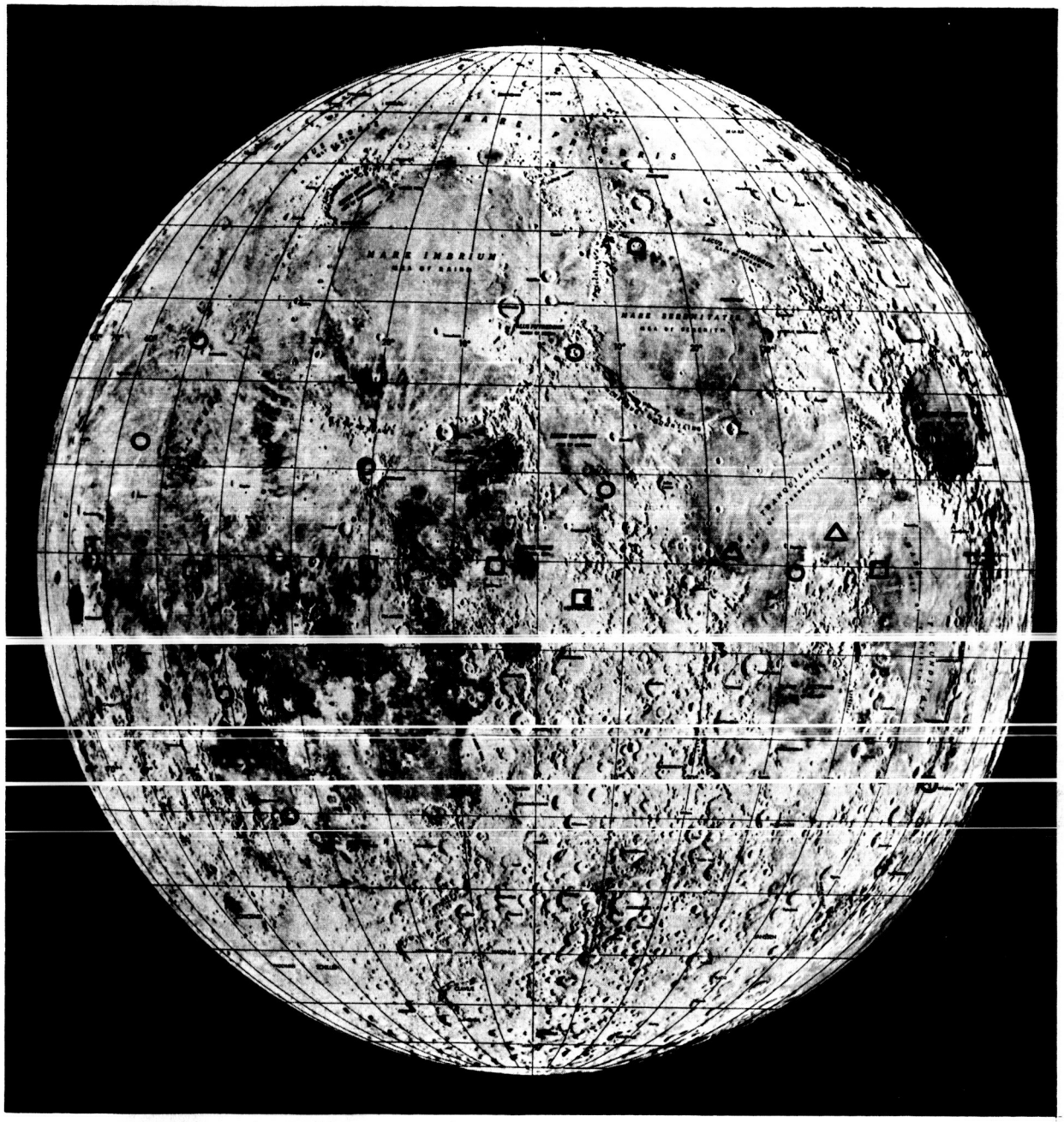

Fig. 2-1. Locations of boulder tracks analyzed.

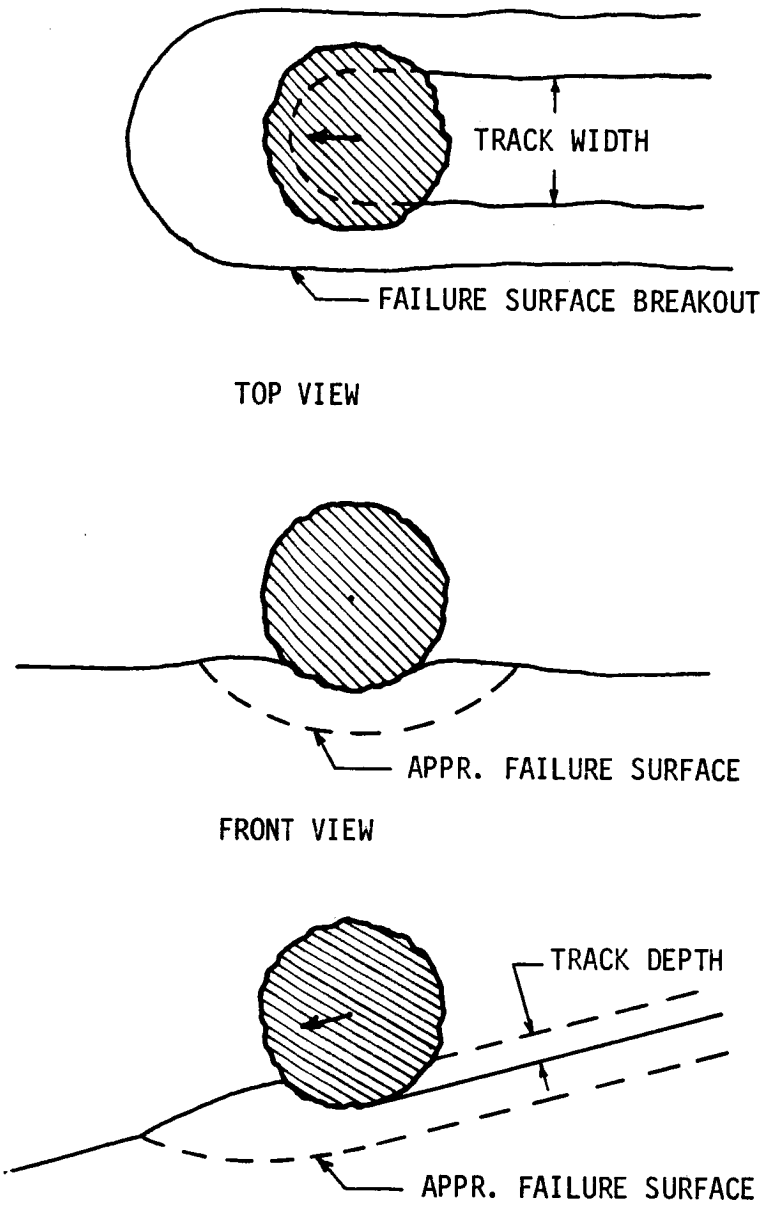

Fig. 2-2. Boulder rolling down slope.

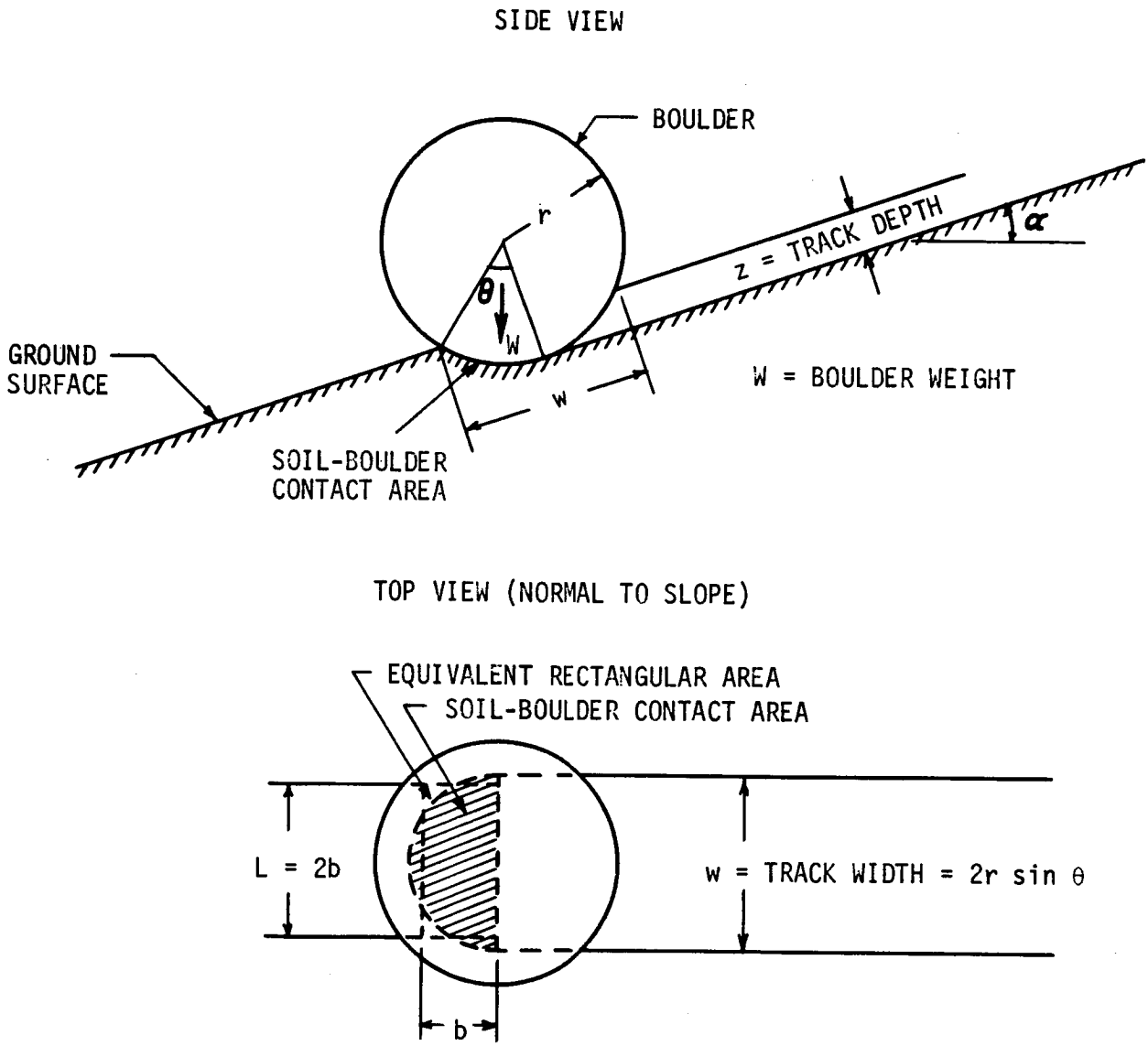

Fig. 2-3. Geometrical relations of sphere and track.

The semicircular soil-sphere contact area may be represented by an equivalent rectangular area defined by

$$2b^2 = \frac{w^2}{4}\frac{\pi}{2} \quad , \tag{2-2}$$

giving

$$b = \frac{w}{4}\sqrt{\pi} = 0.44\ w \ . \tag{2-3}$$

Modified Bearing Capacity Theory

A general bearing capacity equation for a strip footing (Leonards, 1962) is

$$q = \frac{\gamma_s b}{2} N_\gamma + cN_c + q'N_q \ . \tag{2-4}$$

This equation assumes a homogeneous-isotropic soil; other assumptions are discussed in Chapter 5, pages 95 and 101. For a rectangular footing this equation may be modified to

$$q = \frac{\gamma_s b}{2} N_\gamma s_\gamma + cN_c s_c + q'N_q s_q \ . \tag{2-5}$$

In these equations

q = unit bearing capacity

γ_s = soil density in earth gravity

b = width of footing

c = soil cohesion

q' = surcharge

s_γ, s_c, s_q = shape factors, and

N_γ, N_c, N_q = bearing capacity factors which depend on the soil friction angle, ϕ.

Skempton (1951) indicated that, for $\phi = 0$, the value of s_c can be taken as $(1 + 0.2\ b/L)$, where L is the length of a rectangular footing. For $\phi > 0$, the vaue of s_c would probably not be significantly different. Meyerhof (1951) proposed that, for $\phi = 30°$, s_q equals approximately

(1 + 0.2 b/L). The friction angle for lunar soil is probably close enough to 30° to justify the use of this value for s_q. The shape factor, s_γ, is given by (1 - 0.3 b/L) according to Lundgren and Hansen (1955) and Hansen (1957).

Substituting these shape factors into the bearing capacity equation we get

$$q = \frac{\gamma_s b}{2}\left(1 - 0.3\,\frac{b}{L}\right)N_\gamma + c\left(1 + 0.2\,\frac{b}{L}\right)N_c + q'\left(1 + 0.2\,\frac{b}{L}\right)N_q. \qquad (2\text{-}6)$$

for the sphere b/L = 1/2 and b = 0.444 w. If, in addition, an average surcharge depth is taken to be z/2,

$$q = \frac{0.85}{2}(0.444\ w)\gamma_s N_\gamma + 1.1\ cN_c + \frac{1.1}{2}\gamma_s z N_q. \qquad (2\text{-}7)$$

A convenient equation in dimensionless form results by dividing both sides by $(w\gamma_s)$ to give

$$\frac{q}{w\gamma_s} = 0.188\ N_\gamma + 1.1\left(\frac{c}{w\gamma_s}\right)N_c + 0.55\ \left(\frac{z}{w}\right)N_q. \qquad (2\text{-}8)$$

Defining q_e as the unit bearing capacity in earth gravity and γ_s as the unit weight of soil in earth gravity, the equation for the unit bearing capacity of a sphere in the earth gravity field becomes

$$\frac{q_e}{w\gamma_s} = 0.188\ N_\gamma + 1.1\left(\frac{c}{w\gamma_s}\right)N_c + 0.55\left(\frac{z}{w}\right)N_q. \qquad (2\text{-}9)$$

This equation is readily adapted for estimating the bearing capacity on the moon by noting that, for a given soil mass density, the unit weight on the moon will be reduced by a factor of 6. Thus, if q_m designates the bearing capacity on the moon, Equation (2-9) becomes

$$\frac{q_m}{w\gamma_s} = 0.0314\ N_\gamma + 1.1\left(\frac{c}{w\gamma_s}\right)N_c + 0.0916\left(\frac{z}{w}\right)N_q. \qquad (2\text{-}10)$$

The influence of the slope angle, α, can be incorporated by using Meyerhof's bearing capacity factors (Meyerhof, 1951). For the purpose of this study, the charts for Meyerhof's bearing capacity factors were enlarged and are presented on Figures 2-4, 2-5, and 2-6.

An expression for the average bearing pressure under a sphere can be developed from the ratio of sphere weight to bearing area. This gives

$$q = \frac{4/3\pi r^3 \gamma_r}{\frac{\pi}{2}\frac{w^2}{4}} = \frac{32}{3}\frac{r^3}{w^2}\gamma_r = \frac{4}{3}\frac{D\gamma_r}{(w/D)^2} , \qquad (2\text{-}11)$$

where

r = sphere radius

D = sphere diameter, and

γ_r = rock or sphere density in earth gravity.

Dividing both sides of this equation by $w\gamma_s$, we have

$$\frac{q}{w\gamma_s} = \frac{4}{3}\frac{\gamma_r/\gamma_s}{(w/D)^3} . \qquad (2\text{-}12)$$

Again, for the lunar gravity field, lunar soil unit weight equals $\gamma_s/6$. Then the average bearing pressure for a sphere in lunar gravity is given by

$$\frac{q_m}{w\gamma_s} = \frac{2}{9}\frac{\gamma_r/\gamma_s}{(w/D)^3} . \qquad (2\text{-}13)$$

Table 2-1 lists some possible rock and soil combinations that might be found on the lunar surface.

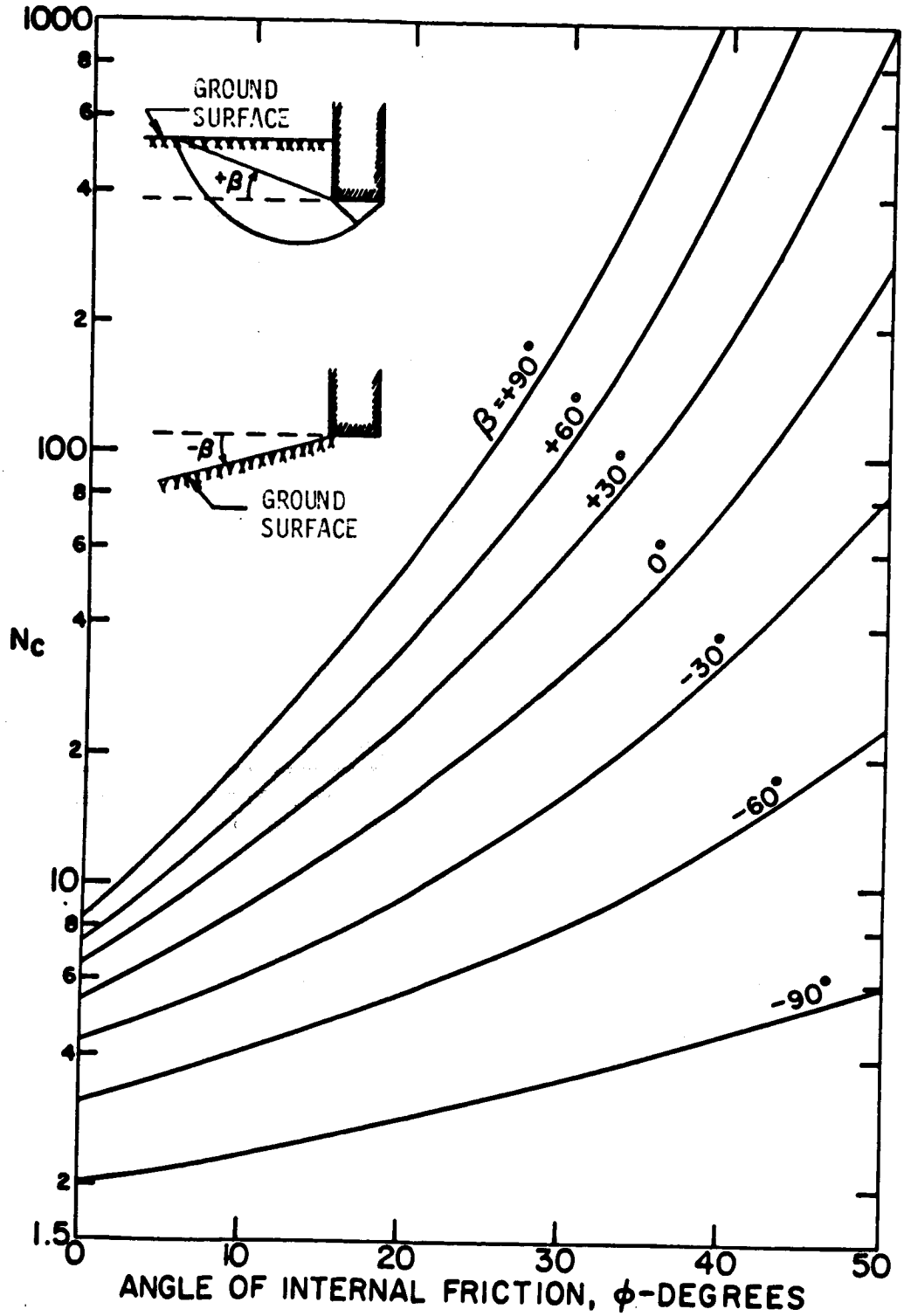

Fig. 2-4. General bearing capacity factor N_c for strip foundation (after Meyerhof, 1951).

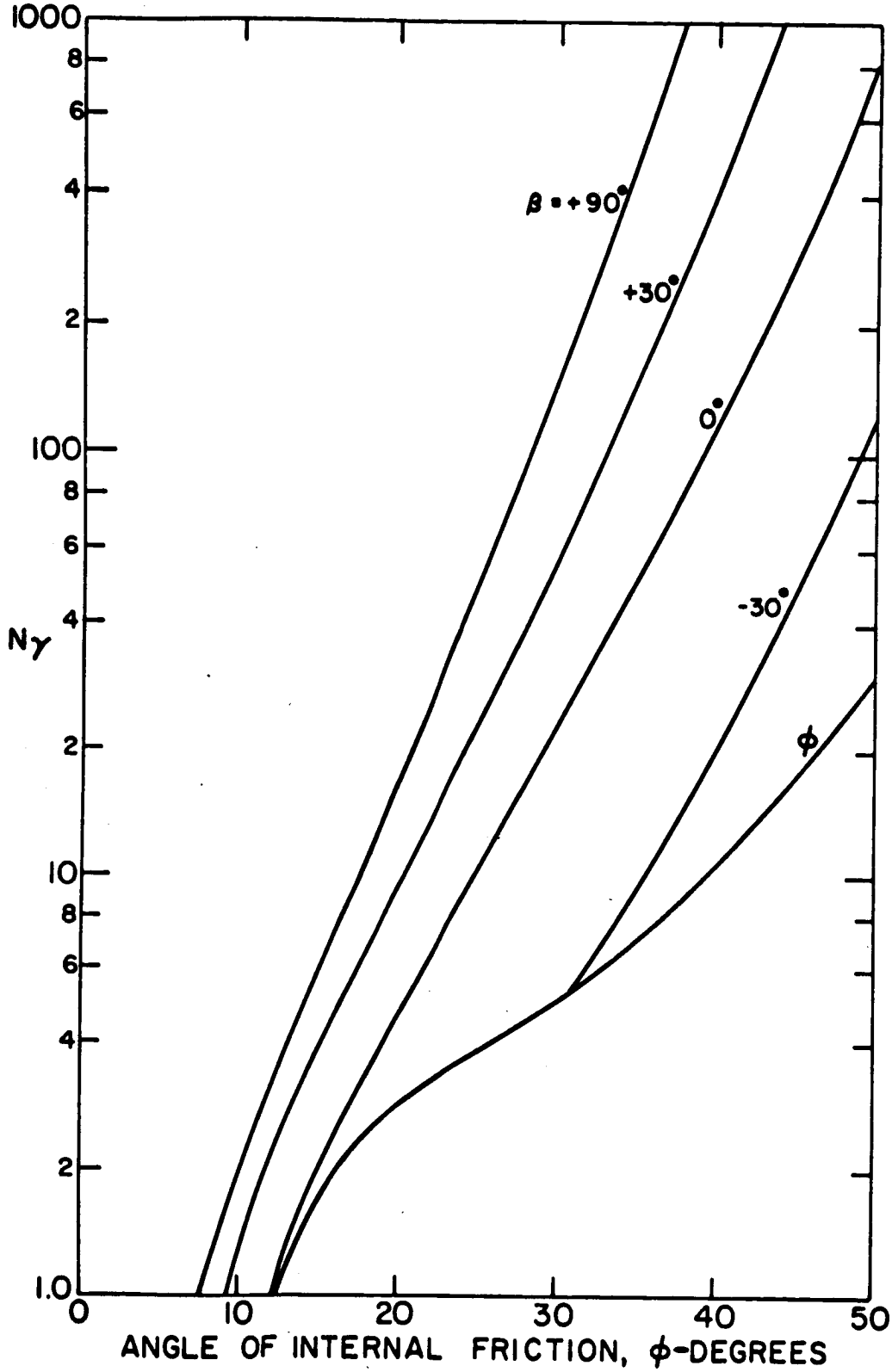

Fig. 2-5. General bearing capacity factor N_C for strip foundation (after Meyerhof, 1951).

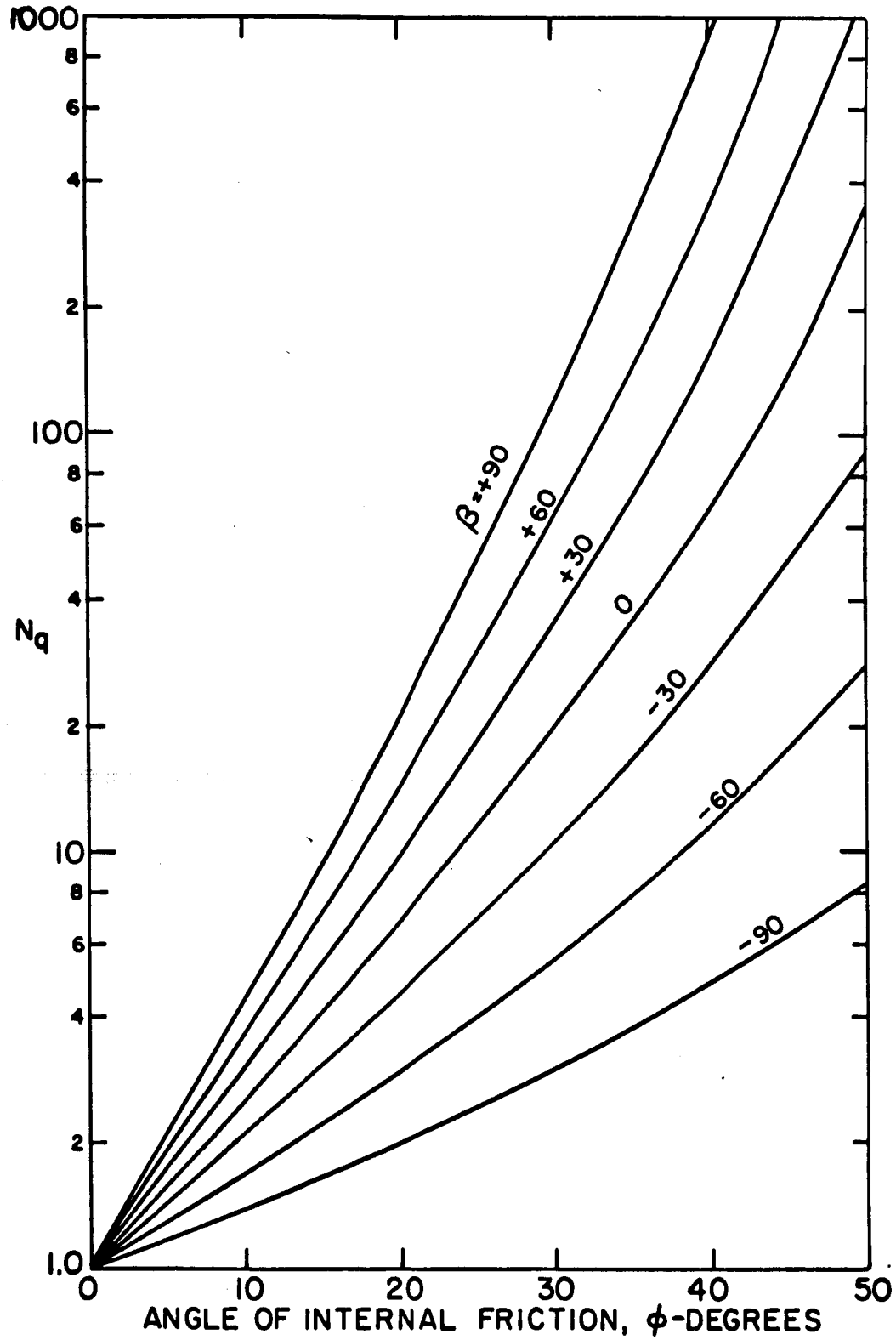

Fig. 2-6. General bearing capacity factor N_C for strip foundation (after Meyerhof, 1951).

Table 2-1. Possible Lunar Rocks and Soils.

Description					Likelihood of ratio occurrence
Rock type	γ_r gm/cc	Soil type	γ_s gm/cc	$\frac{\gamma_r}{\gamma_s}$	
Basaltic, vesicular	2.7	Mixed and maria soil	1.6	1.7	Probably common
Basaltic, average porosity (Surveyor results)	3.1	Mixed and maria soil (Surveyor results)	1.5	2.0	Probably common
Porous volcanic rock	1.8	Relatively dense basaltic soil	1.8	1	Possible
Basaltic, average porosity	3.1	Volcanic ash or porous material	1.1	3	Possible
Extra dense volcanic or meteoritic rock	4.2	Light volcanic ash or porous material*	0.7	6	Probably rare
Pumice-like rock	0.7*	Dense basaltic soil	2.3	0.3	Probably very rare

*Bendix Corporation 1968

Equation (2-13) was solved using the density ratios listed in Table 2-1 and gave the results plotted in Figure 2-7.

The angle of internal friction, ϕ, can now be determined by using Equation (2-10) and either Equation (2-13) or Figure 2-7, provided c is known or can be estimated. It is to be noted that Equation (2-10) is an upper bound to bearing capacity because it gives a solution based on the maximum resistance available for given values of c and ϕ. In principle, Equation (2-13) is an exact value of bearing capacity, since for any lower value of q_m the track width would be greater, and for any greater value of q_m the track width would be smaller.

SELECTION OF BOULDERS AND MATERIAL PROPERTIES

The procedure followed for study of different boulder tracks consisted of (1) locating suitable boulder tracks on high resolution Lunar

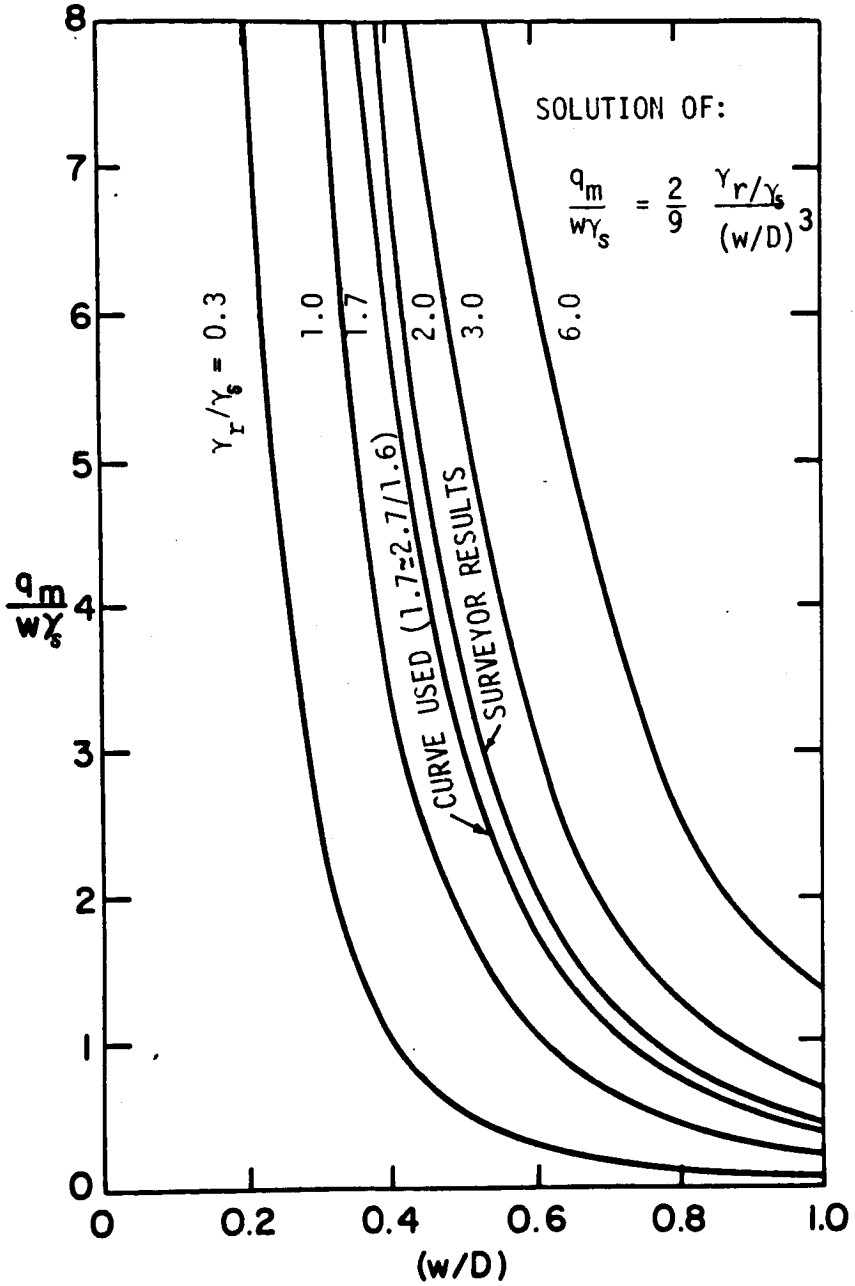

Fig. 2-7. Graph of Equation (2-13).

Orbiter photographs, (2) determining the scale of the photograph or frame, (3) measuring the boulder and track dimensions, and (4) estimating the slope angle for selected portions of the track. Some of the above phases of the analysis are described in greater detail below.

Scale of the Photographs

The Orbiter Supporting Data* for the Lunar Orbiter missions give the latitude and longitude of 44 equally spaced angles along the photo frame periphery. Points 1, 12, 23, and 34 correspond to the corners of the frame, and can be easily identified. Hence, the distance from one corner to another can be measured on the frame, and the corresponding ground distance can be calculated from the latitude and longitude of the corners given in the supporting data. Thus, the scale to be used is:

$$\text{Scale} = \frac{\text{Distance on Frame}}{\text{Distance on Ground}} .$$

The distance on the ground is either given in the supporting data or can be determined from geometrical relationships of a sphere. The length of any circular arc on a sphere is given by

$$L_{AB} = \frac{\pi R_m}{180} \theta_{AB} , \qquad (2\text{-}14)$$

where

L_{AB} = arc distance between points A and B

R_m = radius of the moon $\cong$ 1740 km

θ_{AB} = angle between A and B.

The geometrical relationships are illustrated on Figure 2-8. By the Pythagorean theorem, neglecting surface curvature, we have for the central angle

$$\theta_{AB} = \left[\left(\theta_{LO} \cos \frac{|b_A| + |b_B|}{2}\right)^2 + \theta_{LA}^2\right]^{\frac{1}{2}} .$$

---

* Revised data dated 2-5-69 give the latitude and longitude of additional points including the corners of the frame (Boeing, 1969).

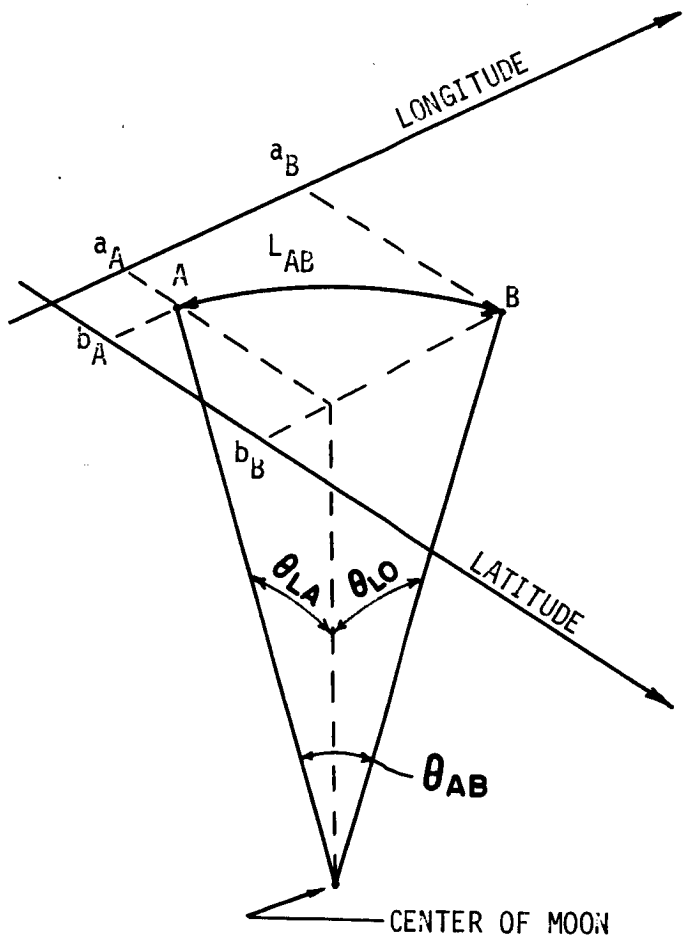

Fig. 2-8. Geometry for determining arc length.

and

$$L_{AB} = \frac{\pi R_m}{180}\left[\left(\theta_{LO}\cos\frac{|b_A| + |b_B|}{2}\right)^2 + \theta_{LA}^2\right]^{\frac{1}{2}}. \qquad (2\text{-}15)$$

In these equations

$$\theta_{LO} = |a_A - a_B|,\ \theta_{LA} = |b_A - b_B|$$

a_A = longitude of point A,

b_A = latitude of point A,

a_B = longitude of point B,

b_B = latitude of point B, and

θ_{LO} is adjusted by $\cos\frac{|b_A| + |b_B|}{2}$ since a degree longitude is smaller near the poles than near the equator. A more correct expression for the distance L_{AB}, which accounts for surface curvature (Roggeveen and Goodman 1968), is

$$L_{AB} = \frac{\pi R_m}{180}\left[\left(\theta_{LO}\cos\frac{|b_A| + |b_B|}{2}\cos\theta'\right)^2 + \theta_{LA}^2\right]^{\frac{1}{2}}, \qquad (2\text{-}16)$$

where

$$\theta' = \frac{|b_A - b_B|}{2}.$$

For central angles less than 3 degrees, $\cos\theta' \cong 0.999$. Therefore, for most of the Orbiter high-resolution photographs where boulder tracks are found, Equation (2-15) is sufficiently accurate.

The Orbiter Supporting Data also give other information including the camera tilt angle and azimuth, and the scale factor. The scale factor for the high-resolution photographs is based on the original size of the frame being approximately 55 mm across and each framelet about 2.54 mm wide. It is understood that these measurements are fairly constant.* If the photograph at hand covers only part of a frame so

---

* Verbal communication with Dr. Henry J. Moore.

that measurements cannot be made from corner to corner, the above information makes it possible to determine the scale nevertheless. This is done simply by multiplying the given scale factor by the ratio of framelet width of photograph at hand to 2.54 mm.

These methods were applied for determination of the scale of the photographs used in the analysis.

Measurements of Boulder and Track

The boulders and tracks were first measured on high-resolution Orbiter frames (approx. 39.8 cm wide). Then the measurements were repeated for most of the boulders on photographs further enlarged, having a scale roughly five times that of the high-resolution frames. The two measurements were averaged and the resulting values of boulder diameter and track width were used in the analysis. Equal weight was given to both measurements because, although objects appeared larger on the enlarged photographs, their boundaries were more blurred and harder to define. The two measurements differed from each other by an average of about 10 per cent, and the maximum difference was about 30 per cent. Such a variation is not surprising, since the smaller boulders were close to the limit of resolution of the photography.

In the analysis of the boulder tracks it was assumed that the boulders were spherical. To make this assumption as valid as possible, only boulders appearing equidimensional on the photographs and leaving relatively smooth and well defined tracks were selected for study.

Estimation of Slope Angle

The slope angle was estimated from shadow relationships on the photograph, using the sun angle as listed in the supporting data. For example, if it can be assumed that a boulder is spherical, the slope can be calculated from measurements of boulder diameter, track width, and length of shadow cast by the boulder. This slope will, of course, be in the direction of the shadow which may not be the direction wanted. A better determination results from the shadow cast by a crater rim or a relatively horizontal upper surface adjacent to a rille. All these

methods, however, depend on certain assumptions based on the investigator's interpretation of the photograph and may therefore be considerably in error. These methods were used to estimate the slope angle, α, for the boulders analyzed. Some slope angles were also provided by the USGS through their photogrammetry procedure.

Material Properties Used

A rock density of 2.7 gm/cc, a soil density of 1.6 gm/cc, and a cohesion of 1×10^3 dynes/cm^2 were used in analyzing the selected boulder tracks.*

RESULTS

The results of the analysis are presented in Figures 2-9 and 2-10. Figure 2-9 shows the relationship between the track width to boulder diameter ratio and the friction angle. Figure 2-10 shows the frequency distribution of the results. As shown in the figure, the friction angles determined as described in this chapter were between 27 and 41 degrees for most of the boulder tracks analyzed. The average friction angle was about 34 degrees.

Some comment on the potential usefulness of the type of plot presented in Figure 2-9 is in order. A fairly well-defined single curve is shown, even though the data represent analyses for slope angles, α, between 0 and 30 degrees. Therefore, such a curve appears suitable for a rough estimate of the friction angle of lunar soils for a variety of conditions from boulder-track measurements. Even without knowing the slope angle, the resulting friction angle would in the extreme case be possibly 5 degrees in error but usually only 1 to 3 degrees from the correct value based on this theory. If a better theory could be developed, similar graphs could be prepared, and fairly reliable values of the actual friction angle of lunar soils could be

---

* Measurements on samples returned by Apollo 11 and 12 (subsequent to these analyses) indicate a rock density of about 3.1 gm/cc.

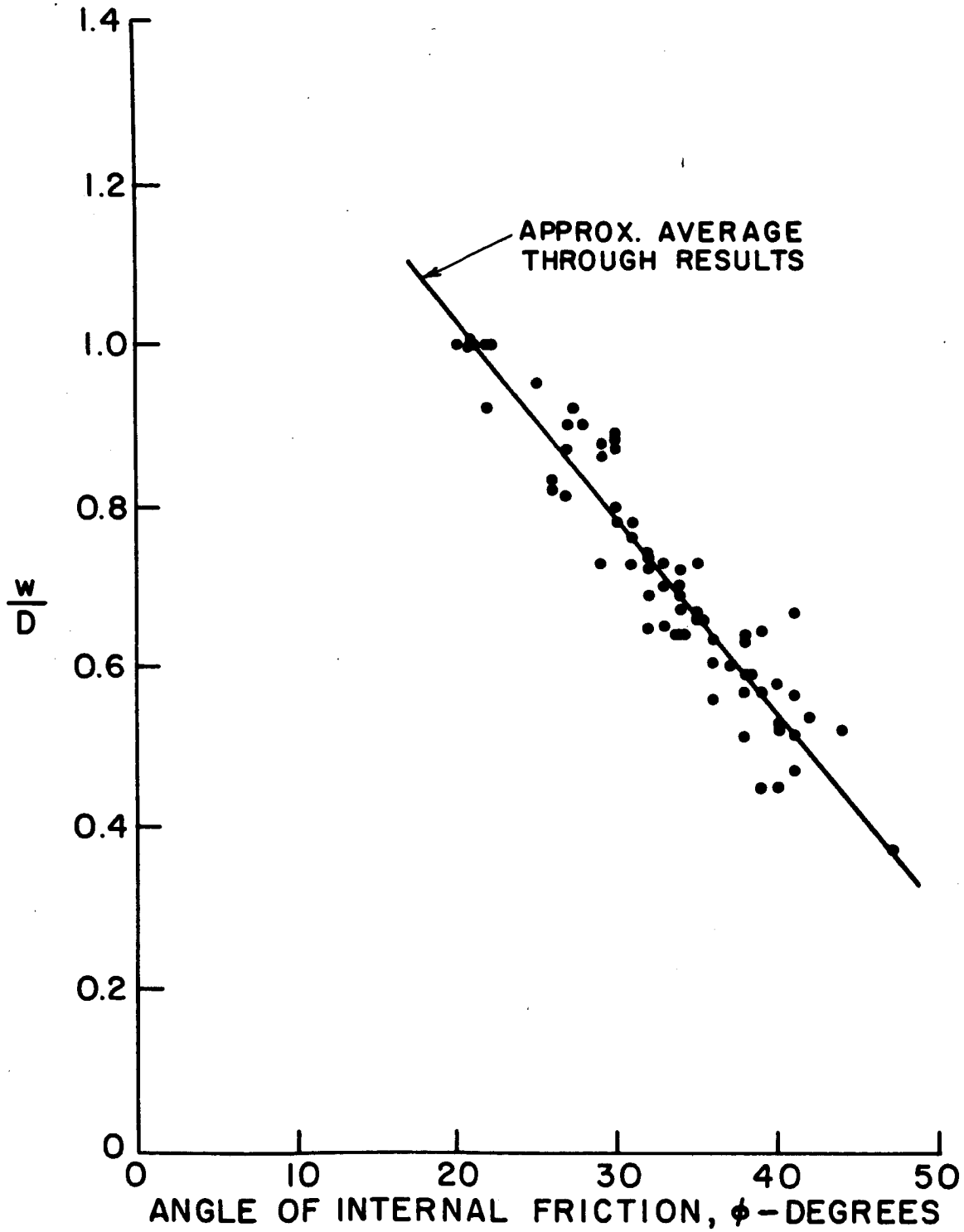

Fig. 2-9. Track width over diameter ratio vs friction angle.

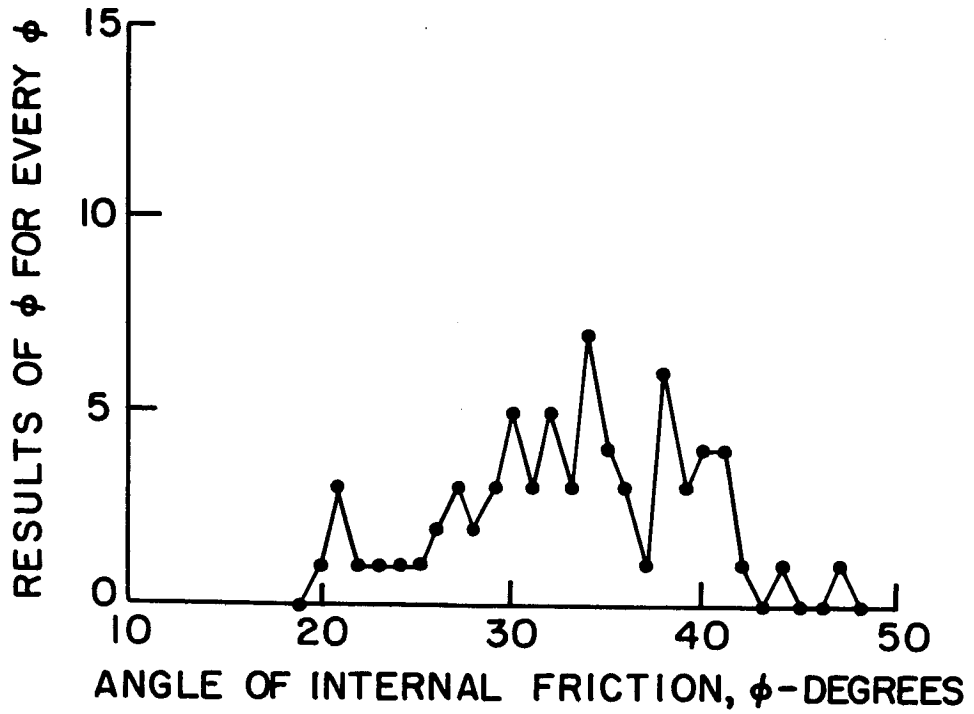

(a)

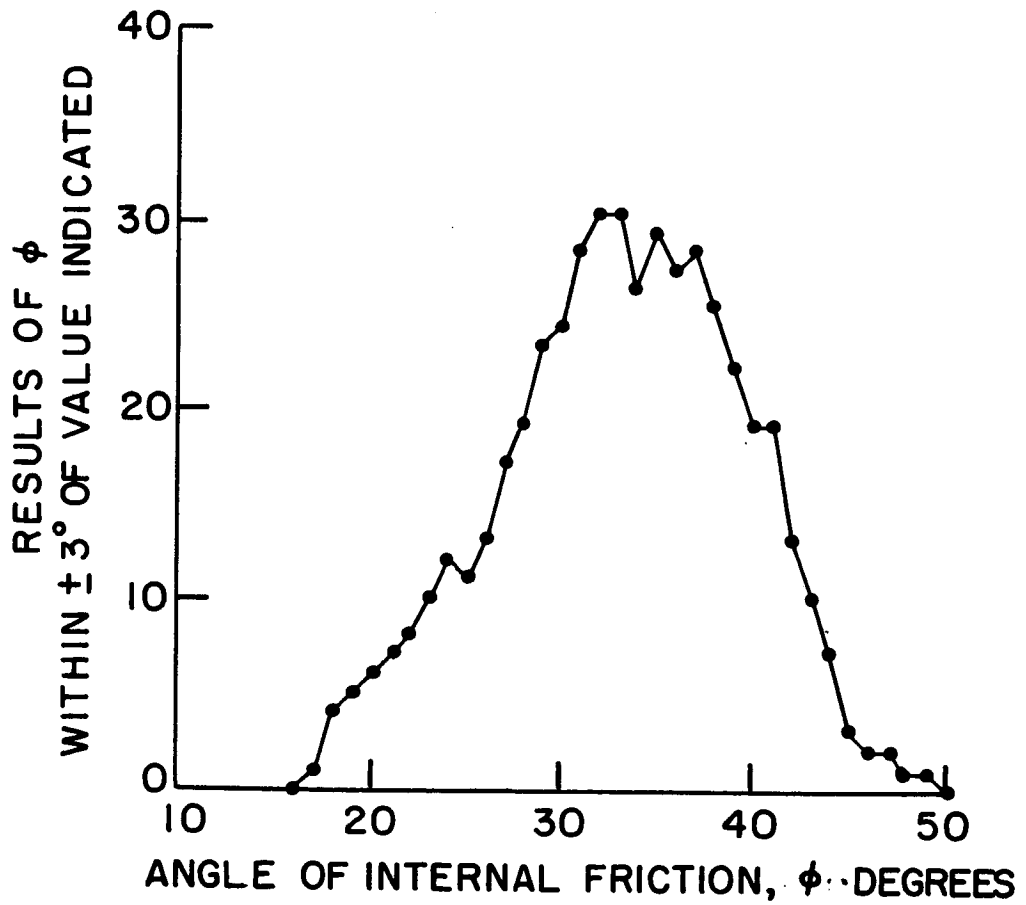

(b)

Fig. 2-10. Frequency distribution of the results.

easily determined from the boulder-track relationship.

Detailed data and results on each boulder track studied are presented in Chapter 7 (Table 7-1A, B, C) where the boulder tracks are reevaluated using an improved theory.

Chapter 3. MODEL STUDIES OF THE FAILURE MECHANISM ASSOCIATED WITH A SPHERE ROLLING DOWN A SOIL SLOPE

Model experiments were conducted to form a rational basis for theoretical developments, and to gain some understanding of the three-dimensional nature of the sphere-soil slope interaction phenomenon. This chapter describes how the models were constructed, presents photographs of the results, and discusses possible interpretation of the observed features. A failure mechanism is proposed, which may also be applicable to many cases of wheel-soil interaction.

MATERIALS AND EQUIPMENT

The models were constructed in a rectangular pan approximately 50 cm long, 30 cm wide, and 12 cm deep, using a mixture of ten parts fine to medium air-dry sand and two parts plaster of paris. Gradation of the sand (PCA Lapis Lustre #0 fine sand) and the mixture are shown in Figure 3-1. Figure 3-1 also compares this gradation to the sand used for the rolling sphere tests at WES (Yuma Sand), and to that of actual lunar soil (Apollo 11 samples).

Additional test equipment consisted of:

1. a glass cylinder or jar used for compaction,
2. a shaker and a dropper used for deposition of intermittent dark layers and vertical markers, respectively, and
3. a sphere (diameter of 12.10 cm, density of 3.69 gm/cc).

The sphere was rolled over the sand/plaster of paris models, which were then hardened by saturation. It was noted that the top of the models settled about 1 mm during saturation. After saturation and solidification, density measurements were made on pieces of the models. From these measurements, the following approximate values of density and void ratio were obtained:

density before saturation = 1.59 gm/cc
void ratio before saturation = 0.68
density after saturation = 1.61 gm/cc
void ratio after saturation = 0.66.

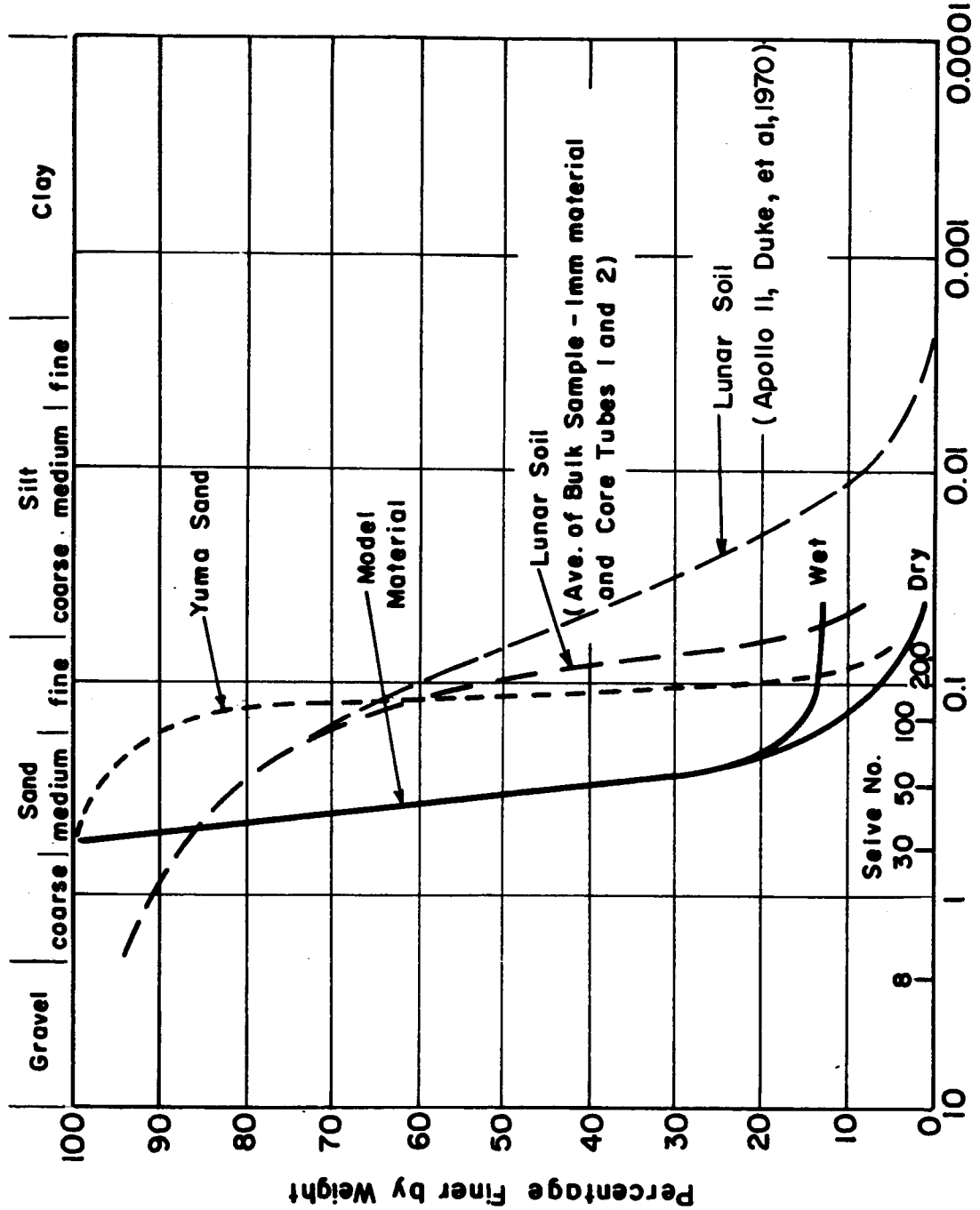

Fig. 3-1. Particle size distribution for model material, Yuma sand, and lunar (Apollo 11) soil.

MODEL PREPARATION AND TESTING PROCEDURE

The models were prepared and tested as follows:

1. A 1-cm-thick layer of clean coarse sand was placed on the bottom of the pan to serve as a drain.

2. The first layer (about 1-cm thick) of the sand and plaster of paris mixture was placed gently on the coarse sand layer and leveled off with the top of the pan.

3. This layer was compacted by rolling a glass jar once over the surface. Additional material was then added and leveled to make the layer exactly 1-cm thick.

4. A thin (approximately 1 mm) layer of a cement and coal powder mixture was deposited using a shaker.

5. The next layer of sand/plaster of paris mixture was placed in the same fashion. The soil directly on the dark layer of cement and coal powder had to be placed with great care to prevent disturbance. The model was built up to the desired height using 1.0- and 0.5-cm-thick layers.

6. Vertical markers were inserted to enable the determination of horizontal movements. This was accomplished by making a 1-mm-wide slot vertical to the drainage layer with a spatula. By moving the spatula gently back and forth it was possible to make the slot stay open when the spatula was removed. Coal powder was then deposited into the slot using a dropper.

7. A template with small holes in a hexagonal pattern was placed on the surface of the model, and a cement-coal powder mixture was shaken over the template. Removal of the template left a hexagonal pattern of dark dots on the top surface of the model. Distortion of this pattern indicated surface movements.

8. The sphere was placed on one end of the model, and the model was gradually tilted to an angle of about 13 degrees, at which point rolling was impending. The sphere was rolled the desired distance and taken off, and the model tilted back to a horizontal position.

9. The model was water-saturated slowly from the bottom; this process took about 1 hour.

10. The model was left to harden and cure.

11. After solidification, the model was sawed along desired sections.

RESULTS

Photographs of the models are presented in Figures 3-2 through 3-6. Deviations from straight lines in both top view and section photographs show the extent and nature of deformations.

Figure 3-2 gives a top view of Model 1 and the numbering of the cross sections. Knife marks along the edges show where the model was subsequently cut to expose cross sections. One longitudinal section was made down the center of the track. Cross sections of Model 1 are shown on Figure 3-3, and the longitudinal section is shown on Figure 3-4.

Model 2 was constructed primarily to study general shear in greater detail by using thinner layers (0.5 cm) and to study lateral movements. The cross sections of Model 2 are shown in Figure 3-5, a longitudinal section in Figure 3-6.

DISCUSSION

The most noticeable features on the preceeding photographs appear to be:

1. Forward movement of soil as shown in both top-view and longitudinal section photographs. Lateral movement of soil is relatively small.

2. Volume change of soil (compression directly under the sphere and dilation to the sides and front) as shown in the cross sections.

3. Shear planes, particularly in the longitudinal sections, and also in the cross sections.

Forward Movements

Perhaps the most interesting observation from these models is the pronounced forward movement of soil immediately under the track. The nature of this movement is shown in Figures 3-2, 3-4, and 3-6. It is of interest

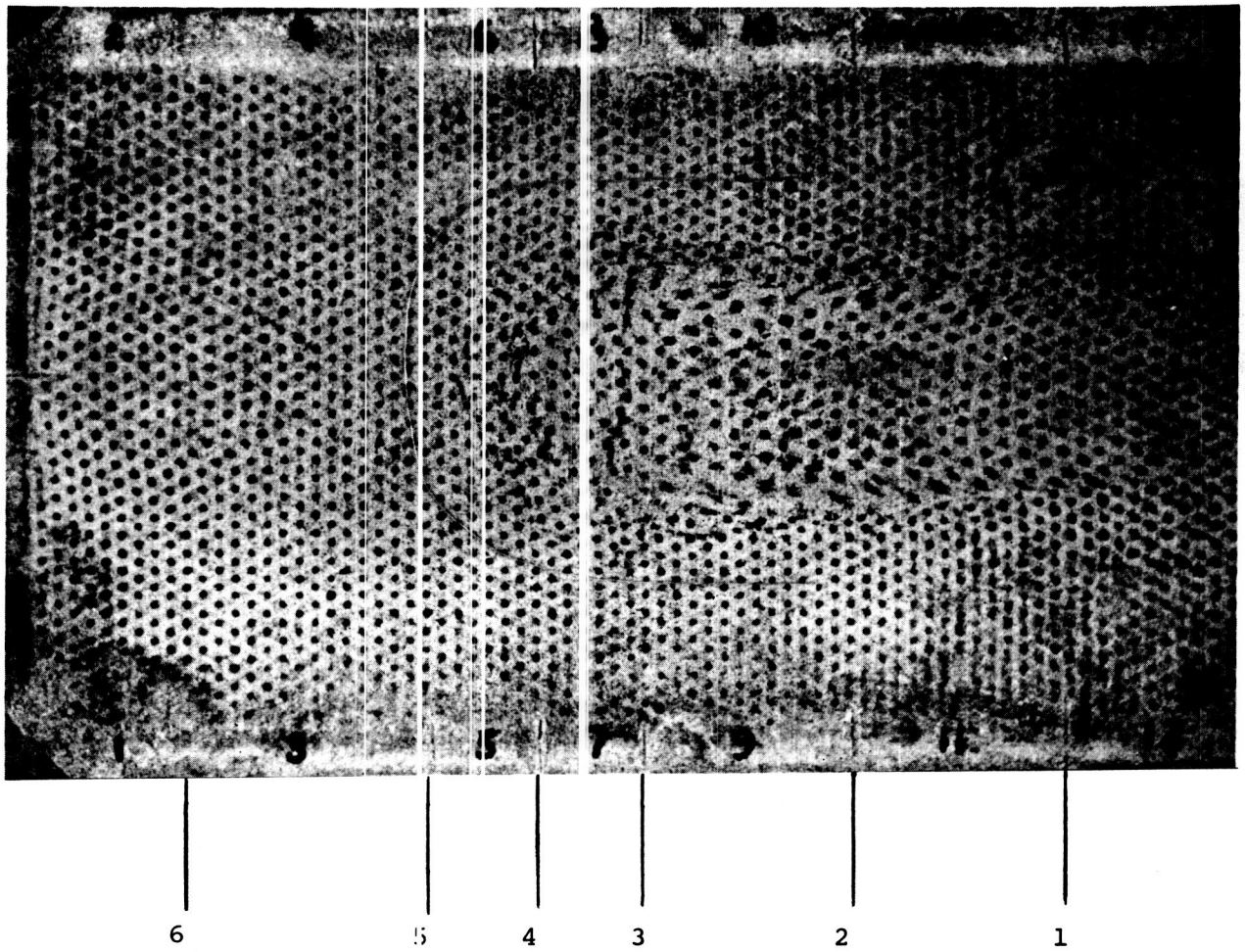

Fig. 3-2. Top view of model 1 showing surface deformation. The small numbers are the cross section numbers.

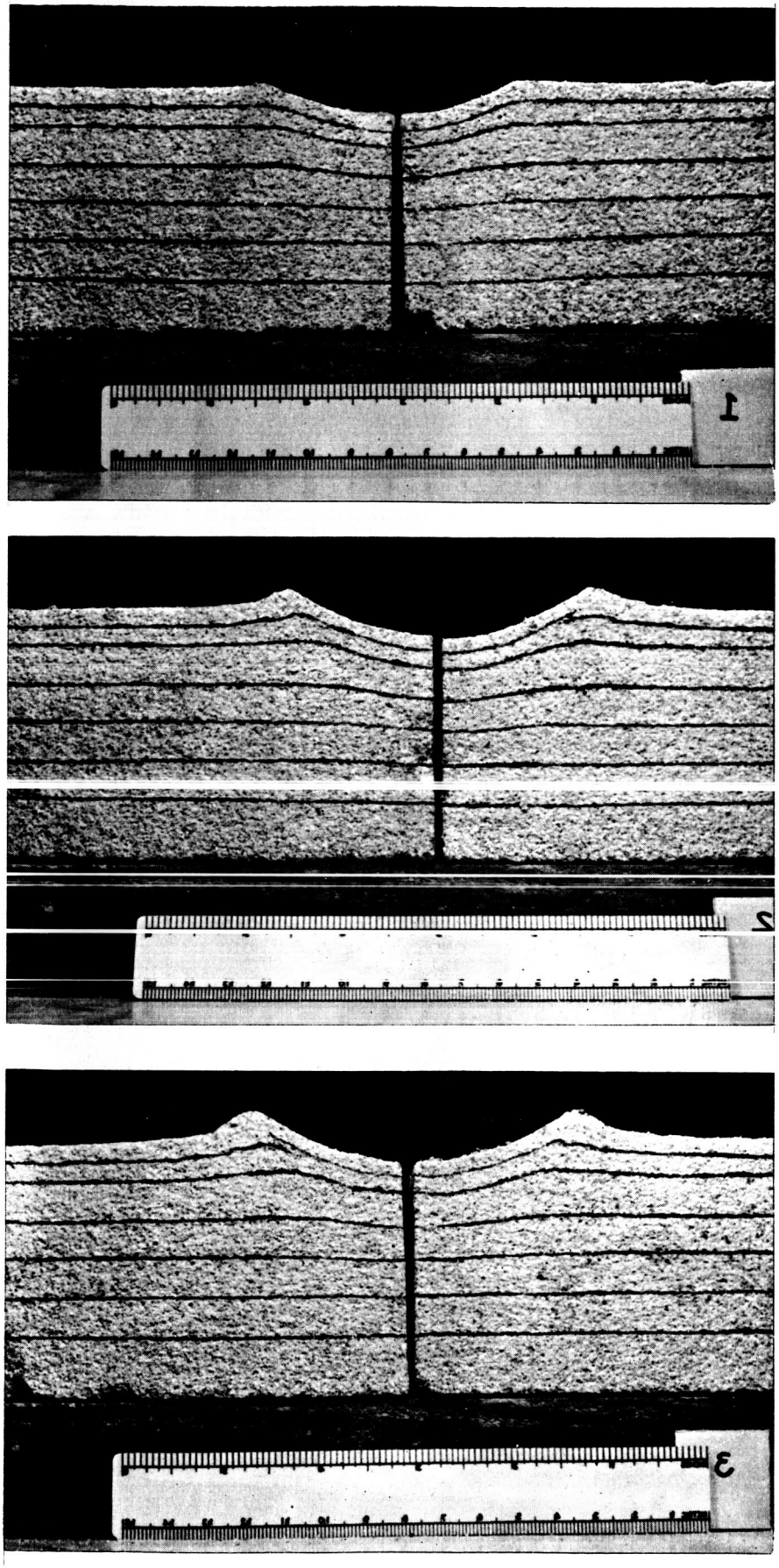

Fig. 3-3a. Cross sections of model 1.

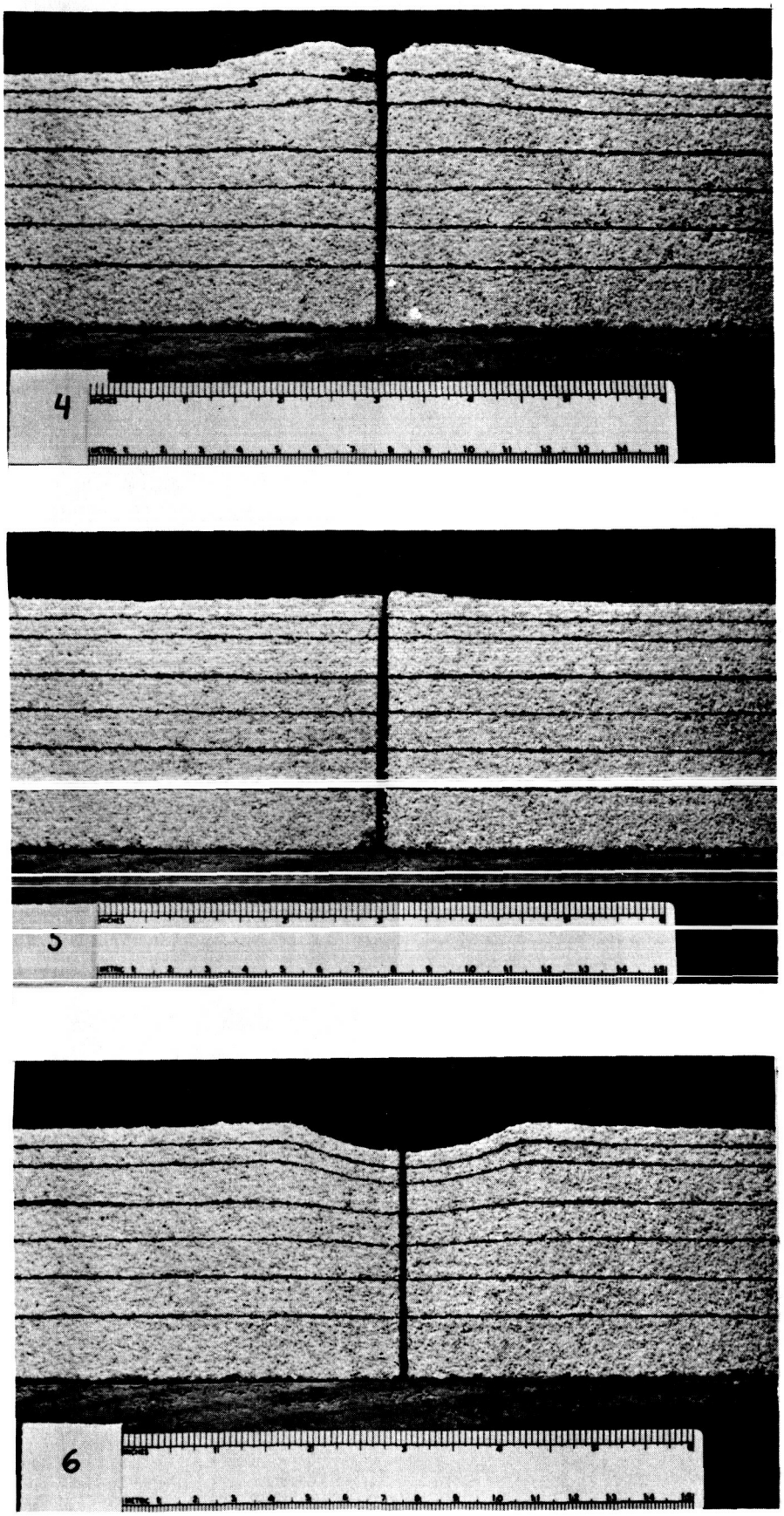

Fig. 3-3b. Cross sections of model 1.

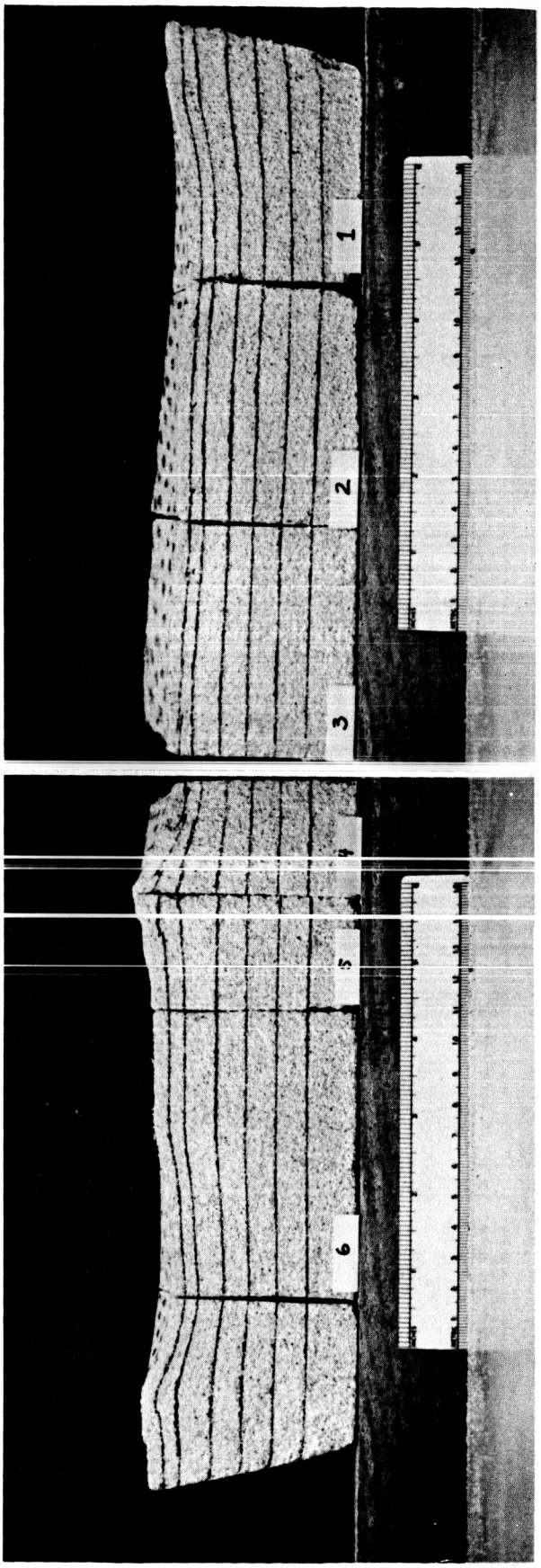

Fig. 3-4. Longitudinal section of model 1.

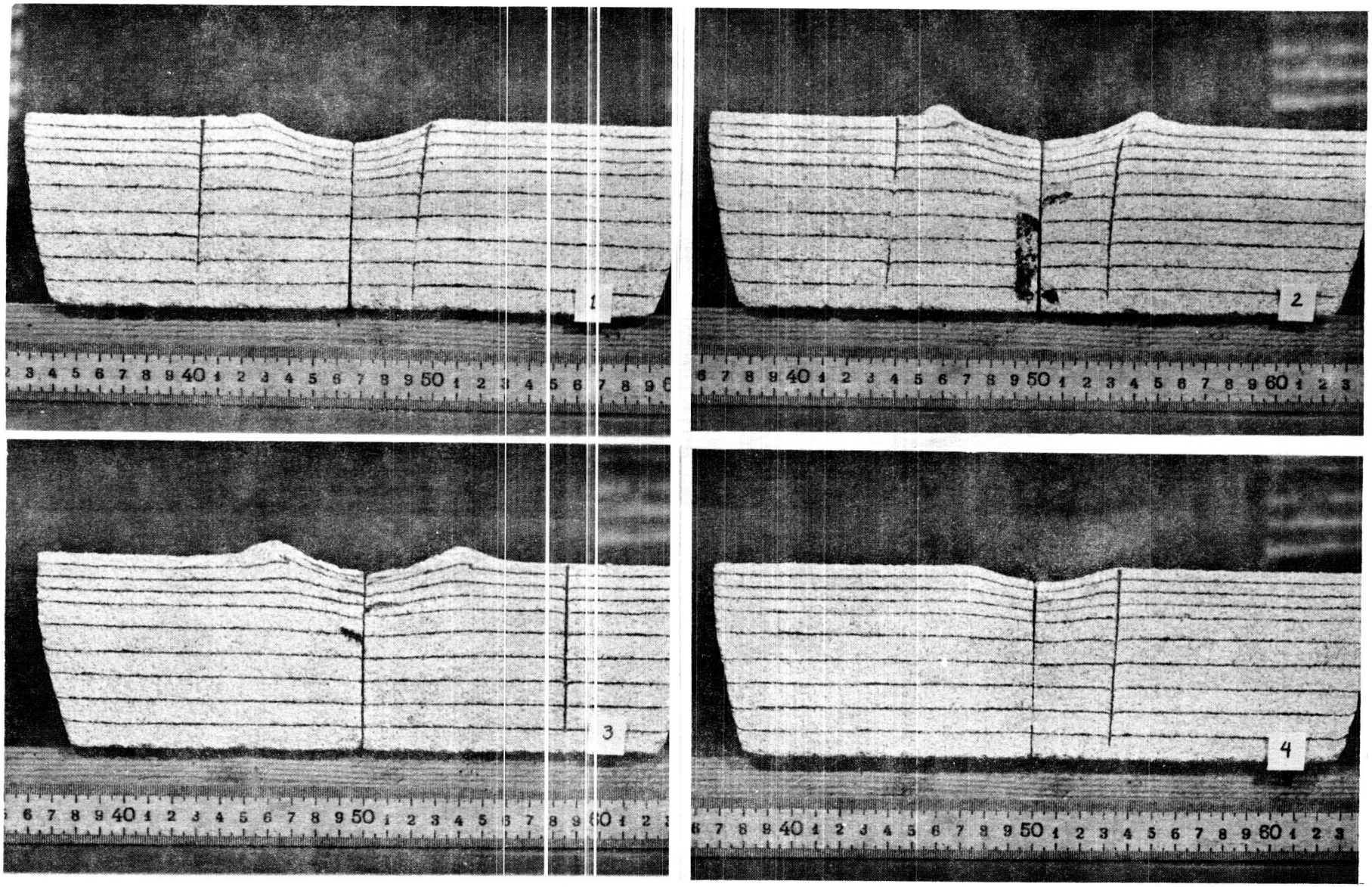

Fig. 3-5. Cross ections of model 2.

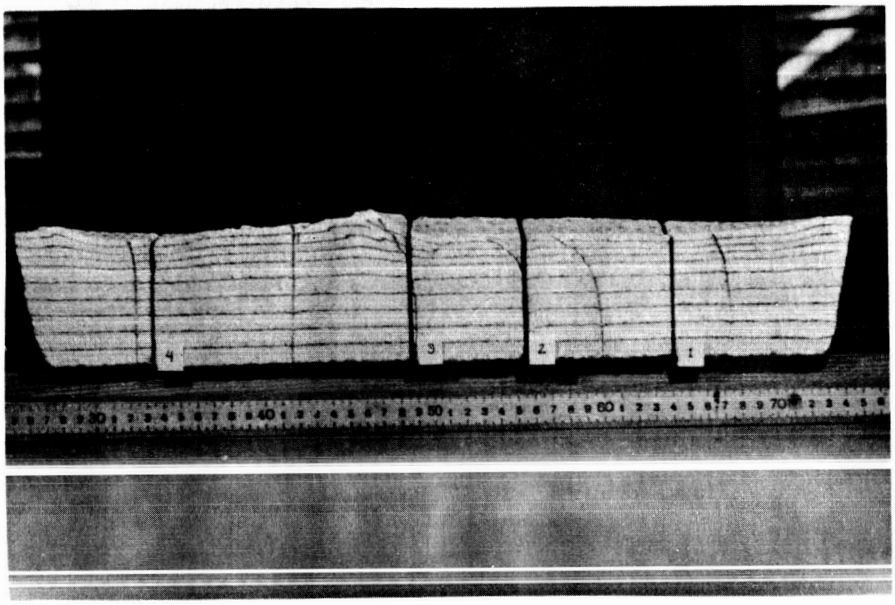

Fig. 3-6. Longitudinal section of model 2.

to consider the subsurface movements in more detail and to see if the subsurface and surface movements are related.

Subsurface movements are best seen on the longitudinal section of Model 2 (Figure 3-6) where forward movements are represented by bending of the originally vertical dark markers. To illustrate certain details, the same section with some added lines is presented in Figure 3-7a. An enlargement of part of the model (Figure 3-7b) gives the position of the sphere when it stopped -- just back of the fourth vertical marker. On the enlargement, the third vertical marker is superimposed on the location of the fourth. Two conclusions can be drawn:

1. Most of the forward movement takes place before the edge of the sphere encounters the soil, as shown by the bending of the fourth marker.

2. Some additional forward movement takes place as the point on the sphere where soil contact is made moves to the position vertically below the center of the sphere (indicated by the bending of the third marker).

The net effect of rolling a sphere over a soil slope is, therefore, a forward bending of the originally vertical sections. It seems that the bent shape could be reproduced simply by bending the section forward as if it were a steel spring. Minor stretching would be required, and it is believed that this is associated with general shear close to the surface. It should be noted that, while bending of these sections (markers) extends to a depth of approximately 5 cm, no general shear planes can be seen below a depth of 1.5 cm from the bottom of the track. Hence, subsurface deformations observed must be largely due to shearing distortion and volume change.

To compare forward movements as measured from the longitudinal section of Model 2 with those measured from the top-view photograph of Model 1, it is desirable to identify the movements on the top-view photograph of Model 1 more clearly. Figure 3-8 is the same top-view of Model 1 as that in Figure 3-2, with grid lines added. The line around the track outlines the approximate outer limit of surface deformation, and the inner closed line is the approximate limit of soil-sphere contact. In this case, a track width that is slightly smaller than the crest-to-crest distance is defined.

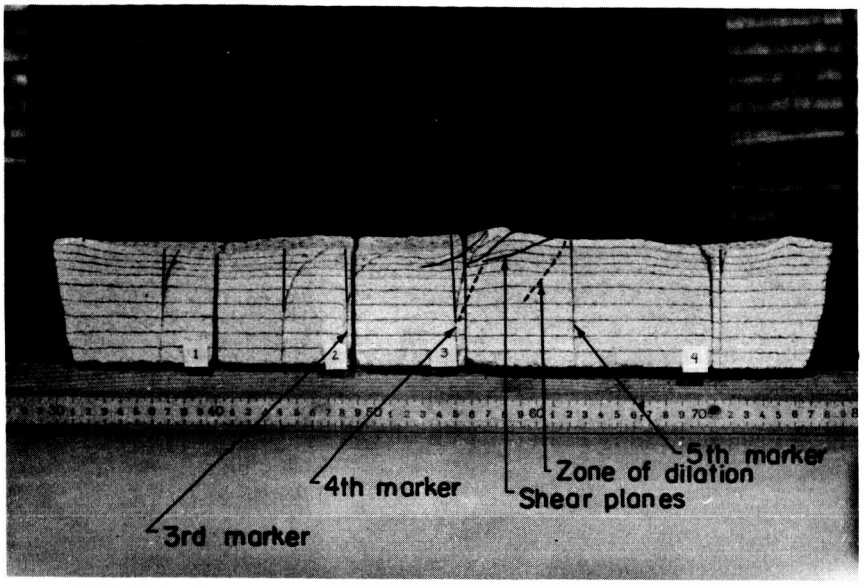

a) Longitudinal section of Model 2.

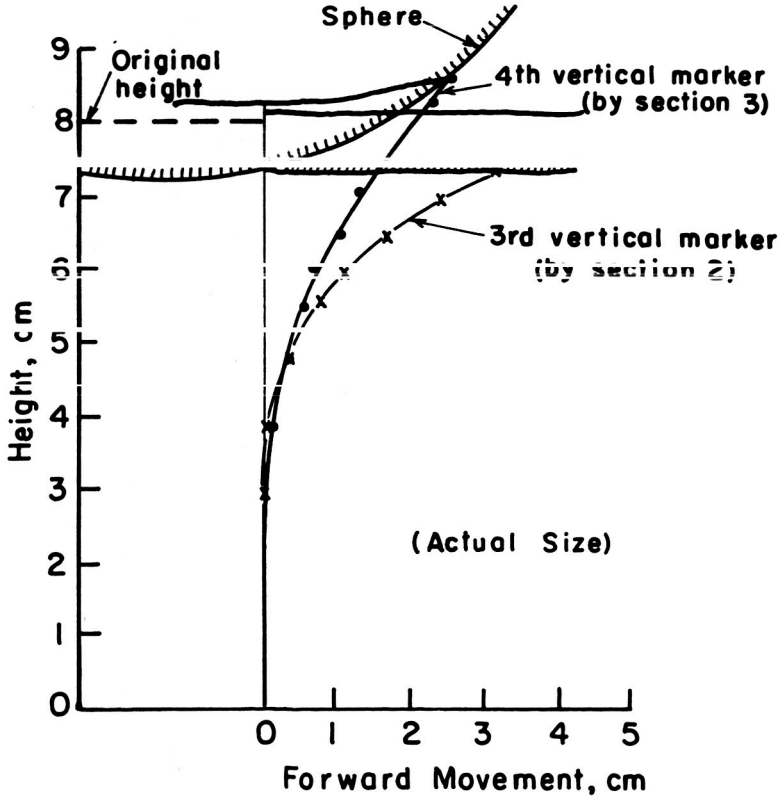

b) 3rd and 4th vertical markers (Model 2)

Fig. 3-7. Forward movement as shown in the longitudinal section of model 2.

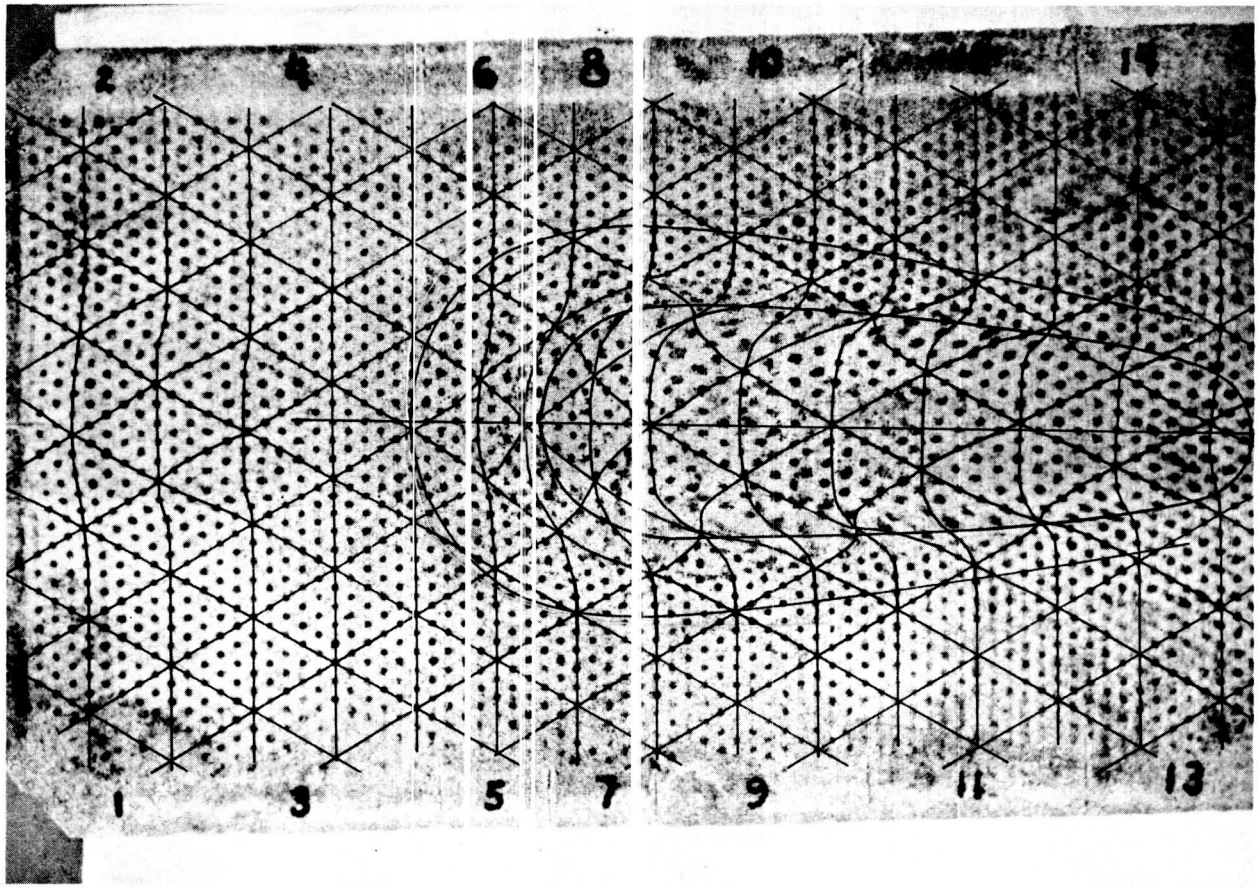

Fig. 3-8. Top view of model 1 showing surface deformation and track.

A comparison of forward movements as measured on Figure 3-8 and from the longitudinal section of Model 2 (Figure 3-7a) is presented on Figure 3-9. This figure shows that the movements are comparable and that, for this material, surface deformations are indicative of subsurface movements. Some deviation is seen at small track width or at the beginning of the track. This deviation is probably due to differences in the formation of the tracks for the two models.

Volume Changes

By studying the cross section photographs, it appears possible to distinguish zones of compression, dilation, and shear. In the following discussion these zones are determined, and the cross sections are analyzed in greater detail.

Zones of compression were determined by noting at what points the distance between the dark interfaces decreased from the original values. (Linear measurements were made using a magnifying glass with a built-in scale reading to one-tenth of a millimeter.) Zones of dilation were determined similarily by noting at what point the distance between two dark interfaces increased from the original values. These criteria are illustrated in the cross sections in Figures 3-10 and 3-11. The region directly below the sphere is a zone of volume decrease. Regions immediately under the crests of the track are zones of dilation. The region in front of the sphere is also a zone of dilation (see Figure 3-11, cross section 4, and photographs of the longitudinal sections).

The magnitude of volume changes was measured from the photographs using a planimeter. Compression or volume decrease is represented by the segment of the circle below the respective reference line drawn parallel to the original surface or dark interface (Figures 3-10 and 3-11). Dilation or volume increase is represented by the area above the reference line and is associated with the crests of the track. The results of these measurements, as given in Figure 3-12, present dilation and compression versus the depth below the original surface of Model 1. These results are compared below with those of pressure under a sphere as a function of depth.

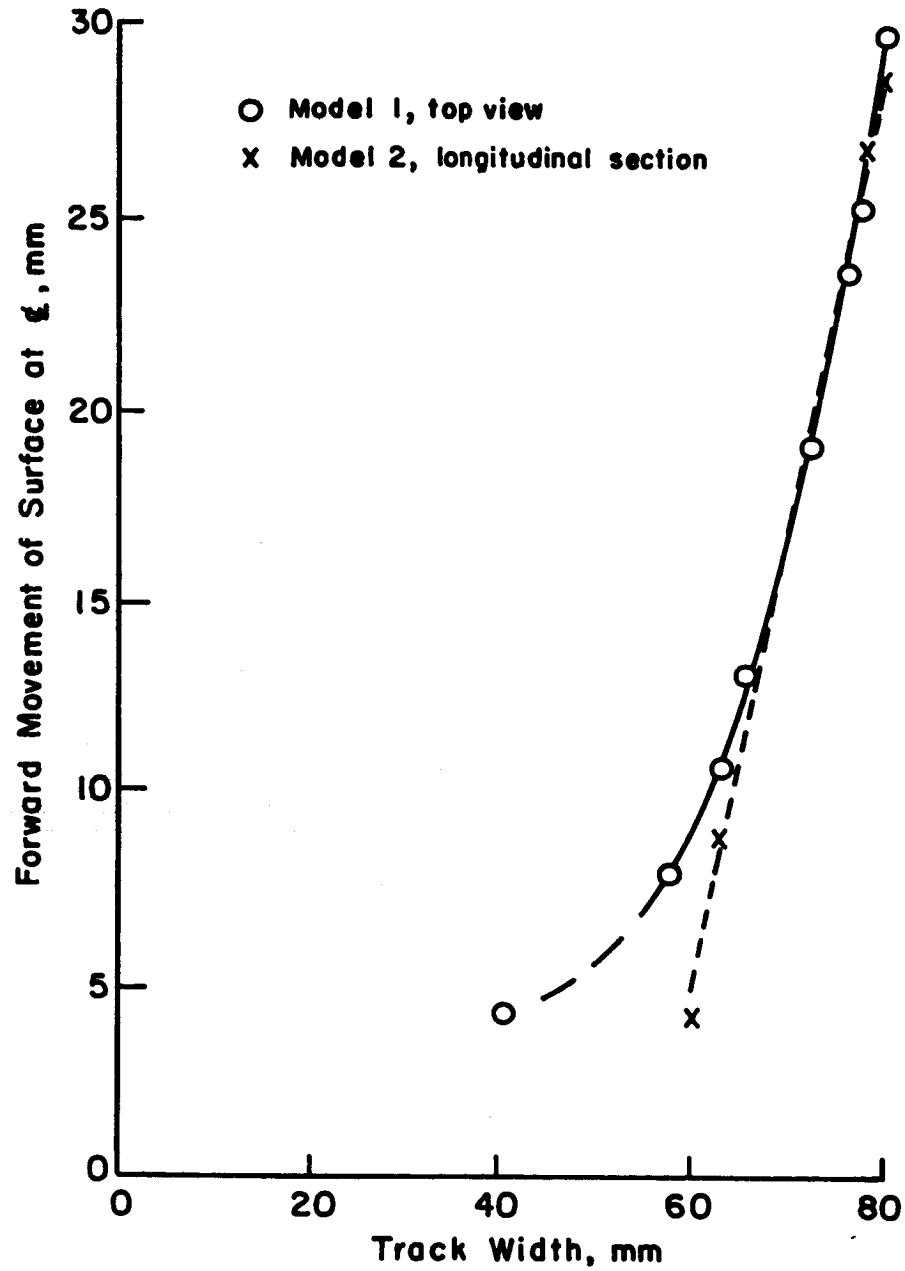

Fig. 3-9. Comparison of forward movement of surface as measured from top view and longitudinal section.

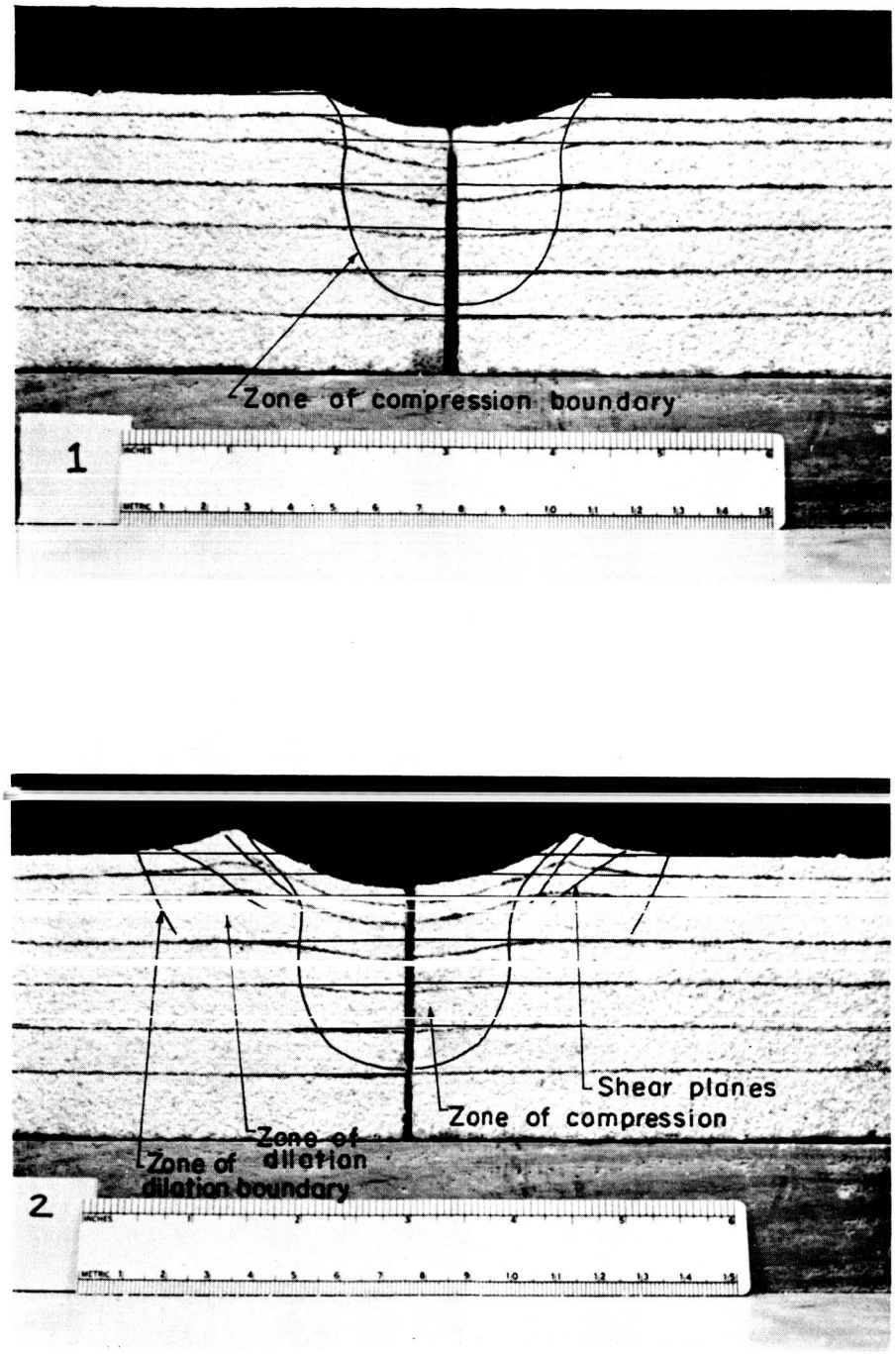

Fig. 3-10. Cross sections 1 and 2 of model 1 showing zones of compression and dilation.

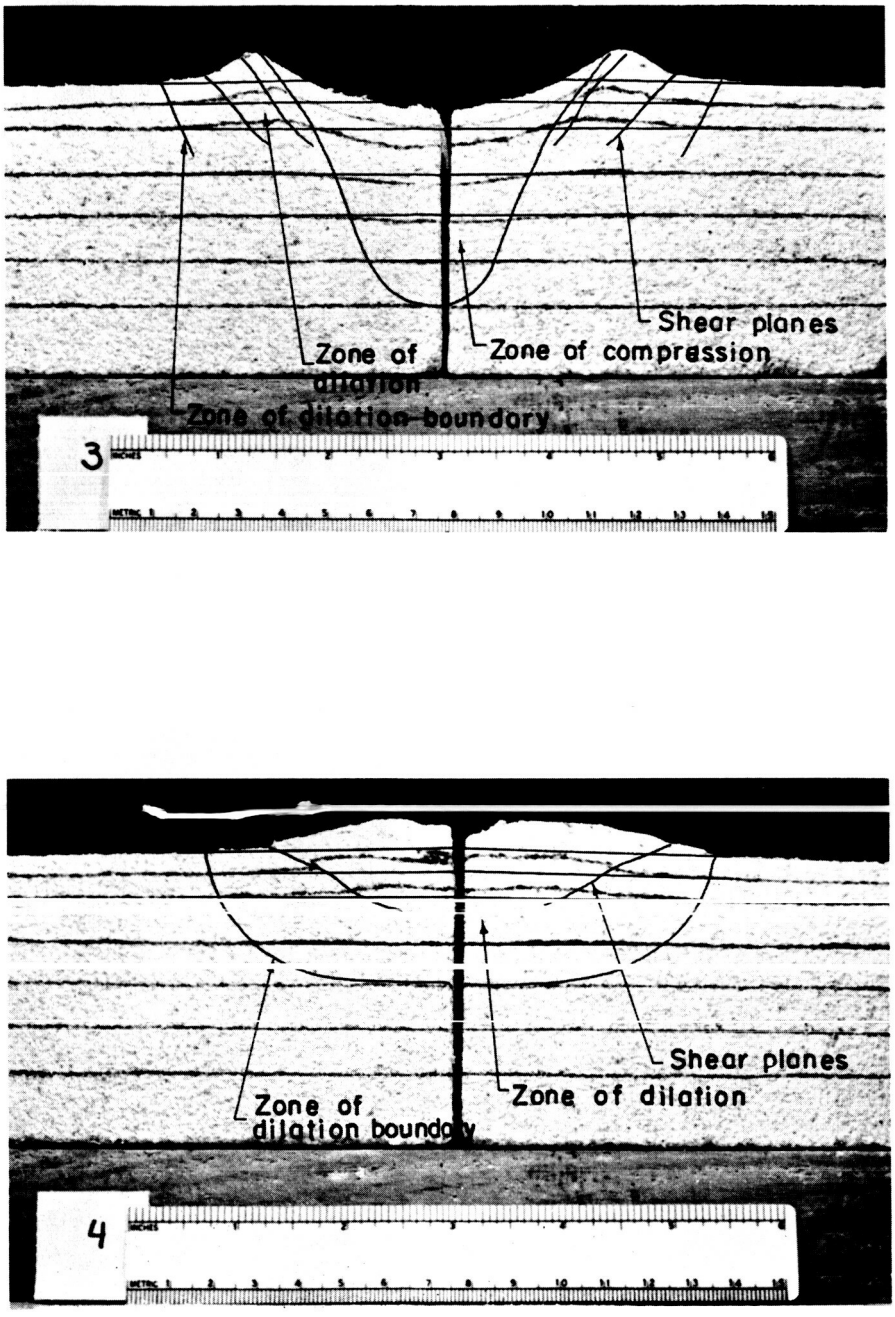

Fig. 3-11. Cross sections 3 and 4 of model 2 showing zones of compression and dilation.

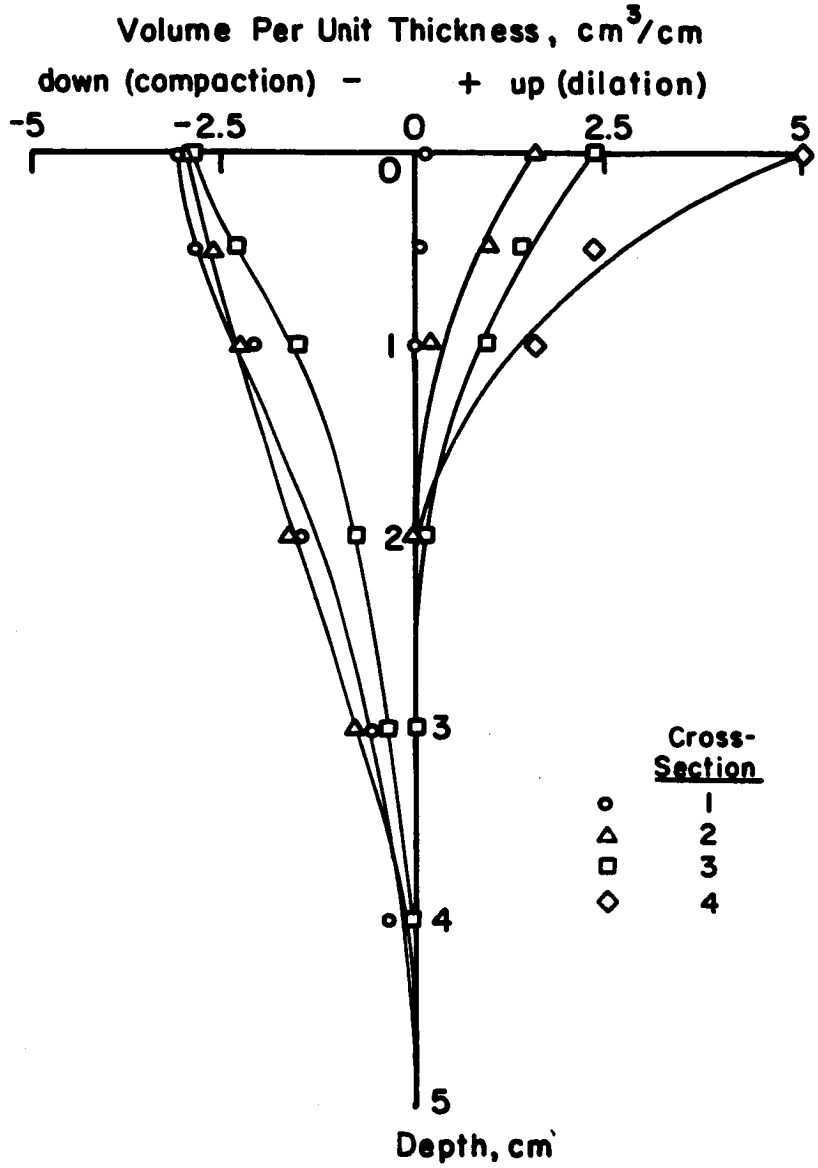

Fig. 3-12. Volume change vs depth below original surface for model 1.

An assumption in many problems is that deformations are proportional to the applied pressure. This assumption is generally considered valid for sands, although the proportionality coefficient, k_s (Terzaghi, 1943), is a function of depth. It is of interest to determine to what extent this proportionality is valid for the case of the rolling sphere. This can be accomplished by considering Boussinesq's solution of the pressure distribution beneath a circular loaded area. The pressure distribution at the soil-sphere contact is believed to be approximately parabolic. In the vicinity of the second cross section of Model 1 the track width was approximately 8 cm. Since the actual contact area is somewhere between circular and semicircular (Hovland and Mitchell, 1970), an average width of 6 cm was assumed for comparison purposes. Figure 3-13 compares pressure and deformation as functions of depth. The deformation curves are actual measurements from the cross sections. It is apparent that the pressure curve and the deformation curve for the second cross section are almost identical. These curves should also be compared with Figure 3-12. From the similarity thus established, it can be concluded that the deformations are approximately proportional to the applied pressure.

General Shear

General shear has been shown to develop predominately in the forward direction (Model 2, Figure 3-7a). The lateral shear in the cross section of Model 2 is probably a consequence of forward shearing.

To explain some of the details observed on the longitudinal sections associated with general shear, the sequence of rolling and shearing of a sphere is diagrammed in Figure 3-14; (a) the soil before the sphere has rolled over it; (b) the shear planes and deformations that develop as the sphere rolls to the right, to position B; and (c) the appearance of the section after the sphere has rolled past. These same features can be observed in the photographs.

Observations of particular interest are:

1. Shear planes do not appear to originate at the sphere surface (see Figure 3-14b), as is often considered the case with shear under a loaded footing.

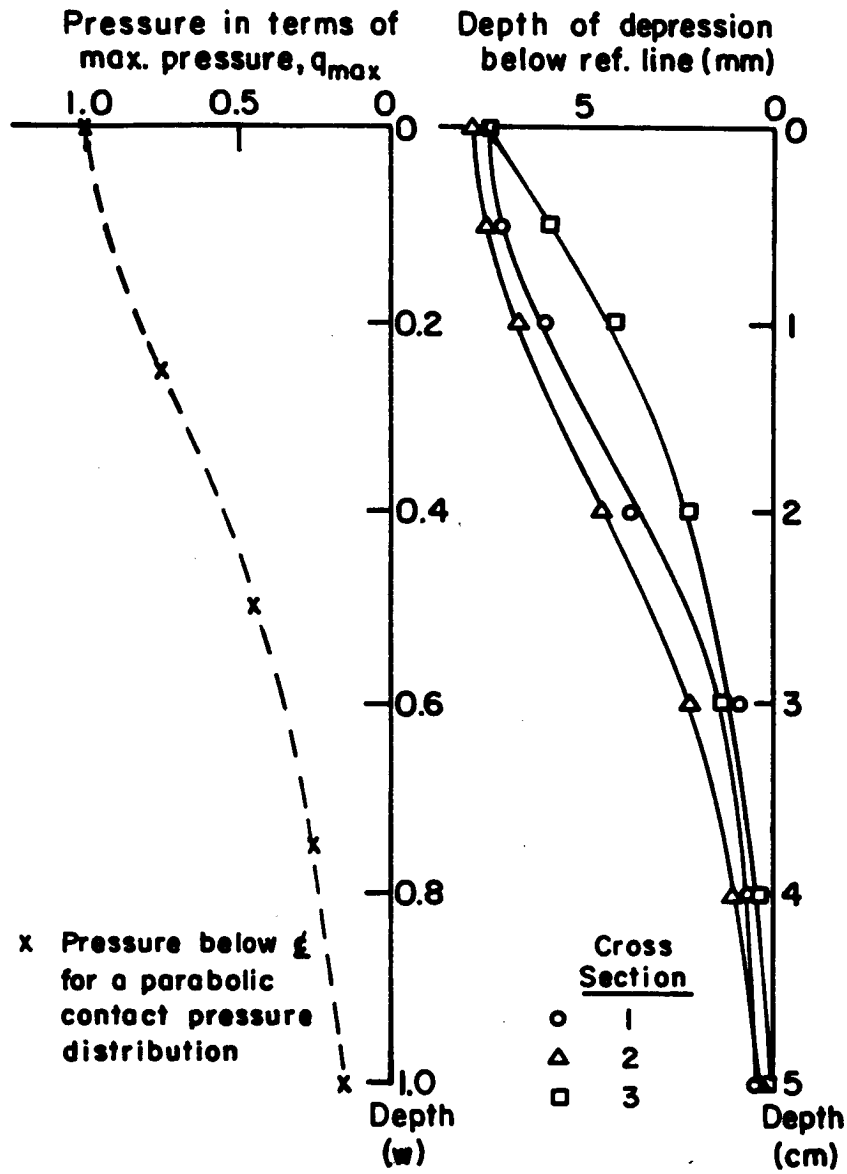

Fig. 3-13. Comparison of pressure and deformation as functions of depth.

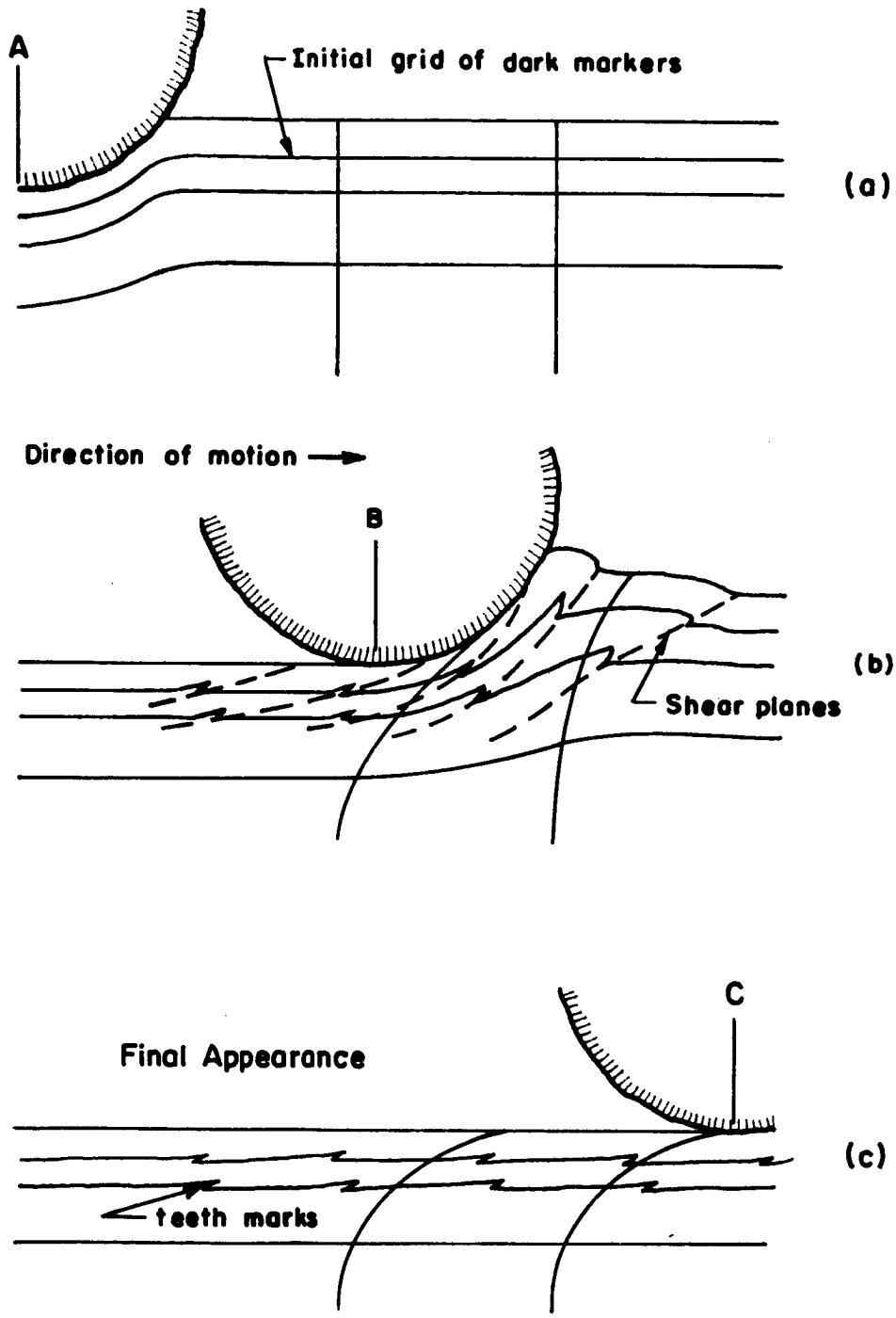

Fig. 3-14. Sequence of soil shearing under a rolling sphere.

2. At the time a shear plane develops, its lower end is roughly parallel to the sphere surface. It diverges from a direction parallel to the sphere surface as it proceeds up and forward.

3. A wedge of soil is apparently pushed up and forward.

4. Movement along any one shear plane is restricted, as implied by the relatively short but constant displacements.

5. Shear planes are spaced at relatively constant intervals as can be seen from the spacing of the teeth marks (compressed remnants of once active shear planes).

It is possible to conclude that the shearing process is not continuous, but consists of separate small shear failures spaced at relatively constant intervals with respect to space and time. The spacing of the shear planes as well as the amount of movement along any one shear plane is undoubtedly a function of soil type. Hence, although the rolling of a sphere down a slope may appear continuous to the naked eye, it is possible that the acceleration of the sphere changes slightly from one shear plane to the next.

The fact that shearing along any one shear plane appears to be restricted to a relatively small amount is perhaps associated with the change in direction of the shear plane and of the stress causing the movement. Most of the movement along a shear plane probably takes place when the plane is first formed. At that time, it is directed forward at the critical angle of $45° - \phi/2$ to the direction of the major principal stress (Scott, 1963). Hence, one can also estimate the direction of the principal stresses along the shear plane, provided it is in the position where it was first formed. As the sphere moves forward, the shear plane bends or turns toward a more vertical position. As the sphere passes, the shear plane is again bent down toward a final, more horizontal position (Figure 3-14).

PROPOSED FAILURE MECHANISM

The proposed hypothesis of a failure mechanism presented below is restricted to a rigid sphere rolling on a deformable material such as a sand slope. For such a material, the failure mechanism is dependent on the state of compaction. In a very loose state, the material would be compressible and the deformations would consist of both volume change and shearing distortion, but no general shear planes would develop. In a very dense state, general shear would be more significant, although volume change and shearing distortion would also take place. The usual case would involve all three phenomena: Initial volume change accompanied by shearing distortion would be followed by general shear if the material were sufficiently dense.

The following steps appear to be involved as a sphere rolls over a sand slope:

1. Compression occurs under the sphere.
2. Initially vertical sections are bent forward.
3. A horseshoe-shaped zone of dilation, which extends from the sides and around the front of the sphere, develops. This zone moves forward with the sphere (analogous to a compressional wave). The external evidence of this zone of dilation is the bow wave that forms in front of the sphere as material accumulates.
4. When volume changes and shearing distortion can no longer account for all the soil displacement, general shear planes develop. The development of general shear planes is probably influenced by the magnitude of shearing distortion and the magnitude and direction of the major principal stress. The amount of shearing distortion that can occur without the development of shear planes is proportional to the confining pressure. Confining pressure increases with depth, and the applied stress at the sphere-soil contact increases approximately parabolically from the edge of sphere-soil contact. Therefore, shear planes would develop where the deformation reaches a critical magnitude with respect to the confining pressure. These planes would be oriented approximately in a direction of $45° - \phi/2$ to the direction of the major principal stress.

5. Sliding along the shear planes continues only for a short time and distance, as previously described.

6. After a certain distance, a new shear plane develops and the shearing cycle repeats itself.

7. As the sphere rolls down the slope, deformations assume a final position, as shown on the photographs, and excess material from the bow wave is wasted to the sides to form the crests of the track.

CONCLUSIONS AND RECOMMENDATIONS

Models such as those used for this study have proved valuable in the investigation of surface and subsurface deformations. The vertical dark markers proved to be particularly helpful.

Due to the limited model length, the track was short. It is possible that some additional effects would develop with long, continuous rolling. The proposed failure mechanism is reasonable.

Resistance to rolling on sand appears to be caused by volume change, shearing distortion, and general shear. At higher velocities, inertia effects may also be important. Determination of the relative contributions of these phenomena to the total resistance requires further investigation.

Chapter 4. PRESSURE DISTRIBUTION AND SOIL FAILURE BENEATH A SPHERICAL WHEEL IN AIR-DRY SAND

To develop a theoretical explanation of the rolling sphere-soil slope interaction phenomenon, the pressure distribution beneath the sphere, in addition to the failure mechanism, must be understood. A failure mechanism associated with a sphere rolling down a soil slope was proposed in Chapter 3. This chapter describes studies to determine the pressure distribution.

Experiments were carried out using an instrumented spherical wheel at the U. S. Army Engineer Waterways Experiment Station (WES), Vicksburg, Mississippi. The assistance provided by the WES to this effort was funded through NASA Defense Purchase Request (DPR) H-58504A from MSFC to WES. The results provided information on the following:

1. The distribution of contact pressure beneath a towed spherical wheel rolling on air-dry sand, and
2. The appearance of the resulting track, revealing surface features of soil deformation and failure.

The equipment, facilities at WES, and soil used are described first. This is followed by a description of the testing procedure and results. The discussion and analyses are primarily concerned with the contact pressure distribution.

EQUIPMENT, FACILITIES, AND SOIL

Equipment

A special spherical wheel was designed and instrumented in order to measure normal pressure at the sphere-soil interface during rolling. The spherical wheel was intended to simulate a solid spherical boulder. Therefore, it was designed to act as a rigid body. Figures 4-1 and 4-2 show side and front views of the spherical wheel. The outer shell was 1/2 inch thick. Deformations were calculated using an axisymmetric finite element program based on shell theory (M. Khojasteh-Bakht, 1967). For a 1/2-inch-thick hemispherical shell, 24 inches in diameter, loaded by an axisymmetric parabolic pressure distribution, the maximum deflection of the shell, which takes place directly under the point of maximum pressure, was found to be 0.0011 inches for a maximum pressure of 40 psi.

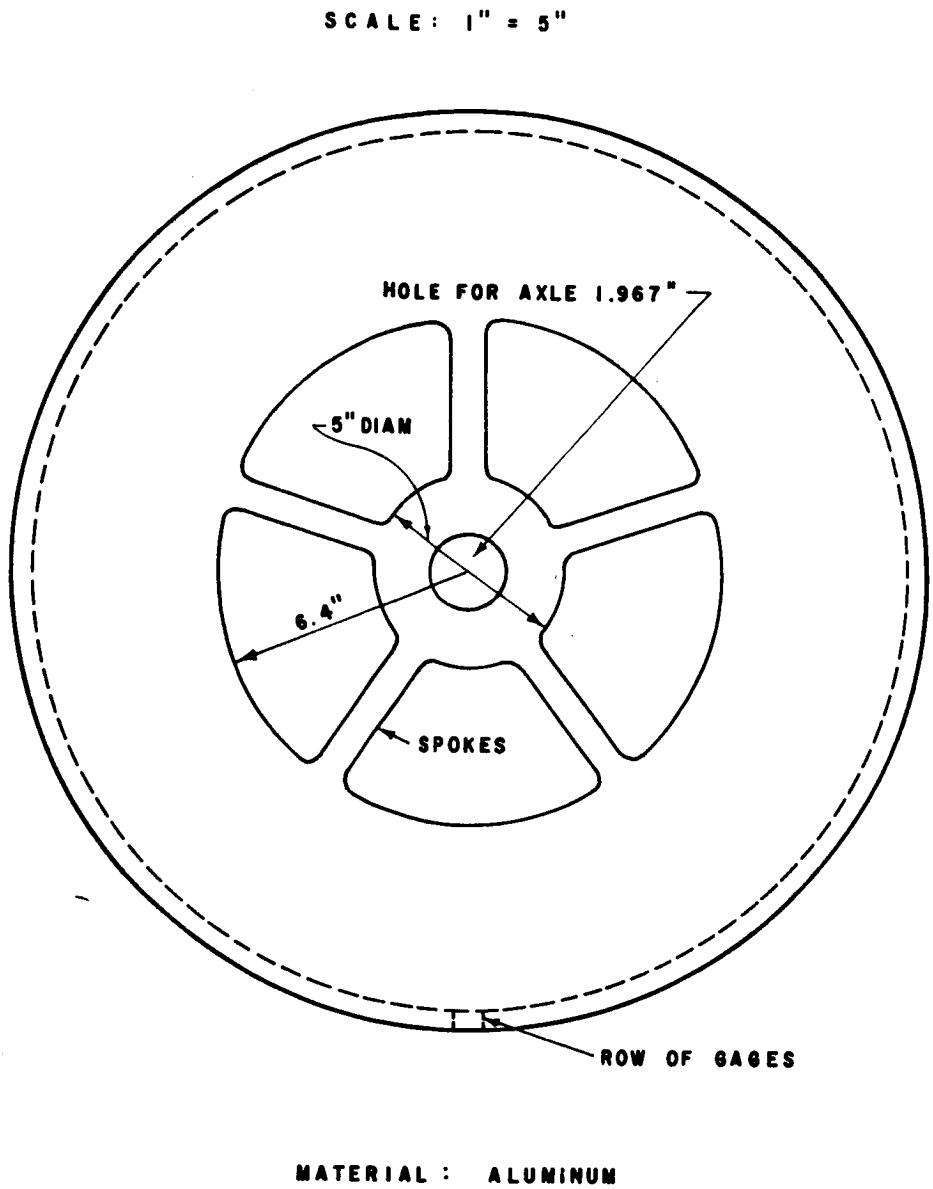

Fig. 4-1. Side view of spherical wheel.

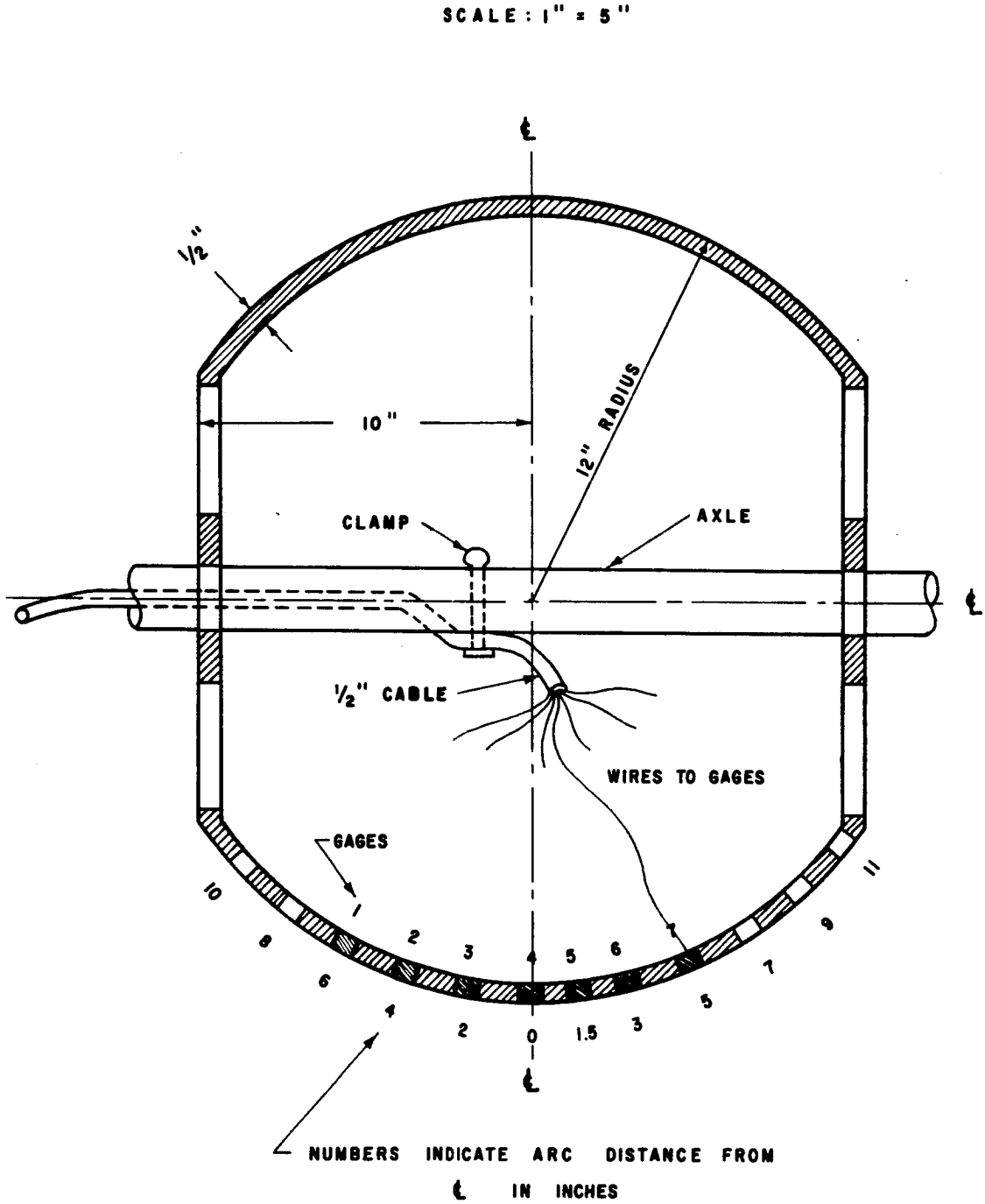

Fig. 4-2. Front view of spherical wheel.

A row of semiconductor diaphragm gages was located along the periphery of the spherical wheel as shown in Figures 4-1 and 4-2. The gages were designed to measure the normal pressure at the sphere-soil contact as the sphere rolled through the soil. A total of seven gages was used; their location and numbering are shown in Figure 4-2. Additional positions (holes) were provided to make it possible to relocate the gages for better coverage of pressure at large sinkage. Such relocation turned out to be unnecessary, and the holes were filled using a screw.

Figure 4-3 shows details of a diaphragm gage. The gages were screwed in from the inside with a special key and locked in position with a lock nut as shown in Figure 4-3. The diaphragm was designed using formulas presented by Timoshenko and Goodier (1951). Theory indicated that for a 40-psi normal pressure applied to a 1/2-inch-diameter and 0.012-inch-thick diaphragm of cold rolled 1045 steel, the maximum strain would be about 700 microinches per inch for a maximum deflection of about 500 microinches. This design proved to be satisfactory.

The semiconductor strain gages used are described by the manufacturer (BLH Electronics, Inc.) as follows:

Type: SPB 3-12-12
Resistance: 120 ohms
Gage Factor: +116
Length: 0.12 inches.

The gages were calibrated at WES. Wires from the semiconductor gages were run to a slip-ring assembly, and resistors were added to complete a wheatstone bridge. The slip-ring assembly, a panel of added resistors, and the spherical wheel in position in the carriage are shown in Figure 4-4. To prevent diaphragm damage by point loads from larger soil grains, a strip of thin rubber was stretched to cover each gage face. Lastly, fine uniform sand was glued to the spherical wheel surface to make the surface rough like the surface of a boulder.

Facilities

The spherical wheel was towed on the soil car shown in Figure 4-5. This car was 64 inches wide, 36 inches deep, and more than 50 feet long.

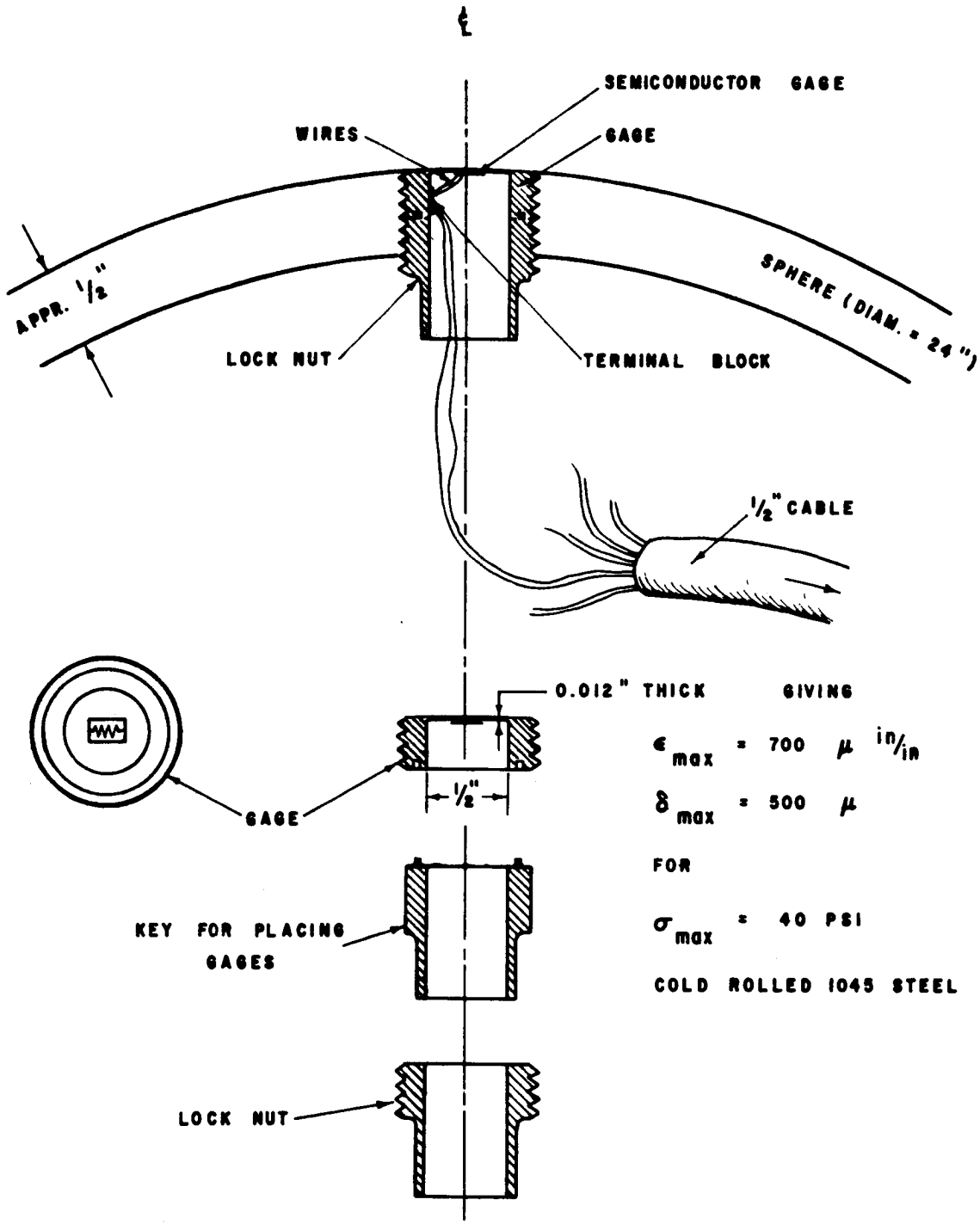

Fig. 4-3. Detail of diaphragm gage.

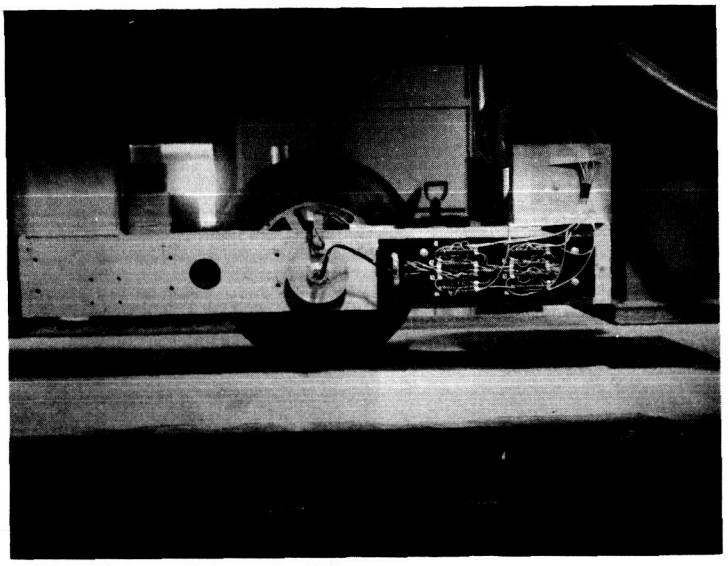

Fig. 4-4. Spherical wheel in carriage (photograph also shows the slip-ring assembly and panel of added resistors).

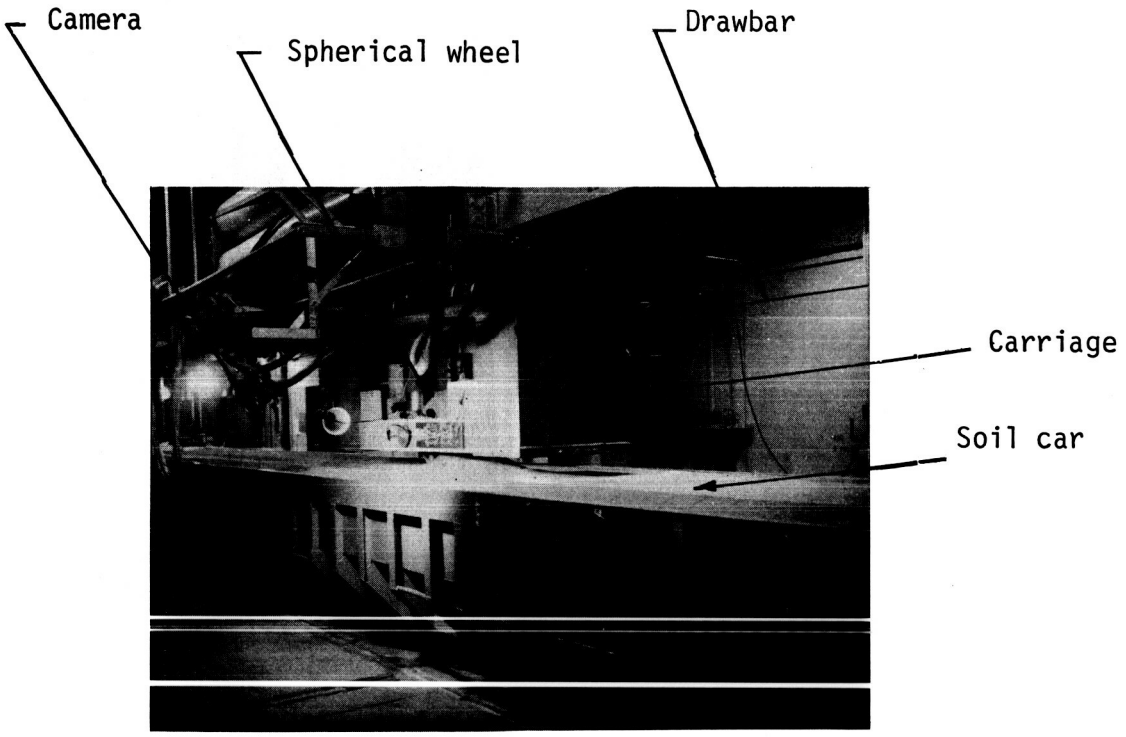

Fig. 4-5. Testing facilities at WES.

Figure 4-5 also shows the cable which applied the towing force to the carriage (upper right), and the movie camera (left of the floodlight) which followed the carriage and filmed the sphere rolling through the soil.

The pressure registered by the gages, as well as the towing force, wheel load, velocity, acceleration, and inertia effects of the carriage were recorded continuously on an oscillograph as the spherical wheel rolled through the soil.

Soil

A gradation curve for the Yuma sand used in these tests is shown in Figure 3-1. Yuma sand is a uniform very fine sand with an effective grain size of about 0.08 mm and a uniformity coefficient of about 1.5. In its loosest state (D_r = 0%), air-dry Yuma sand has a friction angle of about 35 degrees. In its densest state (D_r = 100%), air-dry Yuma sand has a friction angle of about 47 degrees. The air-dry soil densities corresponding to the loosest and densest states are 1.39 gm/cc and 1.66 gm/cc, respectively. The specific gravity of Yuma sand is 2.67.

TESTING PROCEDURE

Testing proceeded through the following steps:

1. The soil in the car was prepared to the desired density using techniques established at WES as described in Appendix A. With this procedure, a particular density could be repeated to within plus or minus 2 per cent. The Yuma sand used in this study was compacted to give a cone index gradient value of approximately 2.00 meganewtons per cubic meter (7.42 lb/in^3).
2. The pressure gages were calibrated, and the wheel load to be used was selected.
3. The spherical wheel was rolled approximately two revolutions on the soil car at a velocity of about 2 feet per second.
4. The pressures registered by the gages and other parameters of carriage motion were recorded.
5. The tracks formed by the rolling wheel were measured and photographed.

RESULTS

The spherical wheel was tested under five wheel loads. These wheel loads, although applied at the axle, gave an effect identical to solid spheres of different densities, since the sphere was rigid. The loads were selected to give equivalent density ratios (density of rock/density of soil = γ_r/γ_s) corresponding to solid spheres built to investigate the dynamics of spheres rolling down a sand slope (see Chapter 6). The loads used and the corresponding equivalent density ratios are shown in Table 4-1.

Table 4-1. Wheel loads.

Wheel load N	Corresponding density, γ_r gm/cc	Soil density γ_s gm/cc	Density ratio γ_r/γ_s
635	0.55	1.57	0.35
1241	1.08	1.58	0.68
2100	1.83	1.58	1.16
2503	2.18	1.57	1.39
4275	3.71	1.57	2.36

The resulting tracks showing soil deformation and failure under these wheel loads, and the measured distribution of contact pressure as projected on a horizontal plane are shown in Figures 4-6 through 4-15. The pressures shown in Figures 4-6 through 4-15 were plotted from the oscillograph data presented in Appendix C.

DISCUSSION

In general, results show that the contact pressure normal to the surface of the spherical wheel has a bell-shaped distribution. In the discussion below, the pressures, the resulting tracks, and some analytical formulations are considered.

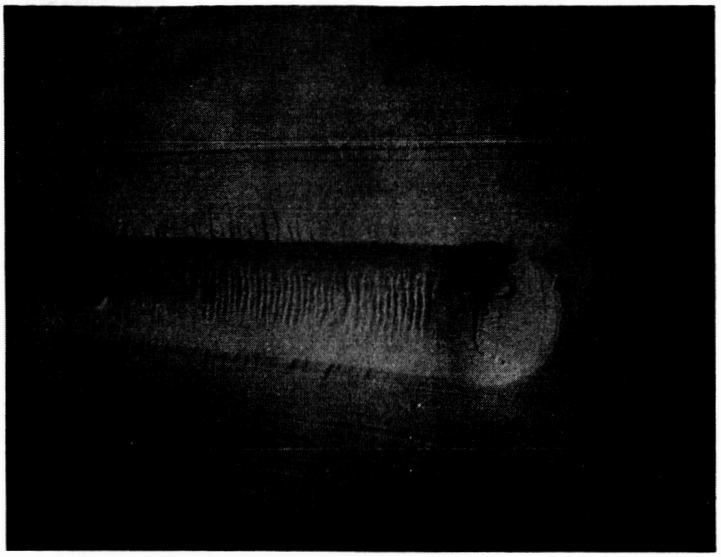

a) Track resulting from a wheel load of 635 newtons.

vert. scale: 1" = 10 cm
hor. scale: 1" = 10 in.

cross section, St. 29.0

longitudinal section, St. 29.55

b) Sections for the above track.

Fig. 4-6. Track and sections for a wheel load of 635 newtons (143 lb).

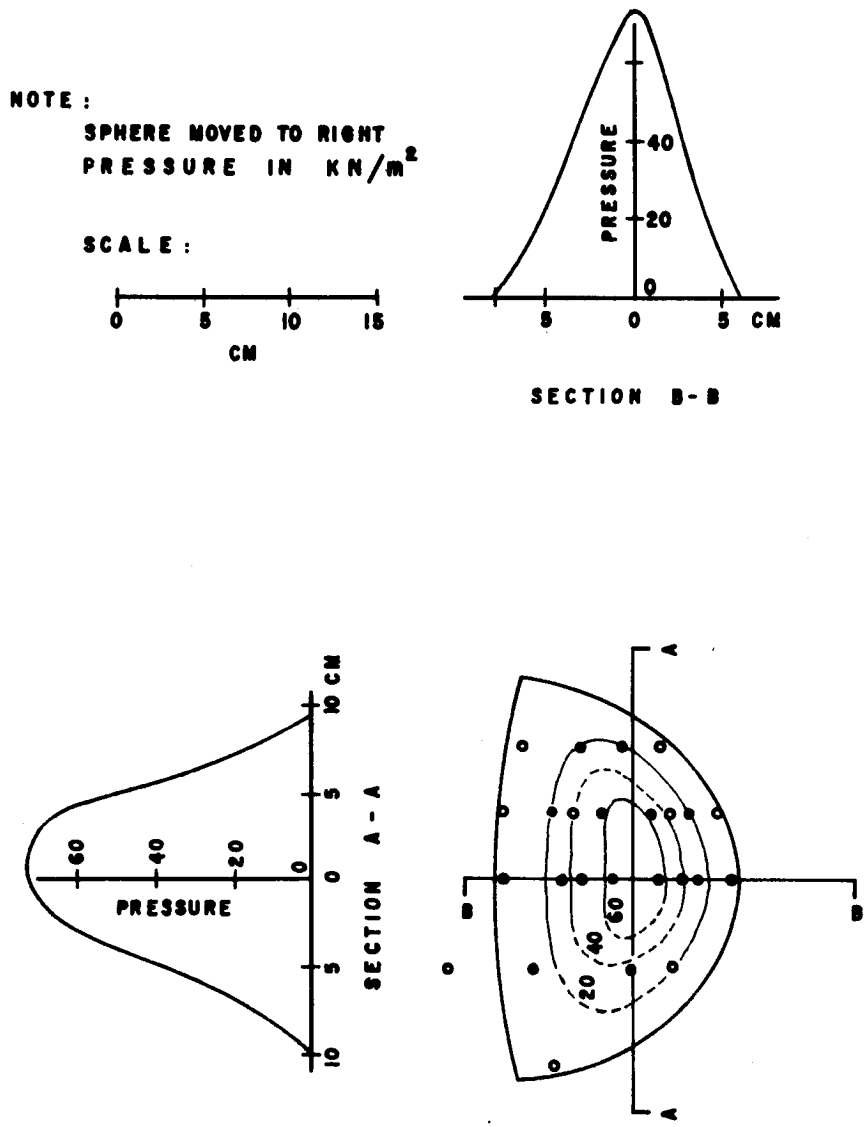

Fig. 4-7. Contact pressure beneath sphere wheel load = 635 newtons (143 lb).

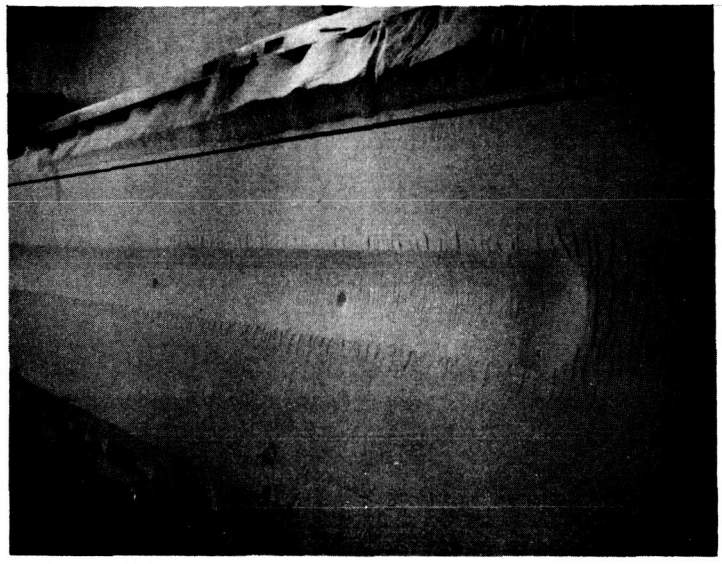

a) Track resulting from a wheel load of 1241 newtons.

vert. scale: 1" = 10 cm
hor. scale: 1" = 10 in.

cross section, St. 25.0

longitudinal section, St. 25.0

b) Sections for the above track.

Fig. 4-8. Track and sections for a wheel load of 1241 newtons (280 lb).

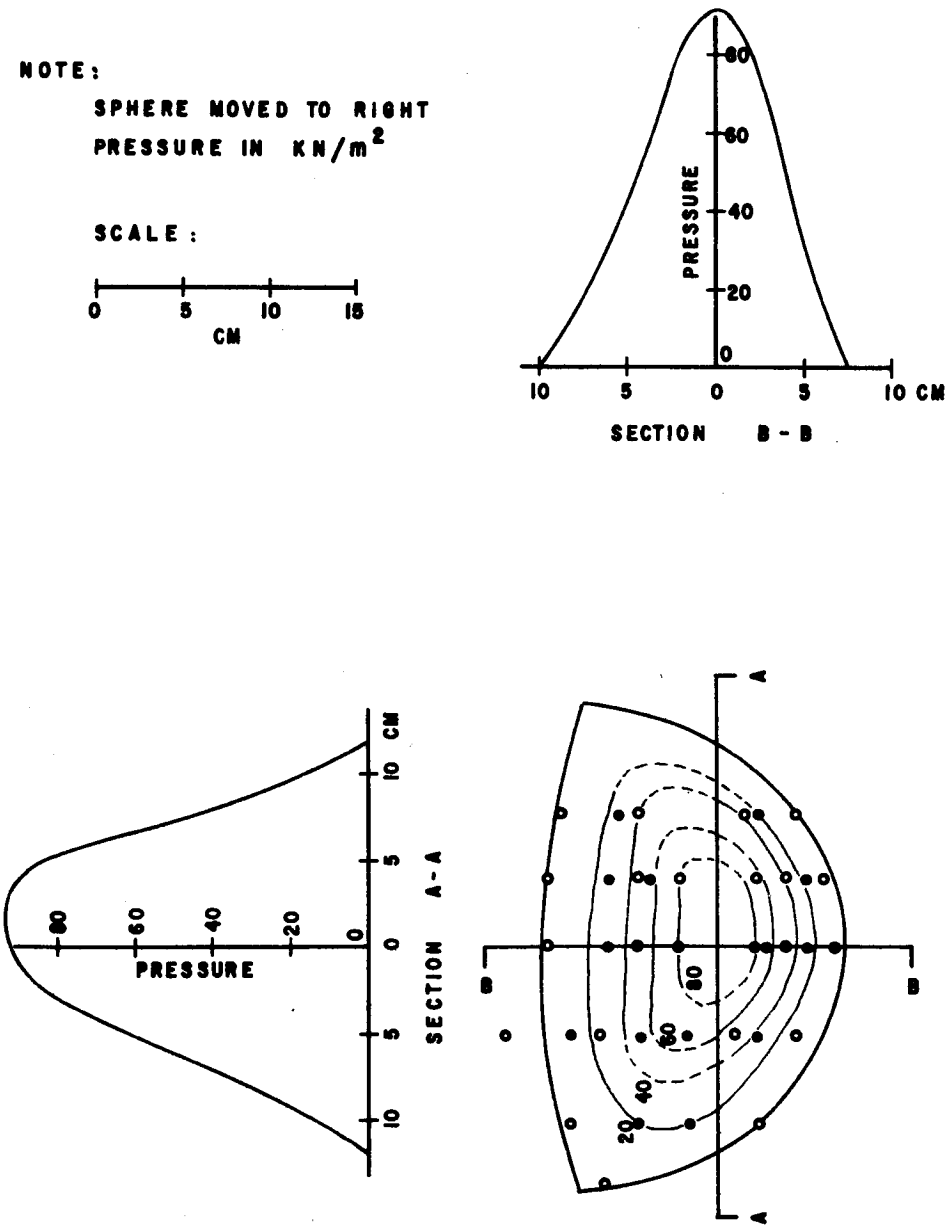

Fig. 4-9. Contact pressure beneath sphere wheel load = 1241 newtons (280 lb).

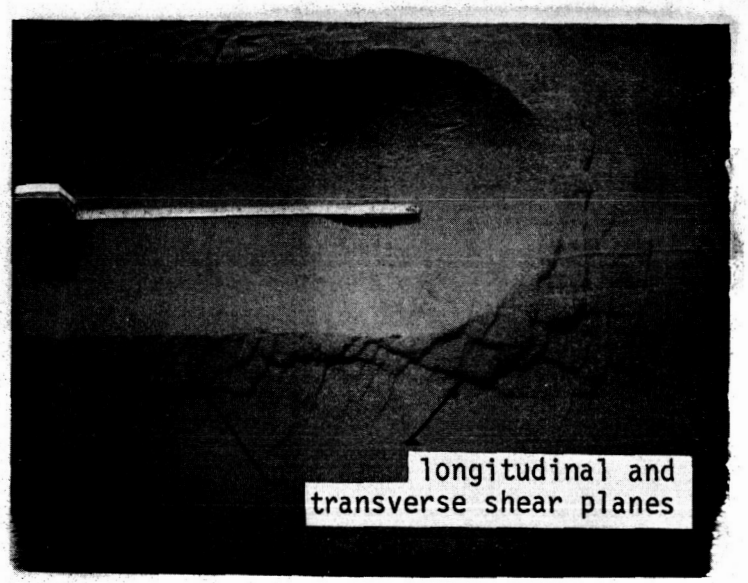

a) Track resulting from a wheel load of 2100 newtons.

vert. scale: 1" = 10 cm
hor. scale: 1" = 10 in.

cross section, St. 19.5

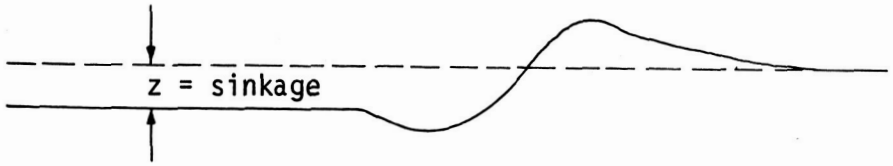

longitudinal section, St. 19.5

b) Sections for the above track.

Fig. 4-10. Track and sections for a wheel load of 2100 newtons (472 lb).

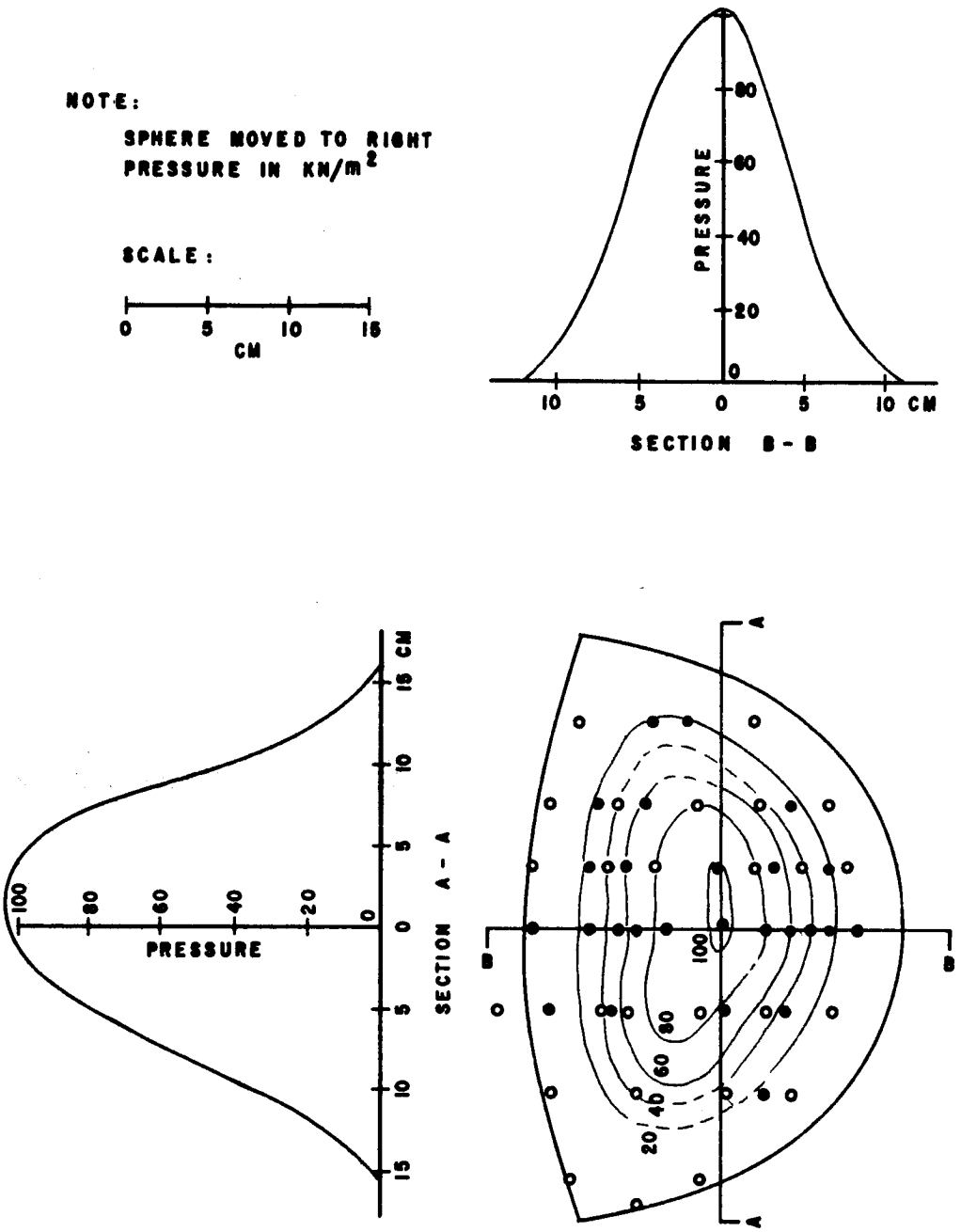

Fig. 4-11. Contact pressure beneath sphere wheel load = 2100 newtons (472 lb).

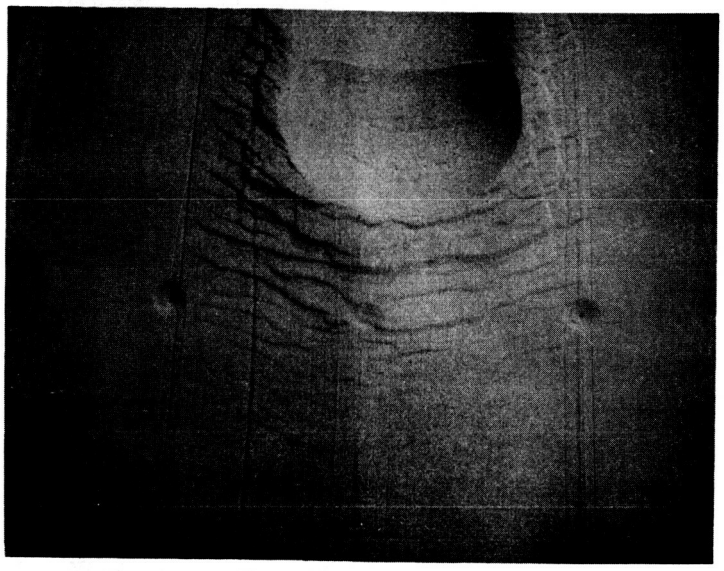

a) Track resulting from a wheel load of 2503 newtons.

vert. scale: 1" = 10 cm
hor. scale: 1" = 10 in.

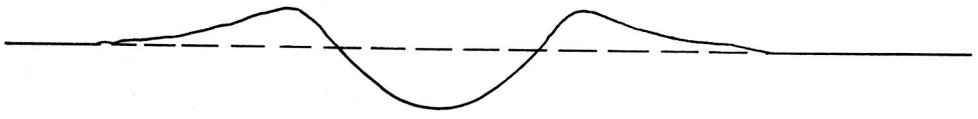

cross section, St. 19.0

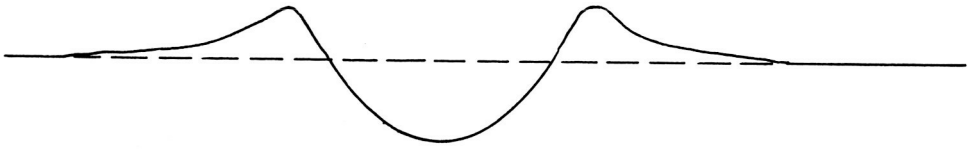

cross section, St. 20.7

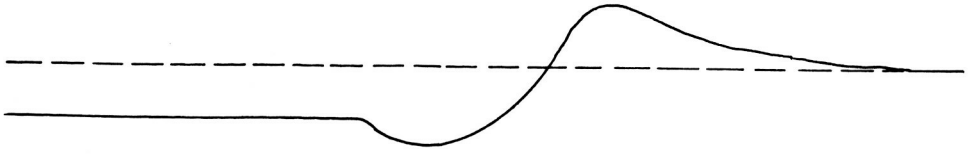

longitudinal section, St. 20.7

b) Sections for the above track.

Fig. 4-12. Track and sections for a wheel load of 2503 newtons (564 lb).

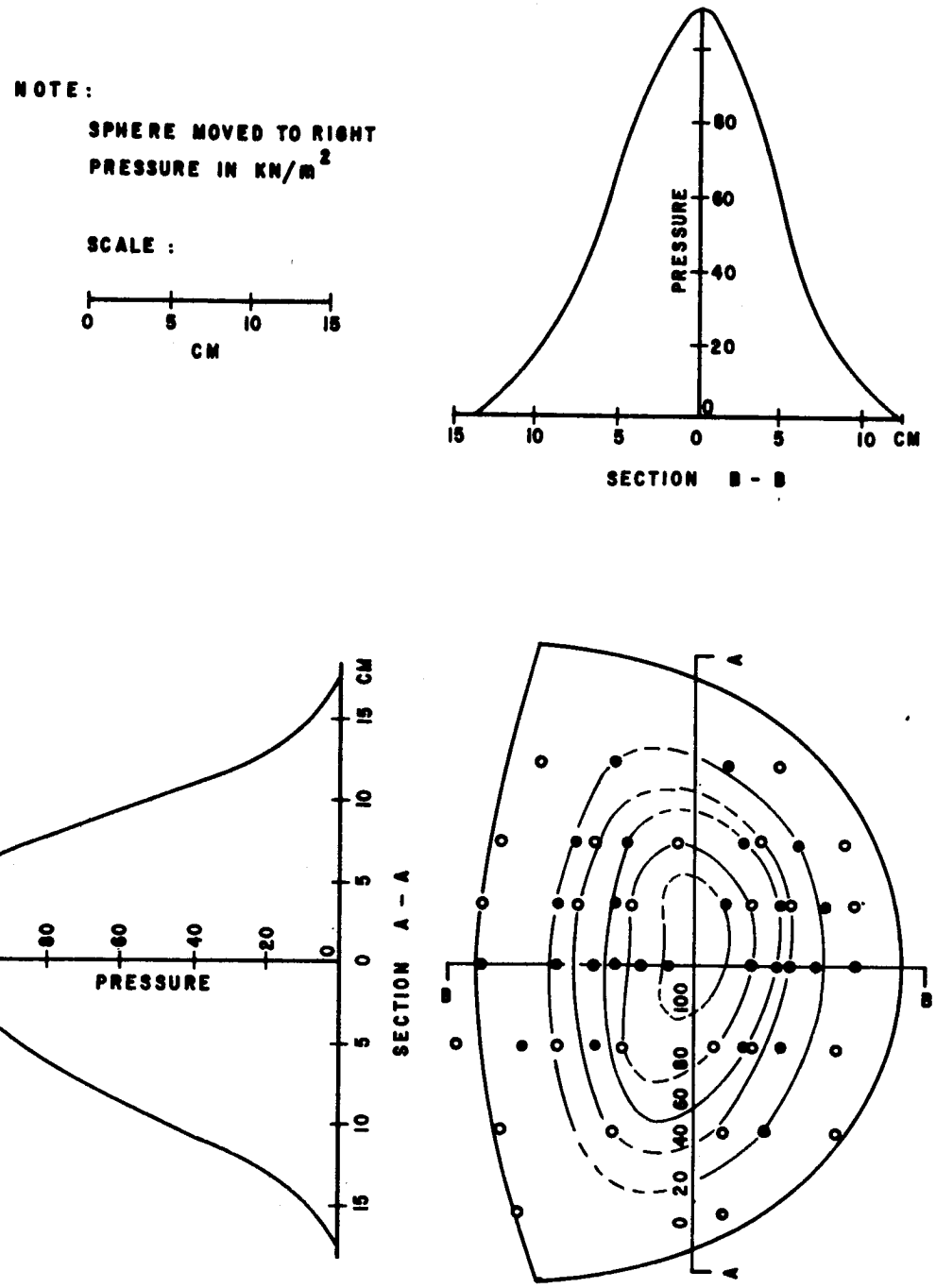

Fig. 4-13. Contact pressure beneath sphere wheel load = 2503 newtons (564 lb).

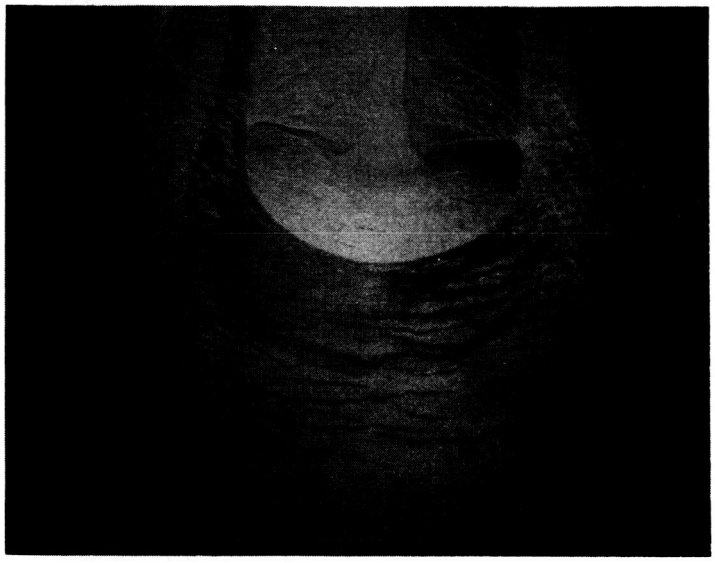

a) Track resulting from a wheel load of 4275 newtons.

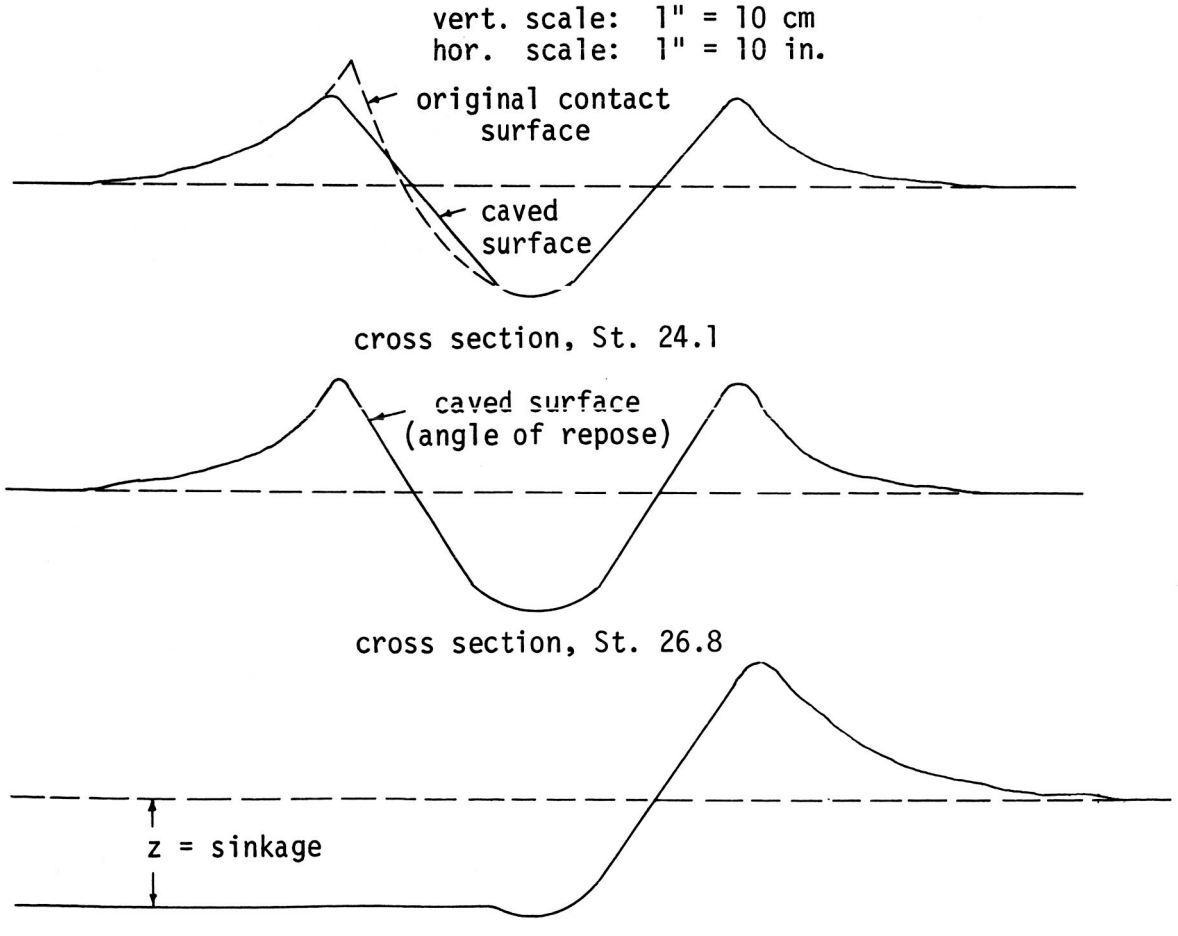

b) Sections for the above track.

Fig. 4-14. Track and sections for a wheel load of 4275 newtons (962 lb).

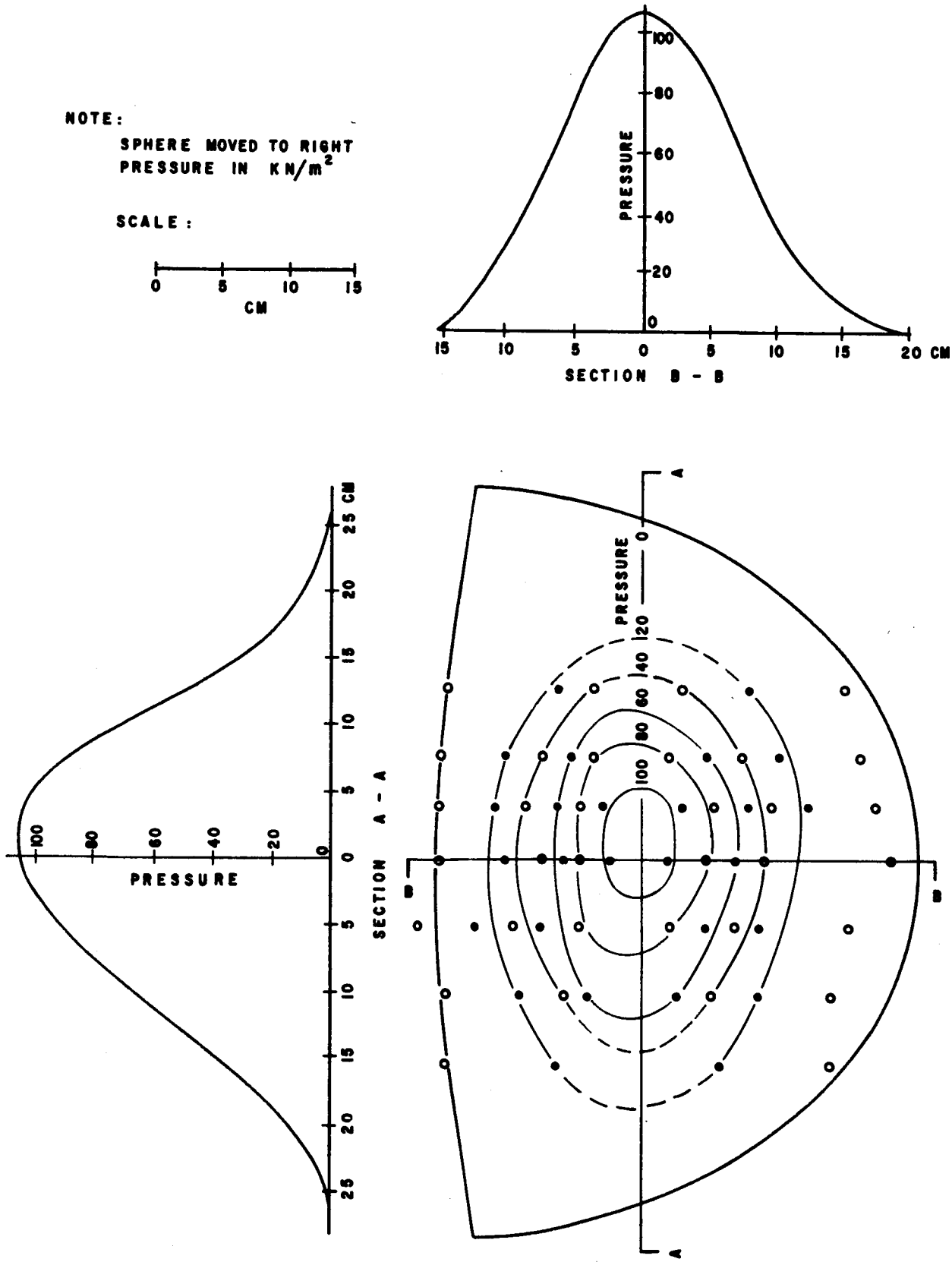

Fig. 4-15. Contact pressure beneath sphere wheel load = 4275 newtons (962 lb).

Pressure at the Sphere-Soil Interface

The contact pressure normal to the surface for each wheel load was projected or plotted on a horizontal plane. Figure 4-16 shows the contact pressure plotted on the curved surface of the sphere along a longitudinal section through the center of the track. Figure 4-16a shows the actual location of the pressure distribution for the lightest wheel load used (635 newtons), and Figure 4-16b shows the same information for the heaviest wheel load (4275 newtons). The figure also shows the direction of the resultant of towing force and wheel load, and the direction of maximum pressure.

The ratio of towing force to wheel load increased with increasing wheel load, as shown by Figure 4-17. (For these wheel loads, slip varied as shown in Figure 4-20.)

As illustrated in Figure 4-16, the direction of the resultant of towing force and wheel load is not quite parallel to the direction of maximum pressure. This deviation was investigated and is plotted on Figure 4-18. (β_s is the angle between the vertical and the direction of maximum pressure.) Since the resultant of towing force and wheel load must be equal and opposite to the resultant of the sum of pressure, the resultant of the sum of pressure must act slightly below or behind the location of maximum pressure. This conclusion is reasonable since the contact area is considerably wider toward the back.

To check the reliability of the measurements, the sum of all pressure within the pressure distribution was computed by determining areas between the pressure contours in Figures 4-7, 4-9, 4-11, 4-13, and 4-15, using a planimeter, and multiplying each area by its average pressure. To add these incremental forces (pressure times area), however, their components parallel to the direction of the maximum pressure had to be found. This was done by dividing each force by the cosine of the angle between the direction of each respective force and the maximum pressure. Table 4-2 shows a comparison between the resultant of wheel load and towing force and the sum of pressure (reaction force) computed as described above.

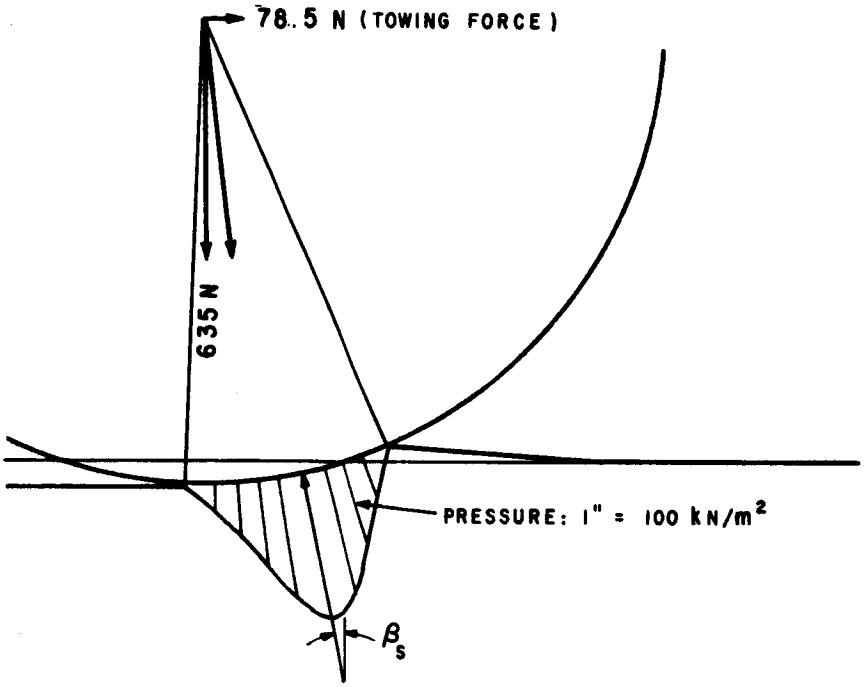

a) Wheel load = 635 newtons (143 lb).

Scale: 1" = 5"

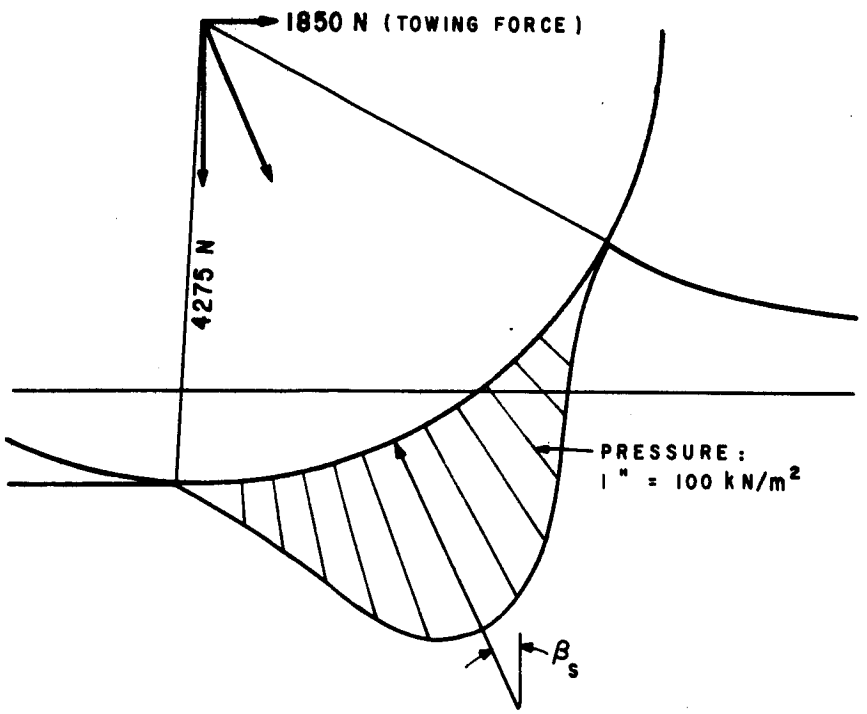

b) Wheel load = 4275 newtons (962 lb).

Fig. 4-16. Contact pressure beneath spherical wheel.

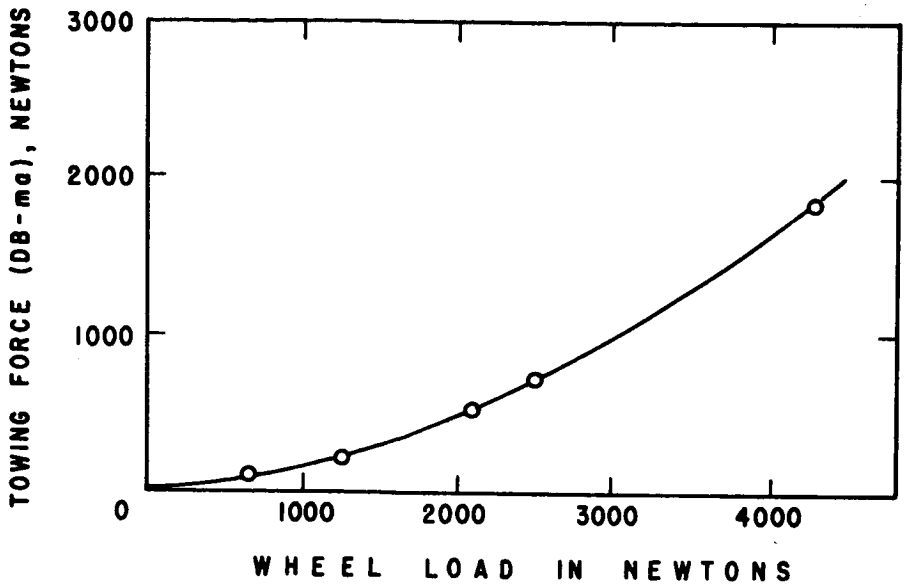

Fig. 4-17. Towing force vs wheel load.

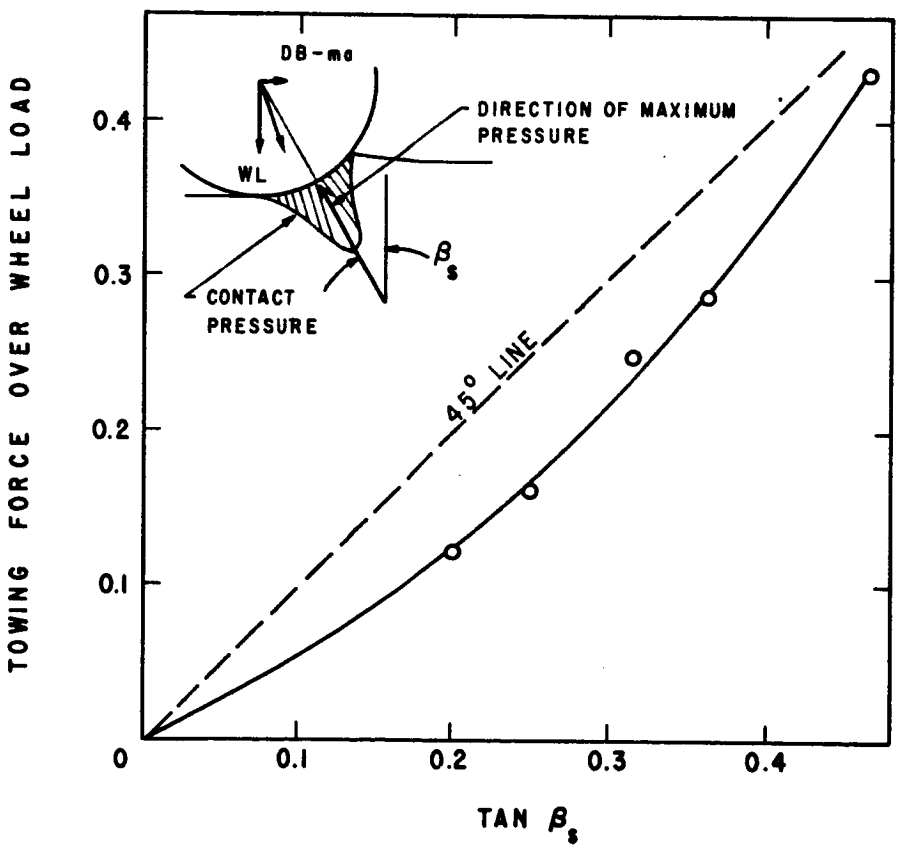

Fig. 4-18. Towing force over wheel load vs tan β_s.

Table 4-2. Comparison between applied and measured loads.

Wheel load (N)	Towing force (N)	Resultant (N)	Reaction force computed from pressure diagrams (N)
635	79	640	611
1241	205	1255	1216
2100	520	2165	2178
2503	723	2610	2546
4275	1850	4650	4637

There is good agreement between the resultant and the reaction force as presented in Table 4-2. The average deviation is about 1 per cent, and the maximum deviation is about 4 per cent. On this basis, we can conclude that the pressure gages reliably measured the normal contact pressure between the spherical wheel and the soil.

While the sum of pressure (reaction force) within the bell-shaped distribution increased in proportion to the applied loads, the maximum pressure did not. The maximum pressure resulting from the increasing applied loads is plotted in Figure 4-19. This plot implies that the maximum pressure increases until the soil begins to fail. For higher loads, the maximum pressure remains nearly constant, and added resistance is supplied by greater sinkage of the sphere, resulting in a larger contact area. It appears reasonable to conclude that shear failure is more directly a function of the maximum pressure than of the average bearing pressure.

Slip (defined as the distance revolved minus the distance traveled divided by the distance traveled) was found to increase with increasing wheel loads or density ratios, as shown in Figure 4-20. All slip was found to be negative. The negative slip does not necessarily mean that there is a net shear stress acting on the sphere surface. As shown from the model studies (Chapter 3), a soil wedge is pushed up and forward, which would cause an opposite shear stress on the front part of the sphere. This interpretation agrees with the previous experimentation

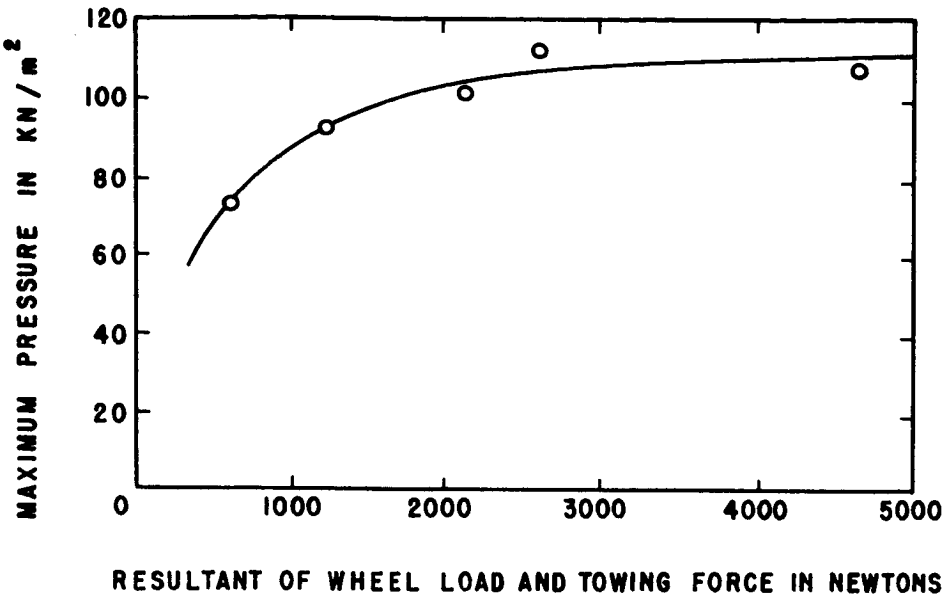

Fig. 4-19. Maximum pressure vs resultant of wheel load and towing force .

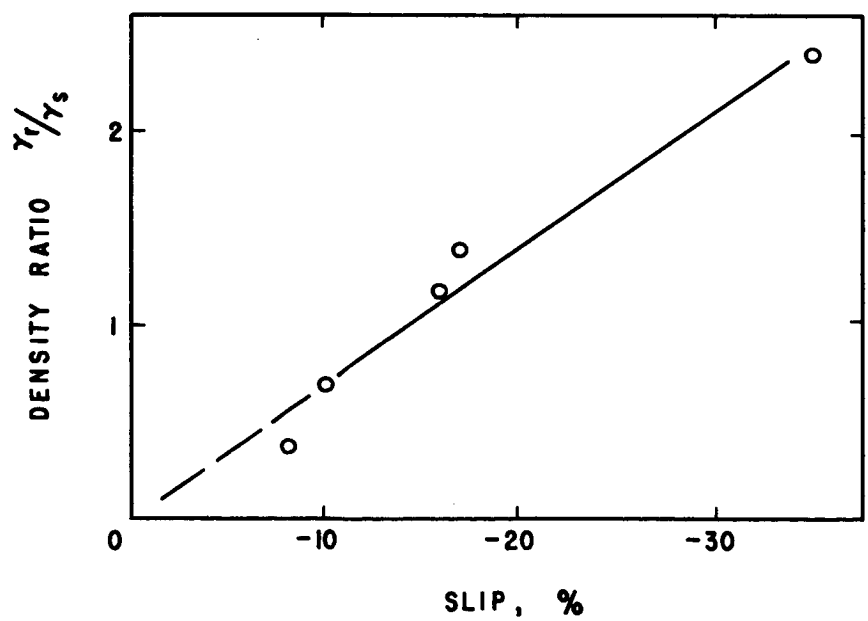

Fig. 4-20. Slip vs density ratio .

with towed wheels (Green and Murphy, 1965).

Tracks

Photographs of the tracks (Figures 4-6 through 4-14) show certain repeated features that agree with the failure mechanism proposed in Chapter 3. Other visible features, important to an understanding of wheel-soil interaction are:

1. The track for the lightest wheel load (Figure 4-6a) shows no evidence of general shear, which agrees with the above interpretation of Figure 4-19.

2. The tracks for the lighter wheel loads (Figures 4-6a and 4-8a) also show ripples in the center of the track. Such ripples are not seen in the tracks resulting from the heavier wheel loads.

3. Two sets of well-defined shear planes are clearly shown in the tracks resulting from the heavier wheel loads (Figures 4-10a, 4-12a, 4-14a). One set runs in front of the spherical wheel across the track with a slight curvature. The other runs approximately perpendicular to the first set, diverging out from the direction of travel at an angle of about 30 degrees.

4. Very little lateral movement of soil took place, as shown by the fact that the small longitudinal grooves seen in Figures 4-6 through 4-15 were not distorted. (These grooves were left on the soil surface by the screeding or leveling operation.) This agrees with the results of model studies described in Chapter 3.

Experimental information on shear zones (the zone within which failure planes could be detected in the soil) and the number of failure planes within the shear zone are presented in Figure 4-21. The maximum width of the shear zones extending both forward and to the sides was measured from the crest of the track for each track; the results are plotted (Figure 4-21a) as a function of the density ratio. This figure should provide a valuable comparison to theoretically predicted shear zones (example, Chapter 5, p. 94). The number of failure planes within the shear zones were counted and are presented (Figure 4-21b) as functions of track depth. This plot suggests that there were between one and two failure planes per centimeter depth of soil within the shear zones. Most

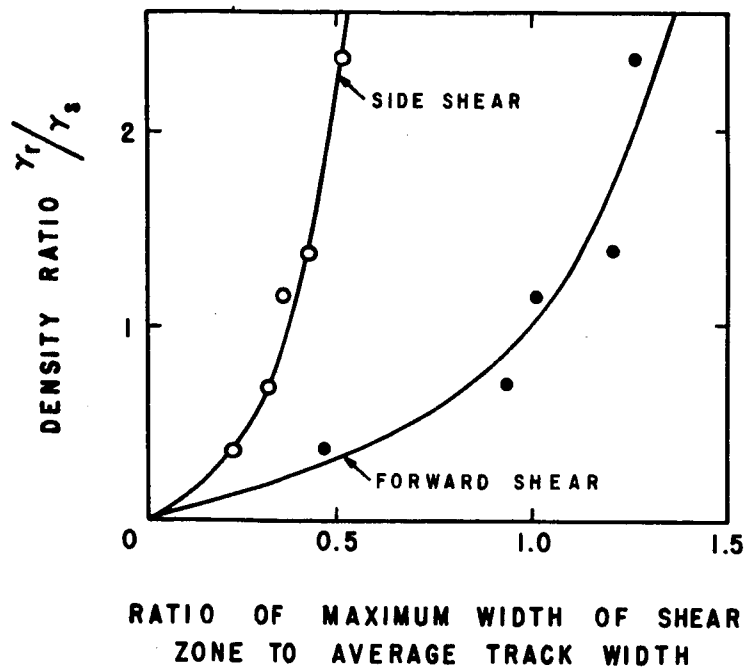

a) Density ratio vs width of shear zone.

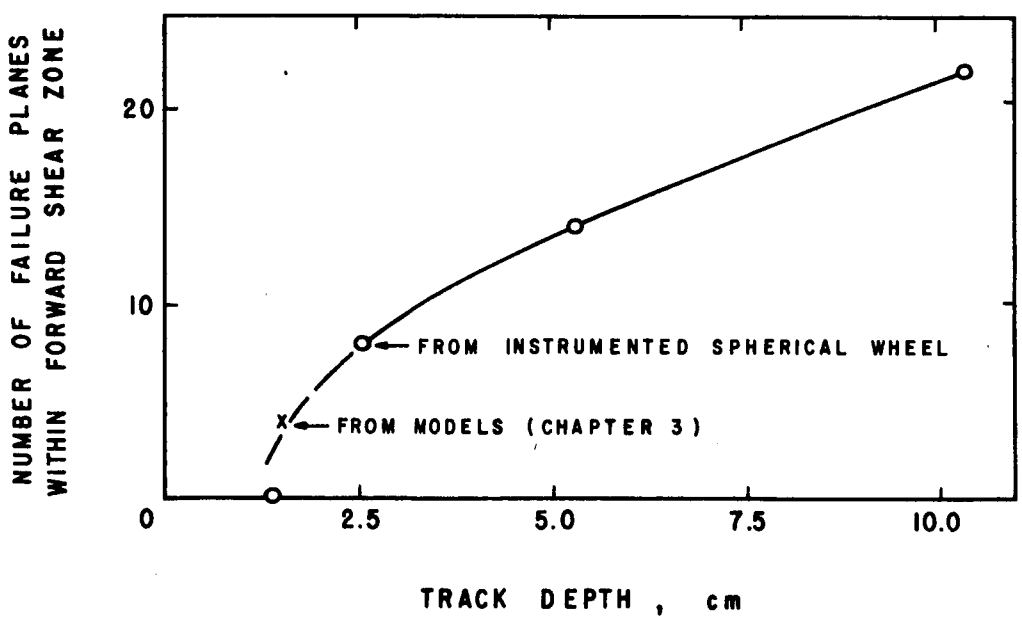

b) Number of failure planes within the forward shear zone as a function of track depth.

Fig. 4-21. Experimental information on shear zones and failure planes within the shear zone.

of the data for Figure 4-21 are from the spherical wheel rolling on Yuma sand. It is interesting that the one point from the models reported in Chapter 3 fits quite well within the data, as shown in Figure 4-21, even though the models were constructed of a somewhat different material.

Analytical Considerations

It is possible to approximate the bell-shaped pressure distribution with a parabolic function, as shown in Figure 4-22. Therefore, we may represent the contact pressure in a direction parallel to the direction of the resultant of wheel load and towing force by the expression

$$\sigma = \sigma_{max} - ay^2 \ . \tag{4-1}$$

When $y = y_{max}$, $\sigma = 0$. Therefore, $a = \sigma_{max} / y^2_{max}$; y_{max} is the radius of a circular area equal to the actual approximately semicircular contact area. Therefore,

$$\pi y^2_{max} = \frac{\pi}{2} \frac{w^2}{4} , \tag{4-2}$$

where w equals the crest-to-crest track width. From this expression,

$$y^2_{max} = \frac{1}{8} w^2 \ . \tag{4-3}$$

Then

$$a = 8 \frac{\sigma_{max}}{w^2} \ . \tag{4-4}$$

The total applied force is the resultant of wheel load and towing force. The reaction to this resultant is the sum of all pressure within the pressure distribution described by Equation (4-1), which acts in a direction opposite to the total applied force. (It is assumed that net shear along the sphere surface is zero.) The total applied force and its reaction can be equated by the solid of revolution approach to give

$$R = \pi \int_0^{\sigma_{max}} f^2(\sigma) d\sigma = \frac{\pi}{a} \int_0^{\sigma_{max}} \left(\sigma_{max} - \sigma\right) d\sigma \ , \tag{4-5}$$

where R is the resultant of wheel load and towing force. This approach assumes that the actual approximately semicircular area can be represented by an equal circular area. Substituting the value for "a" from Equation

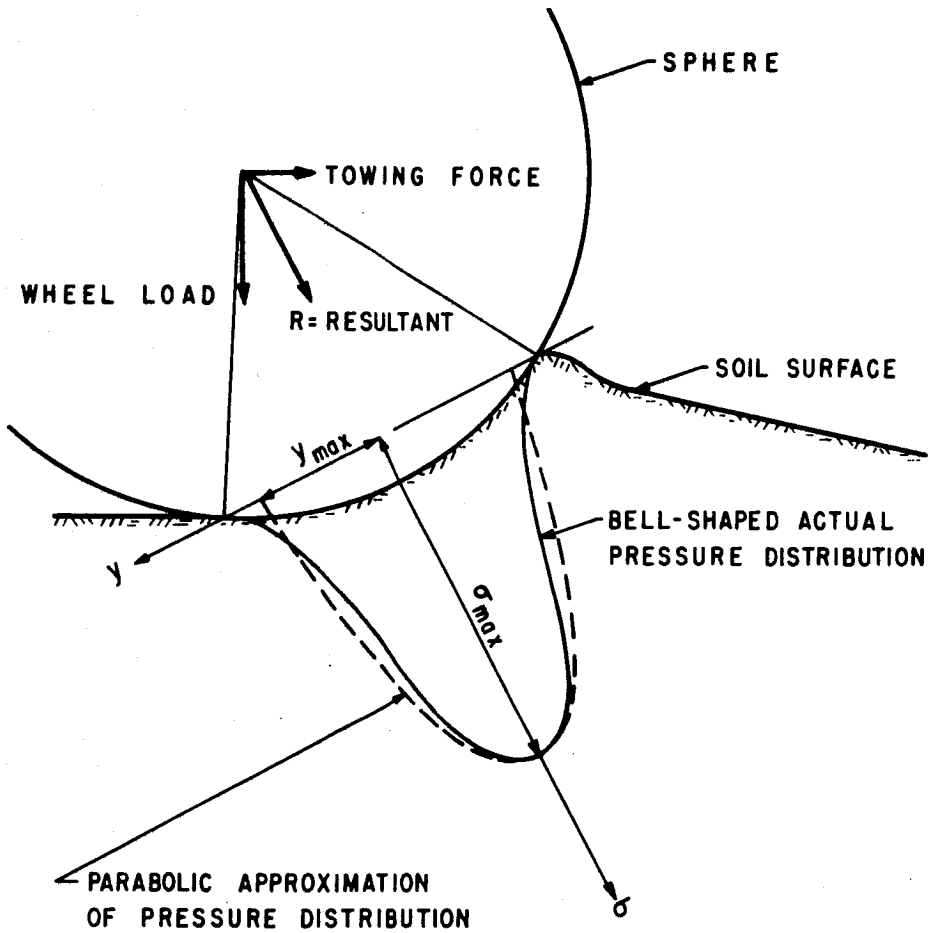

Fig. 4-22. Pressure distribution beneath a sphere.

(4-4) into Equation (4-5), and carrying out the integration gives

$$R = \frac{\pi}{16} w^2 \sigma_{max} \quad , \tag{4-6}$$

or since the area equals $A = \frac{\pi}{2} \frac{w^2}{4}$,

$$R = \frac{1}{2} A \sigma_{max} \quad , \tag{4-7}$$

from which

$$\sigma_{max} = 2 \frac{R}{A} = 2q \quad , \tag{4-8}$$

where $q = R/A$ is the average pressure often referred to as "unit bearing pressure." Equation (4-8) shows that the maximum pressure beneath the spherical wheel is about twice the average unit bearing pressure.

To determine how closely the above equations describe the contact pressure beneath the spherical wheel, the resultant, R, was computed using Equation (4-6) with measured σ_{max}, and the maximum pressure was computed using Equation (4-8) with measured R. Table 4-3 presents the comparison.

Table 4-3. Comparison between applied and calculated loads and pressures.

Wheel load N	Applied R N	Calculated R N	Measured σ_{max} KN/m^2	Calculated σ_{max} KN/m^2
635	640	630	73	74
1241	1255	1330	93	88
2100	2165	2170	102	102
2503	2610	2680	112	109
4275	4650	4790	106	103

The comparison shows a very good agreement, and it is believed that for a spherical wheel in air-dry sand, the ratio between σ_{max} and q is about 2.

Combining Equations (4-1), (4-4), and (4-8) leads to an equation for the contact pressure beneath a sphere in air-dry sand,

$$\sigma = 2q\left[1 - 8\left(\frac{y}{w}\right)^2\right]. \qquad (4\text{-}9)$$

CONCLUSIONS

It has been illustrated in this chapter that the distribution of contact pressure beneath a rigid sphere or spherical wheel in air-dry sand is bell-shaped. This bell-shaped distribution can be closely approximated by an equivalent parabolic function.

Shear failure appears to be more directly related to the maximum pressure beneath the sphere than to the average pressure or unit bearing pressure. The maximum pressure beneath a rigid sphere or spherical wheel in air-dry sand is shown to be about two times the average pressure.

The pattern of deformation and failure of the soil appears to agree with the failure mechanism proposed in Chapter 3.

It is believed that the results clarify the behavior of a rigid sphere rolling in air-dry sand. Further theoretical analysis can be based upon these findings.

Chapter 5. THEORETICAL STUDIES

Investigation of the rolling sphere-soil slope interaction problem has been emphasized only recently. To the writer's knowledge, the only existing theory is that proposed by Lin and Haythornthwaite (1969). They studied ping-pong-ball size spheres rolling down a slope of granular media at constant velocity. They proposed a solution based on the assumption that failure of the soil in front of the sphere is caused by bulldozing. Their theory and experimental data are for a cohesionless ($c = 0$) soil.

Existing theories for wheel-soil interaction have been either quasi-theoretical (Bekker, 1956), or empirical (Reece, 1965-1966; Roth, 1960; Waterways Experiment Station, 1954). Due to mathematical complexities associated with three-dimensional analyses, it has also been suggested that the wheel-soil interaction problem be assumed to be two-dimensional (Yong and Osler, 1966). Model studies of soil deformation under wheels have been carried out to investigate two-dimensional behavior (Wilson and Krzywicki, 1966).

Due to the quasi-theoretical or empirical nature of existing theories, much design has depended on experimentation for each new specific condition. It has not been demonstrated to what extent the failure mechanism observed in a two-dimensional model approximates the three-dimensional wheel-soil or sphere-soil interaction.

This chapter begins with a summary of the significant conclusions from the results presented previously as a basis for theoretical developments. This is followed by step-by-step development of a theory to provide a method by which soil properties can be evaluated from boulder track data. Simplifying assumptions are used in order to make the problem tractable.

BASIS FOR THEORETICAL DEVELOPMENT

From the results of the investigations of the failure mechanism using model studies and the pressure distribution of the soil-sphere contact using an instrumented spherical wheel, the following

characteristics of behavior have been determined:

1. Resistance to rolling appears to be a function of volume change, shearing distortion, general shear, and soil inertia.

2. For loose sands at the beginning of rolling, soil deformations consist of volume change (compression) and shearing distortion.

3. When volume changes and shearing distortion can no longer account for all the soil that must be displaced, general shear planes develop. These shear planes probably develop where the deformations reach a critical magnitude with respect to the confining pressure. These shear planes are initially oriented approximately in a direction of $45° - \phi/2$ to the direction of the major principal stress.

4. It appears that a wedge of soil, originating approximately radially below the center of the sphere-soil contact area, is pushed up and forward during the shearing process.

5. Initially vertical sections are bent forward as the sphere rolls down the slope and deformations assume a final position as shown in Chapter 3. Material from the bow wave is wasted to the sides to form the crests of the track.

6. Deformations (compression) beneath the sphere at any depth are almost directly proportional to the pressure at that depth.

7. The distribution of contact pressure beneath a rigid sphere in air-dry sand is bell-shaped. This bell-shaped distribution can be closely approximated by an equivalent parabolic function,

$$\sigma = 2q\left[1 - 8\left(\frac{Y}{w}\right)^2\right], \qquad (5\text{-}1)$$

where

σ = contact pressure at any point parallel to the resultant of applied forces, R.

q = average contact pressure parallel to σ, or R/contact area.

y = distance from location of maximum pressure perpendicular to the direction of maximum pressure.

w = crest-to-crest tract width.

y_{max} is related to w according to $y_{max} = w/2.825$.

8. General shear failure appears to be more directly related to the maximum pressure beneath the sphere than to the average pressure. The maximum pressure, σ_{max}, is about 2q or twice the average pressure.

9. The maximum width of the shear zone measured from the edge or crest of the track was found to be about 1.3 w in the forward direction for the heaviest sphere load and a sphere-to-soil density ratio of 2.2 for Yuma sand. The ratio of side shear to forward shear was found to be about 0.38 for all wheel loads.

10. Negative slip increases with wheel load or sphere density, or with increased sinkage.

Any theory must consider the above stated characteristics of behavior. Further requirements of theory are:

1. Dynamic equilibrium must be satisfied.
2. The three-dimensional nature of the problem must be recognized and satisfied or closely approximated.
3. Soil and sphere properties must be accounted for.
4. Soil deformation and volume change must be considered.
5. General shear must be evaluated.
6. Inertia effects must be evaluated.

DYNAMIC EQUILIBRIUM

A sphere rolling down a deformable surface, such as a soil slope, is shown in Figure 5-1.

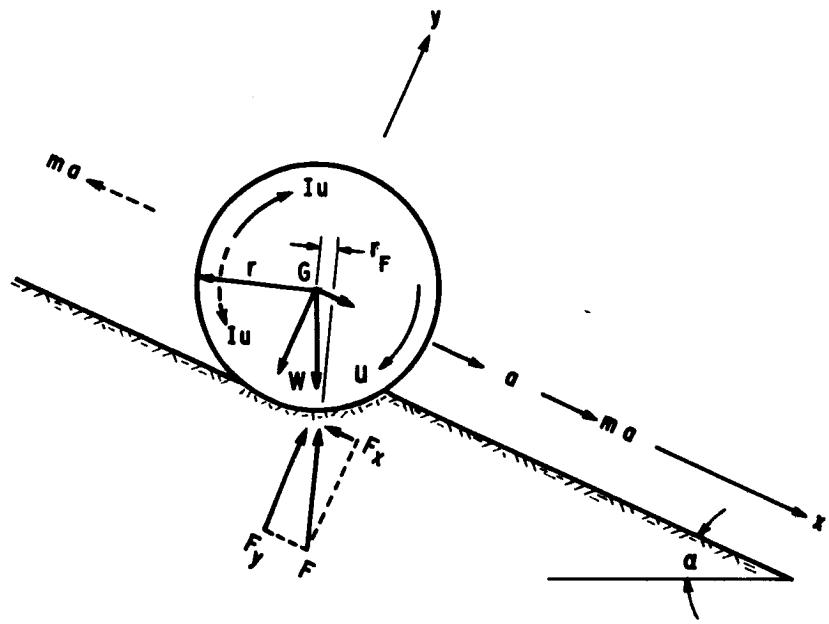

Fig. 5-1. Sphere rolling down a soil slope.

The symbols in Figure 5-1 are defined as follows:

W = weight of sphere.

m = mass of sphere = W/g.

F = resultant soil reaction force.

F_x = component of F parallel to slope.

F_y = component of F normal to slope.

r = radius of sphere.

r_F = distance from center of sphere to line of action of F.

I = moment of inertia of sphere $= (2/5)mr^2$.

a = linear acceleration of sphere .

u = angular acceleration of sphere .

x,y = coordinate directions .

α = slope angle .

Negative slip will usually take place as a sphere rolls down a slope. Therefore, with respect to translation down the slope, $a \neq ur$. Any shear stresses that act on the sphere surface are assumed to be included as a part of forces F, F_x , and F_y.

In applying Newton's Second Law using the method of dynamic equilibrium, ma and Iu are considered acting opposite to their actual sense, as shown by the dotted arrows in Figure 5-1. We then have:

$$+\uparrow \sum F_y = 0 = F_y - W \cos \alpha, \qquad F_y = W \cos \alpha \tag{5-2}$$

$$\pm \rightarrow \sum F_x = 0 = W \sin \alpha - F_x - ma, \qquad F_x = W \sin \alpha - W \frac{a}{g} \tag{5-3}$$

$$+) \sum M_G = 0 = Fr_F - Iu, \qquad F = \frac{2}{5} W \frac{r^2}{r_F} \frac{u}{g}. \tag{5-4}$$

Equation (5-2) states that the normal component of soil reaction is always equal to the component of the weight of the sphere in the same direction. One cannot, however, conclude that the normal component, F_y , is independent of sphere motion, since it has been observed that at high velocities the sphere may even start bouncing. Equation (5-3) states that if the sphere is to be accelerating, the component of soil reaction parallel to the slope, F_x , must be less than the component of the weight of the sphere in the same direction. In other words, if $a = 0$ (sphere resting on the slope or rolling with constant velocity), the resultant of soil reaction, F, is exactly equal to the weight of the sphere, W, and has the same line of action. If the sphere is accelerating, the inclination of F moves toward the normal to the slope.

Interpretation of Equation (5-3) is aided by Figure 5-2, which shows that:

1. Positive values of F_x/W represent soil resistance parallel to

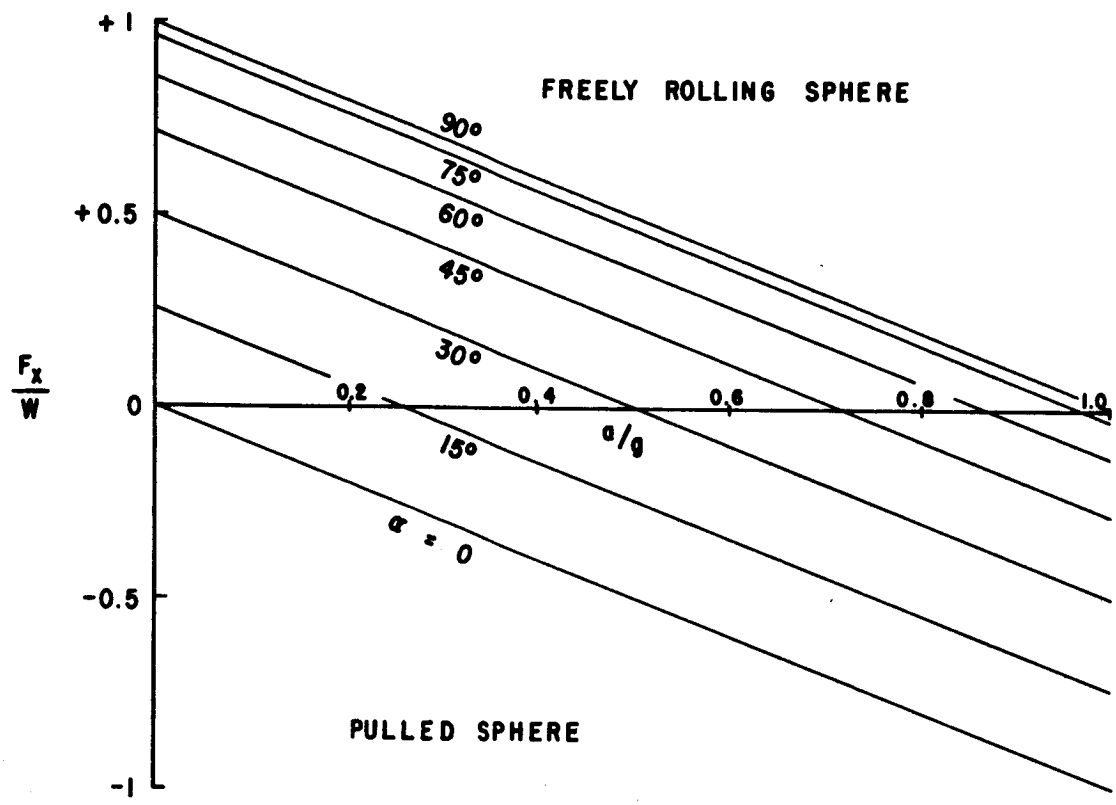

Fig. 5-2. Resisting force parallel to slope F as a function of a/g.

the slope and opposite to the direction of motion of a freely rolling sphere.

Here:

a. The condition $\alpha = 90°$, $F_x/W = 1$, represents a sphere suspended in the air or falling at constant velocity.

b. The condition $\alpha = 90°$, $F_x/W = 0$, represents a freely falling body.

c. The positive vertical axis, F_x/W, represents necessary soil resistance for constant velocity rolling for a sphere in motion, or the force necessary to prevent rolling for a sphere at rest.

2. Negative values of F_x/W represent pull that must be applied to cause further acceleration.

Here:

a. The condition $\alpha = 0$, $F_x/W = 0$, represents a sphere resting or moving at constant velocity on a horizontal surface.

b. Any pull applied above and beyond the soil resistance will cause the sphere to accelerate.

The resultant, F, in terms of F_y and F_x, is

$$F^2 = F_x^2 + F_y^2. \tag{5-5}$$

Substituting F_y and F_x from Equations (5-2) and (5-3) into Equation (5-5) gives

$$F = W\left[\left(\sin \alpha - \frac{a}{g}\right)^2 + \cos^2 \alpha\right]^{\frac{1}{2}}. \tag{5-6}$$

The remaining unknowns in Equations (5-4) and (5-6) are F, a, u, and r_F. From experiments performed at WES, a and u are determinable for most spheres rolled. Therefore, F and r_F could be determined. This would give the magnitude and direction of the resultant soil reaction, F, as well as its point of action on the sphere surface.

While this relationship is useful for checking theory and experimental work, it could not be used for the evaluation of lunar boulder tracks since accelerations a and u are unknown.

The amount by which the resultant, F, differs from the weight of the sphere, W, and the amount by which F deviates from the vertical is important to know. Figure 5-3 shows a plot of Equation (5-6) giving the value of F/W as a function of a/g. It may be noted that for a slope angle of 15 degrees, which was the average for 69 lunar boulder tracks studied (Hovland and Mitchell, 1970), F/W is between 0.97 and 1.00 for reasonable values of a/g (a/g = 0 to 0.5). For other possible slope angles, F/W will vary between 0.85 and 1.10. Therefore, little error should be associated with the assumption that the resultant equals the weight of the sphere.

Figure 5-4 shows the deviation of F from the vertical as a function of a/g for various slope angles. This figure shows that for a slope angle of 15 degrees and a/g approximately equal to 0.26, F will deviate from the vertical by about 15 degrees. This means that F is normal to the slope, and that $F = F_y$, and $F_x = 0$. This situation ($F_x = 0$) would only arise for a frictionless slope. For a soil slope, experiments (to be reported in Chapter 6) indicate that the maximum value of a/g will be approximately 0.5 times the values for a frictionless slope. These maximum values of a/g were measured for light spheres rolling on dense moist soil. All other sphere and soil combinations would result in smaller values of a/g. The range of a/g for likely sphere-soil combinations would be from zero to 0.15. Therefore, the direction of the resultant would probably deviate only between 0 and 8 degrees from the vertical.

In summary, the following conclusions can be added to the previous list of behavior characteristics:

1. The magnitude of the resultant of soil reaction will usually be nearly equal to the weight of the sphere.
2. The direction of the resultant of soil reaction will usually be nearly vertical.

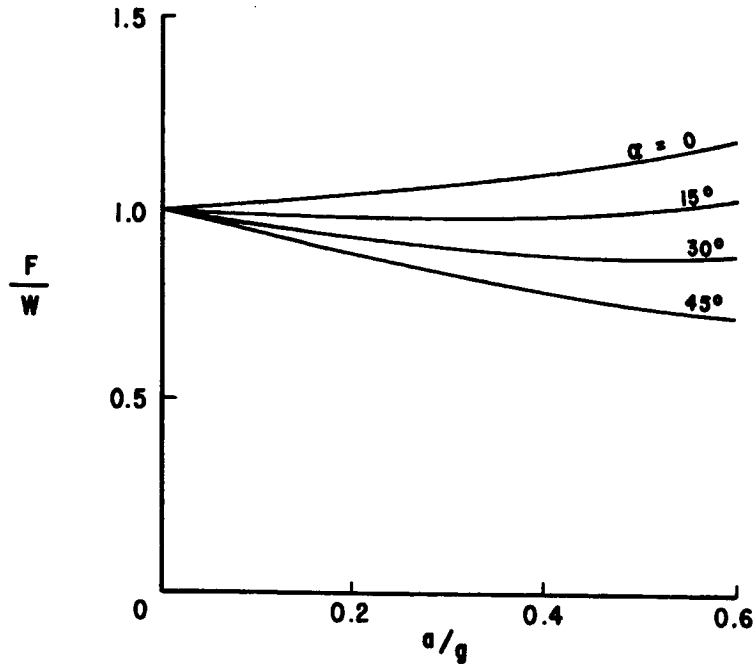

Fig. 5-3. Resultant, F, as a function of a and α.

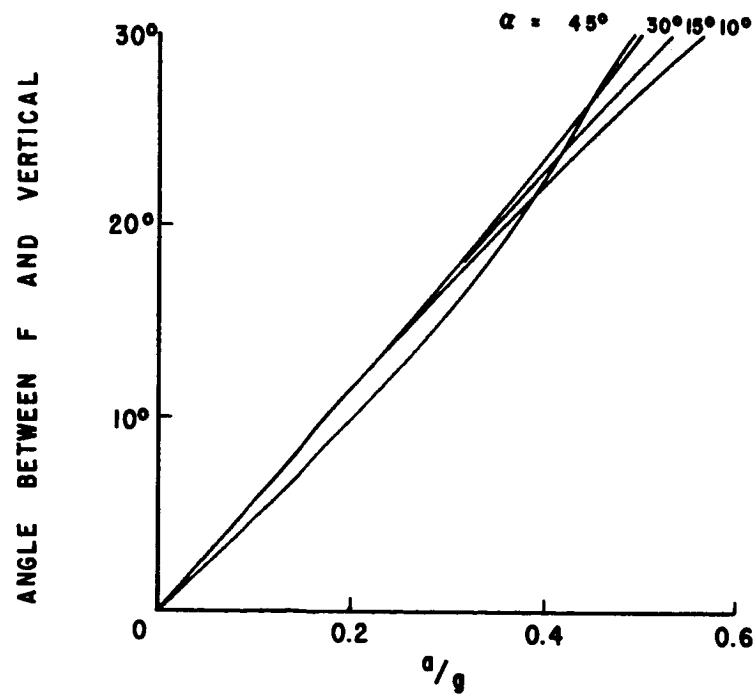

Fig. 5-4. Angle between F and the vertical as a function of a and α.

The total soil reaction consists of resistance caused by volume change and shearing distortion, general shear, and inertia effects. This may be expressed per unit area by

$$q = q_v + q_s + q_I , \tag{5-7}$$

where q_v is resistance caused by volume change and shearing distortion, q_s is resistance caused by general shear, and q_I is resistance caused by soil inertia effects. The contribution of these terms will be investigated in the following sections.

In the above discussion and in the sections to follow, volume changes and shearing distortions are assumed to be complete before general shear begins. For the purpose of this analysis, general shear is defined as a sliding of a mass of soil along a shear surface, which occurs without a significant volume change.

RESISTANCE DUE TO VOLUME CHANGE

General

For cases of track formation, where general shear takes place the maximum soil resistance available will be given by the resistance due to general shear plus resistance due to soil inertia; it is assumed that volume change and shearing distortion need not be considered. The greater part of the shearing distortion resulting from the rearrangement of particles and soil structure takes place prior to the onset of general shear. That is, when a state is reached at which the soil will fail by general shear rather than further shearing distortion, resistance to failure is no longer a function of shearing distortion. Except for very loose soils, a condition of general shear is forced in nearly all rolling sphere-soil slope interaction cases. On the basis of such reasoning,

$$q_v = 0. \tag{5-8}$$

Volume changes are, however, important in evaluating inertia effects of a shearing soil wedge during general shear; the looser the soil, the shorter will be the displacement along the shear plane, since more of

the deformation associated with rolling has been taken up by shearing distortion and volume change. To be able to evaluate displacements along the shear plane at various soil densities, a relationship between sinkage and volume change is needed.

Relationship Between Sinkage and Volume Change

It is assumed that volume changes are complete before general shear begins. Figure 5-5 shows the geometry for the volume of soil displaced during densification and before general shear.

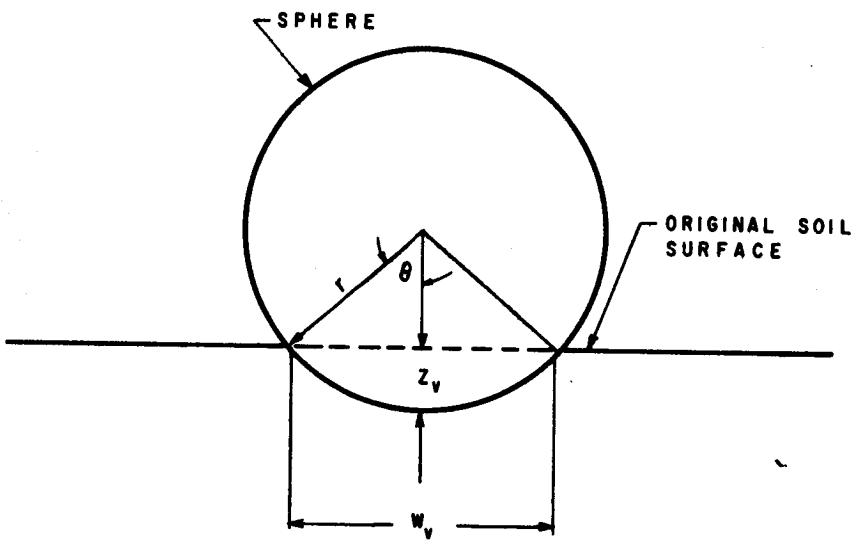

Fig. 5-5. Geometry for analysis of soil displaced before general shear.

The symbols in Figure 5-5 are defined as follows: z_v = track depth or sinkage for maximum volume change before general shear ($z_v \leq z$), w_v = track width for maximum volume change before general shear ($w_v \leq w$).

The volume of soil displaced, ΔV, per unit length in the track

direction is given by the segment of the circle below the original soil surface in Figure 5-5, and equals

$$\Delta V = \frac{r^2}{2}\left(\frac{\pi\theta_v}{90°} - \sin 2\theta\right) , \tag{5-9}$$

where

$$\theta_v = \sin^{-1}\left(\frac{w_v}{D}\right) . \tag{5-10}$$

Substituting Equation (5-10) into Equation (5-9), ΔV can be expressed in terms of the track width to diameter ratio:

$$\Delta V = \frac{D^2}{8}\left\{\frac{\pi}{90°}\sin^{-1}\left(\frac{w_v}{D}\right) - \sin\left[2\sin^{-1}\left(\frac{w_v}{D}\right)\right]\right\} . \tag{5-11}$$

In terms of the sinkage, z_v, it is also easy to show from Figure 5-5 that

$$\theta_v = \cos^{-1}\left(1 - \frac{z_v}{r}\right) . \tag{5-12}$$

Then the volume change as a function of sinkage becomes:

$$\Delta V = \frac{r^2}{2}\left\{\frac{\pi}{90°}\cos^{-1}\left(1 - \frac{z_v}{r}\right) - \sin\left[2\cos^{-1}\left(1 - \frac{z_v}{r}\right)\right]\right\} . \tag{5-13}$$

While it may not be possible to determine z_v exactly, it can be estimated from Equation (5-13) by assuming that

$$\Delta V = V_w - V_r , \tag{5-14}$$

where V_w = volume of track below original soil surface, and V_r = volume of rims above original soil surface. Equations (5-11) and (5-13) are plotted in Figure 5-6. The quantities V_w and V_r are measured from track cross sections.

RESISTANCE DUE TO GENERAL SHEAR

Selection of the Failure Surface

In analyzing soil failure on the basis of a limit design method,

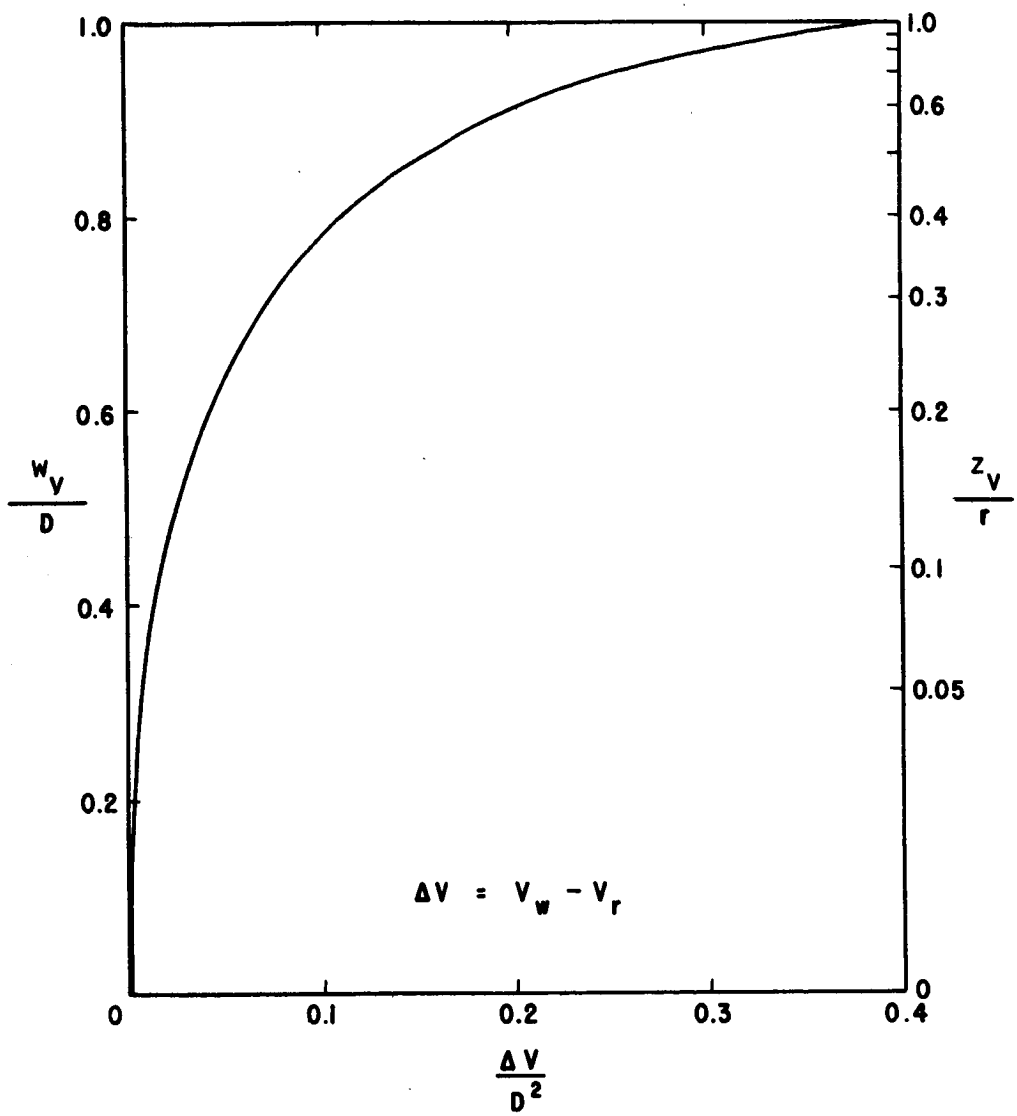

Fig. 5-6. Track width, w_v, as a function of volume change, ΔV.

such as general shear, it is necessary to select a realistic failure surface.

As shown in Chapter 4, general shear appears to be related to the maximum pressure, which is about twice the average pressure along the sphere-soil contact. Therefore, the contact area controlling general shear is considered to be described by a smaller area than the total contact area. A contact area controlling general shear defined by $r\theta/2$ in the longitudinal section as shown in Figure 5-7a was selected because it establishes a failure surface which agrees with experimental data (Figure 4-21a).

The sphere-soil contact or boulder-soil contact is usually rough. Meyerhof (1955) found that the base angle, ψ, (see Figure 5-9a) for a rough strip foundation on cohesionless material was close to $1.2\ \phi$. A line drawn through distances $r\theta/4$ laid off along the sphere surface and vertically below, as shown in Figure 5-7b, defines an angle ABC close to $1.2\ \phi$. This defines the beginning of the failure surface directly beneath the sphere. In the zone of radial shear, the failure surface in sand is a logarithmetic spiral (log-spiral). This is a consequence of the requirement that slip lines intersect at an angle of $90° \pm \phi$ (Scott, 1963). In the passive Rankine zone, the failure surface is a plane.

In analyzing boulder track phenomena, the only measurable quantities usually are the track width, w, the boulder diameter, D, and the slope angle α. Having measured these quantities, the following additional steps establish the failure surface:

1. Estimate an initial value for the angle of shearing resistance, ϕ.
2. Calculate θ_2 and θ_3 (Sokolovski, 1960; Karafiath and Nowatzki, 1968):

$$\theta_2 = \frac{1}{2}\left[\frac{\pi}{2} - \phi - \alpha + \sin^{-1}\frac{\sin\alpha}{\sin\phi}\right] \qquad (5\text{-}15)$$

$$\theta_3 = \frac{\pi}{2} - \phi - \theta_2 . \qquad (5\text{-}16)$$

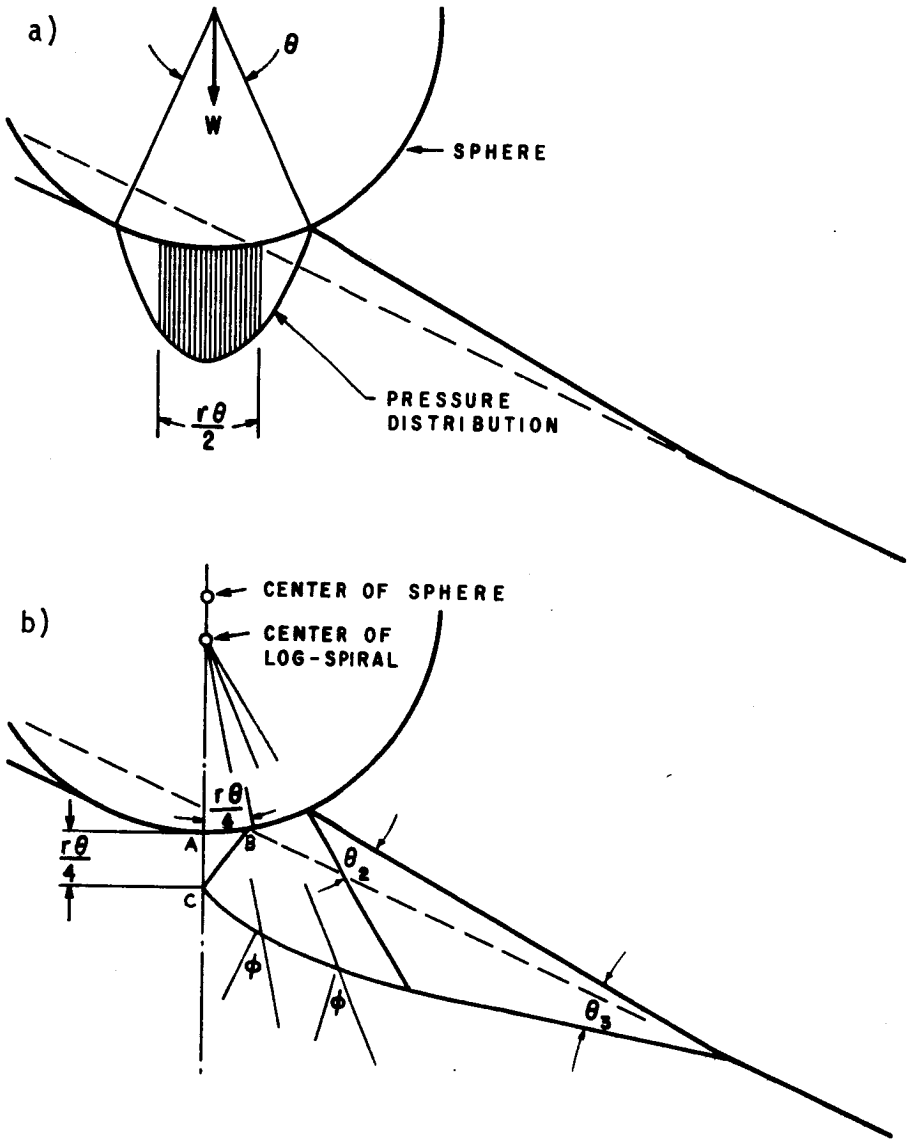

Fig. 5-7. Proposed log-spiral failure surface.

It is to be noted that θ_2 and θ_3 are for the slope angle, α, without considering the bow wave. Experimental evidence on track formation (Chapter 4) shows that the bow wave is for many cases as high above the original surface as the bottom of the track is below. Figure 5-7 was drawn to reflect this, and it was assumed that θ_2 and θ_3 are adequately representative also for the somewhat steeper slope angle caused by the bow wave.

3. Extend the θ_2 line to intersect the bisector of the contact area; this establishes the center of the log-spiral. (The center of the log-spiral is assumed to be located as described because this location gives a realistic failure surface supported by experimental data discussed below.)

4. Determine the log-spiral surface, and draw the failure surface to exit the slope at an angle θ_3 as shown in Figure 5-7b.

To see how well a longitudinal section of the failure surface, selected by the procedure outlined above, describes the true failure surface, predictions were compared with actual measurements. Figure 5-8 shows the results of this comparison. Predicted distance of forward shear (the distance at which the failure surface exits the slope) is plotted in comparison with measured distance of forward shear (Figure 4-21a). The measured distance of forward shear is the distance from the crest of the track to the furthest shear surface; it is the width of the forward shear zone. The measured distance of side shear is also shown. It is the width of the shear zone on the side of the track measured from the crest of the track.

The selected failure surface appears to be adequate. The failure surface as shown in Figure 5-7b also compares well in shape with those observed in model studies (Chapter 3). The ratio of measured side shear to measured forward shear is close to 0.38 for the range of γ_r/γ_s ratios shown. This value is the experimental basis for the width of the failure zone.

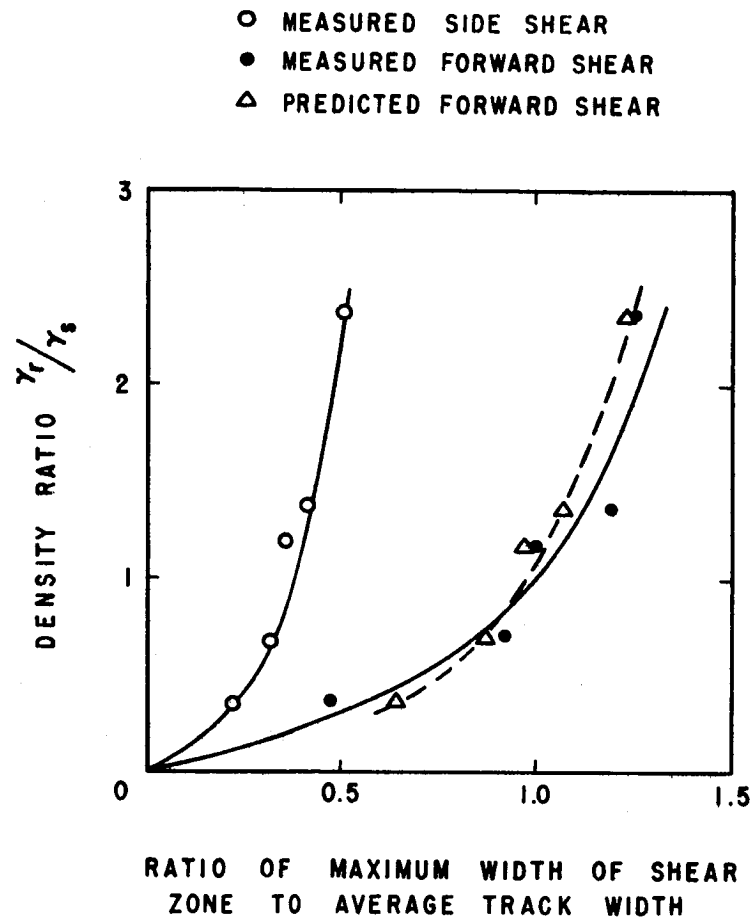

Fig. 5-8. Density ratio vs predicted and measured width of shear zone.

Resistance Due to General Shear

Previously (Hovland and Mitchell, 1970) a method was developed for evaluating boulder track phenomena using modified bearing capacity theory (see Chapter 2). The general bearing capacity equation, (2-4), was first derived for an infinitely long footing on a horizontal surface by Terzaghi (1943). The derivation was accomplished by solving separately for the contributions of density, cohesion, and surcharge. These contributions were added to get the total soil resistance by assuming superposition to be valid. It has since been shown that superposition is not exactly valid for this case (Scott, 1963), but that it is a very good assumption and that Equation (2-4) is in close agreement with experimental and field data.

Subsequently the bearing capacity factors (N_γ, N_c, N_q) in Equation (2-4) have also been determined for an infinitely long footing on a slope (Meyerhof, 1951).

The general bearing capacity equation has been modified to make it applicable to footings of various shapes other than an infinitely long footing. The approach has been to adjust the basic equation, (2-4), by shape factors (s_γ, s_c, s_q) as described in Chapter 2. It has been found from experimentation that a change in the shape of the footing is much less significant than a change in ϕ on the resulting bearing capacity. Adjusting Equation (2-4) by shape factors is believed to be logical and generally valid.

In solving the rolling sphere-soil slope interaction problem, the actual semicircular contact area was first approximated with a rectangular area of equal size (Chapter 2). By using shape factors, Equation (2-4) was modified for an approximation of the rolling sphere-soil slope interaction problem. The resulting expression was

$$\frac{q_s}{w\gamma_s} = 0.188\, N_\gamma + 1.1 \left(\frac{c}{w\gamma_s}\right) N_c + 0.55 \left(\frac{z}{w}\right) N_q . \qquad (5\text{-}17)$$

In Equation(5-17) q_s is the unit bearing capacity in earth gravity and γ_s is the soil unit weight in earth gravity. N_γ, N_c, and N_q are the

bearing capacity factors.

Equation (5-17) predicts soil resistance due to general shear for the sphere-soil contact area as if the failure surface was as predicted from bearing capacity theory for a footing. Based on experimental evidence (Chapters 3 and 4), a method of predicting a more realistic failure surface for the rolling sphere-soil slope interaction problem was described in the previous section. It is now possible to modify Equation (5-17) to reflect the more realistic failure surface.

Cohesion acts only along the failure surface. Therefore, for the same conditions and same bearing area, the ratio of the failure surface area for the rolling sphere, S_s, to that of a footing, S_f, is an index of the extent by which the cohesion contribution to resistance to rolling differs from the contribution of cohesion to bearing capacity under a footing. A footing resting on a horizontal surface with a usual failure surface is illustrated in Figure 5-9a. The failure surfaces for a rolling sphere and a footing for analogous conditions are illustrated in Figure 5-9b. (S_s and S_f were measured as the traces of the failure surfaces in the vertical plane.) The ratio S_s/S_f was determined graphically for several conditions of w/D, ϕ, and slope angle α. The results are plotted in Figure 5-10. In the comparison, a $\psi = 45 + \phi/2$ was used for the footing; this value of ψ was used by Meyerhof (1951) in determining the bearing capacity factors.

From Figure 5-10,

$$\frac{S_s}{S_f} \cong 0.37 + 0.25 \frac{w}{D} . \tag{5-18}$$

Therefore, from the proportionality,

$$\frac{N_{cs}}{N_c} = \frac{S_s}{S_f} , \tag{5-19}$$

$$N_{cs} = \left(0.37 + 0.25 \frac{w}{D}\right) N_c , \tag{5-20}$$

where N_{cs} is the bearing capacity factor for cohesion for a rolling sphere.

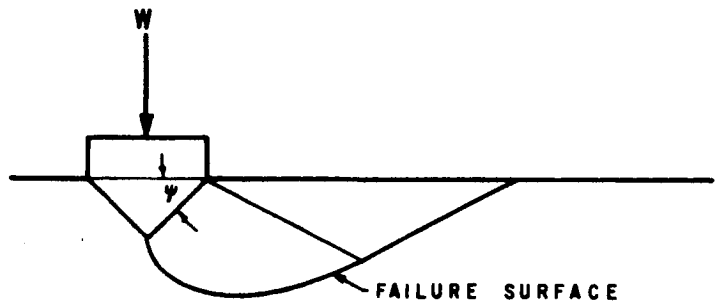

a) Failure surface for a footing as indicated by bearing capacity theory.

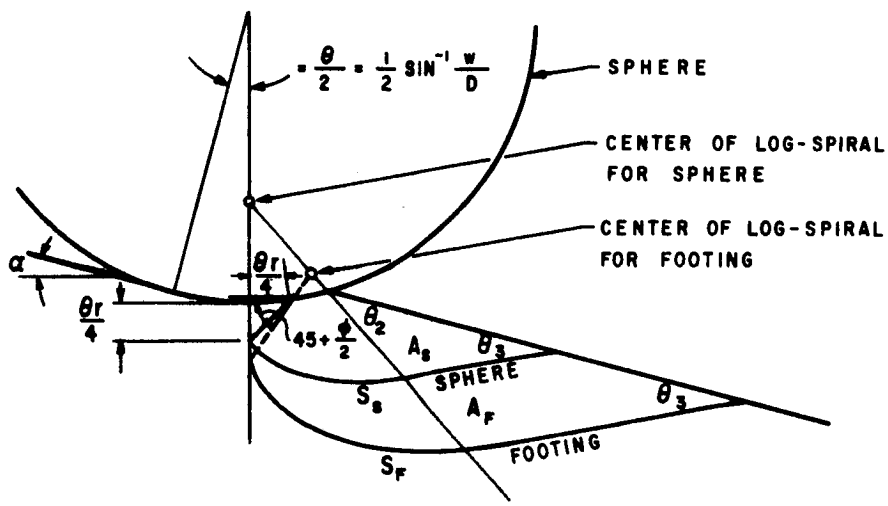

b) Failure surfaces for a sphere and a footing for analogous conditions as indicated by bearing capacity theory. (For failure condition on a plane normal to the direction of travel, see Figure 5-13).

Fig. 5-9. Illustration of the failure surfaces for a rolling sphere and a footing.

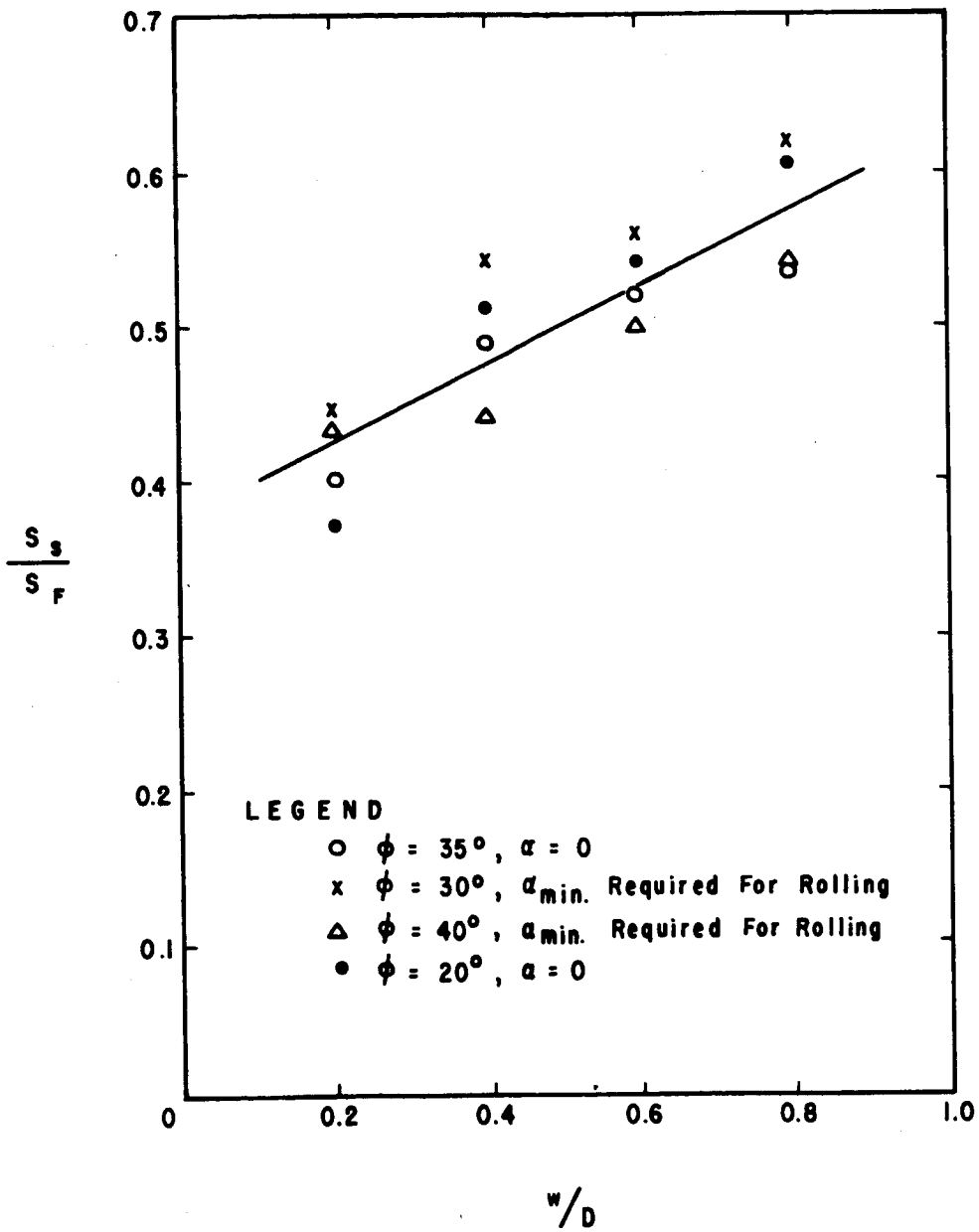

Fig. 5-10. Failure surface of a sphere as a function of failure surface of a footing and the w/D ratio.

Surcharge acts on an area confined by the failure surface and is, therefore, a function of the extent of the failure surface similar to cohesion. The relationship between N_c and N_q has been established and can be found in many books and papers on the subject (Terzaghi, 1943):

$$N_c = \cot \phi \left[N_q - 1 \right] . \tag{5-21}$$

Therefore,

$$N_{qs} = \left(0.37 + 0.25 \frac{w}{D} \right) \tan \phi \, N_c + 1, \tag{5-22}$$

where N_{qs} is the bearing capacity factor for surcharge for a rolling sphere.

Resistance caused by the weight of soil, the N_γ term, is a function of the longitudinal section area of the failure wedge. The ratio of the longitudinal section area of the failure wedge for a rolling sphere, A_s, to that of a footing, A_f, may therefore be taken as an index of the extent by which $N_{\gamma s}$ differs from N_γ. ($N_{\gamma s}$ is the bearing capacity factor for soil weight for a rolling sphere.) These areas are illustrated in Figure 5-9b. The ratio of A_s/A_f was determined graphically for the same conditions of w/D, ϕ, and α used to determine S_s/S_f. The results are plotted in Figure 5-11. A comparison of values of S_s/S_f and A_s/A_f in Figures 5-10 and 5-11 show that

$$\frac{A_s}{A_f} \cong \left(\frac{S_s}{S_f} \right)^2 . \tag{5-23}$$

Therefore, from the proportionality

$$\frac{N_{\gamma s}}{N_\gamma} = \frac{A_s}{A_f} , \tag{5-24}$$

$$N_{\gamma s} = \left(0.37 + 0.25 \frac{w}{D} \right)^2 N_\gamma . \tag{5-25}$$

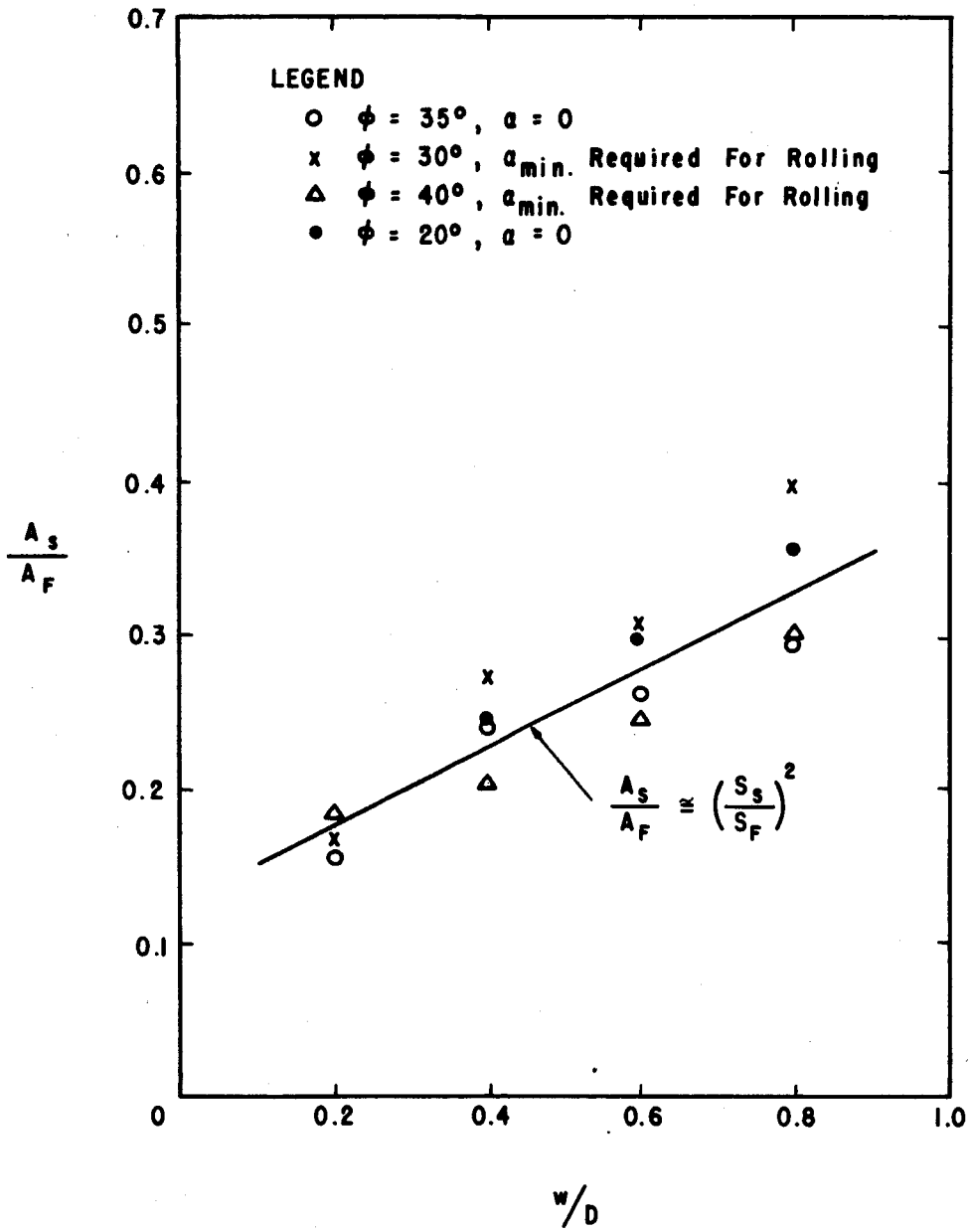

Fig. 5-11. A_s/A_f ratio vs w/D.

Replacing the bearing capacity factors in Equation (5-17) with $N_{\gamma s}$, N_{cs}, and N_{qs}, we have

$$\frac{q_s}{w\gamma_s} = 0.188\ N_{\gamma s} + 1.1\left(\frac{c}{w\gamma_s}\right) N_{cs} + 0.55\left(\frac{z}{w}\right) N_{qs}\ . \qquad (5\text{-}26)$$

Equation (5-26), therefore, provides an expression for rolling sphere-soil slope interaction based on the selected failure surface.

Summary

In summary, the steps and assumptions leading to Equation (5-26) are reviewed.

1. The general bearing capacity equation (2-4) which was derived by Terzaghi (1943), is the basis for Equation (5-26). Equation (2-4) was developed for an infinitely long footing, which implies a two-dimensional analysis. Superposition of the effects of N_γ, N_c, and N_q was also assumed.
2. Equation (5-17) was developed from Equation (2-4) using shape factors.
3. Studies of the failure mechanism (Chapter 3) and the pressure distribution (Chapter 4) showed that the actual failure wedge (zone of shearing soil) in the rolling sphere problem is much smaller than that predicted for a footing of equal area from bearing capacity theory. It was further shown that shear failure is more directly related to the maximum pressure than to the average pressure underneath the sphere. These two characteristics were considered in this section, and on that basis, Equation (5-26) was developed from Equation (5-17).

Therefore, Equation (5-26) was developed from a two-dimensional analysis and modified to be applicable to the rolling sphere-soil slope interaction problem. It is believed that it closely approximates the actual three-dimensional case. Theoretical predictions are compared with experimental data in the next chapter.

RESISTANCE DUE TO SOIL INERTIA

It is possible to speak of two types of motion for a rolling sphere: uniform rolling and bouncing. Apparently the effects of even minor irregularities in the soil slope and sphere geometry become magnified as the velocity increases. At a certain velocity, depending on the situation, conditions of uniform rolling are influenced to the point that bouncing begins. The theoretical developments in this chapter are only for uniform rolling.

Experimental investigations on accelerating spheres have shown that the track width is essentially independent of sphere velocity until the sphere starts bouncing. Therefore, one might suspect that inertia effects of the moving soil would be insignificant. On the other hand, because of the reduced lunar gravity, inertia effects on the moon will be six times more important, relative to soil resistance due to friction and surcharge, than on the earth. Thus, inertia forces must be evaluated in order to determine their importance.

The resistance due to the inertia force of the moving soil, F_I, is the product of the mass of soil involved, m_s, and its acceleration, a_s;

$$F_I = m_s a_s . \tag{5-27}$$

These items will be analyzed below.

Mass of the Moving Soil

Due to mathematical complexities in expressing exactly the volume of soil bounded by the log-spiral failure surface, an approximation of the volume of soil is developed. Should the volume of soil turn out to be significant, a more precise determination may be necessary.

A longitudinal section of the failure surface confining the moving soil, and an approximation to that surface confining approximately the same area of soil as shown in Figure 5-12a. The ratio of d/d_o is plotted in Figure 5-12b; this ratio was determined graphically. Mathematically, the curve in Figure 5-12b can be expressed by

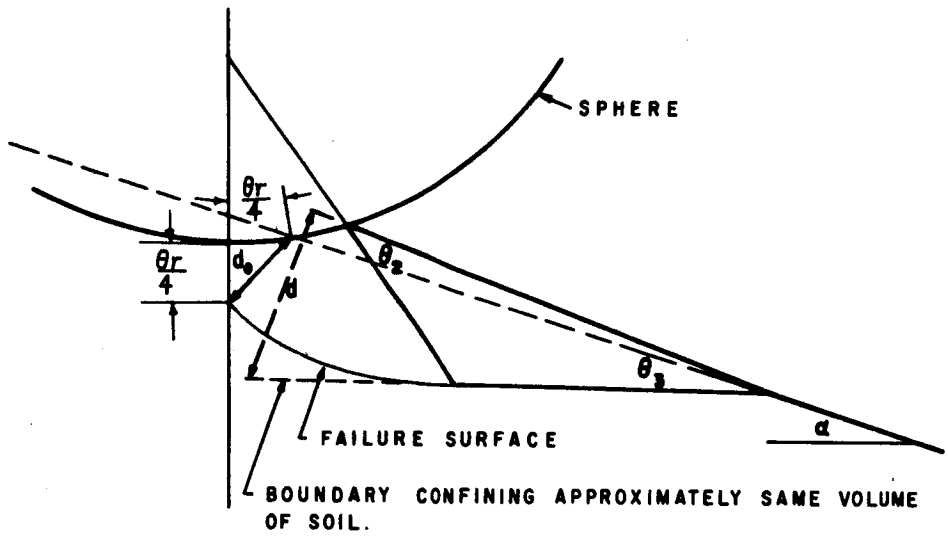

a) Boundary confining approximately the same area of soil as the actual failure surface.

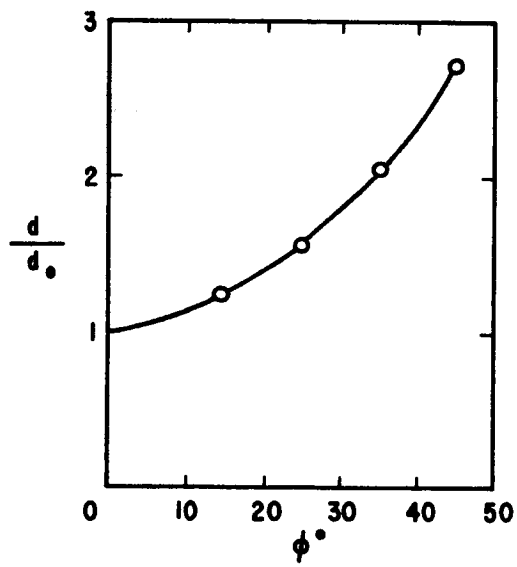

b) Ratio of d/d_0 as a function of ϕ.

Fig. 5-12. Geometry for volume of moving soil.

$$\frac{d}{d_o} = 1 + 0.002\phi^{1.77} \quad , \tag{5-28}$$

where ϕ is in degrees.

From Figure 5-12a, the volume of soil is approximately

$$V_s = \frac{1}{2} \frac{b_s}{\tan \theta_3} d^2 \quad , \tag{5-29}$$

where b_s is the width of the moving soil wedge.

From Figure 5-8, the maximum width of the side shear zone is shown to be 0.45 w for $\gamma_r/\gamma_s = 1.7$. The depth of the failure surface below the bottom of the track can be estimated graphically to be about 0.6 d_o from drawings similar to that shown in Figure 5-12a for various w/D ratios. With these dimensions and a w/D ratio of 0.6, a cross section for the maximum depth and width of the moving soil wedge can be drawn as shown in Figure 5-13. As shown in Figure 5-13, the width of the failure wedge for purposes of computing V_s can be approximated with $b_s = 1.4$ w.

From Figure 5-12a

$$d_o \cong \frac{r\theta}{4} (2)^{\frac{1}{2}} = \frac{r}{2(2)^{\frac{1}{2}}} \sin^{-1} \frac{w}{D} \quad . \tag{5-30}$$

Substituting into Equation (5-29) for b_s, d, and d_o, and dividing through by r^2w results in a dimensionless expression for the volume of moving soil:

$$\frac{V_s}{r^2 w} = \frac{0.7}{8} \frac{\left(1 + 0.002\phi^{1.77}\right)^2}{\tan \theta_3} \left(\sin^{-1} \frac{w}{D}\right)^2 . \tag{5-31}$$

Equation (5-31) is plotted in Figure 5-14. The approximate mass of moving soil is then found simply by multiplying the volume by the soil unit weight and dividing by the acceleration of gravity:

$$m_s = \frac{V_s \gamma_s}{g} \quad . \tag{5-32}$$

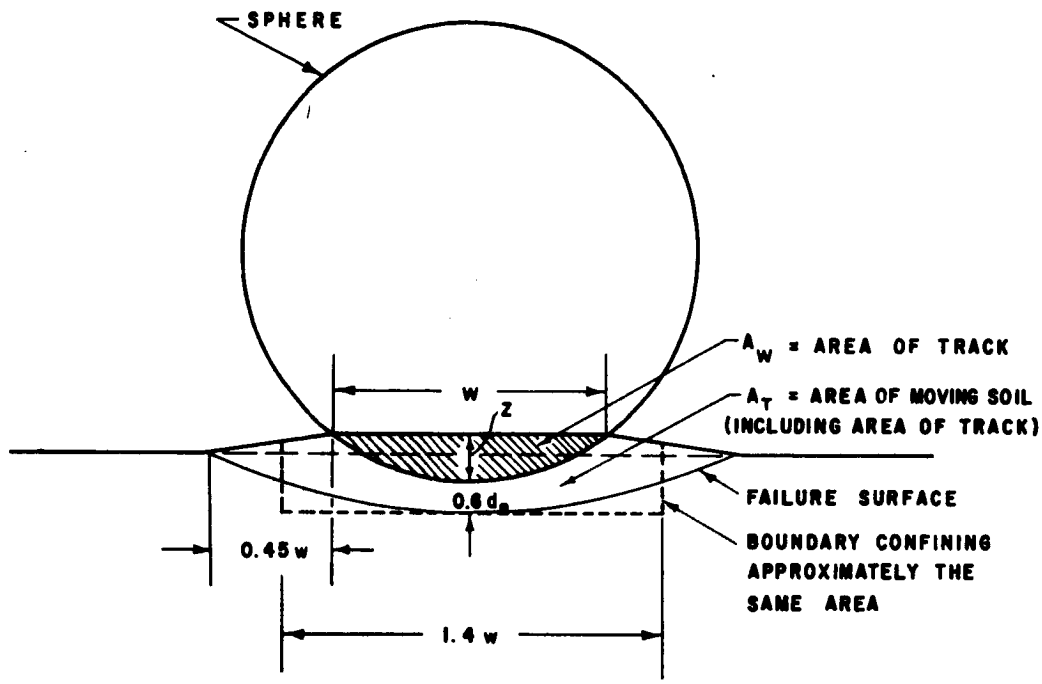

Fig. 5-13. Cross section of moving soil wedge.

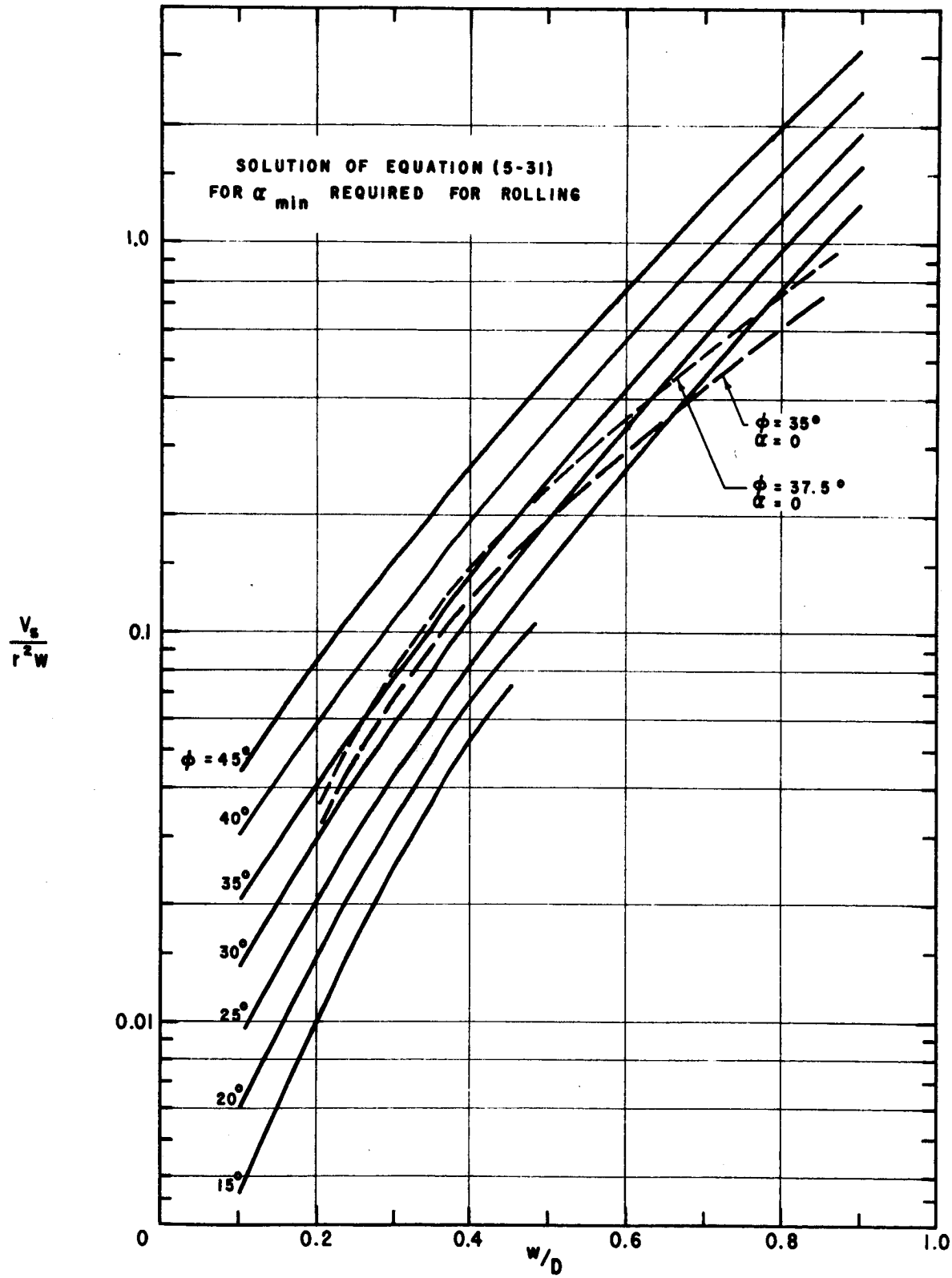

Fig. 5-14. Volume of sheared soil wedge as a function of w/D and ϕ.

Acceleration of the Moving Soil

Relationships between the velocity of the sphere and the velocity of moving soil:

The acceleration and the velocity of the moving soil must be related to the velocity of the sphere. Since the velocity of the sphere can be readily determined experimentally, it is desirable to express the velocity of the moving soil in terms of the velocity of the sphere.

Referring to Figure 5-13, continuity requires that

$$v_s A_t = v A_w \ , \tag{5-33}$$

where v_s is the velocity of moving soil, v is the velocity of the sphere, A_t is the total cross-sectional area of moving soil, and A_w is the relevant cross-sectional area of the track.

For loose sand, compression of the soil beneath the sphere reduces the magnitude of displacement along a failure surface. The relevant track area is, therefore, somewhat smaller than the track area associated with the crest-to-crest track width. Both the track area associated with the crest-to-crest track width and the reduction due to volume change (compression) can be expressed in the form of Equation (5-9) to give for A_w,

$$A_w = \frac{D^2}{8}\left(\frac{\pi}{90}\,\theta - \sin 2\theta\right) - \frac{D^2}{8}\left(\frac{\pi}{90}\,\theta_v - \sin 2\theta_v\right) \ , \tag{5-34}$$

or

$$A_w = \frac{D^2}{8}\left[\frac{\pi}{90}\left(\theta - \theta_v\right) - \sin 2\theta + \sin 2\theta_v\right] \ . \tag{5-35}$$

The total cross-sectional area of the moving soil, A_t, can be expressed from Figure 5-13 as

$$A_t \cong 1.4\ w\ (0.6 d_o + z) \ . \tag{5-36}$$

Combining Equations (5-33), (5-35), and (5-36), the velocity of

of the moving soil is

$$v_s = \frac{A_w}{A_t} v = \frac{\frac{D^2}{8}\left[\frac{\pi}{90}\left(\theta - \theta_v\right) - \sin 2\theta + \sin 2\theta_v\right]}{1.4w\left(0.6d_o + z\right)} v , \qquad (5\text{-}37)$$

since

$$d_o \cong \frac{\theta r}{4} (2)^{\frac{1}{2}} ,$$

$$\theta = \sin^{-1} \frac{w}{D} ,$$

$$\theta_v = \sin^{-1} \frac{w_v}{D} , \text{ and}$$

$$z = r\left(1 - \cos \theta\right) = r\left\{1 - \left[1 - \left(\frac{w}{D}\right)^2\right]^{\frac{1}{2}}\right\} .$$

Equation (5-37) can also be expressed as

$$v_s \cong \frac{\frac{\pi}{90}\left(\sin^{-1} \frac{w}{D} - \sin^{-1} \frac{w_v}{D}\right) - \sin\left(2 \sin^{-1} \frac{w}{D}\right) + \sin\left(2 \sin^{-1} \frac{w_v}{D}\right)}{4 \frac{w}{D}\left\{0.3 \sin^{-1} \frac{w}{D} + 1.4 - 1.4\left[1 - \left(\frac{w}{D}\right)^2\right]^{\frac{1}{2}}\right\}} v . \qquad (5\text{-}38)$$

In order to appreciate the relative magnitudes of v_s and v, Equation (5-38) was solved for w/D = 0.69 (average value for the lunar boulder tracks analyzed), and assuming that $\Delta V = 0$ (meaning that $w_v = 0$). This gave

$$v_s = 0.32 \, v . \qquad (5\text{-}39)$$

An alternative approach for estimating the velocity of the moving soil results from consideration of a longitudinal section of the rolling sphere-soil slope problem. Figure 5-15 shows the conditions to be analyzed.

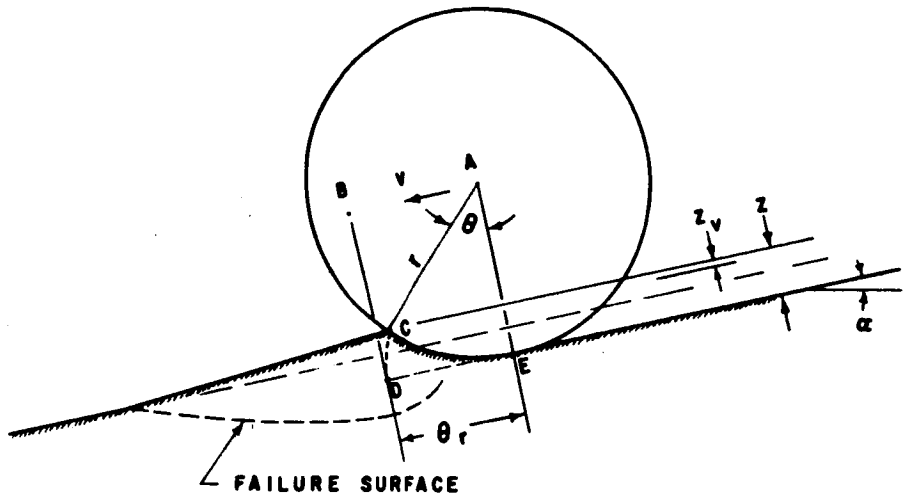

Fig. 5-15. Sphere and soil movements.

In the time required for the sphere to move from A to B, t_{sphere}, the soil at C must have moved from C to D. (That the soil moves approximately from C to D was demonstrated experimentally from model studies, see Figure 3-7.) Due to compression of the soil (volume change), the displacement generated along the failure surface will be somewhat smaller than the distance CD. This displacement can be expressed by $(z - z_v)$. Equating the time intervals,

$$t_{sphere} = t_{soil} = \frac{\theta r}{v} = \frac{\left(z - z_v\right)}{v_s} \quad , \tag{5-40}$$

from which

$$v_s = \left(z - z_v\right) \frac{v}{\theta r} \, . \tag{5-41}$$

Equation (5-41) expresses a relationship between the magnitudes of v_s and v; it says nothing about their directions, which are irrelevant in this consideration.

Since $\theta = \sin^{-1}\frac{w}{D}$ and $z = r\left\{1 - \left[1 - \left(\frac{w}{D}\right)^2\right]^{\frac{1}{2}}\right\}$, we also have

$$v_s = \left(1 - \frac{z_v}{z}\right)\left\{\frac{1 - \left[1 - \left(\frac{w}{D}\right)^2\right]^{\frac{1}{2}}}{\sin^{-1}\frac{w}{D}}\right\} v. \qquad (5\text{-}42)$$

In order to compare Equation (5-42) with Equation (5-38), Equation (5-42) was solved for w/D = 0.69 and $z_v = 0$ (meaning $w_v = 0$). This gave

$$v_s = 0.36\ v. \qquad (5\text{-}42b)$$

Since Equations (5-38) and (5-42) give nearly the same results as shown by Equations (5-39) and (5-42b), and since both are approximate, Equation (5-42) will be used because of the simpler calculations involved.

Equations (5-41) and (5-42) give the velocity of the shearing soil wedge as a function of the velocity of the sphere. The z_v and z terms can be determined from Figure 5-6 which applies to both, although marked out for z_v.

Expressing the distance through which the soil moves by $(z - z_v)$ as done above, is an approximation and implies three situations:

1. When there are no raised rims; $\Delta V > 0$, $z_v = z$, and there is theoretically no movement of a mass of soil since there is no general shear. This case is encountered only in very loose soils.

2. When the volume of the rims equals the volume of the track; $\Delta V = 0$, $z_v = 0$, and the soil moves approximately through the distance $(z - z_v)$.

3. When the volume of the rims is greater than the volume of the track (a dilating soil); assume that $\Delta V = 0$, and $z_v = 0$ as above for case 2.

Soil acceleration:

Since the soil wedge moving during general shear starts from rest and comes to rest after the rolling sphere has passed, we know that the initial and final soil velocities are zero. Somewhere in between, the velocity of the shearing soil reaches a maximum. As an illustration, for a parabolic velocity function, the displacement, velocity, and acceleration as a function of time would plot as shown in Figure 5-16.

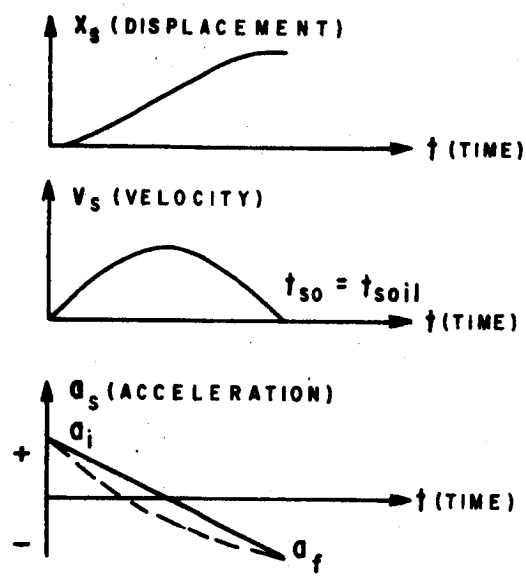

Fig. 5-16. Time functions of x_s, v_s, and a_s.

If the velocity of the soil reached a maximum before $t_{so}/2$, the acceleration function would be curved as shown by the dashed line in Figure 5-16. From a mathematical point of view, it has been found most convenient to represent the acceleration curve by

$$a_s = -B_1 t^{1/n} + B_2 \text{ , where } B_1 \text{ and } B_2 \text{ are} \qquad (5\text{-}43)$$

constants to be determined from the boundary conditions, and n is a

positive number. Therefore, at $t = 0$, $a_s = a_i$, initial acceleration, giving $B_2 = a_i$. At $t = t_{so}$, $a_s = a_f$, final acceleration (actually deceleration) giving

$$a_f = - B_1 t_{so}^{1/n} + a_i \quad , \qquad B_1 = \frac{a_i - a_f}{t_{so}^{1/n}} \quad . \tag{5-44}$$

Then the acceleration becomes

$$a_s = a_i - \left(a_i - a_f\right) \left(\frac{t}{t_{so}}\right)^{1/n} \quad . \tag{5-45}$$

The velocity is found by integrating Equation (5-45)

$$v_s = \int a_s dt = a_i t - \left(a_i - a_f\right) \frac{n}{1 + n} \frac{t^{(1+n)/n}}{t_{so}^{1/n}} + B_3 \quad , \tag{5-46}$$

where B_3 is an integration constant. At $t = 0$, $v_s = 0$ giving $B_3 = 0$. Also, at $t = t_{so}$, $v_s = 0$ giving

$$0 = a_i t_{so} - \left(a_i - a_f\right) \frac{n}{1 + n} t_{so} \quad , \text{ and} \tag{5-47}$$

since $t_{so} \neq 0$,

$$a_f = - \frac{a_i}{n} \quad , \text{ or } \quad n = - \frac{a_i}{a_f} \quad . \tag{5-48}$$

After some manipulation of Equation (5-46),

$$v_s = a_i t \left[1 - \left(\frac{t}{t_{so}}\right)^{1/n}\right] . \tag{5-49}$$

The displacement can be found by integrating Equation (5-49)

$$x_s = \int v_s dt = a_i t^2 \left[\frac{1}{2} - \frac{n}{1 + 2n} \left(\frac{t}{t_{so}}\right)^{1/n}\right] + B_4 \quad , \text{ where} \tag{5-50}$$

B_4 is an integration constant. At $t = 0$, $x_s = 0$ giving $B_4 = 0$. Then

$$x_s = a_i t^2 \left[\frac{1}{2} - \frac{n}{1 + 2n} \left(\frac{t}{t_{so}} \right)^{1/n} \right]. \tag{5-51}$$

We have yet one more condition: at $t = B_5 t_{so}$, $v_s = v_{max}$, and $a_s = 0$. Hence,

$$a_s = 0 = a_i \left[1 - \frac{n + 1}{n} \left(B_5 \frac{t_{so}}{t_{so}} \right)^{1/n} \right], \text{ and} \tag{5-52}$$

since $a_i \neq 0$

$$B_5 = \left(\frac{n}{n + 1} \right)^n . \tag{5-53}$$

Then:

$$v_{max} = a_i \left(\frac{n}{n + 1} \right)^n t_{so} \left\{ 1 - \left[\left(\frac{n}{n + 1} \right)^n \right]^{1/n} \right\}, \text{ and} \tag{5-54}$$

$$a_i = (n + 1) \left(\frac{n + 1}{n} \right)^n \frac{v_{max}}{t_{so}} . \tag{5-55}$$

Substituting a_i from Equation (5-55) into Equations (5-45), (5-49), and (5-51) results in the final general expressions for acceleration, velocity, and displacement respectively:

$$a_s(t) = n \left(\frac{n + 1}{n} \right)^{n+1} \left[1 - \frac{n + 1}{n} \left(\frac{t}{t_{so}} \right)^{1/n} \right] \frac{v_{max}}{t_{so}} \tag{5-56}$$

$$v_s(t) = (n + 1) \left(\frac{n + 1}{n} \right)^n \frac{t}{t_{so}} \left[1 - \left(\frac{t}{t_{so}} \right)^{1/n} \right] v_{max} \tag{5-57}$$

$$x_s(t) = (n + 1) \left(\frac{n + 1}{n} \right)^n \frac{t^2}{t_{so}} \left[\frac{1}{2} - \frac{n}{1 + 2n} \left(\frac{t}{t_{so}} \right)^{1/n} \right] v_{max}. \tag{5-58}$$

We are, however, interested in the total or maximum displacement. This can be obtained by integrating Equation (5-57) between known

limits (0 and t_{so}). Then the total displacement equals

$$x_{total} = \frac{n+1}{2(1+2n)} \left(\frac{n+1}{n}\right)^n v_{max}\, t_{so} . \qquad (5\text{-}59)$$

The maximum inertia force develops for maximum acceleration. It was shown previously that for the function assumed, $a_s = a_{max}$ when time equals zero. Therefore, from Equation (5-56)

$$a_{max} = (n+1)\left(\frac{n+1}{n}\right)^n \frac{v_{max}}{t_{so}} . \qquad (5\text{-}60)$$

Since we are only able to infer the total displacement from measurements of volume change and track dimensions, which implies a relationship with the average velocity, a theoretical expression for a_{max} in terms of average velocity is needed. The theoretical average velocity is

$$v_{at} = \frac{\int_o^{t_{so}} v_s\, dt}{t_{so}} = \frac{x_{max}}{t_{so}} = \frac{n+1}{2(1+2n)} \left(\frac{n+1}{n}\right)^n v_{max} . \qquad (5\text{-}61)$$

This velocity, v_{at}, can be related to the velocity expressed by Equation (5-41), v_s:

$$v_s = v_{at} = (z - z_v)\frac{v}{\theta r} = \frac{n+1}{2(1+2n)} \left(\frac{n+1}{n}\right)^n v_{max} . \qquad (5\text{-}62)$$

Solving for v_{max},

$$v_{max} = \frac{(z - z_v)\frac{v}{\theta r}}{\frac{n+1}{2(1+2n)}\left(\frac{n+1}{n}\right)^n} . \qquad (5\text{-}63)$$

Dividing v_{max} by $t_{so} = \theta r/v$, as expressed by Equation (5-40),

$$\frac{v_{max}}{t_{so}} = \frac{z - z_v}{\frac{n+1}{2(1+2n)}\left(\frac{n+1}{n}\right)^n} \left(\frac{v}{\theta r}\right)^2 . \qquad (5\text{-}64)$$

Substituting Equation (5-64) into Equation (5-60) results in the desired expression for maximum acceleration:

$$a_{max} = 2(1 + 2n)\ (z - z_v)\left(\frac{v}{\theta r}\right)^2 , \qquad (5\text{-}65)$$

where again $\theta = \sin^{-1}\frac{w}{D}$.

Equation (5-65) is a simple expression where the terms in the last two parentheses can be experimentally determined. A suitable means for determining n has not yet been developed; however, some experimental data which are useful for its estimation are presented and discussed in the next chapter. Since $n = -a_i/a_f$, Equation (5-65) also states that the closer the maximum velocity is to the start of motion timewise, the higher is a_{max}.

Inertia Force Associated with the Moving Soil

Combining Equations (5-32) and (5-65), we have for the inertia force:

$$F_I = \frac{V_s\gamma_s}{g}\ 2(1 + 2n)\ (z - z_v)\left(\frac{v}{\theta r}\right)^2 . \qquad (5\text{-}66)$$

This force can be expressed as force per unit area analogous to unit bearing capacity by dividing by the contact area $A = (\pi/2)(w/2)^2$:

$$q_I = \frac{16}{\pi}\ (1 + 2n)\ \frac{V_s\gamma_s}{gw^2}\ (z - z_v)\left(\frac{v}{\theta r}\right)^2 . \qquad (5\text{-}67)$$

A convenient dimensionless expression results from rearranging the terms in Equation (5-67):

$$\frac{q_I}{\gamma_s(z - z_v)}\ \frac{w^2D}{V_s} = 20.3\ \frac{(1 + 2n)}{\left(\sin^{-1}\frac{w}{D}\right)^2}\ \frac{v^2}{gD} . \qquad (5\text{-}68)$$

To show that the inertia resistance is independent of gravity, γ_s can be expressed as ρg, where ρ is the mass density of the soil.

Then Equation (5-68) becomes

$$\frac{q_I}{\rho(z - z_v)} \frac{w^2 D}{V_s} = 20.3 \frac{(1 + 2n)}{\left(\sin^{-1} \frac{w}{D}\right)^2} \frac{v^2}{D} \quad . \tag{5-69}$$

In solving Equation (5-68) or (5-69), V_s is determined from Figure 5-14, and z and z_v can be determined from Figure 5-6. As an aid in solving Equation (5-68) it is plotted in Figure 5-17. Comparison of relative magnitudes of q_I and q_s are presented in Chapter 7. For the solid 12-cm spheres rolled at WES, q_I as a percentage of $(q_I + q_s)$ varied from about 1% to 16% for moist Yuma sand and dry Yuma sand, respectively.

SUMMARY

It is now possible to combine the effects of general shear and soil inertia into one equation; this presumes that superposition is valid. First, it is necessary to rearrange Equation (5-68) to obtain a term comparable to the terms in the bearing equation. Such rearrangement gives

$$\frac{q_I}{w\gamma_s} = B(z - z_v) \frac{V_s}{w^3 D} \quad , \tag{5-70}$$

where

$$B = 20.3 \frac{(1 + 2n)}{\left(\sin^{-1} \frac{w}{D}\right)^2} \frac{v^2}{gD} \quad , \tag{5-71}$$

as obtained from Figure 5-17.

Then, the total unit pressure resistance to rolling is given by

$$\frac{q_e}{w\gamma_s} = 0.188 N_{\gamma s} + 1.1 \left(\frac{c}{w\gamma_s}\right) N_{cs} + 0.55 \left(\frac{z}{w}\right) N_{qs} + \frac{q_I}{w\gamma_s} \quad . \tag{5-72}$$

In Equation (5-72) q_e is the unit resistance in earth gravity. In lunar gravity, replacing the γ_s term by $\gamma_s/6$, the unit resistance

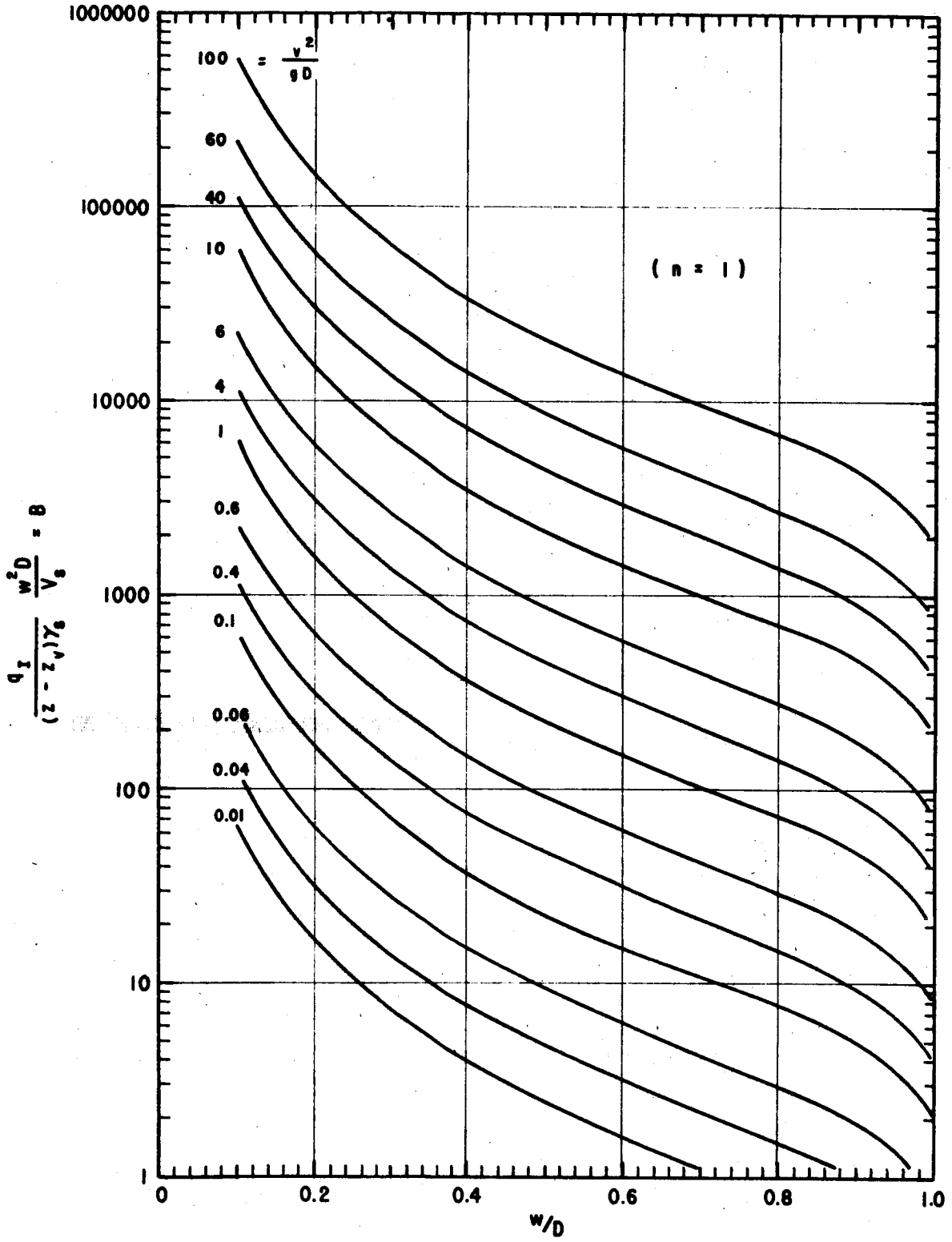

Fig. 5-17. Plot of Equation (5-69).

is given by

$$\frac{q_m}{w\gamma_s} = 0.0314N_{\gamma s} + 1.1\left(\frac{c}{w\gamma_s}\right)N_{cs} + 0.0916\left(\frac{z}{w}\right)N_{qs} + \frac{q_I}{w\gamma_s} \quad . \qquad (5\text{-}73)$$

From the relationship of sphere weight to bearing area (Hovland and Mitchell, 1970), a second expression is obtained. This expresses the average applied pressure, and in earth gravity is

$$\frac{q_e}{w\gamma_s} = \frac{4}{3}\frac{\left(\gamma_r/\gamma_s\right)}{\left(w/D\right)^3} \quad . \qquad (5\text{-}74)$$

In lunar gravity

$$\frac{q_m}{w\gamma_s} = \frac{2}{9}\frac{\left(\gamma_r/\gamma_s\right)}{\left(w/D\right)^3} \quad . \qquad (5\text{-}75)$$

Further, as shown in Figure 5-9b, a unique relationship must exist between w/D and the slope angle, α, for constant velocity rolling. The relationship is

$$\frac{w}{D} = \sin 2\alpha \quad . \qquad (5\text{-}76)$$

We, therefore, have three equations which can be combined to solve for parameters of interest. These equations are:

1. Equations (5-72) or (5-73) expressing total soil resistance,
2. Equations (5-74) or (5-75) expressing the applied pressure, and
3. Equation (5-76) expressing the relationship between w/D and α.

The parameters associated with these equations, known or unknown depending on the situation, are:

1. γ_s , γ_r , ϕ, c, and v (usually variables)

2. w, D, ΔV, α, n, and g (usually measured, known, or assumed)
3. z, z_v, V_s, q_e, and q_I (usually calculated from developed relationships).

Graphs for easy solution of the above equations can be prepared. It is necessary first, however, to examine experimental data in terms of the theory.

Chapter 6. ROLLING SPHERE EXPERIMENTS AND COMPARISON WITH THEORETICAL PREDICTIONS

In order to study simultaneously the influence and interrelationships of a number of pertinent parameters, solid spheres were rolled on Yuma sand at the U. S. Army Engineer Waterways Experiment Station (WES) in Vicksburg, Mississippi. Because of the extensive facilities and excellent cooperation provided by the WES personnel, it was possible for us to extend these experimental studies beyond what was originally planned. The assistance and facilities provided by WES to this effort were funded through NASA Defense Purchase Request H-58504A from MSFC.

This chapter presents a description of the equipment used, the testing technique, and the results of these experimental studies. The results are presented in summary form; additional details and data are to be found in the appendices.

The analysis of the experimental data can be divided into 1) measurements of the tracks left by the rolling spheres, and 2) analysis of films taken of the rolling spheres.

Wherever possible, curves developed according to the theory in the previous chapter are superimposed on the experimental data, with a brief discussion on the significance of the comparison.

DESCRIPTION OF EQUIPMENT AND TESTING TECHNIQUE

The testing was done on Yuma sand prepared to uniform density and moisture content in a large soil car. Methods for preparing the soil car, controlling moisture content, and determining soil properties are described in Appendices A and B. The cars were 27 feet long, 64 inches wide, and contained soil to depths of 18 or 32 inches. Figure 6-1 is a photograph of the car used.

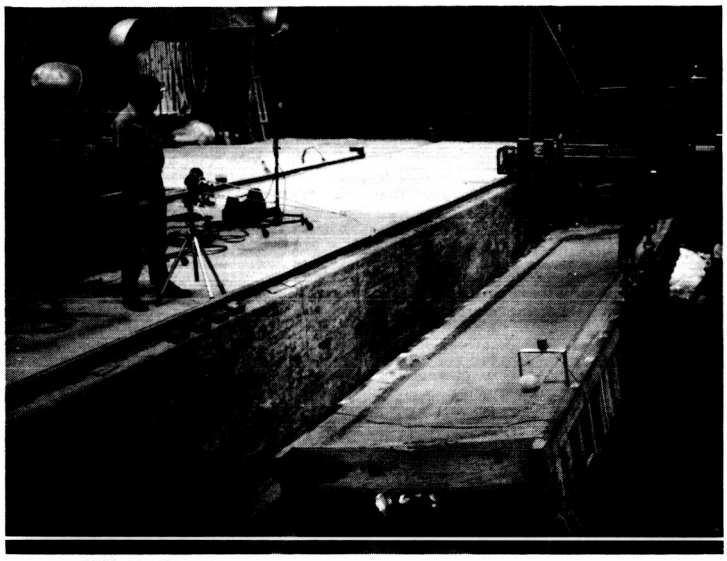

Fig. 6-1. Soil car used for testing at Vicksburg.

Nine soil cars were tested, with soil conditions as indicated in Table 6-1.

Table 6-1. Sand properties in different soil cars.

Car #	ω %	G (MN/m^3)	G (lb/in^3)	γ_d (gm/cc)	ϕ (°)	c KN/m^2	c lb/in^2	D_r (%)
1	0.20	0.57	2.11	1.480	37	0	0	34
2	0.20	0.45	1.67	1.453	37	0	0	26
3	0.20	3.02	11.20	1.618	42	0.20	0.029	86
4	1.50	2.65	9.82	1.473	37.5	1.07	0.156	35
5	1.55	0.20	0.74	1.245	32	0.46	0.067	< 0*
6	1.55	0.24	0.89	1.245	32	0.46	0.067	< 0*
7	1.50	0.35	1.30	1.280	33	0.47	0.069	< 0*
8	1.50	1.90	7.04	1.491	37.5	0.84	0.122	41
9	1.55	1.76	6.52	1.436	36.5	0.88	0.128	20

In Table 6-1, the symbols at the columns are defined as follows:

ω% = moisture content in percent

G = cone index gradient expressed in mega newtons per meter cubed and in pounds per cubic inch

γ_d = dry density of sand in grams per cubic centimeter

ϕ = angle of shearing resistance (friction angle), determined from Figure B-10 and based on triaxial results

c = apparent cohesion expressed in kilo newtons per meter squared and in pounds per square inch

D_r = relative density of sand in percent

---

* $D_r = 0$ refers to the loosest state of air-dry Yuma sand; moist Yuma sand can be prepared to an even looser state with respect to γ_d, therefore giving $D_r < 0$.

Eight different spheres were rolled over the soil in cars 1 through 5, and selected spheres were tested with cars 6, 7, 8, and 9. Two series of data were collected: 1) track formation from spheres of varying density but constant size, and 2) track formation from spheres of varying size but constant density. Data from track measurements are presented in Appendix D.

The spheres were made of concrete, giving a rough contact between soil and sphere. They were cast in hemispherical molds and subsequently the two halves were cemented together using an epoxy cement. The desired variations in density were obtained by using lead shots as a heavy aggregate and styrofoam plastic as a light aggregate. Sphere E, the lightest sphere, was made from a piece of extremely light weight concrete. Characteristics of the spheres are listed in Table 6-2.

Table 6-2. Sphere characteristics.

Series	Sphere	Diameter (cm)	Density (gm/cc)
Density, γ_r	A	12.10	3.69
(constant size)	B	12.15	2.14
	C	12.00	1.73
	D	12.10	1.05
	E	12.02	0.52
Size	1a	7.16	1.86
(constant density)	2(c)	12.00	1.73
	3a	17.40	1.76
	4	25.30	1.79

Movie films were taken of all rolling spheres using a Bell & Howell camera with 1", 2", and 3" lenses. The camera also had variable speed adjustment, and we used speeds of 25 and 50 frames per second depending on the focus and lighting conditions. The movies provided information on the distance, velocity, and acceleration of the spheres as a function of time. Equally significant was the information the movie films provided on the rolling sphere – soil slope interaction

phenomenon and on actual movement of the shearing soil wedge. The film is on file in the University of California, Geotechnical Engineering Laboratories. The films were studied using a film analyser which allowed observation frame by frame. The positions of the camera and soil car, for both cars tilted sideways and cars tilted on edge, are shown in Figures 6-2 and 6-3. With this geometry, distance to the sphere and the scale of any frame could be determined if necessary.

Figure 6-1 shows the soil car tilted to the desired slope, the camera, and the sphere in position retained by a "flip gate". The flip gate was specially designed to open the instant the camera was started. This was achieved by a solenoid on top of the flip gate. The solenoid, the moment triggered, would release the gate allowing the sphere to roll. A detailed drawing of the flip gate is shown in Figure 6-4.

TRACK MEASUREMENTS

Slope Angle Required for Rolling

Records were kept during the testing of the slope angle at which a sphere of a particular density started rolling. This relationship was, of course, a function of the soil conditions. The results are presented in Figure 6-5.

In the previous chapter, Equation (5-76) was developed for track size as a function of slope angle for constant velocity rolling:

$$\frac{w}{D} = \sin 2\alpha, \qquad (5\text{-}76)$$

The theoretical curve for this Equation is shown in Figure 6-6. In order to plot the experimental data on the same figure (Figure 6-6), the straight lines on Figure 6-5, separating rolling and no rolling situations, were combined with experimental information on the relationship between the density ratio, γ_r / γ_s, and the w/D ratio. Experimental data for the relationship between γ_r/γ_s and w/D are presented in Figure 6-7.

Therefore, the experimental verification of Equation (5-76) was achieved for certain soil conditions, by first finding the γ_r/γ_s ratio for a selected slope angle from Figure 6-5 and then finding the w/D ratio

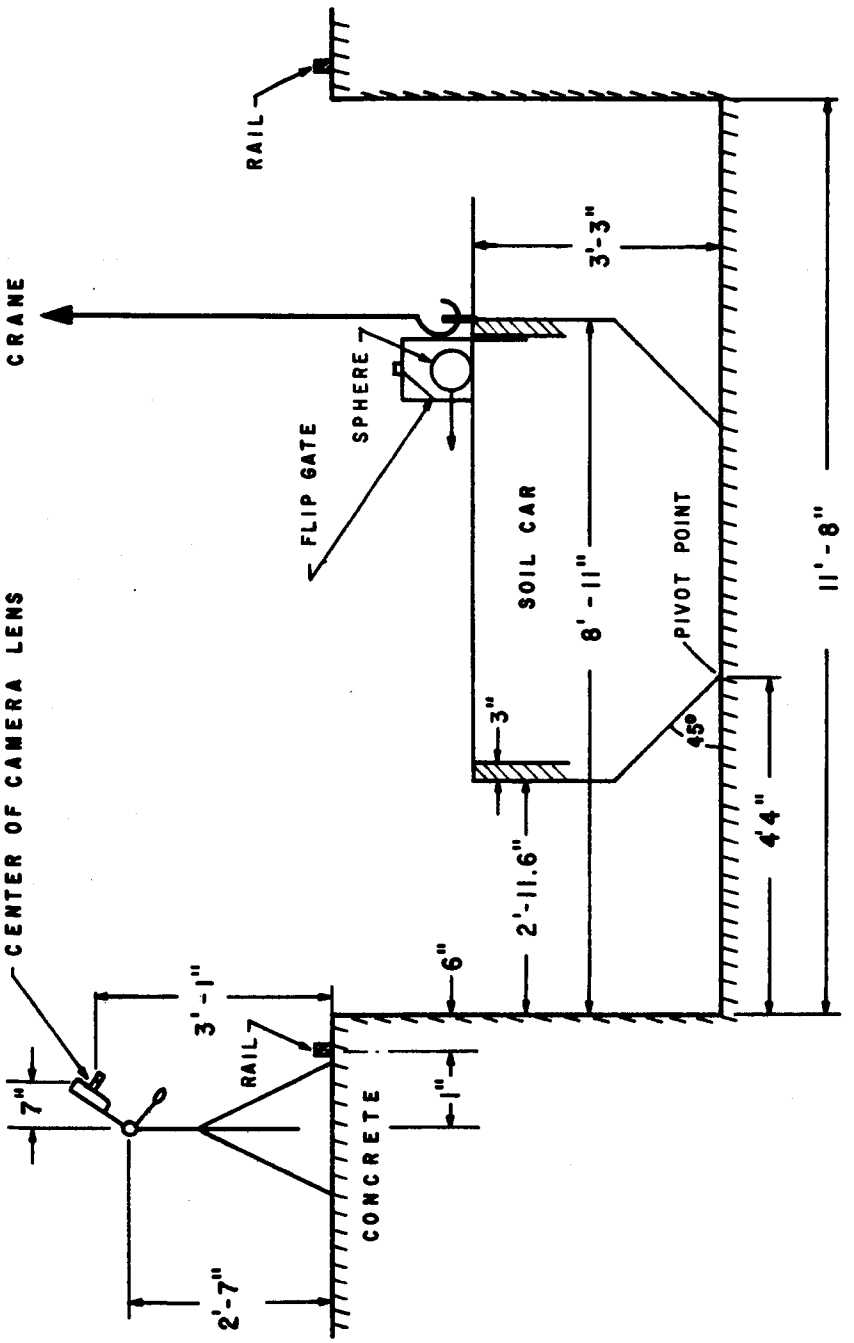

Fig. 6-2. Camera and soil car position for cars tilted sideways.

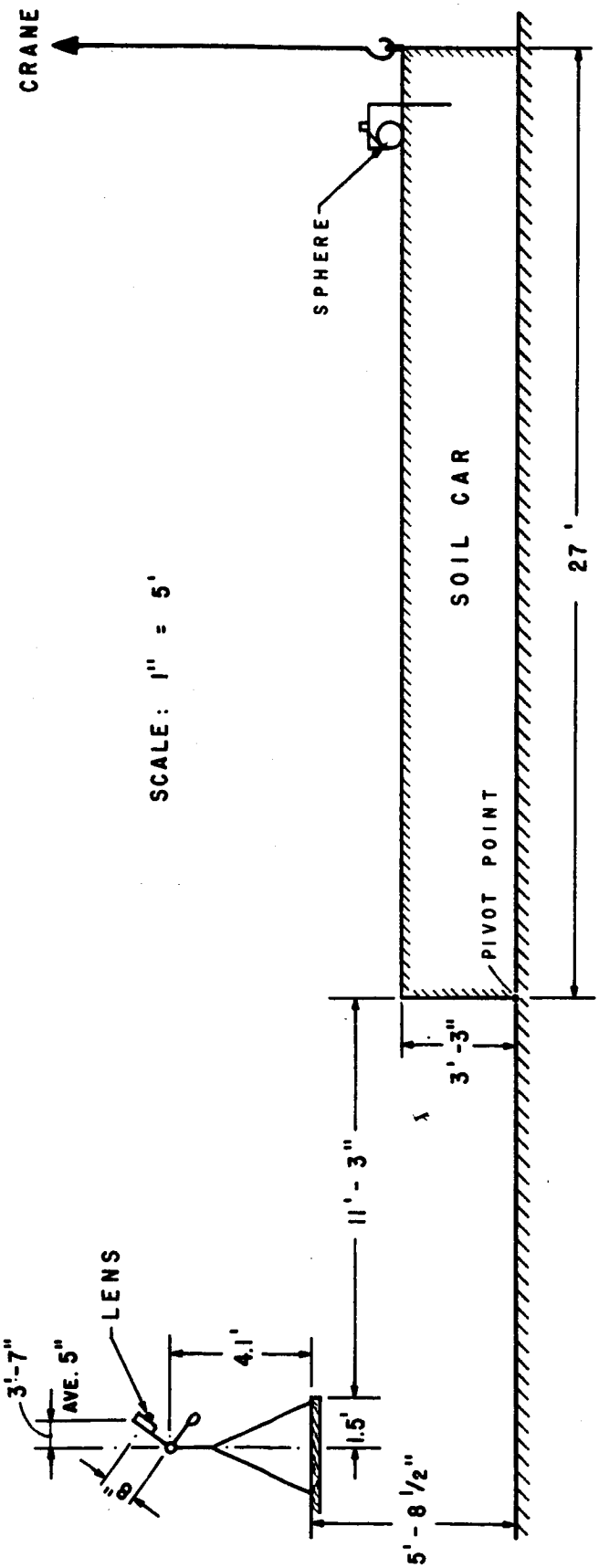

Fig. 6-3. Camera and soil car position for cars tilted on edge.

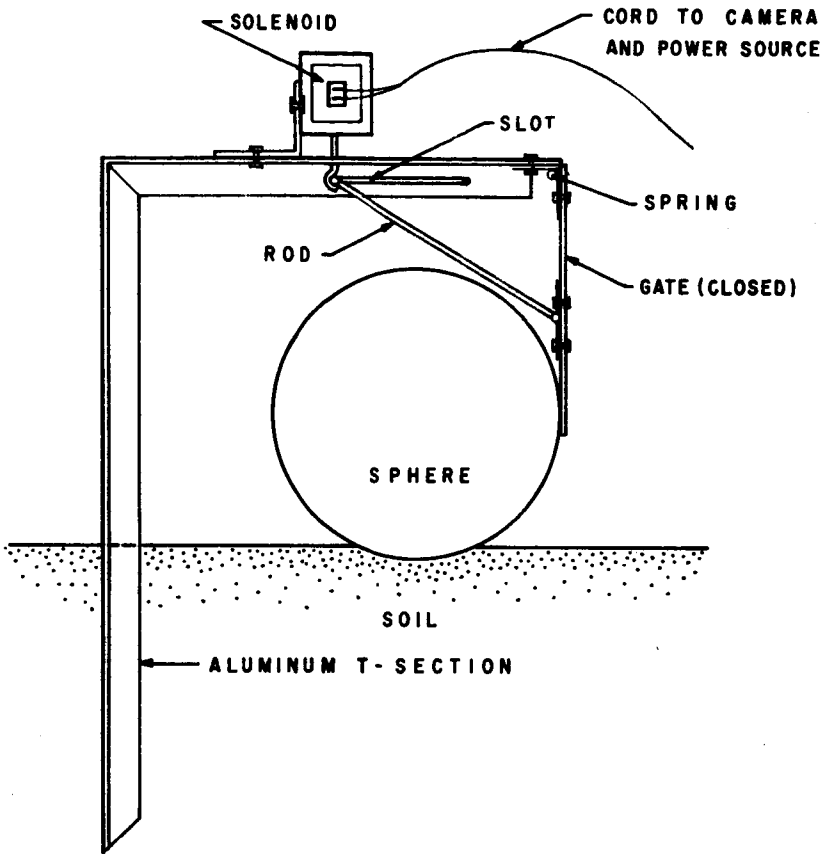

Side view

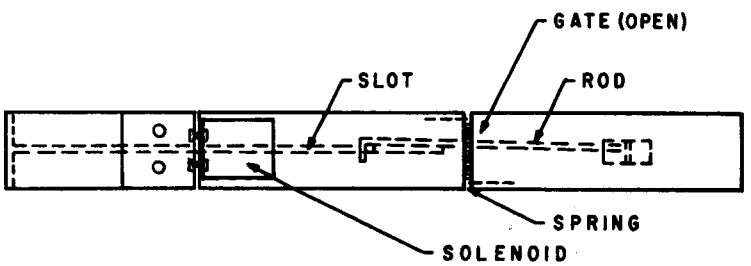

Top view

Scale: 1" = 5"

Fig. 6-4. Detail of flip gate.

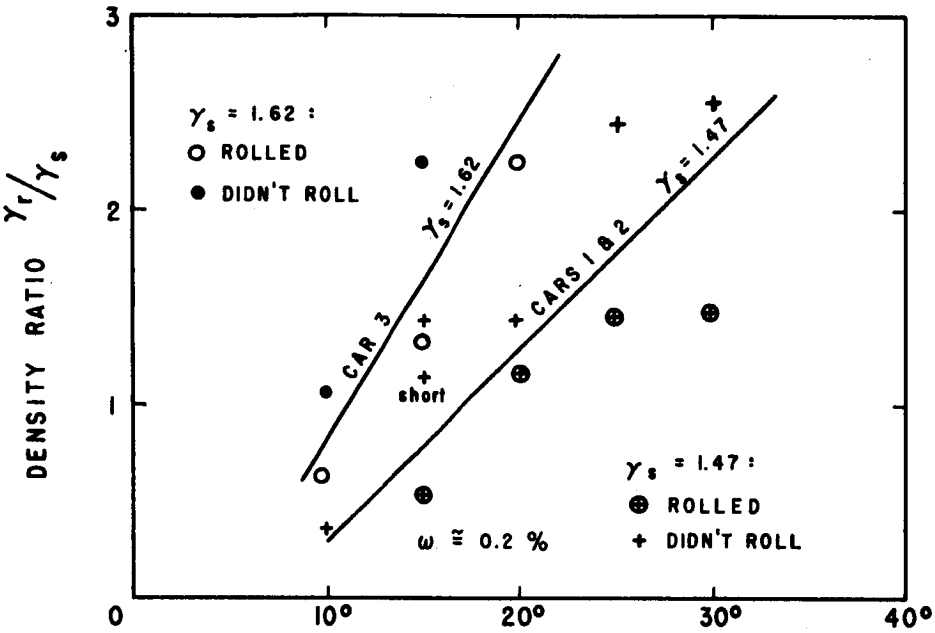

a) Slope angle, α, required for rolling in dry sand

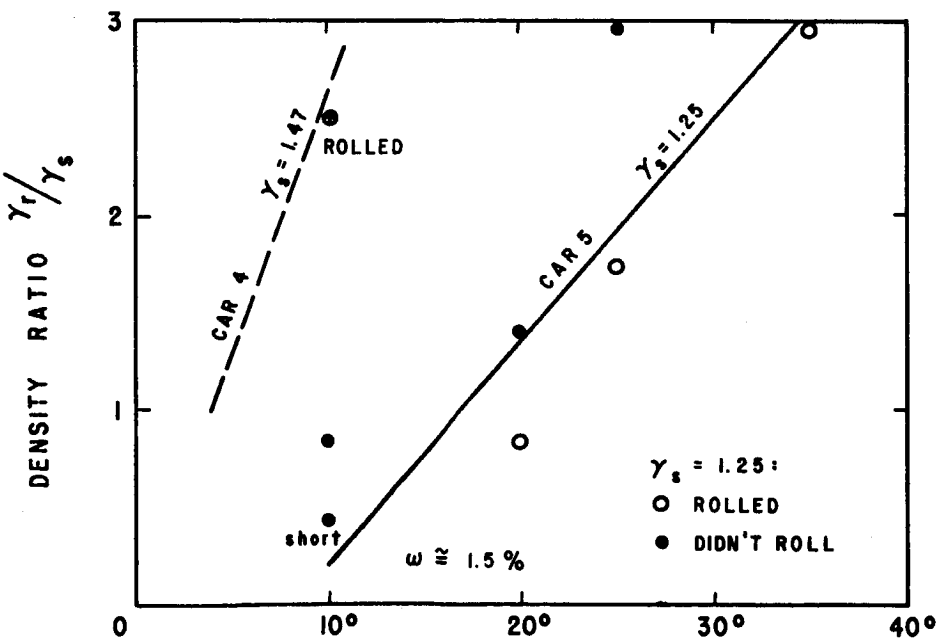

b) Slope angle, α, required for rolling in moist sand

Fig. 6-5. Density ratio vs slope angle required for rolling on Yuma sand.

Slope angle limitations:

1. $\alpha \leq \phi$

2. For constant velocity rolling α and w/D are related by:

   $w/D = \sin 2\alpha$, or $\alpha = \theta/2$

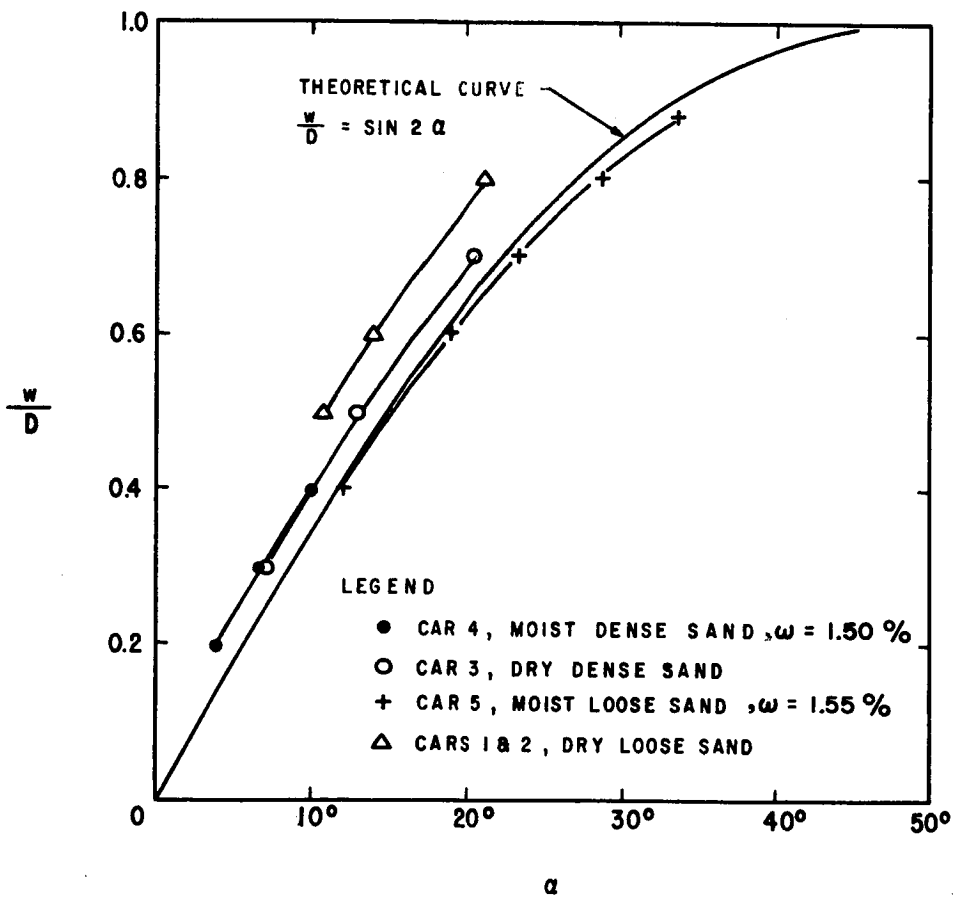

Fig. 6-6. Slope angle, α, required for rolling as a function of w/D.

for that γ_r/γ_s ratio for comparable soil conditions from Figure 6-7. It is to be noted that Figure 6-7 contains experimental data for many slope angles; therefore, the comparable condition is found by matching not only the γ_r/γ_s ratio but also the slope angle, α, on Figure 6-7 as closely as possible with the slope angle selected at the start on the basis of the trend of data from Figure 6-5. Experimental curves were replotted on Figure 6-6 by this procedure. The agreement confirms the proposed relationship, Equation (5-68). The agreement is best for loose moist soil. In this material the tracks left by the rolling sphere had sharp, well defined edges which could be accurately measured. The deviation is greatest for loose dry sand where the tracks tended to cave or slump and the crest-to-crest track width, w, measured was undoubtedly somewhat greater than the track width at the time the sphere was in contact with the soil.

The comparison in Figure 6-6 supports the concept that the contact area between sphere and soil is equal to $\frac{\pi}{2}\left(\frac{w}{2}\right)^2$.

Track Width as a Function of the Density Ratio

The experimental data on the w/D ratio as a function of the γ_r/γ_s ratio and other soil conditions are presented in Figure 6-7. The crucial question was whether this experimental evidence, involving various soil (sand) conditions, could have been predicted from the theory. The appropriate equations, e.g.

$$\frac{q_e}{w\gamma_s} = 0.188N_{\gamma s} + 1.1\left(\frac{c}{w\gamma_s}\right)N_{cs} + 0.55\left(\frac{z}{w}\right)N_{qs} + \frac{q_I}{w\gamma_s} . \qquad (5\text{-}72)$$

$$\frac{q_e}{w\gamma_s} = \frac{4}{3}\frac{\left(\frac{\gamma_r}{\gamma_s}\right)}{\left(\frac{w}{D}\right)^3} \quad , \text{ and} \qquad (5\text{-}74)$$

$$\frac{w}{D} = \sin 2\alpha \qquad (5\text{-}76)$$

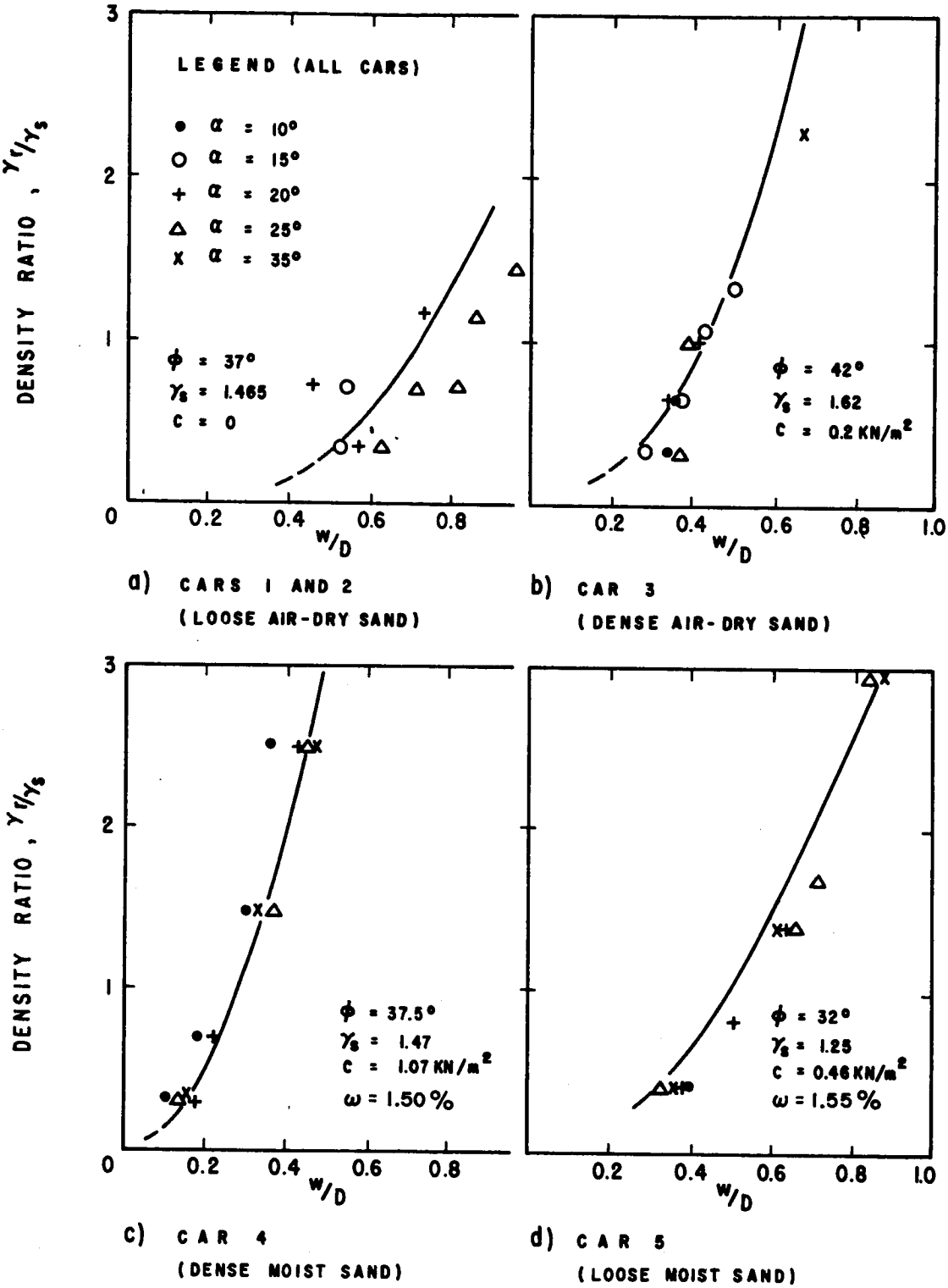

Fig. 6-7. Density ratio vs track width over diameter ratio for spheres rolling on Yuma sand (curves are theoretical for α_{min} required for rolling, points are experimental).

were solved for the same soil conditions. The velocity term, v^2/gD, was determined from data presented subsequently in Figures 6-12 through 6-15. The contribution due to soil inertia, $q_I/w\gamma_s$, was determined as outlined in Chapter 7. The results for smallest and largest values of w/D considered, are presented in Table 6-3.

Table 6-3. Relative contribution of soil inertia.

Soil cars	ϕ	$\frac{w}{D}$	$\frac{q_I}{q_I + q_s} \times 100$	Suggested reason for contribution of q_I
1, 2	37°	0.5	16%	Rel. high because c = 0
		0.9	16%	and $\frac{w}{D}$ was large
3	42°	0.3	12%	Rel. high because cN_{cs} was
		0.7	20%	small and velocity was fairly high
4	37.5°	0.1	1%	Low because cN_{cs} was high
		0.5	6%	and $\frac{w}{D}$ was small
5	32°	0.4	0.6%	Low because soil was loose
		0.9	1.3%	and there was little or no general shear

The theoretical curves determined as explained above are plotted in Figure 6-7.

The agreement supports Equations (5-72), (5-74) and (5-76). It is to be noted, however, that the agreement may be coincidental to some extent since Equation (5-72) was not rigorously developed but contains a number of assumptions and approximations. Therefore, while the comparison in Figure 6-7 should be considered evidence for the validity of the proposed theory for the range of soil conditions and sphere sizes compared, significantly different conditions would at least require some empirical verification. The bearing capacity equation for footings, from which Equation (5-72) came, has extensive credibility in practice for its general validity. Therefore, having matched Equation (5-72) for a limited

number of sphere and soil conditions, it is believed that Equation (5-72) will properly predict many other conditions as well.

Track Width as a Function of Sphere Diameter

During experimentation it was noted that the w/D ratio was dependent on the size of the sphere. Theoretical predictions were made for this relationship using Equations (5-72), (5-74), and (5-76). The comparison between theoretical predictions and experiments is presented in Figure 6-8. The agreement is believed to be good.

Volume Change as a Function of Sphere and Soil Densities

Cross sections were measured for all tracks to investigate soil volume changes as a function of the density of the sphere and initial soil density. The cross sections were usually determined at a distance of 1.5 feet from start of rolling. Examples of track cross sections are to be found in Chapter 4, Figures 4-6 through 4-14. The average volume change was determined using Equation (5-14):*

$$\Delta V = V_w - V_r \ , \qquad (5\text{-}14)$$

where V_w = volume of track below original soil surface,
and V_r = volume of rims above original soil surface.
The sum of V_w and V_r was defined as V_t ($V_t = V_w + V_r$).

The results of the track cross section measurements are presented in Figure 6-9. In this figure, volume increase (dilation) is positive, and volume decrease (compression) is negative. More data were available for a slope angle, α, of 20° or 25° than for other slope angles; therefore, lines were drawn through points for these slope angles as shown in Figure 6-9.

The information in Figure 6-9 can be replotted in more familiar form. Since the lines in Figure 6-9 represent spheres of known densities, the $\Delta V/V_t$ ratio can be determined for assumed soil densities. This is done by

1. assuming a soil density, γ_s,
2. computing the γ_r/γ_s ratio knowing γ_r from Table 6-2,

---

* This method does not account for local volume changes within the regions considered.

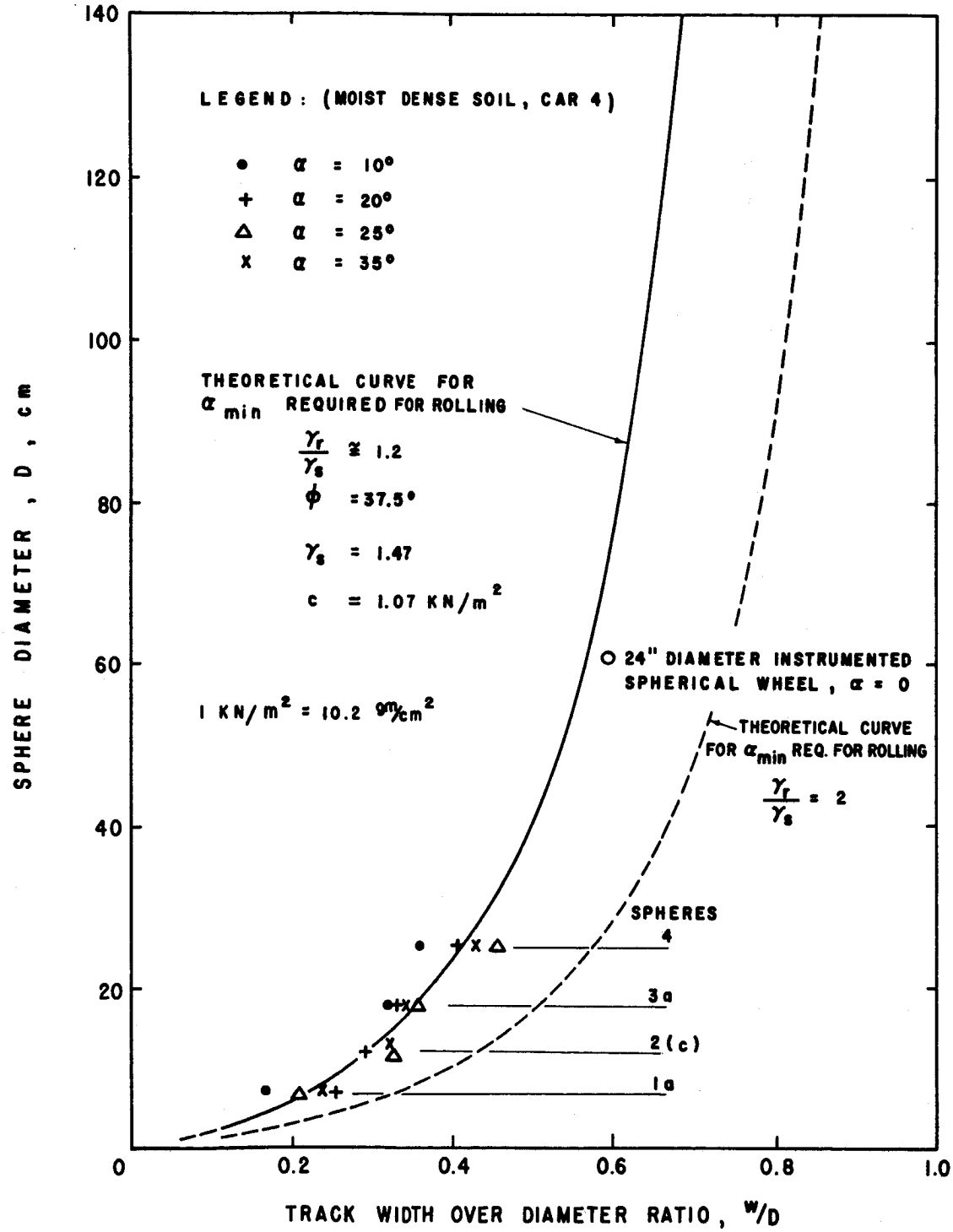

Fig. 6-8. Track width over diameter ratio as a function of sphere diameter.

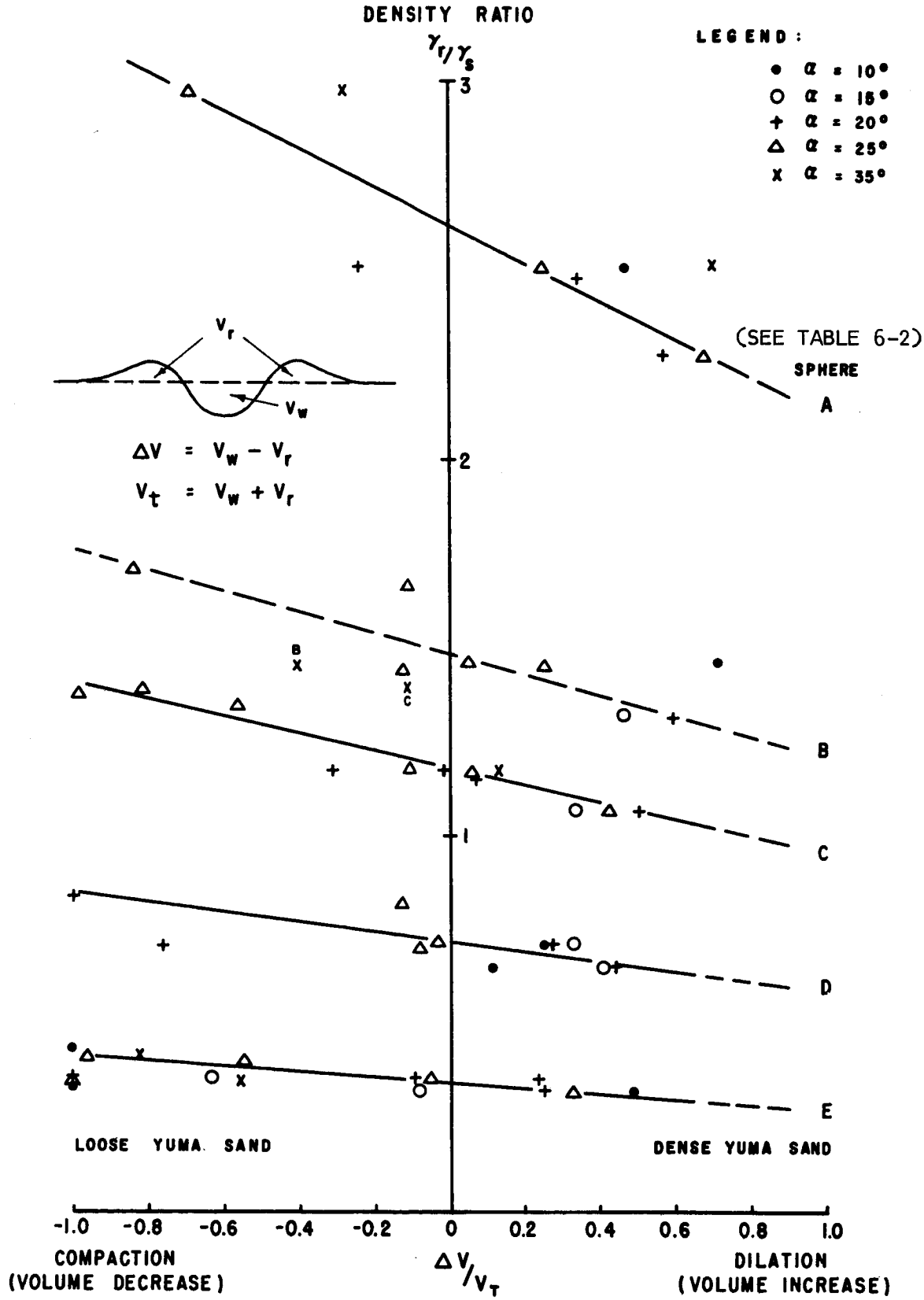

Fig 6-9. Ratio of $\Delta v/v_t$ as a function of γ_r/γ_s.

3. determining the resulting $\Delta V/V_t$ from Figure 6-9 for the particular γ_r (sphere) line, and

4. plotting $\Delta V/V_t$ vs. γ_r for the assumed soil density, as shown in Figure 6-10.

FILM ANALYSIS

Distance, Velocity,and Acceleration vs Time

A measuring tape was placed alongside the anticipated track before the sphere was rolled. Knowing the speed at which the films were taken, it was possible, with the aid of a film analyzer, to determine the distance rolled at any particular time.

From markings on the sphere surface it was also possible to determine the number of revolutions rolled as a function of time. Slip could be determined as the difference between distance revolved and distance travelled (distance revolved as if the sphere had been rolling on a hard surface) divided by the distance travelled.

The data were plotted as functions of time as shown in Figure 6-11. The velocity of the rolling sphere was determined as the slope of the distance vs. time curve. The acceleration of the rolling sphere was determined as the slope of the velocity vs. time curve. The data were adequate to reliably define the velocity of most of the spheres. Based on intermittant checks of the camera speed during testing, the velocities should be accurate to within 8% of the actual value.

The remainder of the data giving distance, velocity and acceleration is on file at the University of California, Geotechnical Engineering Laboratory.

Velocity and Acceleration vs Density Ratio

Velocity and acceleration were plotted against the density ratio as shown in Figures 6-12 through 6-15. These velocities and accelerations were determined at a distance of 45 cm from the starting poing. The curves show that:

1. The lighter the sphere, the faster it will roll for a given slope.

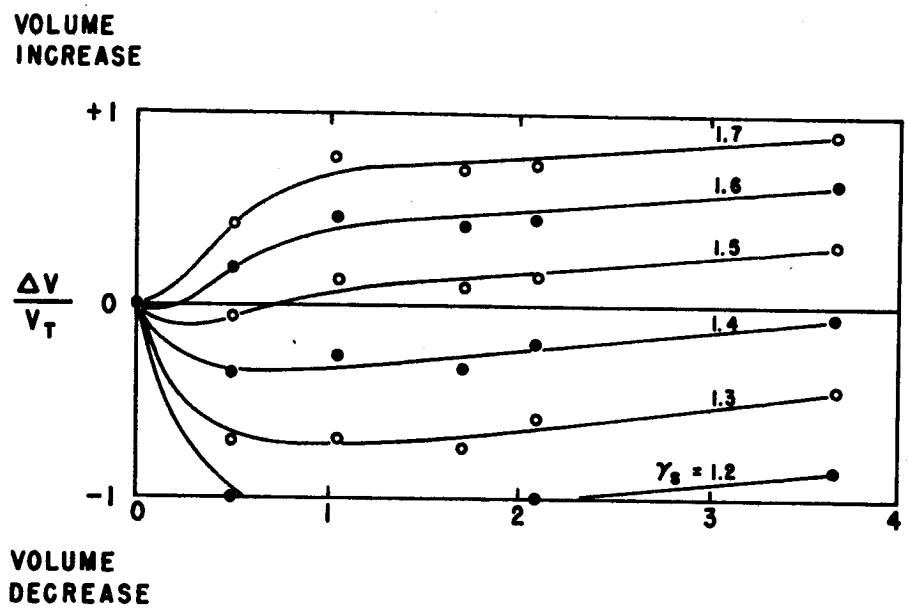

Fig. 6-10. Volume change as a function of sphere density, γ_r, and soil density, γ_s.

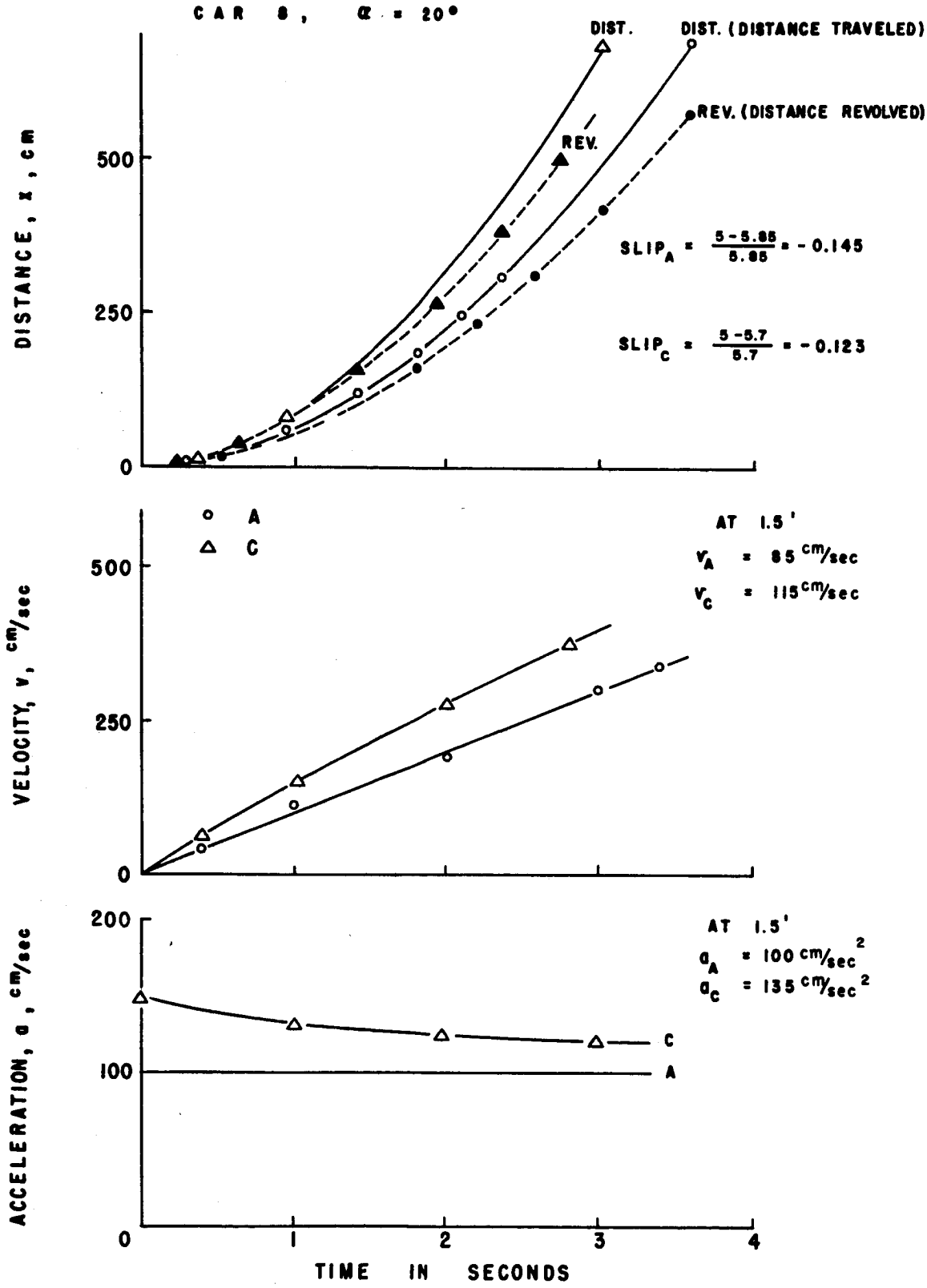

Fig. 6-11. Typical relationship showing distance, velocity, and acceleration as function of time.

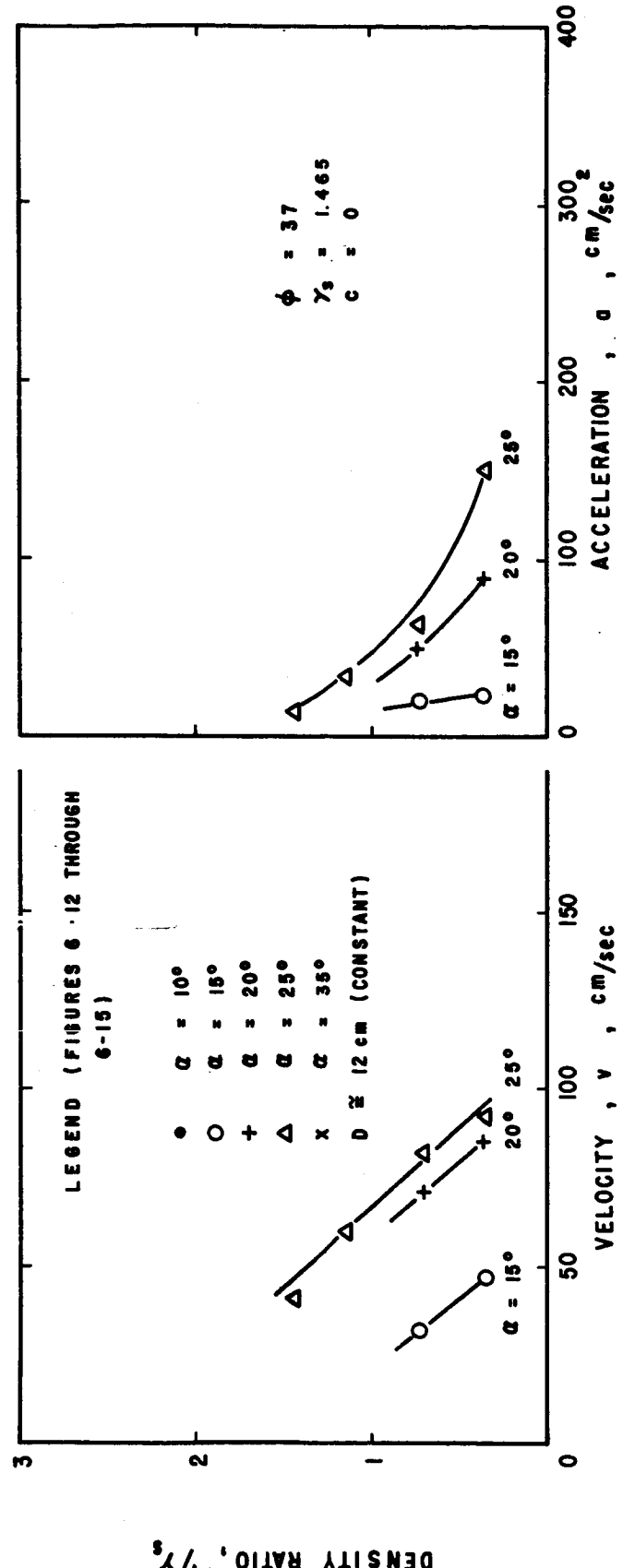

Fig. 6-12. Density ratio vs velocity and acceleration for spheres rolling on loose air-dry Yuma sand (cars 1 and 2).

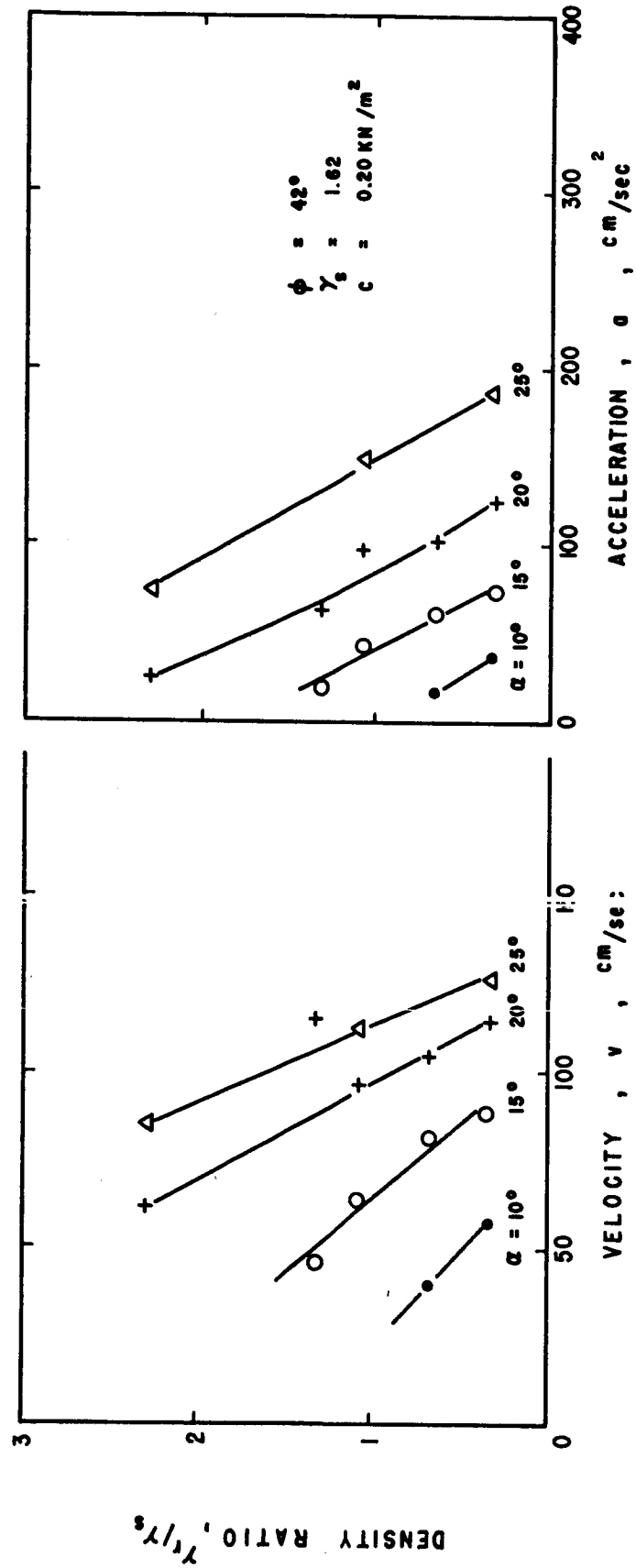

Fig. 6-13. Density ratio vs velocity and acceleration for spheres rolling on dense air-dry Yuma sand (car 3).

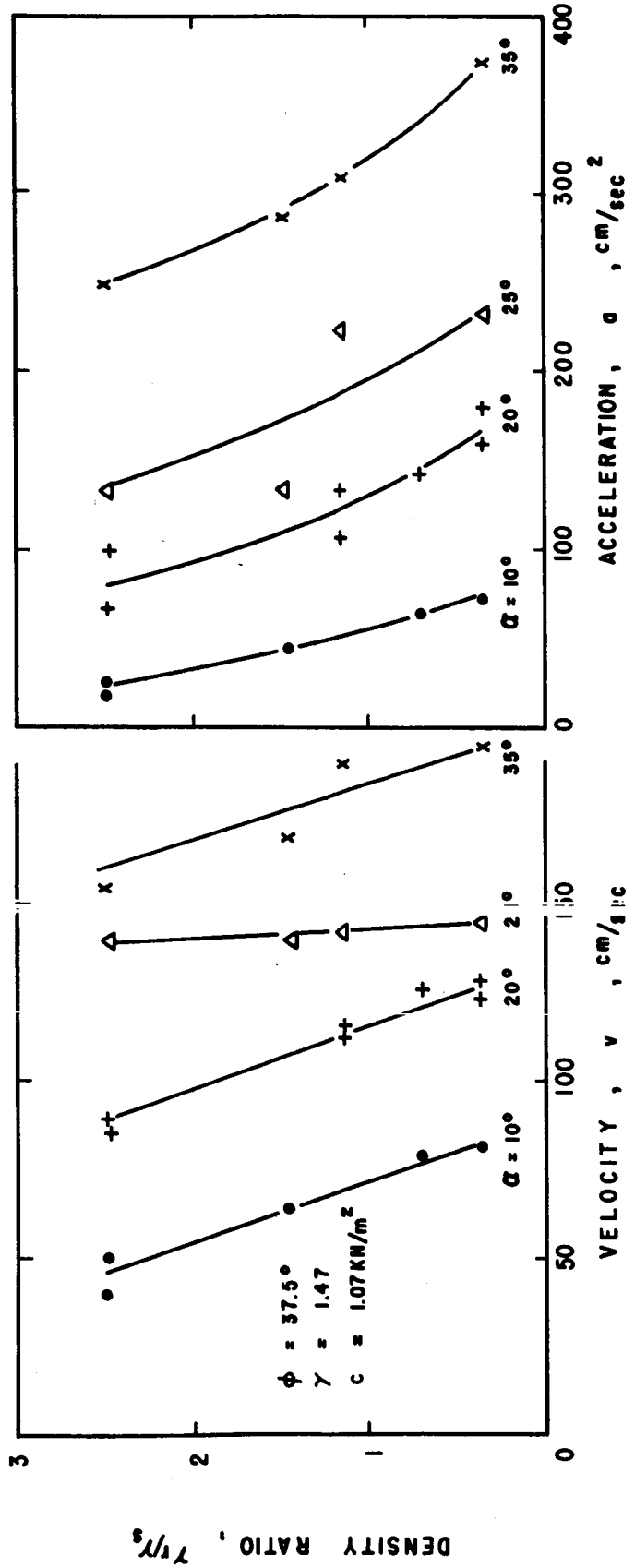

Fig. 6-14. Density ratio vs velocity and acceleration for spheres rolling on dense moist Yuma sand (cars 4 and 8).

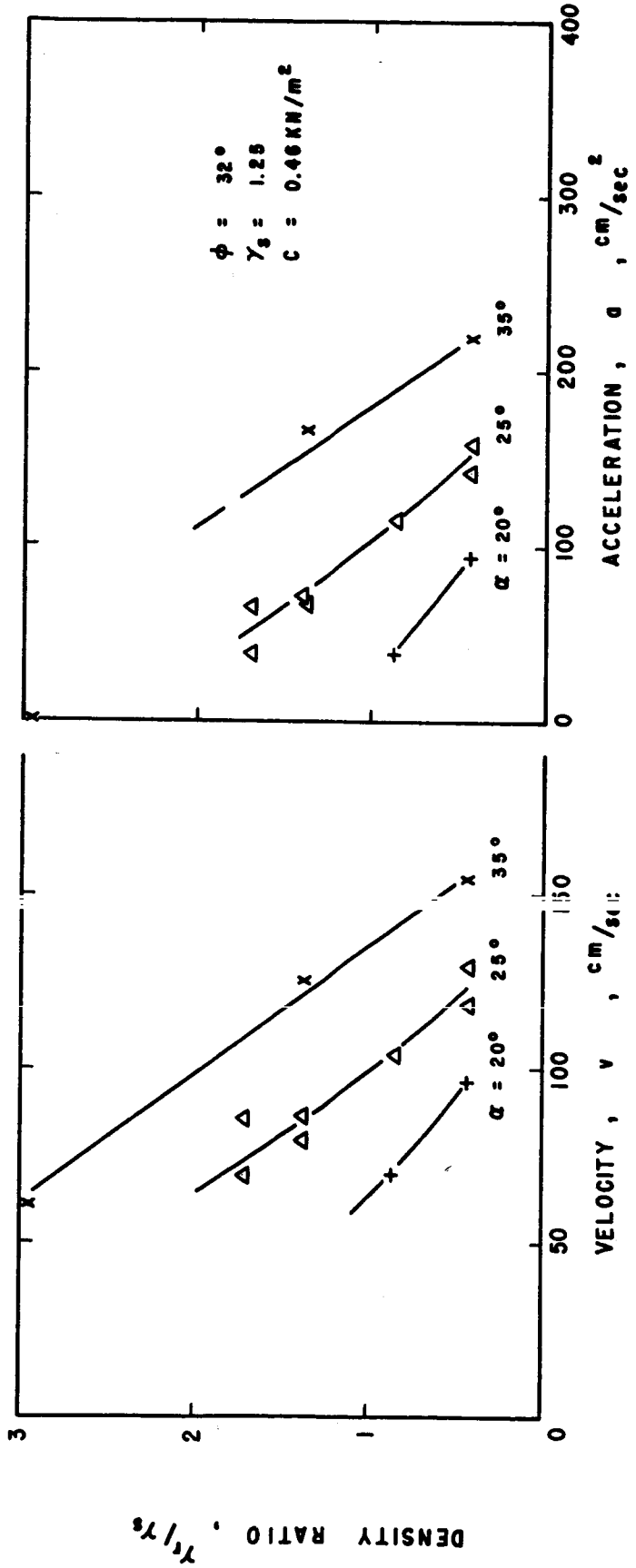

Fig. 6-15. Density ratio vs velocity and acceleration for spheres rolling on loose moist Yuma sand (cars 5 and 7).

2. The steeper the slope angle, the faster the sphere will roll for a given density ratio.

3. The lighter the sphere and the steeper the slope angle, the greater will be the acceleration of the sphere.

4. The acceleration of the sphere will be a relatively small fraction of the acceleration of gravity, and always less than the acceleration of the same sphere on a frictionless slope.

From study of the curves of distance, velocity, and acceleration vs. time, an example of which was presented in Figure 6-11, it also appears that spheres tend to roll at constant acceleration down a slope provided soil and slope conditions are uniform. Of the some 200 spheres rolled during the experimentation reported herein, about 76% could be described as rolling at constent acceleration at 45 cm. after start.

Velocity and Acceleration vs Sphere Diameter

Velocity and acceleration as a function of sphere diameter are plotted in Figure 6-16 through 6-18. It appears that for the range of sphere sizes tested, velocity and acceleration are

1. little effected by sphere diameter in dry sand,
2. more effected by sphere diameter in dense moist sand, and
3. distinctly effected by sphere diameter in loose moist sand.

This implies that the dependence on sphere diameter may be related to cohesion which is nearly zero for dry sand, but has a small value for moist sand.

However, it is important to note that the range of sphere sizes tested was very limited. Since lunar boulders may be about 10 meters in diameter, it may not be possible to extrapolate from the curves or Figures 6-16 through 6-18 to such large sizes. If the curves of acceleration are extended to a 10 meter diameter sphere, the acceleration would be very small or zero. One may conclude, perhaps, that such large spheres would tend to roll at nearly constant velocity, at least much more so than small spheres. This implication could be significant since at constant velocity

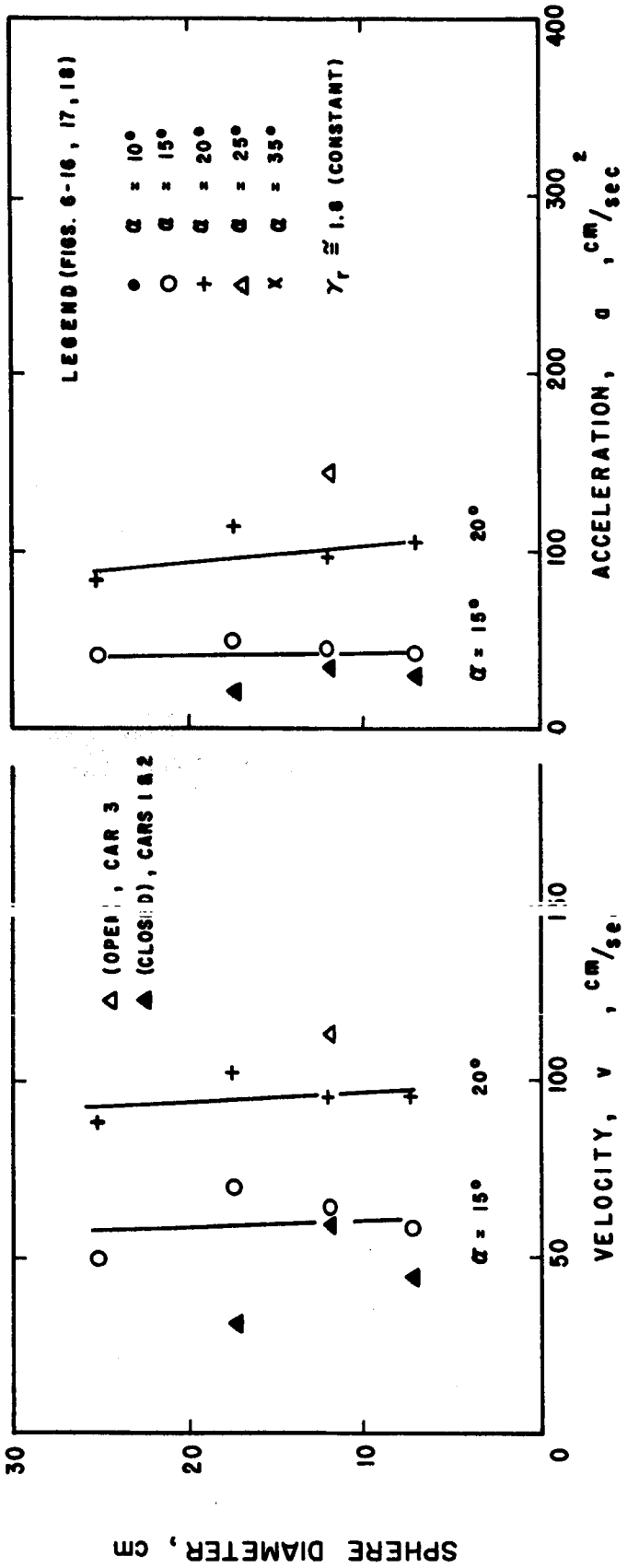

Fig. 6-16. Sphere diameter vs. velocity and acceleration for spheres rolling on air-dry Yuma sand (cars 1, 2, and 3).

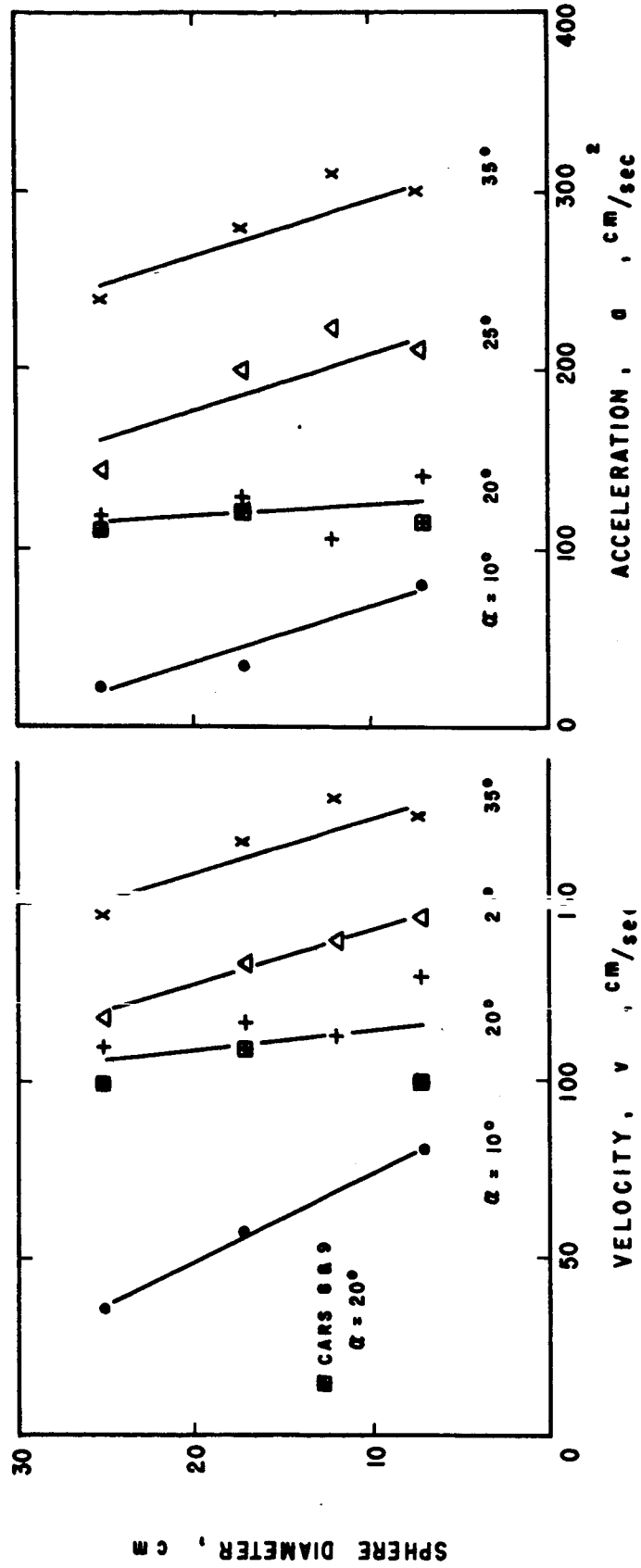

Fig. 6-17. Sphere diameter vs velocity and acceleration for spheres rolling on dense moist Yuma sand (cars 4, 8, and 9).

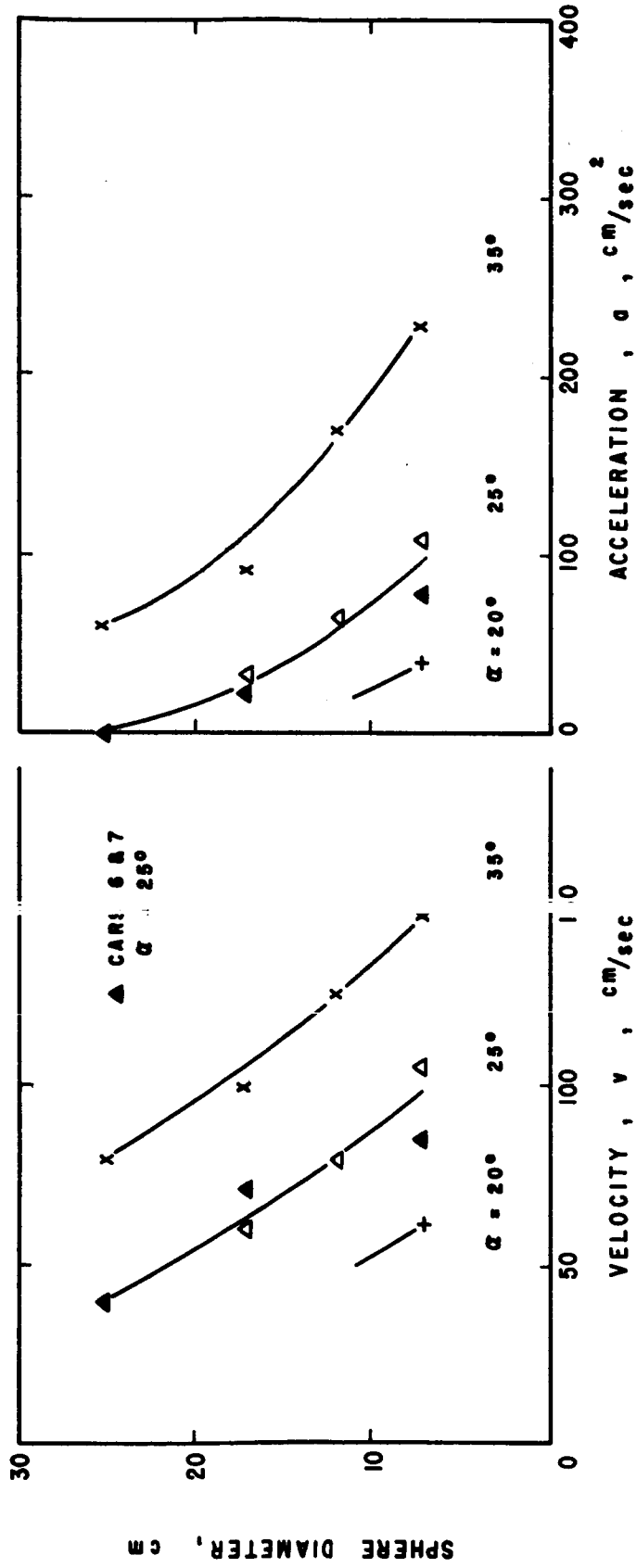

Fig. 6-18. Sphere diameter vs velocity and acceleration for spheres rolling on loose moist Yuma sand (cars 5, 6, and 7).

we have a unique relationship between slope angle, α, and the w/D ratio, as expressed by Equation (5-76).

Slip vs Density Ratio, Sphere Diameter, and Distance Traveled

Information on slip, defined as the distance revolved minus the distance traveled divided by the distance traveled, is presented in Figures 6-19 through 6-21. Figure 6-19 presents slip as a function of the density ratio. Figure 6-20 presents slip as a function of sphere diameter, and Figure 6-21 presents slip as a function of the distance traveled to the interval where the slip was determined. The following behavior is apparent:

1. For loose moist sand, slip is primarily a function of the density ratio and little affected by the slope angle.

2. For dense moist sand, slip is primarily a function of the slope angle and less affected by the density ratio.

3. The data for slip in dry sand showed more scatter. However, the trend of the slope of the lines is similar to those for loose moist soil.

4. Slip appears to be a fairly complex function of sphere size. For dense dry sand, slip decreased with increase in diameter. For loose moist sand (the other extreme tested), slip increased with increase in diameter.

5. Figure 6-21 shows that at least for travel distances greater than about 100 cm, slip was essentially independent of the distance traveled. This means that slip is essentially independent of sphere velocity and acceleration. This statement may also be true for a bouncing sphere; sphere E, car 8, $\alpha = 20°$, bounced continuously beyond a travel distance of approximately 250 cm and yet the slip remained constant, as shown in Figure 6-21.

6. All slip is negative for a freely rolling sphere; that is, the sphere travels further than its revolutions for rolling on a hard surface would indicate.

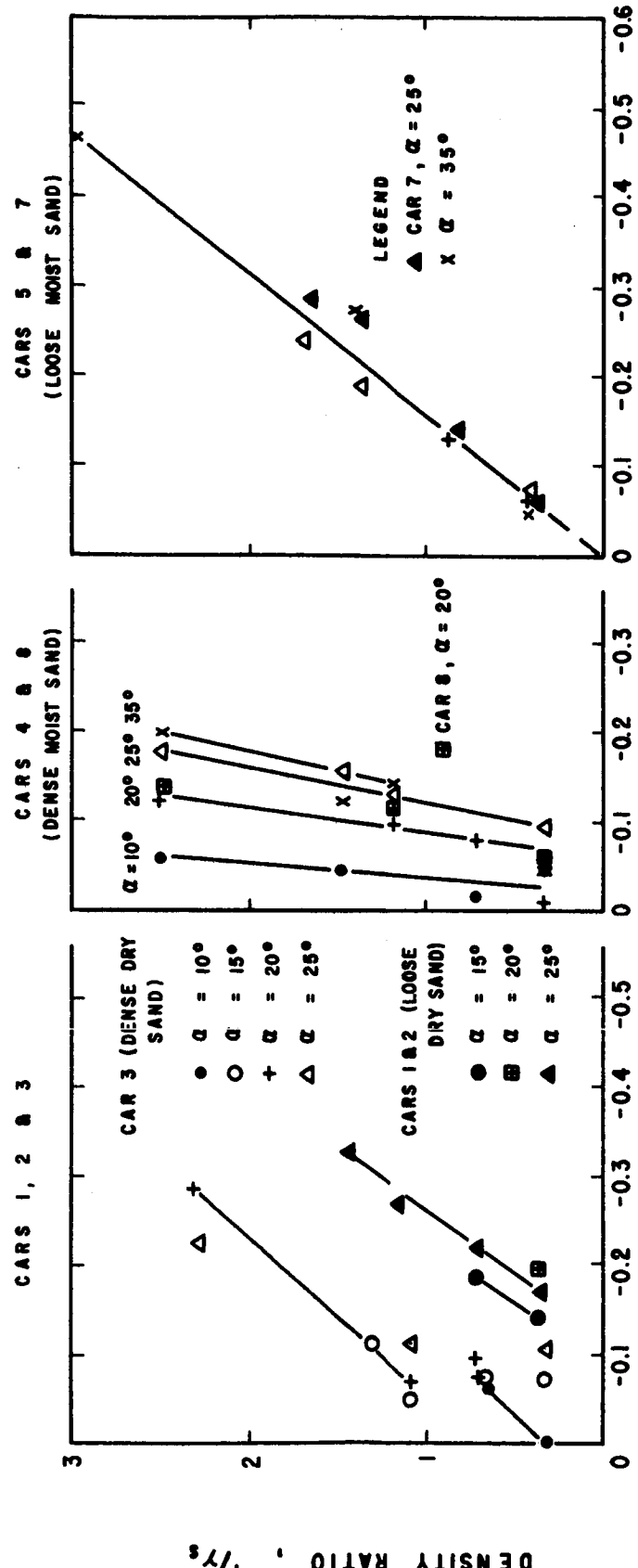

Fig. 6-19. Density ratio vs slip for spheres rolling on Yuma sand.

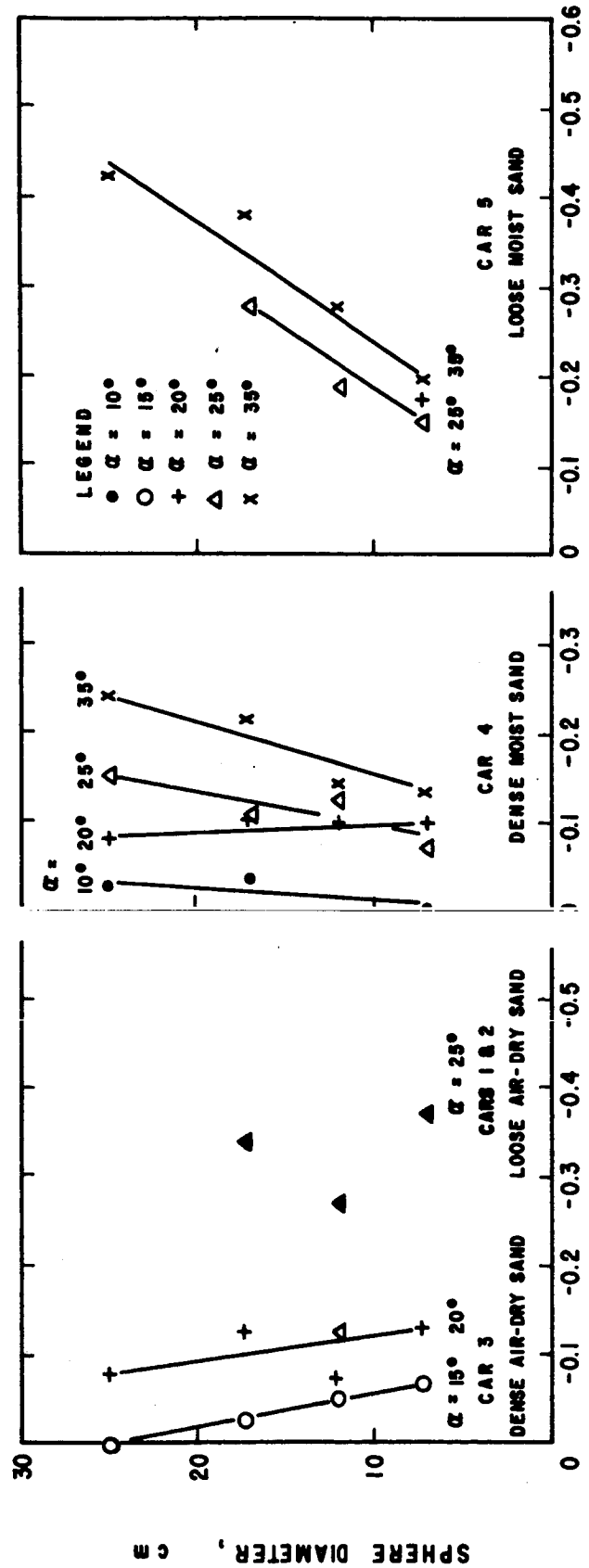

Fig. 6-20. Sphere diameter vs slip for spheres rolling on Yuma sand.

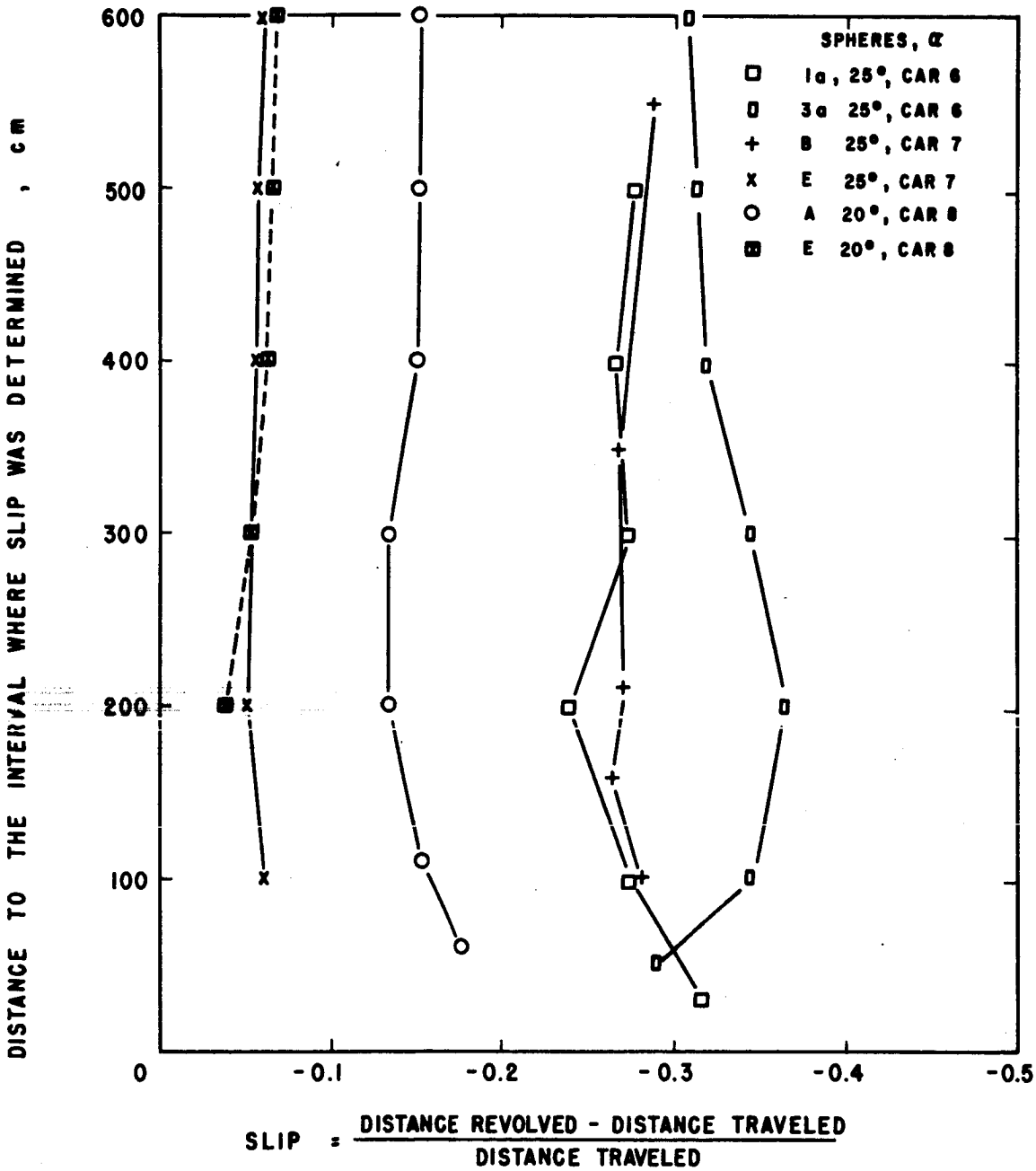

Fig. 6-21. Distance traveled vs slip for spheres rolling on Yuma sand.

7. Slip increases with the density of the sphere and the slope angle, as shown in Figures 6-19 and 6-20.

Measurements of Shearing Soil Wedges

Theoretical studies of the inertia forces associated with the shearing soil wedge showed that the soil acceleration is a function of the exponent, n. While the experimental studies were not aimed directly at the specific measurement of n, analysis of certain sequences of frames in the films permitted determination of the movement of a shearing soil wedge. The results of these measurements are presented in Table 6-4.

Based on the data in Table 6-4 distance, velocity, and acceleration are plotted as functions of time in Figures 6-22 and 6-23. Velocities were determined from the slope of the distance curves, and accelerations were determined from the slope of the velocity curves. The experimental values of maximum velocity and acceleration as reported in Table 6-4 were determined from Figures 6-22 and 6-23. The experimental magnitude of sphere displacement (the distance through which the sphere moved in the same time) was determined from distance vs. time curves for the particular spheres.

Theoretical soil wedge displacements were computed using the procedure suggested in Chapter 5 ($x_{soil} = z - z_v$). The theoretical and experimental soil displacements reported in Table 6-4 are for comparable sphere displacements. Theoretical values for soil acceleration were computed from equation (5-60) using experimental values for v_{max} and t_{so}. The exponent, n, was assumed equal to one.

If the data presented in Table 6-4 and Figures 6-22 and 6-23 can be considered representative of the movement of shearing soil wedges, certain inferences can be made:

1. The exponent, n, appears to be close to one; i.e. the slopes of the increasing and decreasing sides of the velocity curve have nearly equal absolute magnitudes.

2. The acceleration function assumed in Chapter 5 is undoubtedly an oversimplification. It appears that the velocity does not increase parabolically, as predicted by theory for n = 1, but

Table 6-4. Measurement of Shearing Soil Wedges

			Experimental								Theoretical (assumed n = 1)	
Car	Slope α°	Sphere	Basis	Frame	Time sec.	Soil Displ. x_{soil} cm	Sphere Displ. cm	Soil $v_{max.}$ cm/sec	Soil a_{max} cm/sec^2	$n = -\frac{ai}{af}$	Soil Displ. x_{soil} cm	Soil a_{max}
1	20	B	Tape	23	0.96	0	0					
				24	1.00	0.059						
				25	1.04	0.208			67.0	0.82		120.0
				26	1.08	0.480		7.5				
				27	1.12	0.780						
				28	1.17	1.060						
				29	1.21	1.110	4.80				1.80	
4	25	4	Tape,S*	5	0.10	0						
				6	0.12	0.050						
				7	0.14	0.244		13.0	320.0			576.0
				8	0.16	0.464						
				9	0.18	0.600						
				10	0.20	0.801	2.00					
				11	0.22	1.009						
				12	0.24	1.146						
				13	0.26	1.236	4.00				0.93	
4	35	4	Tape	16	0.32	0	0		1060.0			
				17	0.34	0.280						
				18	0.36	0.915		47.0				
				19	0.38	1.790						
				20	0.40	2.360	9.00			1.98		

*With respect to mark on sand surface

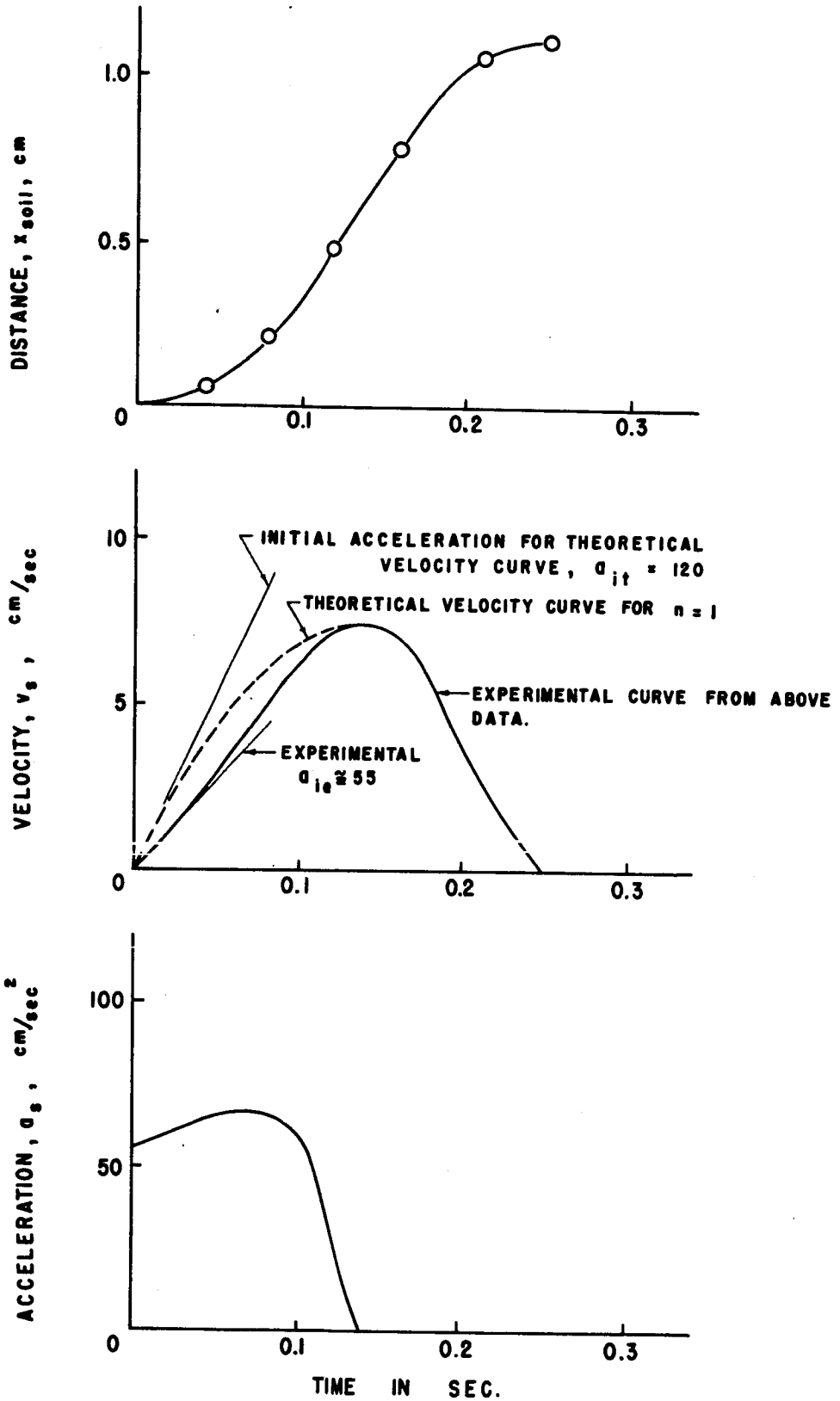

Fig. 6-22. Soil movement as a function of time for sphere B, car 1, $\alpha = 20°$.

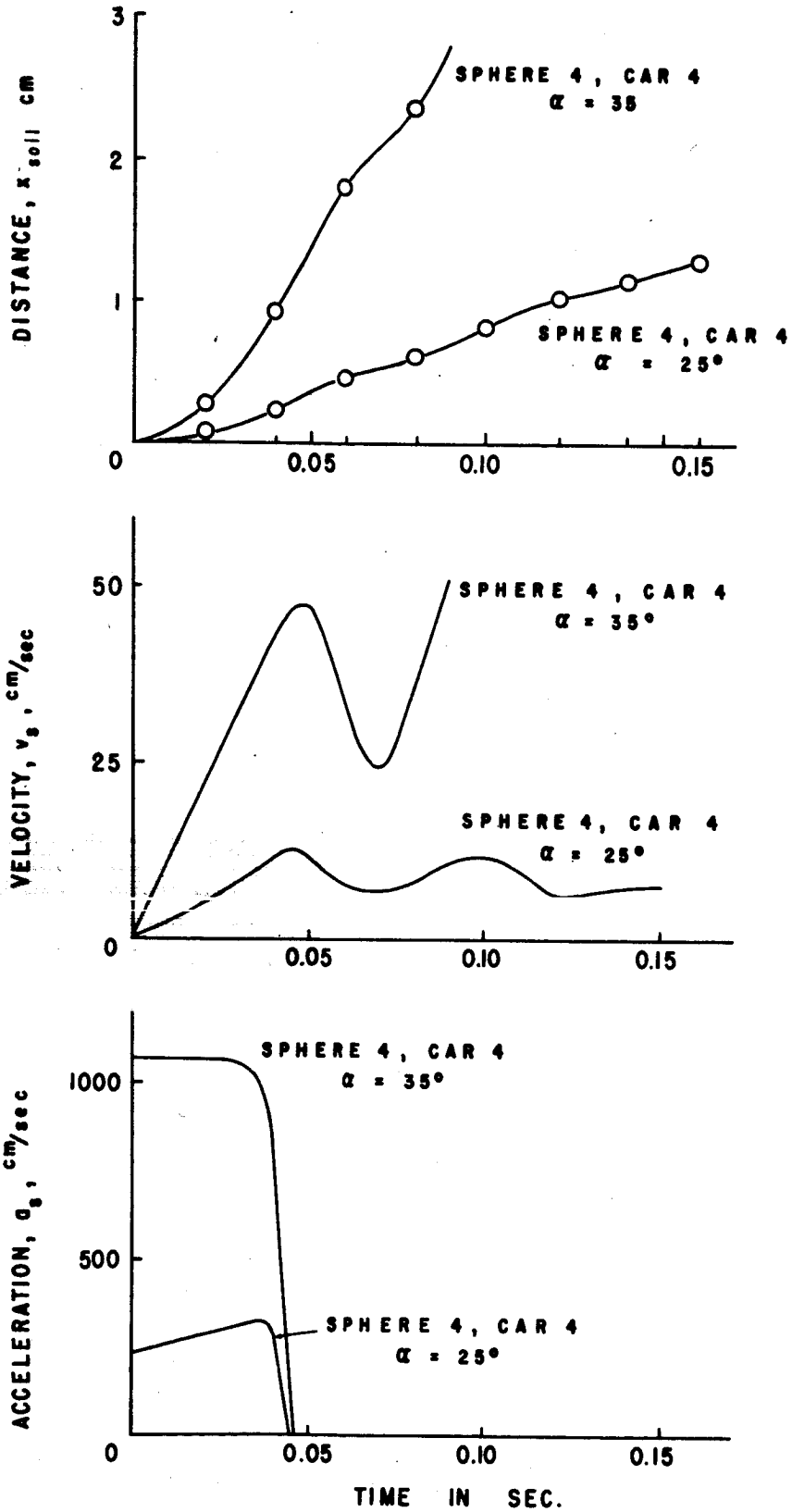

Fig. 6-23. Soil movement as a function of time for sphere 4, car 4.

somewhat more slowly. As shown in Table 6-4, theoretical values of a_{max} were about twice the experimental values. This can be explained from the difference in the theoretical and experimental velocity curves shown in Figure 6-22. The initial slope of the theoretical curves, a_{it}, is about twice the initial slope of the experimental curve, a_{ie}.

3. However, the comparison does suggest that the theory gives results that are within a factor of two of the correct value.

SUMMARY

Testing

The testing reported on in this chapter led to a consideration of certain specific relationships. Some of these relationships were investigated in order to increase information on rolling sphere — soil slope interaction; whereas, others were investigated in order to make a comparison with theoretical predictions. The relationships considered were:

a. For general information

   1. Soil volume change associated with forming of the track, as a function of sphere and soil densities.
   2. Distance, velocity, and acceleration of the rolling spheres as a function of time.
   3. The relationship between velocity and the density ratio, and between acceleration and the density ratio for the rolling spheres.
   4. The relationship between velocity and sphere diameter, and between acceleration and sphere diameter.
   5. The relationship between slip and density ratio, sphere diameter, and distance traveled for the rolling spheres.

b. For both comparison with theory and general information

   1. Slope angle for constant velocity rolling at minimum slope angle required for rolling.

2. The relationship between track width and density ratio for rolling spheres of constant size.

3. The relationship between track width and sphere diameter for rolling spheres of approximately constant density.

4. Distance, velocity, and acceleration of soil wedges moving during general shear.

Comparisons with Theory

For the items listed under b. above, the following conclusions can be made:

1. The experimental data plotted in Figure 6-6 confirm the predicted relationship between track width and slope angle,

$$\frac{w}{D} = \sin 2\alpha, \tag{5-76}$$

for constant velocity rolling or for minimum slope angle required for rolling. This also confirms that the sphere — soil contact area must be approximately semicircular in a view normal to the slope.

2. The comparisons presented in Figure 6-7 confirm the validity of the proposed Equations (5-72) and (5-74),

$$\frac{q_e}{w\gamma_s} = 0.188N_{\gamma s} + 1.1\left(\frac{c}{w\gamma_s}\right)N_{cs} + 0.55\left(\frac{z}{w}\right)N_{qs} + \frac{q_I}{w\gamma_s} \tag{5-72}$$

$$\frac{q_e}{w\gamma_s} = \frac{4}{3}\,\frac{(\gamma_r/\gamma_s)}{(w/D)^3}, \tag{5-74}$$

for the range of sphere and soil conditions investigated. It is believed that the proposed equations are applicable to many other sphere and soil conditions as well.

3. The comparison in Figure 6-8 is further evidence for the general validity of the proposed equations, particularily Equation (5-74)

4. The data on soil wedges moving during general shear are inadequate for definite conclusions. The following inferences can, however, be made:

    1. The velocity does not increase parabolically for n = 1, but somewhat more slowly. It appears that for this reason theoretically predicted accelerations, a_{max}, may be too high.

    2. The proposed theory will give answers for q_I which are within a factor of two of the correct value.

Overall Value of Testing and Theory

In addition to the comparisons between theoretical predictions and experimental data, a considerable amount of experimental data on the dynamic aspects of rolling sphere – soil slope interaction were presented. This information is believed to be valuable for a better understanding of the problem.

It is believed that the proposed theory is adequate for use as a remote reconnassance method for estimating soil conditions. For controlled testing and where q_I can be assumed to be negligable, the proposed theory and the rolling sphere relationship may give values for ϕ which are close to those determined from the results of triaxial tests.

Chapter 7. UTILIZATION OF DEVELOPED THEORY

The implications of the theory, particularily the added inertia term in the bearing capacity equation, can now be considered. The relative contribution to total soil resistance of inertia, friction, cohesion, and surcharge are evaluated for selected situations in this chapter.

A method of analysis of boulder tracks, based on the developed theory is outlined, and the lunar boulder tracks analyzed in Chapter 2 are reanalyzed by the proposed method.

RELATIVE CONTRIBUTION OF INERTIA, FRICTION, COHESION, AND SURCHARGE TO TOTAL SOIL RESISTANCE

The relative contribution of each of the terms in Equation (5-72),

$$\frac{q_e}{w\gamma_s} = 0.188N_{\gamma s} + 1.1\left(\frac{c}{w\gamma_s}\right)N_{cs} + 0.55\left(\frac{z}{w}\right)N_{qs} + \frac{q_I}{w\gamma_s}, \qquad (5\text{-}72)$$

is evaluated below.

The inertia term as expressed by Equation (5-70) is

$$\frac{q_I}{w\gamma_s} = B\left(z - z_v\right)\frac{V_s}{w^3 D}, \qquad (5\text{-}70)$$

where

$$B = 20.3\,\frac{(1 + 2n)}{\left(\sin^{-1}\frac{w}{D}\right)^2}\,\frac{v^2}{gD} \qquad (5\text{-}71)$$

The flow diagram below shows how the inertia term is computed:

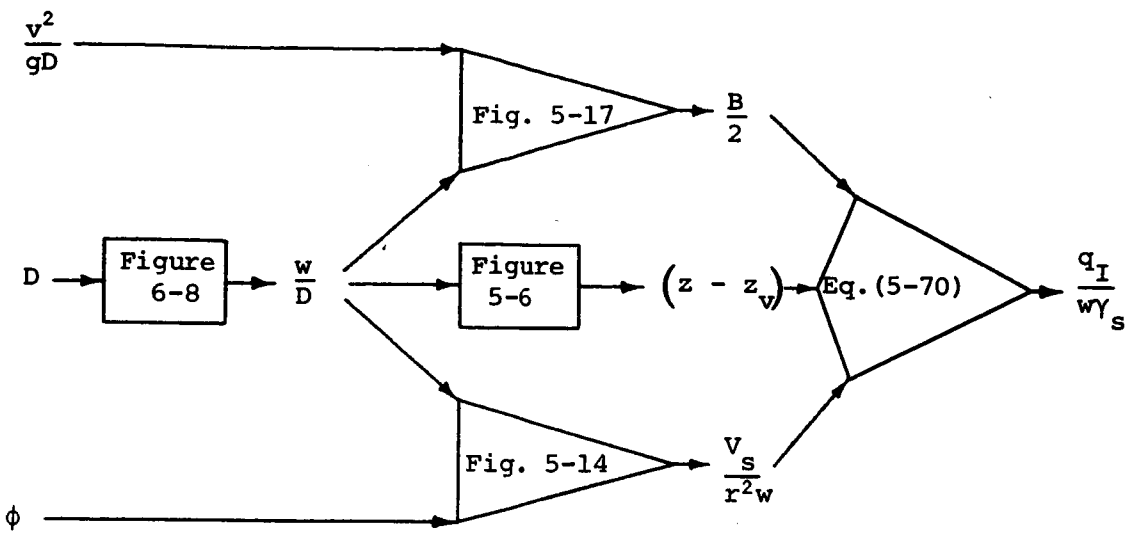

Both z and z_v can be determined from Figure 5-6. Knowing w/D, z would be determined by drawing a horizontal line from w_v/D to z_v/r as if these ratios were w/D and z/r. The value of z_v would be determined by entering Figure 5-6 with a known value of $\Delta v/D^2$.

It was shown in Chapter 6 that the theoretical maximum acceleration may be about twice the experimental or actual value. Therefore, the values of B obtained from Figure 5-17 will be divided by 2.

The other terms in Equation (5-72) are determined using Equations (5-20), (5-22), and (5-25), and Figures 2-4, 2-5, and 2-6. The reduced bearing capacity factors, $N_{\gamma s}$, N_{cs}, and N_{qs}, calculated from Equations (5-20), (5-22), and (5-25) would, in general require an increase in the friction angle of about 6 degrees from that required using N_γ, N_c, and N_q to get the same soil resistance.

Since Equation (5-70) involves many parameters, all of which could vary independently in a real situation, any evaluation will be limited by the assumed conditions. It was considered desirable first to make an evaluation of the inertia term with variable sphere velocity, v_s; and next to make an evaluation of the inertia term with variable sphere diameter, D.

Consider a spherical rigid wheel 60 cm in diameter being pulled on a horizontal surface of sand having the following properties:

apparent cohesion = c = 1 kN/m^2 = 10.2 gm/cm^2

friction angle = ϕ = 37.5°

density = γ_s = 1.6 gm/cc

(Such values were reported by Costes and Mitchell, 1970, and Apollo 11 Soil Mechanics Team, Costes et al., 1970, from their examination of Apollo 11 samples.) If the wheel load is varied leading to varying penetrations or w/D ratios and the velocity is varied, the magnitude of the inertia term will vary as shown in Figure 7-1.

Figure 7-1a shows the percent contribution of the inertia term, $q_I/w\gamma_s$, to total soil resistance as a function of velocity. For these lunar soil conditions inertia contribution begins to be important at a velocity of about 5 miles per hour. For soil conditions used in testing the instrumented spherical wheel on Yuma sand at a velocity of about 1.3 mi/hr or 60 cm/sec, the resistance due to soil inertia was determined to be 3.4% — relatively insignificant.

Figure 7-1b shows the relative contribution to total soil resistance from each of the terms in Equation (5-72) at a selected sphere velocity of 16 km/hr. For other velocities, the magnitude of the density, cohesion, and surcharge terms would remain unchanged but the inertia term would vary as shown in Figure 7-1a. Consequently, a change in the percentage contribution would result. The striking feature of Figure 7-1b is the contribution due to cohesion. For small loaded areas, w/D, the cohesion term provides most of the resistance in spite of the fact that the assumed value of unit cohesion was very small. The reason for this is that a large value of ϕ gives a high N_{cs}.

Next we are to consider an evaluation of the inertia term with the size of the sphere as the principal variable. This evaluation is much more complex because as the size of the sphere increases, penetration and w/D ratio increase as shown in Figure 6-8. As the w/D ratio increases the slope angle required for rolling increases. Because of these dependencies, the velocity of the sphere is, in fact, a function of the size of the sphere. Some experimental data are available for small spheres (7 to 25 cm in diameter). However, no data are available

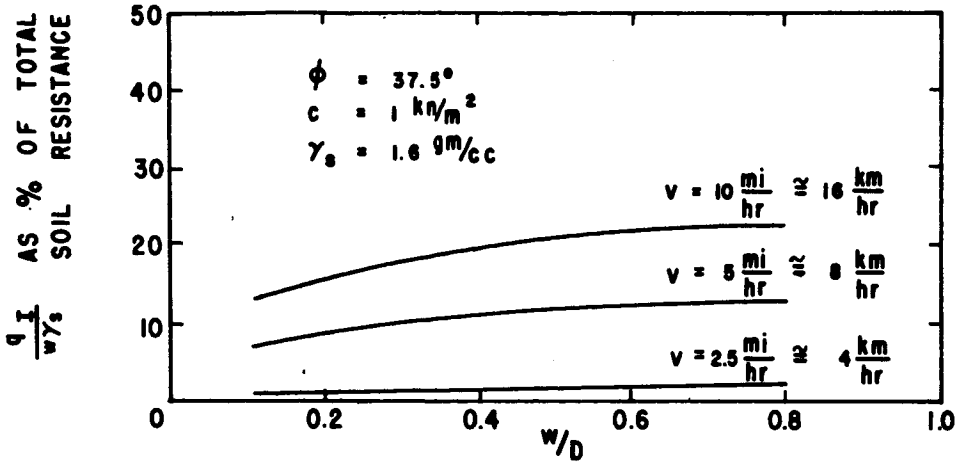

a) Resistance due to soil inertia as a function of sphere velocity.

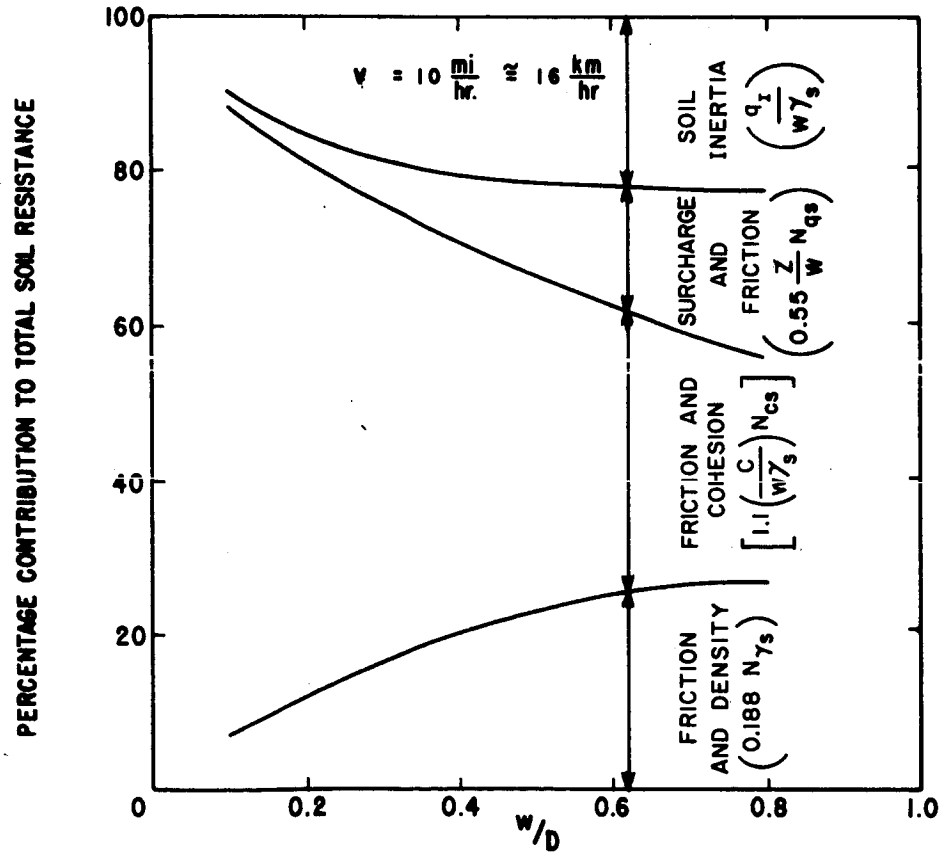

b) Contribution to total soil resistance as a function of w/D.

Fig. 7-1. Relative contribution to total soil resistance from friction and density, cohesion, surcharge, and soil inertia for a spherical wheel (D = 60 cm).

on the velocity of large (10 meter) rolling lunar boulders. It is also doubtful that direct experimental verification will ever become available for large boulders since it is impractical to conduct tests on 10-meter spheres. Therefore, in determining B, it is at the present time difficult to assess values for the velocity term, v^2/gD, for large boulders.

We begin by plotting data for smaller spheres and extrapolate to larger spheres. The velocity term was determined for a 20° slope from Figures 6-16 and 6-17 for dense dry Yuma sand (car 3) and dense moist Yuma sand (car 4). These Figures indicate that larger spheres roll more slowly than smaller spheres, and that a 10-meter sphere rolling on the same soil would roll very slowly indeed. The values of v^2/gD obtained are plotted as the experimental points in Figure 7-2.

The track width for many of the lunar boulders reported in Chapter 2 was determined at a location a short distance before the point where the boulder came to rest or in a region where it appeared to have been rolling uniformly. A velocity of about 2.5 meters per second may be representative for these boulders. This value will be assumed. This would give $v^2/gD \cong 0.08$. Using this value as one of the points in Figure 7-2, a curve was fit to the data and is shown in Figure 7-2.

For selected values of D, the velocity term, v^2/gD, was obtained from Figure 7-2; and the contribution of each of the terms in Equation (5-72) was determined. The same soil conditions ($c = 1$ kN/m^2, $\phi = 37.5°$, and $\gamma_s = 1.6$ gm/cc) were again used. The results are shown in Figure 7-3. Figure 7-3a shows the relative contribution of each term in Equation (5-72) in earth gravity. In lunar gravity, the inertia and cohesion terms remain unchanged while the density and surcharge terms are divided by six. Figure 7-3b shows the relative contribution of each term in lunar gravity.

As shown in Figure 7-3, the contribution to total soil resistance from cohesion is much influenced by the size of the sphere. For the small spheres (7-25 cm in diameter) tested at the WES, the moist Yuma sand behaved much as a cohesive soil, while the air dry Yuma sand behaved much as a cohesionless soil. That the theory predicted correctly the track widths for both conditions, as shown in Figure 6-7 supports its general validity.

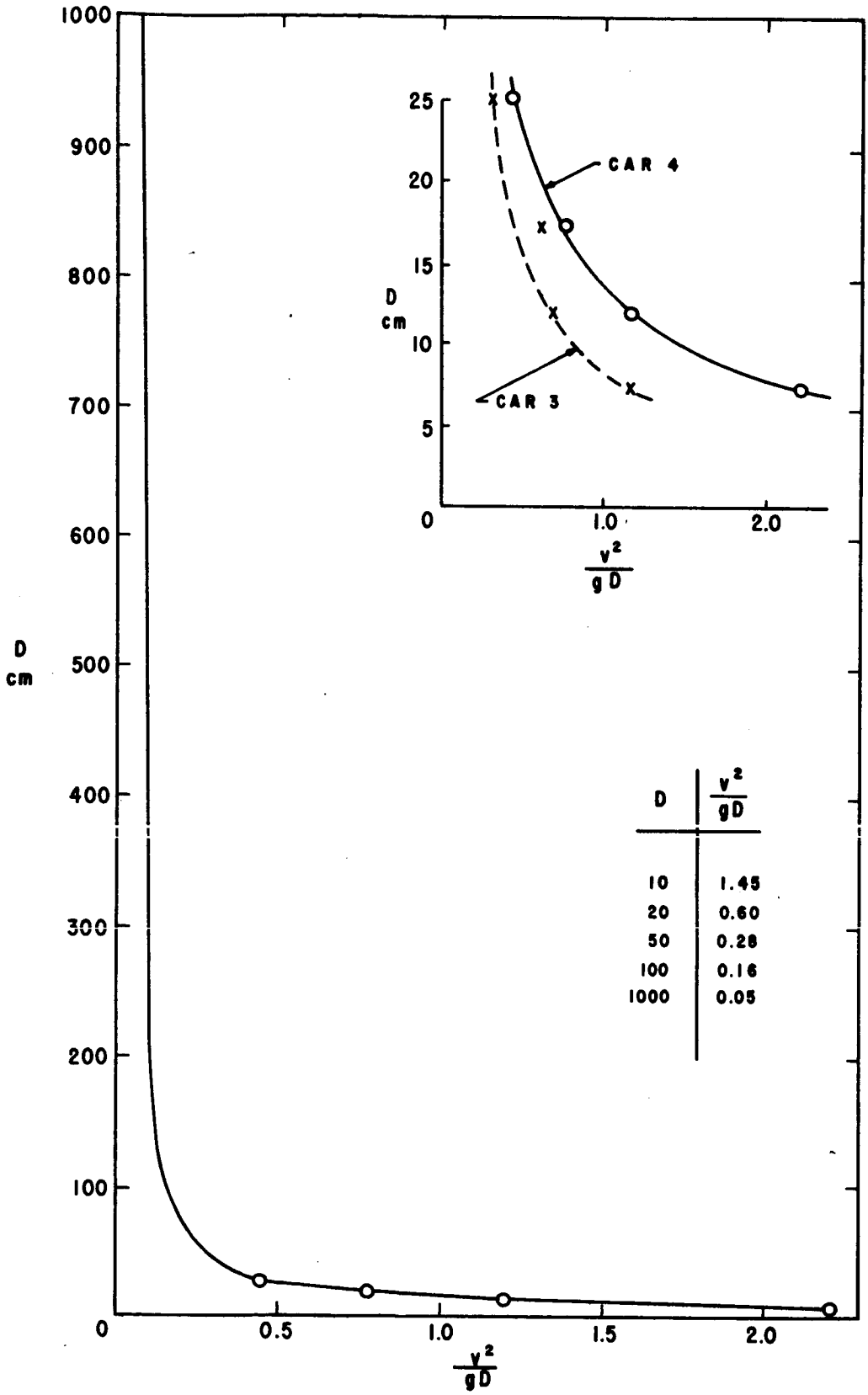

Fig. 7-2. Velocity term, v^2/gD, as a function of sphere diameter.

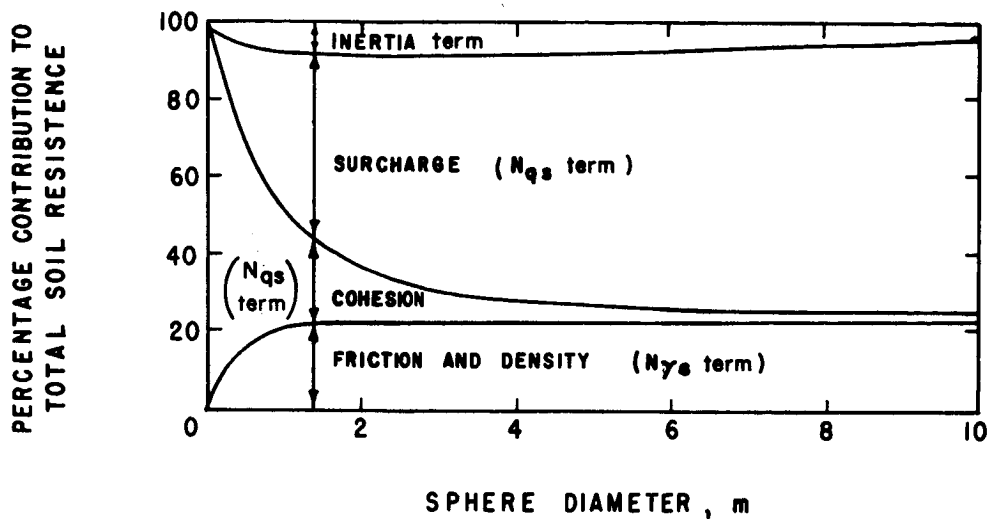

a) Earth gravity.

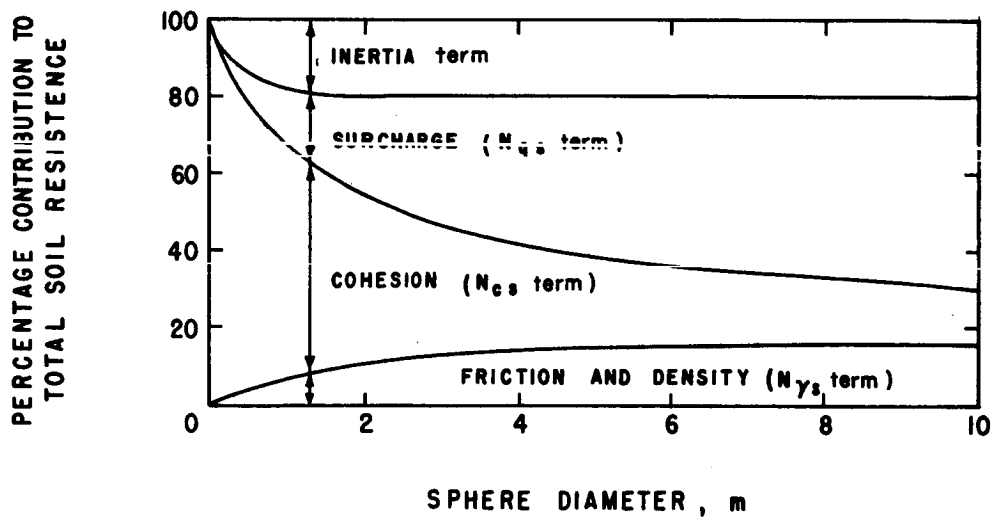

b) Lunar gravity.

Fig. 7-3. Relative contribution to total soil resistance from cohesion, surcharge, friction and density, and soil inertia as a function of sphere diameter.

Figure 7-3b shows that for the conditions assumed, soil inertia may contribute about 20% of the total soil resistance during lunar boulder track formation. It will be recalled that the 20% was calculated using an assumed velocity of about 2.5 meters per second. Some lunar boulders probably rolled faster and some rolled more slowly. The important conclusion is that where as on earth the inertia contribution would have been relatively insignificant, on the moon the inertia contribution is significant.

METHOD FOR SOLVING FOR ϕ FROM LUNAR BOULDER TRACKS

The flow diagram on the following page shows how ϕ can be determined.

For selected values of w, w/D, and α, and lunar soil conditions ($c = 1\ kN/m^2$, $\gamma_s = 1.6$ gm/cc, and $\gamma_r/\gamma_s = 2$), the friction angle was determined as proposed. The resulting curves are presented in Figures 7-4 and 7-5. These figures can be used to solve for the friction angle of lunar soil and to study variability of lunar surface soils.

In evaluating lunar soils by the proposed method, certain behavior accompanying compressibility should be recognized. From studies with simulated lunar soil, Houston, Namiq, and Mitchell (1970) showed that the density, cohesion and friction angle increase with depth. When a friction angle is determined from the boulder-track relationship, it is an average value for the particular failure surface.

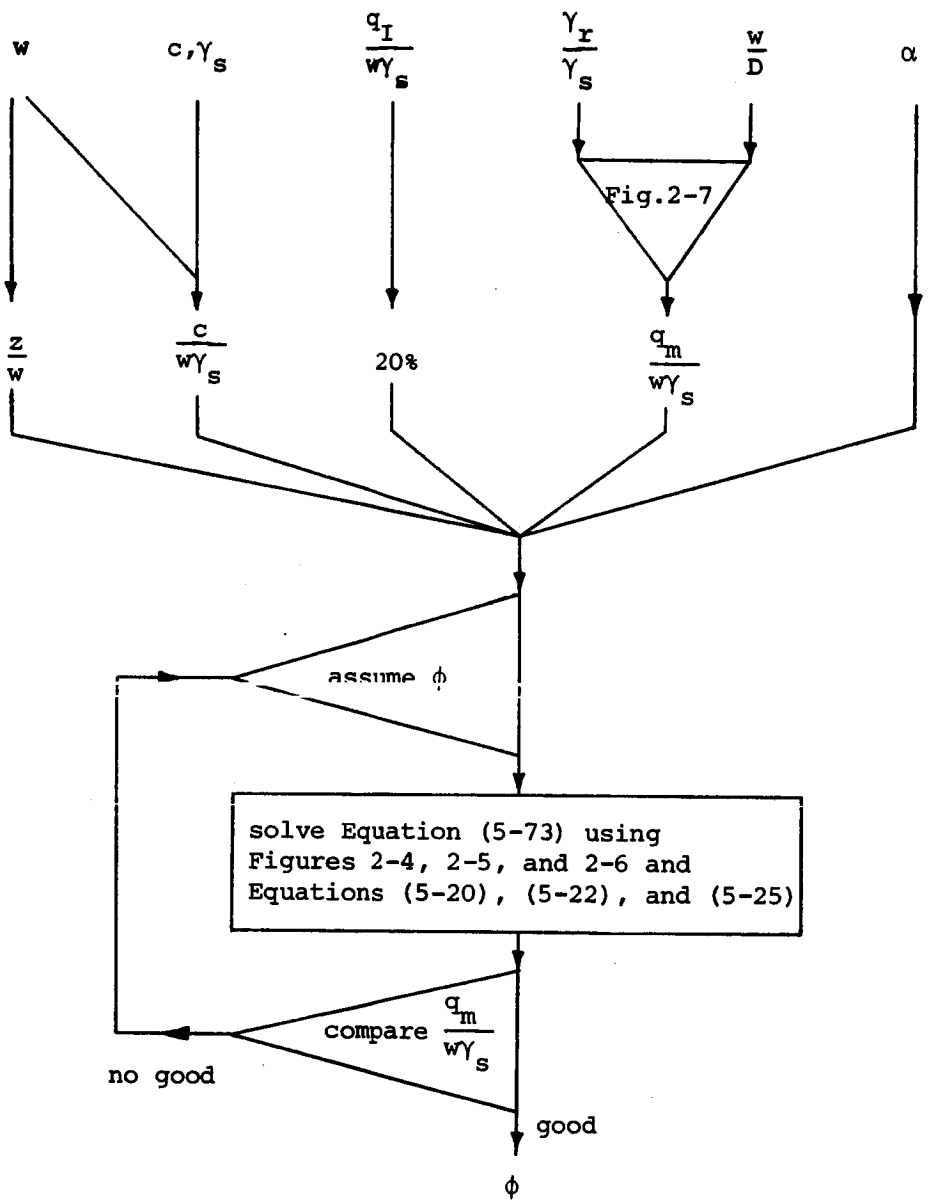

Flow diagram showing how ϕ can be determined.

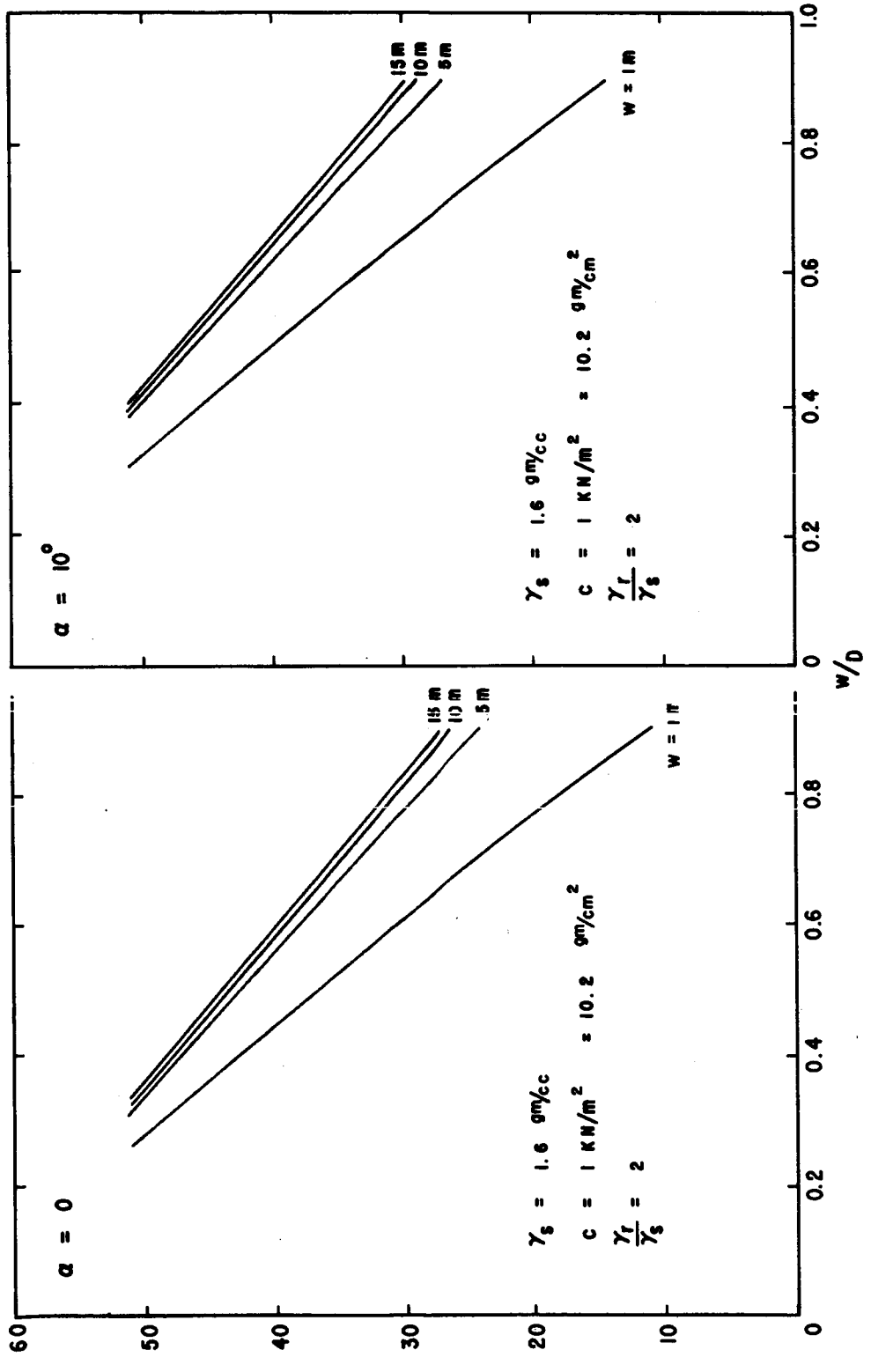

Fig. 7-4. Influence of friction angle on track width to sphere diameter ratio.

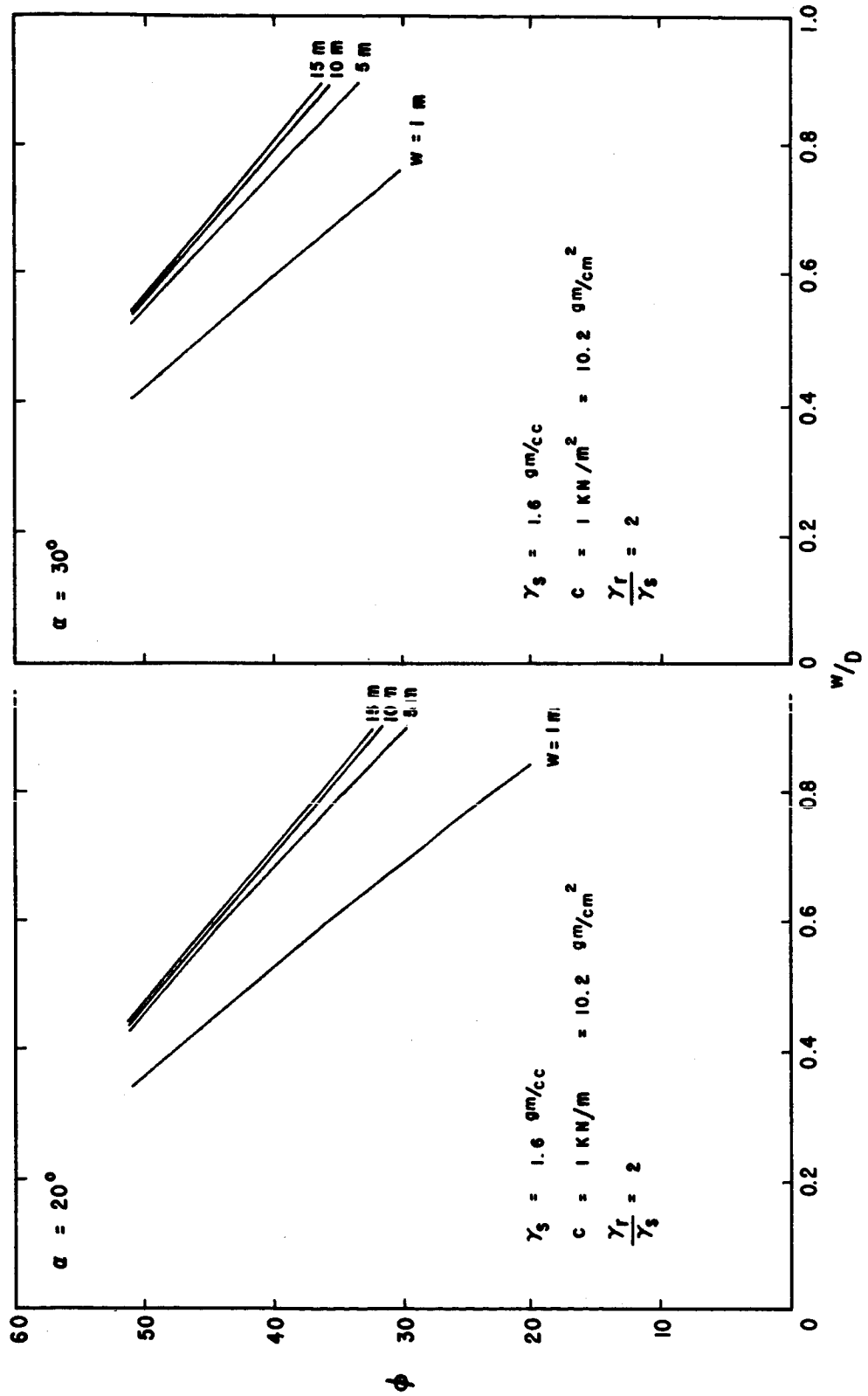

Fig. 7-5. Influence of friction angle on track width to sphere diameter ratio.

REANALYSIS OF LUNAR BOULDER TRACKS BY PROPOSED METHOD

Analysis and Results

For the boulder tracks analyzed in Chapter 2, the assumed soil parameters were:

$$c = 0.1 \text{ kN/m}^2 = 1.02 \text{ gm/cm}^2$$

$$\gamma_s = 1.6 \text{ gm/cc}$$

$$\frac{\gamma_r}{\gamma_s} = 1.7$$

The approximate average of the measurements of the w/D ratio from the 69 boulder tracks was about 0.69. The average slope angle was about 15 degrees, and the average track width was about 6.3 meters. On the basis of all the boulders analyzed, the average friction angle, ϕ, worked out to be 34 degrees.

Tests performed on the lunar samples brought back to earth with Apollo 11 permit a refinement of the soil parameter values. The following values are more reasonable:

$$c = 1.0 \text{ kN/m}^2 = 10.2 \text{ gm/cm}^2$$

$$\gamma_s = 1.6 \text{ gm/cc}$$

$$\frac{\gamma_r}{\gamma_s} = 2.0$$

With these soil and rock parameters, the 69 lunar boulder tracks were re-analyzed using the proposed theory (Figures 7-4 and 7-5). The results are presented in Table 7-1 and Figure 7-6. As shown in Figure (7-6), most of the values of ϕ were between 24 and 47 degrees. The values ranged from 19 to 53 degrees, and the arithmetic average of all values of ϕ worked out to be 37 degrees.

The values of ϕ were also plotted against the boulder diameter as shown in Figure 7-7. This figure includes all results for all w/D ratios and slope angles α. It can be concluded that the higher values of ϕ were associated with the larger boulders. This seems to imply that

1. The friction angle for the lunar regolith increases with

Table 7-1A. Results of boulder track analysis, Orbiter II photographs.

Location	Frame	Framelet (boulder location)	Longitude (degrees)	Latitude (degrees)	Boulder diam. (D) (meters)	Track width (w) (meters)	Slope (α) (degrees)	$\frac{w}{N}$	ϕ (°)
Mare Tranquillitatis (Approx. 100 Km from Apollo Site 1)	II-27H	921	36.54	3.56	6.0	6.0	15	0.50	24
Sabine D (Approx. 30 km from Surveyor 5 and Apollo Site 2)	II-76H*	364	23.68	1.20	8.7	6.4	13	0.23	36
Sinus Medii (Approx. 20 Km from Surveyor 6 and Apollo Site 3)	II-122H	464	-1.32	0.32	6.3	6.3	15	0.50	24
Sinus Medii (Approx. 20 Km from Surveyor 6 and Apollo Site 3)	II-123H	594 + 15mm, 28mm	-1.89	0.29	5.9	5.4	10	0.35	26.5

* Slope angle primarily based on slope determined by photogrammetry.

Table 7-1B. Results of boulder track analysis, Orbiter III photographs.

Location	Frame	Framelet (boulder location)	Longitude (degree)	Latitude (degree)	Boulder diam. (D) (meters)	Track width (w) (meters)	Slope (α) (degrees)	$\frac{w}{D}$	ϕ (°)
Mare Fecunditatis (Approx. 150 Km WNW of Messier A)	III-35H	396 + 4 mm, 258mm	42.81	-1.05	5.0	4.6	25	0.35	30.5
N E Mösting	III-107H	868 + 1mm, 21mm	-5.67	-0.33	3.6	2.8	10	0.23	28
Rima Hipparchus	III-111H	364 + 1mm, 286mm	4.83	-4.92	5.2	5.2	30	0.50	28
		373 + 13mm, 392mm			6.0	4.9	10	0.26	31
Reinhold (Approx. 30Km E. of Reinhold K)	III-125H	204 + 1.5mm, 69mm	-20.04	-0.60	2.3	1.6	15	0.21	33
		204 + 3mm, 75mm			2.5	2.5	15	0.50	19
		204 + 5mm, 76mm			2.5	1.9	15	0.23	30
		205 + 13mm, 53mm			2.7	2.1	15	0.23	28.5
		206 + 15mm, 64mm			4.1	3.7	20	0.31	27
Oceanus Procellarum (Approx. 40 Km from Surveyor 1)	III-181H	567 + 7mm, 284mm	-43.54	-2.11	3.2	2.2	10	0.21	33
Oceanus Procellarum (Approx. 40 Km from Surveyor 1)	III-189H	615 + 1mm, 77mm	-44.17	-2.41	2.9	2.4	5	0.27	24
		617 + 7mm, 91mm			6.2	5.1	5	0.28	29.5

Table 7-1C. Results of boulder track analysis, Orbiter V photographs.

Location	Frame	Framelet (boulder location)	Longitude (degrees)	Latitude (degrees)	Boulder diam. (D) (meters)	Track width (w) (meters)	Slope (α) (degrees)	w/D	ϕ (°)
Central mountains of Petavius (rille)	V-34H	880 + 12mm, 176mm	60.57	-25.70	23.3	13.7	20	0.16	45
		891 + 6mm, 146mm			19.0	13.7	20	0.21	40
Mare Tranquillitatis (Approx. 40 Km west of Censorinus)	V-63H	738 + 14mm, 147mm	32.75	-0.44	7.35	4.8	0	0.18	36
		738 + 16mm, 147mm			8.2	6.0	0	0.23	33
Large hill south of Alexander	V-88H**	011 + 8.5mm, 230mm	13.54	38.92	19.5	10.6	20	0.15	47
S. E. part of Hyginus	V-95H*	942 + 18mm, 365mm	5.94	7.56	13.1	8.8	30	0.19	45
		957 + 11.5mm, 164mm			8.9	6.2	15	0.20	38
		959 + 12.5mm, 161mm			9.5	5.6	15	0.17	43
		962 + 3mm, 167mm			8.6	4.6	15	0.15	45
		965 + 11mm, 239mm			10.0	5.7	15	0.16	44
		968 + 13mm, 253mm			11.2	4.2	20	0.11	53.5
		970 + 7mm, 246mm			14.4	9.2	20	0.18	43
		978 + 13mm, 252mm			6.0	4.8	15	0.25	33
		960 + 9mm, 146mm			4.9	4.9	30	0.50	28

* Slope angle primarily based on slope determined by photogrammetry.

** Photogrammetrically determined slope is about 30°; 20° slope is primarily based on shadow technique.

Table 7-10. (Cont'd)

Location	Frame	Framelet (boulder location)	Longitude (degrees)	Latitude (degrees)	Boulder diam. (D) (meters)	Track width (w) (meters)	Slope (α) (degrees)	w/D	ϕ (°)
N E part of Hyginus	V-96H*	092 + 1mm, 46mm	5.96	7.85	15.9	10.6	10	0.19	39
N E part of Hyginus	V-97H	175 + 11mm, 268mm	5.98	8.14	11.0	5.7	15	0.14	46
		175 + 13mm, 275mm			7.6	4.3	25	0.15	47
		178 + 10mm, 224mm			7.1	4.3	10	0.17	40
		178 + 14mm, 222mm			7.1	4.0	10	0.16	42
		180 + 5mm, 230mm			6.2	4.3	15	0.20	37.5
		180 + 4mm, 229mm			7.6	4.8	15	0.17	41
		180 + 1mm, 235mm			7.1	5.2	15	0.21	36
Hadley Rille	V-105H*	233 + 8mm, 232mm	2.95	25.00	14.9	9.6	25	0.19	44.5
		233 + 11mm, 234mm			13.5	8.9	15	0.19	40
		234 + 8mm, 235mm			13.2	8.6	5	0.19	38
Rima Bode	V-122H	475 + 9mm, 121mm	-3.97	12.92	12.2	9.0	15	0.22	37
Copernicus (center)	V-151H	280 + 17mm, 184mm	-20.34	9.42	9.1	6.6	10	0.21	35.5
		315 + 11mm, 282mm			12.2	5.5	5	0.12	46.5

Table 7-1C. (Cont'd)

Location	Frame	Framelet (boulder location)	Longitude (degrees)	Latitude (degrees)	Boulder diam. (D) (meters)	Track width (w) (meters)	Slope (α) (degrees)	w/D	ϕ (°)
Copernicus (NW of center)	V-155H	845 + 14mm, 340mm	-20.24	10.58	10.6	4.8	0	0.12	45
Copernicus (NW of center)	V-156H	962 + 8mm, 135mm	-20.21	10.87	11.9	10.7	10	0.32	29
Center of Vitello	V-168H	518 + 9mm, 188mm	-37.57	-30.61	19.2	19.2	15	0.50	27.5
		519 + 1mm, 185mm			11.4	5.4	10	0.12	46.5
		520 + 2mm, 184mm			8.0	4.8	15	0.17	42
		520 + 9mm, 188mm			11.9	7.9	15	0.19	40
North rim of Gassendi	V-179H	972 + 7mm, 250mm	-39.97	-16.29	8.6	5.5	15	0.18	41
		972 + 15mm, 333.4mm			5.6	5.3	15	0.35	26
		972 + 15.2mm, 338mm			5.4	4.7	15	0.31	29.5
		005 + 15mm, 244mm			16.4	14.1	15	0.29	33
		973 + 10mm, 345mm			9.4	6.0	10	0.18	39.5
		973 + 3mm, 285mm			6.8	6.0	20	0.29	31.5
		977 + 10mm, 340mm			16.0	14.0	15	0.30	31
		977 + 17mm, 325mm			7.0	6.1	20	0.28	32
		977 + 17mm, 305mm			5.6	5.0	25	0.31	32
		979 + 6mm, 352mm			7.5	4.8	10	0.19	39

Table 7-1C. (Cont'd)

Location	Frame	Framelet (boulder location)	Longitude (degrees)	Latitude (degrees)	Boulder diam. (D) (meters)	Track width (w) (meters)	Slope (α) (degrees)	$\frac{w}{D}$	ϕ (°)
Schröter's Valley	V-203H	111 + 7mm, 246mm	-49.51	25.13	7.4	5.4	10	0.22	35
		111 + 7mm, 246mm			7.4	5.4	20	0.22	38
Schröter's Valley	V-203H*	227 + 8mm, 41mm	-49.48	25.52	9.4	6.2	15	0.19	40
		221 + 18mm, 161mm			12.6	6.5	5	0.14	44
		210 + 15mm, 242mm			12.6	7.2	15	0.16	44.5
		210 + 14mm, 177mm			10.5	5.5	25	0.14	49
		202 + 7mm, 253mm			19.4	12.3	20	0.18	43
Oceanus Procellarum (Approx. 130 Km NW of Marius)	V-213H	417 + 7mm, 294mm	-56.03	13.50	7.4	4.3	20	0.16	44.5
		431 + 10mm, 290mm			6.4	3.3	15	0.14	44

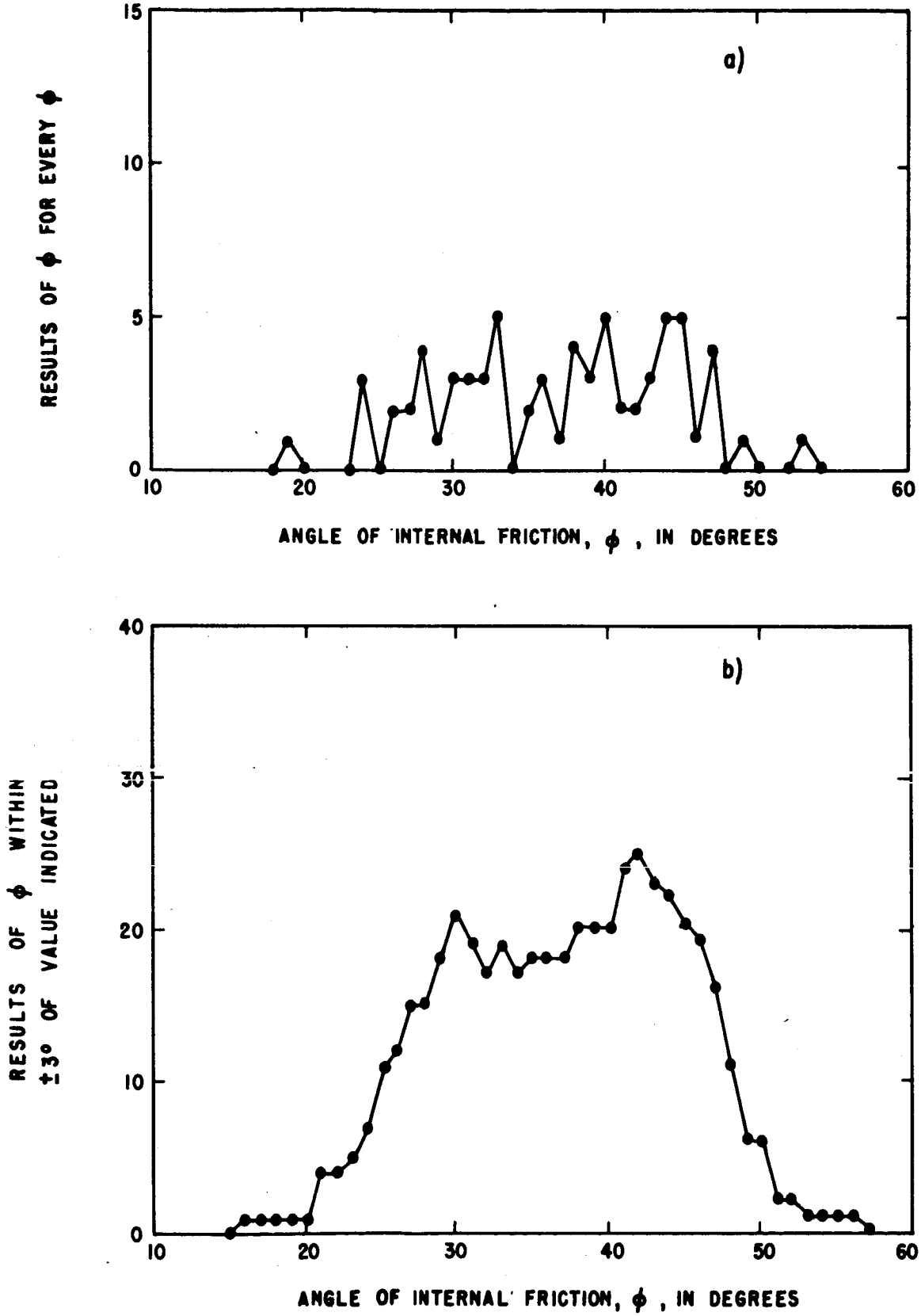

Fig. 7-6. Frequency distribution of the results.

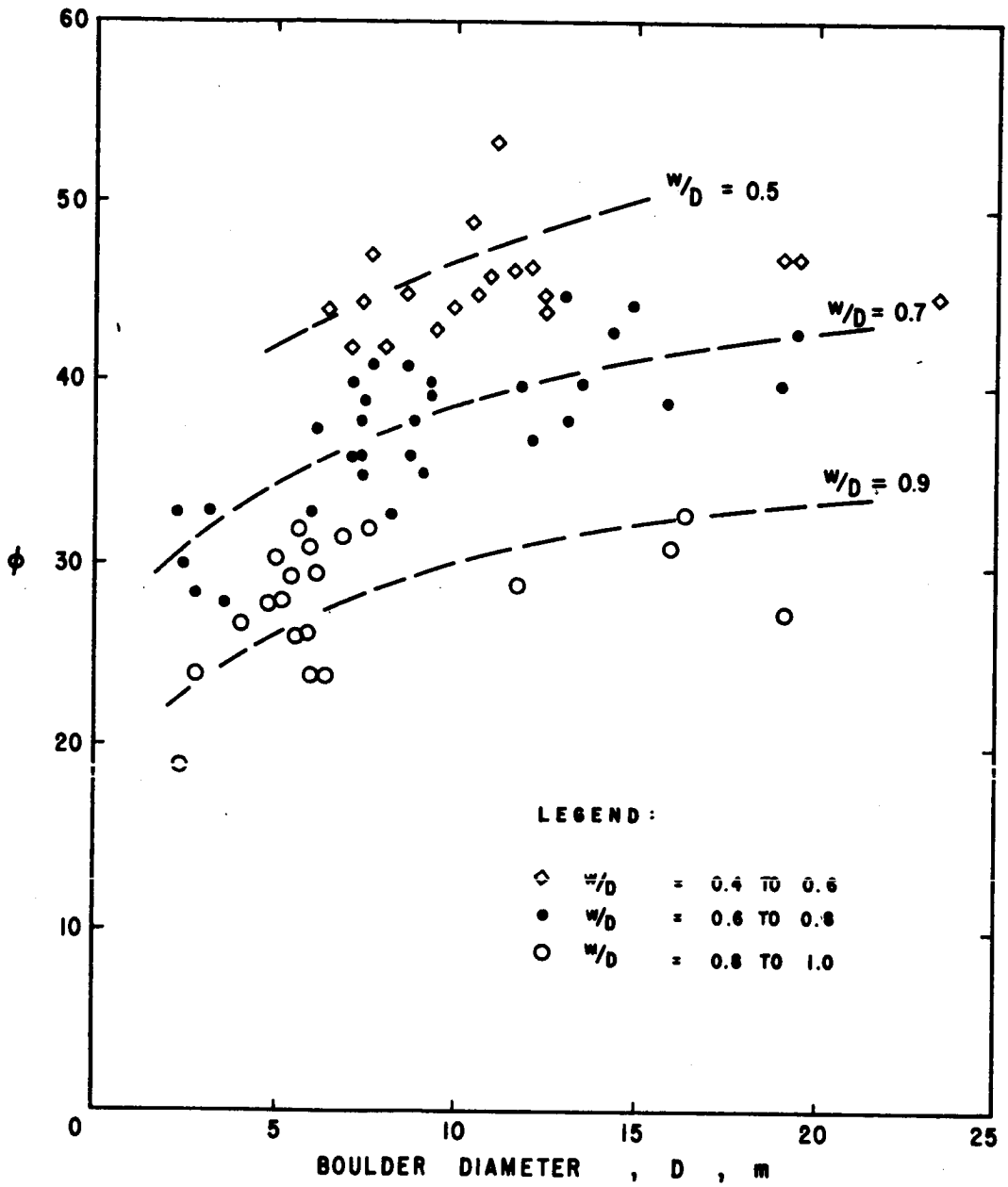

Fig. 7-7. Results of ϕ plotted against boulder diameter.

depth. This is probably a consequence of an increase in soil density with depth. These inferences are based on the fact that the larger boulders would generate a deeper failure surface. Analogous behavior has been predicted from studies on simulated lunar soil (Houston, Namiq, and Mitchell, 1970).

2. Alternatively, it is possible that the larger boulders were influenced by a layer of harder material below the lunar regolith. This could have resulted in a lower value of w/D and an apparently higher ϕ. In this case the implication is that the thickness of the lunar regolith in the vicinity of the boulder tracks was close to the radius of the larger boulders (10 to 15 meters).

Discussion

As shown in Table 7-1 and on Figure 7-6, ϕ varied considerably - from 19 to 53 degrees. In some locations, the measurements indicated a significant variability within the same slope. That is, the sinkage, z/w, of one boulder was significantly greater than that of an adjacent boulder also analyzed (Frames III-125H, V-95H, and V-168H). Possible interpretations for such variations would be that: 1) the soil properties differed at the two locations, 2) the boulder causing the track somehow did not conform to the assumptions of the theory used; perhaps it was not spherical or it had inertial energy beyond that assumed, and 3) other as yet unknown causes. For most of the locations, on the other hand, the results were more constant.

For many tracks, the measured track width, w, was equal to the boulder diameter, D. Hence, we can conclude that in such cases the thickness of unconsolidated soil on the slope must have been at least half the boulder diameter.

Since the Surveyor results (Surveyor VII Mission Report, 1968) and Apollo 11 results (Costes and Mitchell, 1970) quite consistently indicate that the friction angle for lunar soil may be in the range of 37 to 39 degrees, it is of interest to consider possible causes of the considerably larger range found here. As stated before, the results of this analysis indicate an average ϕ of 37 degrees with a

range from 19 to 53 degrees. It is appropriate, however, to assess the degree of confidence that may be placed in these results.

Sensitivity of results to variations in soil density:

The influence of variations in densities of rock and soil can be appreciated by considering Equation (5-75), which gives the left side term of Equation (5-73). The $q_m/w\gamma_s$ term is directly proportional to the density ratio, γ_r/γ_s, and inversely proportional to the w/D ratio cubed. As shown in Figure 2-7, for any one w/D ratio, the $q_m/w\gamma_s$ term could almost triple within the range of possible values of γ_r/γ_s between 1.7 and 3. This range of values for the $q_m/w\gamma_s$ term would lead to a ± 5° change in the apparent friction angle, ϕ, determined from the boulder track relationship.

Sensitivity of results to variations in cohesion:

The significance of cohesion depends on the relative magnitude of the cohesion term in Equation (5-73). The sensitivity of the results to variations in cohesion was investigated using average values (ϕ = 37°, c = 10.2 gm/cm^2, z/w = 0.234, w = 7m, γ_s = 1.6 gm/cm^2, and α = 15°) for the boulder tracks analyzed. For a 10 and 100 fold increase in cohesion, the required friction angle for the same soil resistance is:

Cohesion c	Resulting friction angle ϕ
10^3 dynes/cm^2	39°
10^4 dynes/cm^2	37°
10^5 dynes/cm^2	27°

Sensitivity of results to measurements:

To see how serious errors or inconsistencies in measuring the boulder and track dimensions might be, the measurements were made on two different scale photographs as previously described. The difference in the two measurements were computed as follows:

For the diameter

$$\Delta D = \left[1 - \frac{D_{smaller}}{D_{larger}}\right] \times 100$$

For the track width

$$\Delta w = \left[1 - \frac{w_{smaller}}{w_{larger}}\right] \times 100$$

Similarily, the difference in the w/D ratio was computed by

$$\Delta\left(\frac{w}{D}\right) = \left[1 - \frac{(w/D)_{smaller}}{(w/D)_{larger}}\right] \times 100$$

The results of the comparison and the resulting change in the friction angle, $\Delta\phi$, are shown in Table 7-2. The basis for this comparison is $(w/D)_{ave} = 0.69$ and $\phi_{ave} = 37°$.

Table 7-2. Sensitivity of results to measurements

Comparison	ΔD (%)	Δw (%)	Δ w/D (%)	$\Delta\phi$ (°)
Average	9	12	9.6	2
Maximum	32	28	22	5

As shown in Table 7-2 above, the average difference in ϕ for the two measurements would be about 2 degrees. If it can be assumed that the friction angle resulting from averaging the measurements, as was done for the results presented, is closer to the correct value than the result of either of the measurements independently, the friction angles

presented in Table 7-2 may be regarded as including a one degree average error and about 3 degree maximum error due to inconsistencies in measurements. This is quite good considering the scale of the photographs; as better photographs become available, it should be possible to considerably reduce measurement inaccuracies.

Sensitivity of results to the slope angle:

The influence of changes in the slope angle, α, on the resulting friction angle was determined from Figures 7-4 and 7-5. Again the basis for the evaluation was the average friction angle of 37 degrees, and the average slope angle of 15 degrees. The results are presented below:

Slope angle, α	Friction angle, ϕ
0°	33°
5°	34°
10°	35.5°
15°	37°
20°	38.5°
25°	40°
30°	42°

Since slope angles cannot be very accurately determined at this time, the results of ϕ presented in Table 7-1 should be considered to have a probable error of ±1.5° due to incorrect estimation of the slope angle. This would correspond approximately to a ±5° difference in the slope angle as shown above.

Summary

From a consideration of the possible effects of incorrect assumptions as to soil parameters, incorrect measurements, incorrect estimates of the slope angle, and inadequacies of the theory, probable uncertainties in the results are as follows:

Cause:	Effect on ϕ (°)
Variation in density ratio from γ_r/γ_s = 1 to 3	±5
Variation in c (for every 1×10^4 dynes/cm^2, $10^3 \leq c \leq 10^5$ dynes/cm^2)	±1 to 2
Incorrect value of w/D ratio (measurements)	±1 to 2
Incorrect slope angle (±5°)	±1 to 2

Of the causes listed above, incorrect estimates of the density ratio have the largest effect on the results. Since the values of ϕ varied from 19 to 53 degrees, it appears that the density ratios may have varied considerably for the boulder tracks analyzed. Possibly the state of soil compaction or the specific gravities varied. Incorrect assessment of cohesion and determination of the w/D ratio and the slope angle probably also contributed to the spread in the values of ϕ.

CONCLUSIONS

Certain implications and applications of the developed theory were considered in this chapter. The following conclusions can be made:

1. The cohesion term provides most of the resistance for small (5 × 5 cm to 10 × 10 cm) loaded areas in moist sand; because although c may be as low as 10 gm/cm^2, N_c is large for a high friction angle.
2. The resistance due to inertia of the moving soil is more significant on the moon than on earth.
3. A method for solving for the friction angle for lunar soils from the boulder track relationship was outlined. It is believed that Figures 7-4 and 7-5 can be used to determine a friction angle and to study variability of lunar surface soils. Provided assumptions regarding other soil and rock parameters are realistic and measurements of boulder and track dimensions are adequate, the proposed method should give friction angles comparable to ϕ determined from

conventional triaxial tests.

4. The 69 lunar boulder tracks reviewed in Chapter 2 were reevaluated using the proposed method. The values of ϕ ranged from 19 to 53 degrees, and the arithmetic average for the friction angle of lunar soil was found to be 37 degrees.
5. Lunar soil and rock properties (cohesion, density, and friction angle) are possibly more variable than anticipated from previous investigations.
6. The results also indicate that the soil parameters (density, cohesion, and friction angle) increase with depth below the lunar surface (Figure 7-7).

Chapter 8. CONCLUSIONS AND RECOMMENDATIONS

GENERAL

The studies reported herein were motivated by observations of boulder tracks both on the moon and on earth. From such boulder-track records usually only the track width, the boulder diameter, and the slope angle can be measured. With this in mind, both experimental and theoretical studies were aimed at relating soil and rock parameters to the measurable w/D ratio.

Provided other soil and rock parameters are known from independent analysis, it is possible to determine one unknown from the boulder-track relationship. The experimental data and comparisons presented in Chapter 6 show close agreement with theoretical predictions. The friction angle of lunar soil, for example, was found to be 37 degrees using the proposed theory. Independent studies of lunar soil from Surveyor tests and Apollo 11 samples have resulted in nearly the same value. It is believed that soil conditions can be evaluated from the boulder-track relationship.

In general, the studies provided valuable information on the failure mechanism associated with rolling sphere-soil slope interaction. The failure mechanism for wheel-soil interaction is believed to be similar at least for nearly rigid wheels. The theoretical developments are a first attempt to incorporate the influence of soil inertia as a part of soil resistance.

THE FAILURE MECHANISM

As a sphere rolls down a sand slope, the most important characteristics of behavior are:

1. Track formation is accompanied by soil volume changes and general shear.
2. For loose sands and at the beginning of rolling in general, soil deformations consist of volume change.
3. When volume change (compression) can no longer account for

all the soil that must be displaced, shear planes develop.

4. Within the shear zone in front of the sphere there may be about two shear planes per cm of depth of the shear zone.
5. The shearing is a discontinuous process although rolling appears to be continuous to the naked eye. Separately identifiable shearing soil wedges are pushed out in front of the sphere. These failure wedges appear to form where the soil is weakest; sometimes directly in front of and sometimes slightly to the sides of the sphere.
6. The maximum pressure beneath the sphere is about twice the average pressure, and the maximum pressure appears to control the development of shear failure.
7. The contact pressure distribution is bell-shaped and can be closely approximated by a parabolic function.
8. Vertical sections within the soil are bent forward. This forward movement is pronounced; very little lateral movement takes place.
9. The magnitude of the resultant of soil reaction can usually be considered equal to the weight of the sphere. The direction of the resultant can be assumed vertical for practical purposes.

THEORY

Equations (5-70) through (5-76) can be used to solve boulder-track problems. These equations are quite complete in terms of consideration of the many variables involved in the rolling sphere (boulder)-soil slope interaction problem. Because of the number of variables, however, many assumptions were made. Further, due to the assumptions and the nature of the theoretical development, most of the equations are semiempirical. Independent checks of these assumptions by experimentation are recommended. However, it is believed that the proposed equations can provide a valuable basis for a remote reconnaissance technique for estimating approximate values of soil parameters. Provided assumptions regarding other soil and rock parameters are realistic and measurements of boulder and track

dimensions are adequate, the proposed method should give friction angles comparable to ϕ determined from conventional triaxial tests.

SOIL PROPERTY EVALUATION

From Rolling Spheres

Based on the investigations reported herin, it appears that it should be possible to study surface soil conditions on the basis of sphere or spherical wheel-soil interaction. It has been noted that the resulting track width is very sensitive to changes in soil conditions. Soft pockets are easily detectable from a sudden increase in track width. Data obtained by pulling a spherical wheel on the soil surface would be required. By monitoring the velocity and measuring or continuously photographing the resulting track, all the parameters in Equation (5-72) could be systematically studied.

From Rolling Boulders

Velocity information is not directly available from boulder-track records. Further, assumptions must be made as to other soil and rock properties such as density and cohesion. Therefore, the answers obtained from the analysis of boulder tracks are only as good as the assumptions. Nonetheless, it is believed that the study of boulder-track records can provide valuable information on the variability of soil conditions and estimates of soil parameters for unknown areas.

Properties of the Lunar Regolith

The lunar boulder tracks were reevaluated using the method proposed in Chapter 7: this method is based on the improved theory developed in Chapter 5. The following conclusions seem to be appropriate from the results of the 69 lunar boulder tracks investigated:

1. The results of ϕ ranged from 19 to 53 degrees with the majority being between 24 and 47 degrees.
2. The average friction angle, ϕ, was found to be 37 degrees.
3. Based on the range of ϕ, lunar soil conditions appear to be quite variable.
4. Soil density, cohesion, and friction angle probably increase

with depth below the lunar surface.

Possible implications of the range of ϕ reported above for the boulder tracks from different areas of the moon are:

1. The state of soil compaction of lunar soil may vary.
2. The cohesion may vary.
3. The friction angle may vary.
4. The measured track width, which is the basis for the range of ϕ, was not representative of the crest-to-crest track width immediately after the track was formed.

Of the above possibilities, undoubtedly some of the track widths were not representative of the crest-to-crest track width immediately after the track was formed. On the other hand, some variability of soil conditions should be expected. Particularly the state of compaction of the lunar regolith may vary.

In applying the proposed theory to the solution of lunar boulder-track problems, it should be remembered that inertia forces are relatively more important on the moon than on earth. For the 69 lunar boulder tracks described in this report, soil inertia was considered to provide 20% of the total soil resistance.

RECOMMENDATIONS

It is recommended that the boulder track method be considered as a remote reconnaissance technique for preliminary study of soil conditions at different points on the moon and on other planets where boulder tracks are observed.

It is recommended that efforts in the near future be directed also to a study of wheel-soil interaction. It is believed that the failure mechanism described is applicable to many wheel-soil interaction problems. With some modifications the proposed theory may be suitable for the study of wheels. Since much data are already available in the literature on wheel-soil interactions, it might be possible to check the proposed theory without extensive testing. Such studies are recommended.

The failure mechanism proposed should be considered in relation to existing trafficability theory. A spherical wheel could be designed and tested to study the inertia effects. The testing of such a wheel could provide information on the exponent, n, and on the acceleration of the shearing soil. This could be of considerable value in the design and performance prediction of terrain vehicles and lunar rovers.

REFERENCES

Bekker, M. G., *Theory of Land Locomotion*, University of Michigan Press, Ann Arbor, 1956.

Bendix Corporation, "Summary Report, Lunar Module (LM) Soil Mechanics Study," AM-68-4, November, 1968.

Costes, N. C., Carrier, W. D., Mitchell, J. K. and Scott, R. F., "Apollo 11 Soil Mechanics Investigation," *Science*, Vol. 167, p. 3918, Jan. 1970.

Costes, N. C. and Mitchell, J. K., "Apollo 11 Soil Mechanics Investigation," *Proc. of the Apollo 11 Lunar Science Conf.*, Vol. 3 (Physical Properties, p. 2025, Pergamon Press, New York, 1970.

Duke, M. B., Woo, C. C., Bird, M. L., Sellers, G. A., and Finkelman, R. B. "Lunar Soil: Size Distribution and Mineral Constituent," *Science*, Vol. 167, No. 3918, pp. 648-650, Jan. 30, 1970.

Eggleston, J. M., Patteson, A. W., Throop, J. E., Arant, W. H., and Spooner, D. L., "Lunar Rolling Stones," *Photographic Engineering*, Vol. 34, No. 3, March 1968.

Filice, A. L., "Lunar Surface Strength Extimates from Orbiter II Photographs," *Science*, Vol. 156, p. 1486, 1967.

Freitag, D. R., Green, A. J., and Melzer, K. J., "Performance Evaluation of Wheels for Lunar Vehicles," Technical Report M-70-2, U. S. Army Engineer Waterway Experiment Station, Vicksburg, Mississippi, 1970.

Green, Jr., A. J. and Murphy, Jr., N. R., "Stresses Under Moving Vehicles, Distribution of Stresses Beneath a Towed Pneumatic Tire in Air-Dry Sand," Technical Report No. 3-545, U. S. Army Engineer Waterways Experiment Station, Vicksburg, Mississippi, 1965.

Hansen, J. B., "Foundations of Structures - (a) General Subjects and Foundations Other Than Piled Foundations," *Proc. of the 4th Int. Conf. on Soil Mech. & Found. Eng.*, London, 1957.

Hovland, H. J. and Mitchell, J. K., "Soil Property Evaluations from Boulder Tracks on the Lunar Surface," Final Report, Vol. II of IV, Space Sciences Laboratory, NASA Contract NAS 8-21432, University of California, Berkeley, Jan. 1970.

Houston, W. N., Namiq, L. I., and Mitchell, J. K., "Lunar Soil Simulation," Final Report, Vol. I of IV, Space Sciences Laboratory, NASA Contract NAS 8-21432, University of California, Berkeley, Jan. 1970.

Karafiath, L. L. and Nowatzki, E. A., "A Study of the Effect of Sloping Ground on Bearing Strength and the Landing Performance of Space Vehicles," Grumman Research Department Memorandom, RM-407, New York, 1968.

Khojasteh-Bakht, "Analysis of Elastic-Plastic Shells of Revolution Under Axisymmetric Loading by the Finite Element Method," SESM 67-8, Structural Engineering Laboratory, University of California, Berkeley, 1967.

Leonards, G. A., *Foundation Engineering*, McGraw-Hill Book Co., Inc., 1962.

Lin, Y. K. and Haythornthwaite, R., "The Mechanics of Surface Deformation and Resistance to a Sphere Rolling Down Slopes of Granular Media," 05894-5-F, University of Michigan, 1969.

Lundgren, H. and Hansen, J. B., *Geoteknik*, Teknisk Forlag, Köbenhavn, 1958.

Melzer, K. J., "Measuring Soil Properties in Vehicle Mobility Research; Cone Penetration Resistance and Relative Density," Technical Report being prepared for publication, U. S. Army Engineer Waterways Experiment Station, Vicksburg, Mississippi.

Meyerhof, G. G., "The Ultimate Bearing Capacity of Foundations," *Geotechnique*, Vol. II, p. 301, 1951.

Meyerhof, G. G., "Influence of Roughness of Base and Ground-Water Conditions on the Ultimate Bearing Capacity of Foundations," *Geotechnique*, Vol. V, No. 3, 1955.

Mitchell, J. K, Smith, S. S., and Quigley, D. W., "Material Studies Related to Lunar Surface Exploration," Final Report, Contract NSR 05-003-189, Vol. I, University of California, Berkeley, March 1969.

Mitchell, J. K., Smith, S. S., and Quigley, D. W., "Trafficability," Final Report, Contract NSR 05-003-189, Vol. III, University of California, Berkeley, March 1969.

Mitchell, J. K, and Smith, S. S., "Engineering Properties of Lunar Soils," Final Report, Contract NSR 05-003-189, Vol. I, University of California, Berkeley, March 1969.

Moore, H. and Martin, G., "Lunar Boulder Tracks," *Orbiter Supporting Data*, No. 1, 1967.

Nordmeyer, E. F. and Mason, C. C., "Lunar Surface Mechanical Properties Derived from Track Left by Nine Meter Boulder," NASA, NSC Internal Note No. 67-TH-1, February 1967.

Reece, A. R., "Principles of Soil-Vehicle Mechanics," *Proc. Institution of Mechanical Engineers*, Vol. 180, Part 2A, 1965-1966.

Roggeveen, J. J. and Goodman, R. E., "Lunar Surface Length Measurements from Orbiter Photographs," University of California, Berkeley, 1968.

Roth, B. J., "Aspects of Soil Trafficability," M. S. Thesis, Ohio State University, 1960.

Scott, R. F., *Principles of Soil Mechanics*, Addison-Wesley Publishing Co., Inc., Palo Alto, 1963.

Skempton, A. W., "The Bearing Capacity of Clays," *Proc. Bldg. Res. Congr.*, London, 1951.

Sokolovski, V. V., *Statics of Soil Media*, Butterworths, London, 1960.

Terzaghi, K., *Theoretical Soil Mechanics*, John Wiley and Sons, Inc., New York, 14th printing, 1943.

Timoshenko, S. and Goodier, J. N., *Theory of Elasticity*, McGraw-Hill Book Co., Inc., New York, Second Ed., 1951.

Turnage, G. W., "Track Performance on Yielding Soil," Technical Report being prepared for publication, U. S. Army Engineer Waterways Experiment Station, Vicksburg, Mississippi.

Turnage, G. W. and Green, A. J., "Performance of Soil Under Tire Loads; Analyses of Tests in Sand from Sept. 1962 through Nov. 1963," Technical Report No. 3-66, Report 4, U. S. Army Engineer Waterways Experiment Station, Vicksburg, Mississippi, Feb. 1966.

U. S. Army Engineer Waterways Experiment Station, "Tests on Natural Soils with Self-Propelled Vehicles, 1951-53," Tech. Memo. No. 3-240, 12th Suppl., November 1954.

Wilson, N. E. and Krzywicki, H. R., "Soil Mechanics as it Affects Vehicle Performance," *Canadian Geotechnical Journal*, Vol. III, No. 4, November 1966.

Wong, Jo-Yung and Reece, A. R., "Soil Failure Beneath Rigid Wheels," *Proc. Second. Int. Conf. for Terrain Vehicle Systems*, 1966.

Yong, R. N. and Osler, J. C., "On the Analysis of Soil Deformation Under a Moving Rigid Wheel," *Proc. Second Int. Conf. for Terrain Vehicle Systems*, 1966.

SYMBOLS

A	semicircular contact area based on crest-to-crest track width, w
A_f	longitudinal section area of failure wedge for a footing
A_s	longitudinal section area of failure wedge for a sphere
A_t	total cross-sectional area of moving soil including A_w
A_w	cross-sectional area of track below crest of track
a	linear acceleration of sphere or boulder
a_f	final acceleration (deceleration) of shearing soil
a_i	initial acceleration of shearing soil
a_{max}	maximum acceleration of shearing soil
a_s	acceleration of shearing soil
B	abreviation used in solving Equation (5-61)
B_1, B_2, B_3, B_4, B_5	integration constants
b	width of equivalent rectangular area
b_s	approximate width of shearing soil wedge
c	apparent cohesion
c_i	apparent cohesion determined from in-situ tests
D	diameter of sphere or boulder
D_r	relative density of sand in percent
DB	drawbar pull (towing force)
DB-ma	drawbar pull corrected for carriage inertia
d	dimension defining triangle base proportional to d_o
d_o	dimension of cone underneath sphere
F	resultant of soil reaction
F_I	soil inertia force
F_{ts}	towing force for sphere
F_x	component of F parallel to slope
F_y	component of F normal to slope
G	cone index gradient (cone penetration resistance gradient)
g	acceleration of gravity
I	moment of inertia of sphere = $\frac{2}{5} mr^2$
kN/m^2	kilo newtons per meter squared
k_s	coefficient of subgrade reaction for sand

L	length of equivalent rectangular area
MN/m^3	mega newtons per meter cubed
m	mass of sphere or boulder = W/g
m_s	mass of shearing soil wedge
N	newtons
N_γ, N_c, N_q	Meyerhof (1951) bearing capacity factors
$N_{\gamma s}, N_{cs}, N_{qs}$	bearing capacity factors for rolling spheres
n	exponent defining acceleration function ($n = -a_i/a_f$)
PC	pressure cell
q	unit bearing capacity, bearing pressure, or average soil pressure
q_e	unit bearing capacity in earth gravity
q_I	unit soil resistance due to inertia of moving soil
q_m	unit bearing capacity in lunar gravity
q_s	unit soil resistance due to general shear
q_v	unit soil resistance due to volume change
q'	surcharge pressure
R	resultant of wheel load and towing force
r	radius of sphere or boulder
r_F	distance from center of sphere to line of action of F
S_f	area of failure surface for a footing per unit depth perpendicular to the paper
S_s	area of failure surface for a rolling sphere per unit depth perpendicular to the paper
s_γ, s_c, s_q	shape factors (for shape of loaded area) for the bearing capacity equation
t	time
t_{so}	time of soil movement
u	angular acceleration of sphere
V_r	volume of track rims above original soil surface, per unit depth
V_s	volume of shearing soil wedge
V_t	total volume ($\lvert V_r \rvert + \lvert V_w \rvert$)
V_w	volume of center of track below original soil surface, per unit depth
v	velocity of sphere parallel to slope

v_{at}	average soil velocity w.r.t. time
v_{max}	maximum soil velocity
v_s	velocity of soil moving along failure surface
W	weight of sphere or boulder
WL	wheel load
w	crest-to-crest track width
w_v	crest-to-crest track width for maximum volume change before general shear ($w_v < w$)
x	distance traveled by sphere (Chapter 6)
x,y	coordinate directions
x_s	soil displacement during general shear
x_{total}	total displacement of a shearing soil wedge
y	coordinate distance from location of maximum pressure perpendicular to direction of maximum pressure
z	sinkage or track depth based on crest-to-crest track width
z_v	track depth based on w_v or track depth for maximum volume change before general shear
α	slope angle
β	angle defining equivalent free surface on Meyerhof's charts
β_s	angle between vertical and direction of resultant of soil reaction for a sphere
ΔV	volume of compressed soil per unit depth perpendicular to track ($\Delta V = V_w - V_r$)
δ_{max}	maximum deflection of diaphragm
ε_{max}	maximum strain in diaphragm
γ_d	dry density of soil in earth gravity
γ_m	soil density in lunar gravity ($\gamma_m = \gamma_s/G$)
γ_r	rock or sphere density in earth gravity
γ_s	soil density in earth gravity
θ	angle at sphere center defined by bisecting the track width, w
θ_v	angle at sphere center defined by bisecting w_v
θ_2	angle of intersection of slope and upper end of passive Rankine zone
θ_3	angle of intersection of slope and failure surface

σ	pressure at the sphere-soil contact parallel to the resultant, R
σ_{max}	maximum contact pressure at y = 0
σ_n	normal stress
σ_1	major principal stress
σ_3	minor principal stress
ϕ	angle of shearing resistance or internal friction
ϕ_i	angle of internal friction based on in-situ tests
ϕ_s	secant friction angle
ϕ_t	tangent friction angle
ψ	base angle (angle defining frictional resistance at a footing base-soil contact)
τ	shear stress
ω	moisture content (percent moisture per dry-weight of soil)
II	Orbiter II
III	Orbiter III
V	Orbiter V

Appendix A. PREPARATION OF SOIL CARS AT THE WATERWAYS EXPERIMENT STATION

Preparation of a soil car began by raking the soil as shown in Figure A-1 to break up the previous soil structure.

Next the surface was leveled with the top of the car by screeding with a straight aluminum member. Then the soil was compacted to desired density using vibrators attached to a heavy piece of plywood, as shown in Figure A-2. The WES personnel have developed techniques through experience by which a desired density can be produced and reproduced. Desired densities in dry (air-dry) sand can be achieved quite easily. Moist sand requires greater precision and care.

The soil strength or resistance to penetration is tested by the cone index test as shown in Figure A-3. A photoelectric eye located at the top of the cone indicates contact with the soil and starts the automatic recording process. A load cell measures soil resistance. The slope of the stress vs. depth plot is the cone index gradient G expressed in MN/m^3 in this report. In air-dry sand, the density would be determined from the curves in Appendix B, entering the charts with G determined as explained above.

For moist sand, the density must be determined by an in-place density test. An in-place density box designed by Dr. Hvorslev was used for this purpose as shown in Figure A-4. Entering the charts in Appendix B with G, the density, and moisture content (determined as explained above) other parameters, such as cohesion, can be obtained.

In general, the raking and compacting process produced a relatively uniform soil to a depth of about 20 cm. The failure planes for all of the spheres are believed to have been much shallower, and therefore, the preparation of the soil cars was probably adequate. That is, the underlying denser sand probably had little influence on the results.

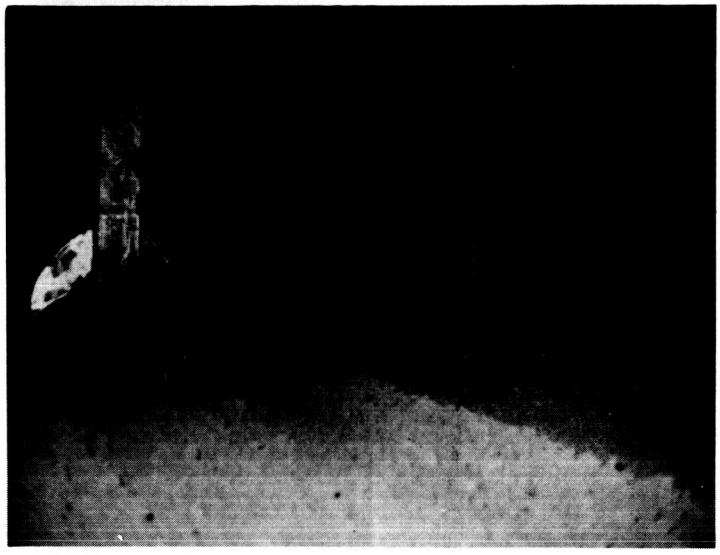

Fig. A-1. Raking the soil.

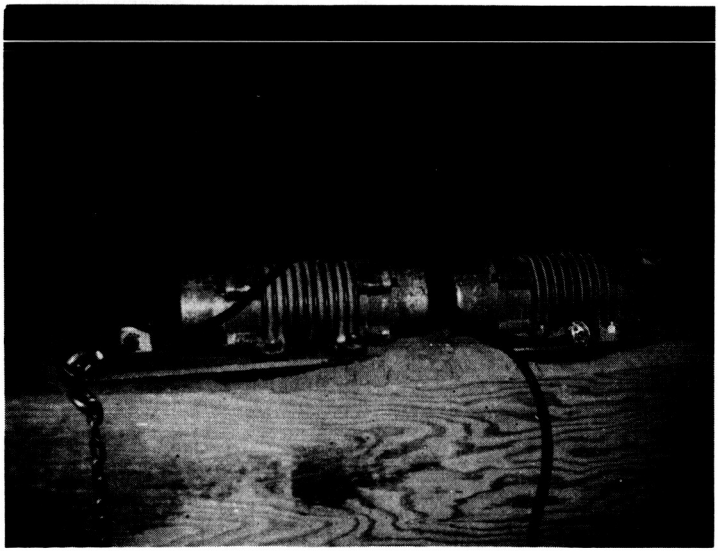

Fig. A-2. Vibrating the soil.

Fig. A-3. Cone index test.

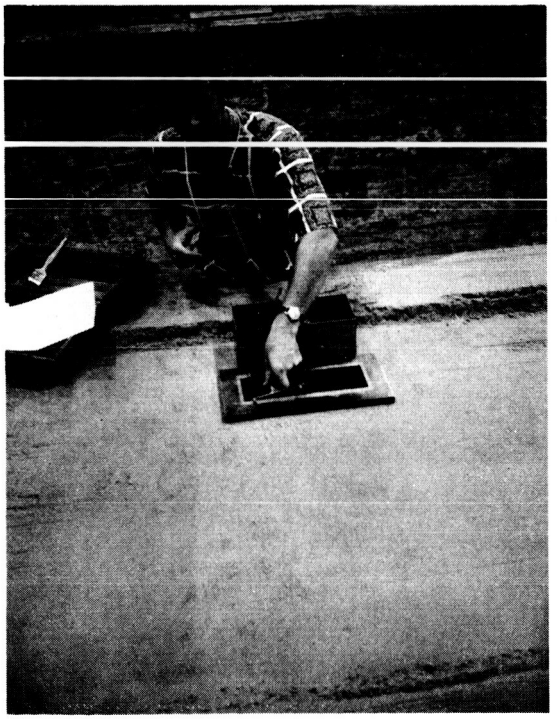

Fig. A-4. In-place density test.

Appendix B. PROPERTIES OF YUMA SAND

(Determined by the U. S. Army Engineer Waterways Experiment Station, Vicksburg, Mississippi)

Soil property relationships for Yuma sand as determined by WES are presented in Figures B-1 through B-10.

As shown in Figure B-10 there is generally a seven to eight degree difference between the angles of internal friction determined from laboratory tests and those determined from plate in situ shear tests. This difference is probably due to the different failure mechanisms associated with the various tests (Freitag, Green, and Melzer, 1970).

The main component of the plate in situ shear test device was a hollow aluminum plate 60 cm long, 30 cm wide, and 2.5 cm thick. Sand was glued to the surface to be in contact with the soil to assure soil-to-soil shearing. The plate was loaded vertically and pulled horizontally at a constant speed of 1 mm/min until failure occurred. Further details of the testing procedures for the relationships presented in Figures B-1 through B-10 are to be found in the report by Freitag, Green, and Melzer (1970).

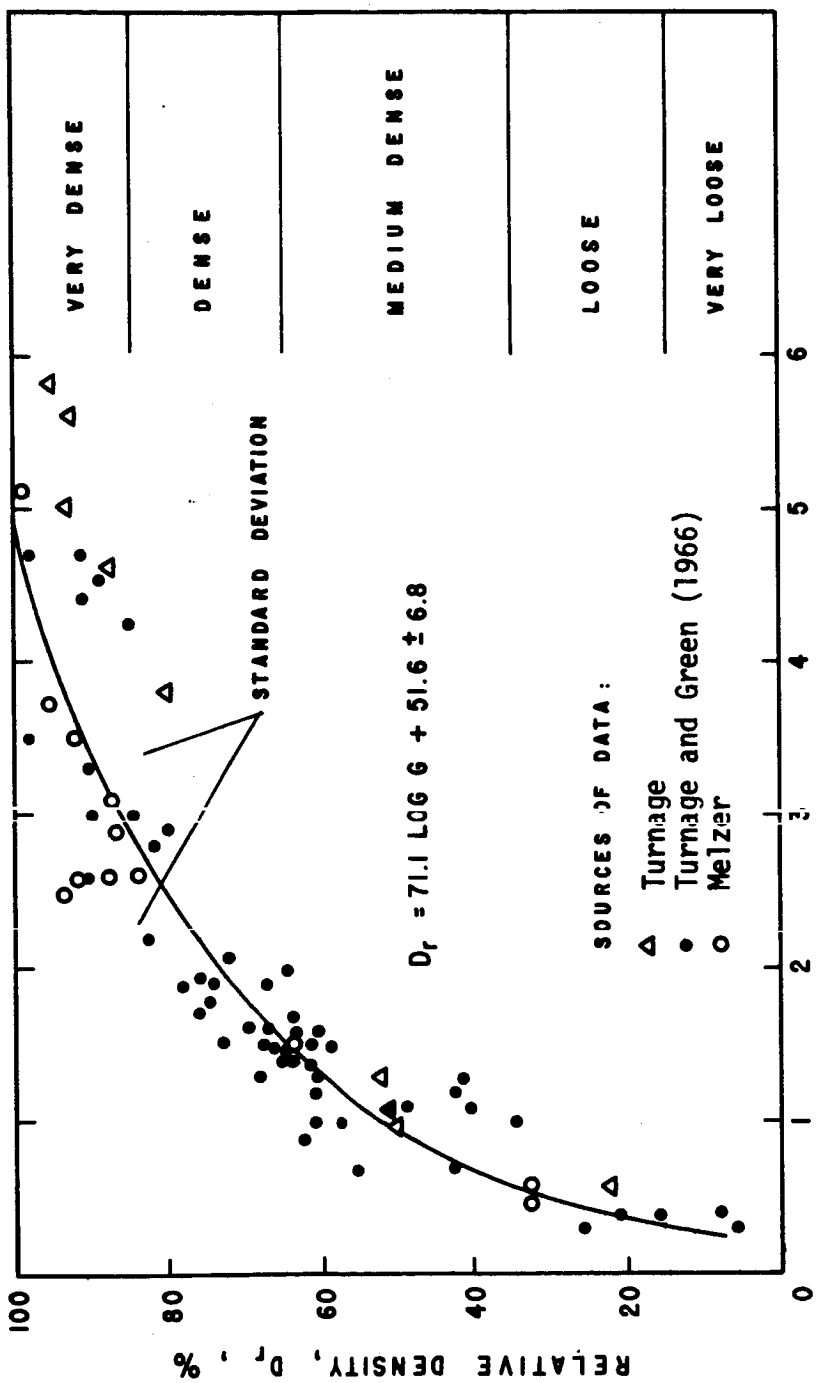

Fig. B-1. Relation between relative density and gradient, G.

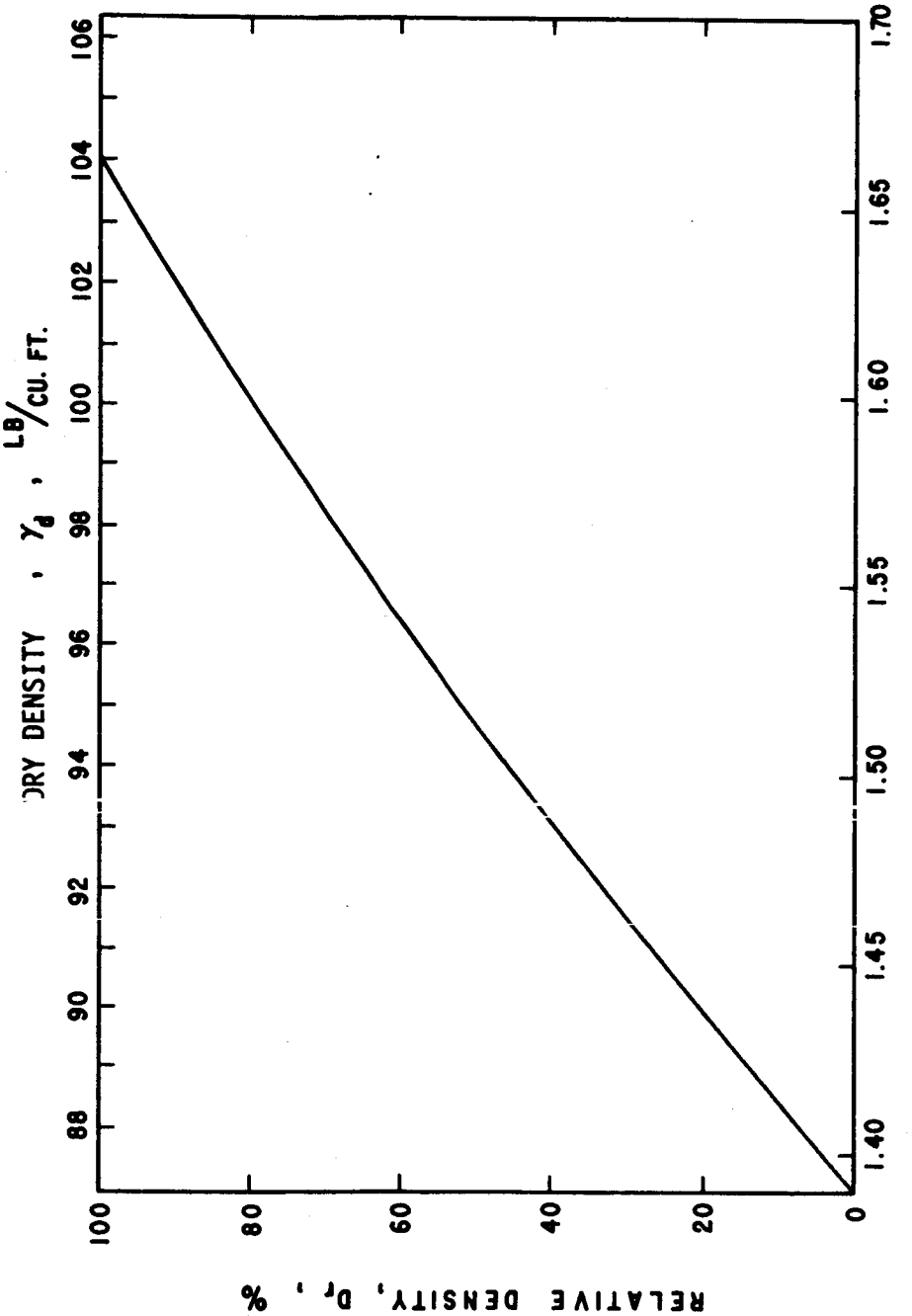

Fig. B-2. Relation between relative density and dry density.

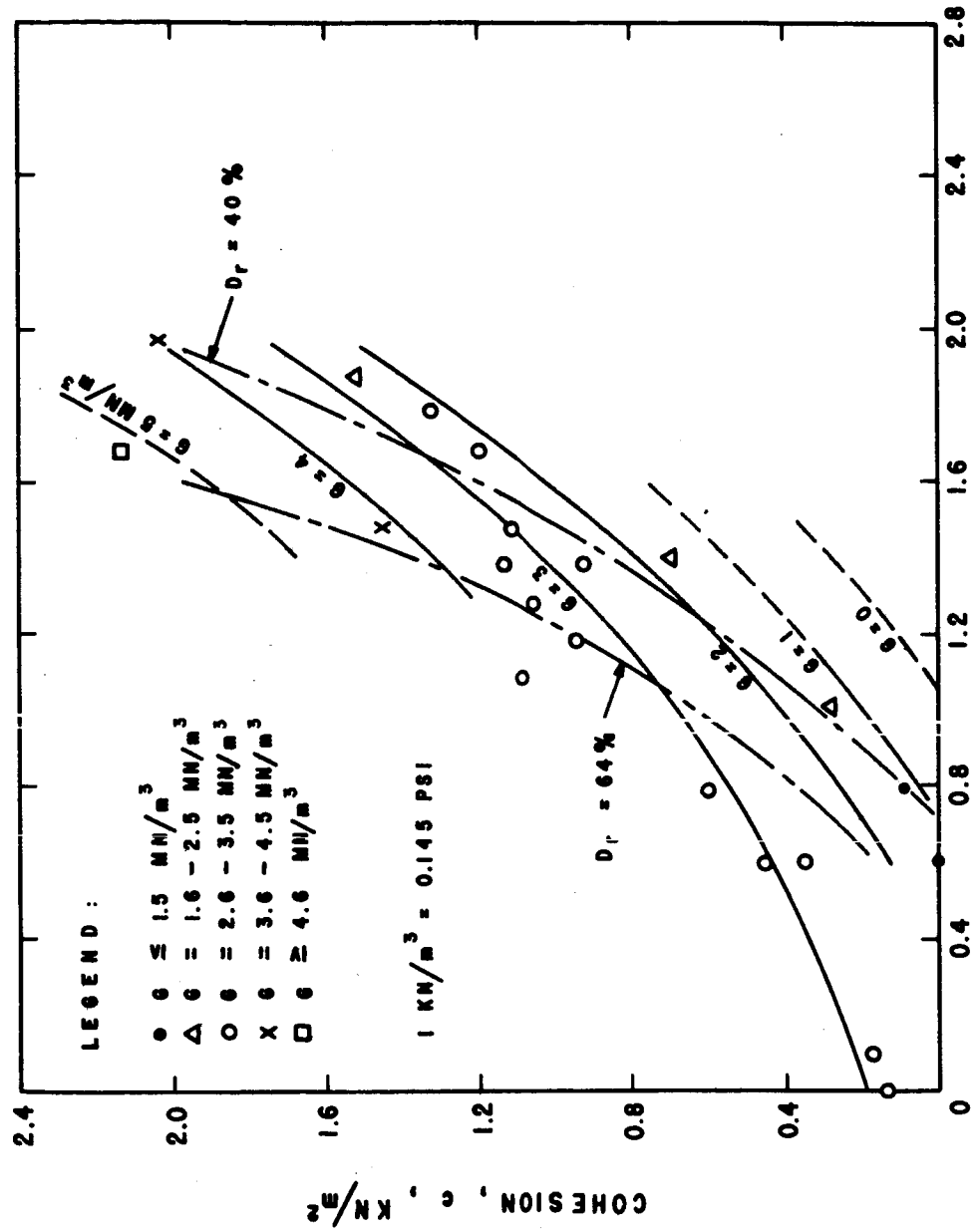

Fig. B-3. Relation between cohesion, c, moisture content, ω, and gradient, G.

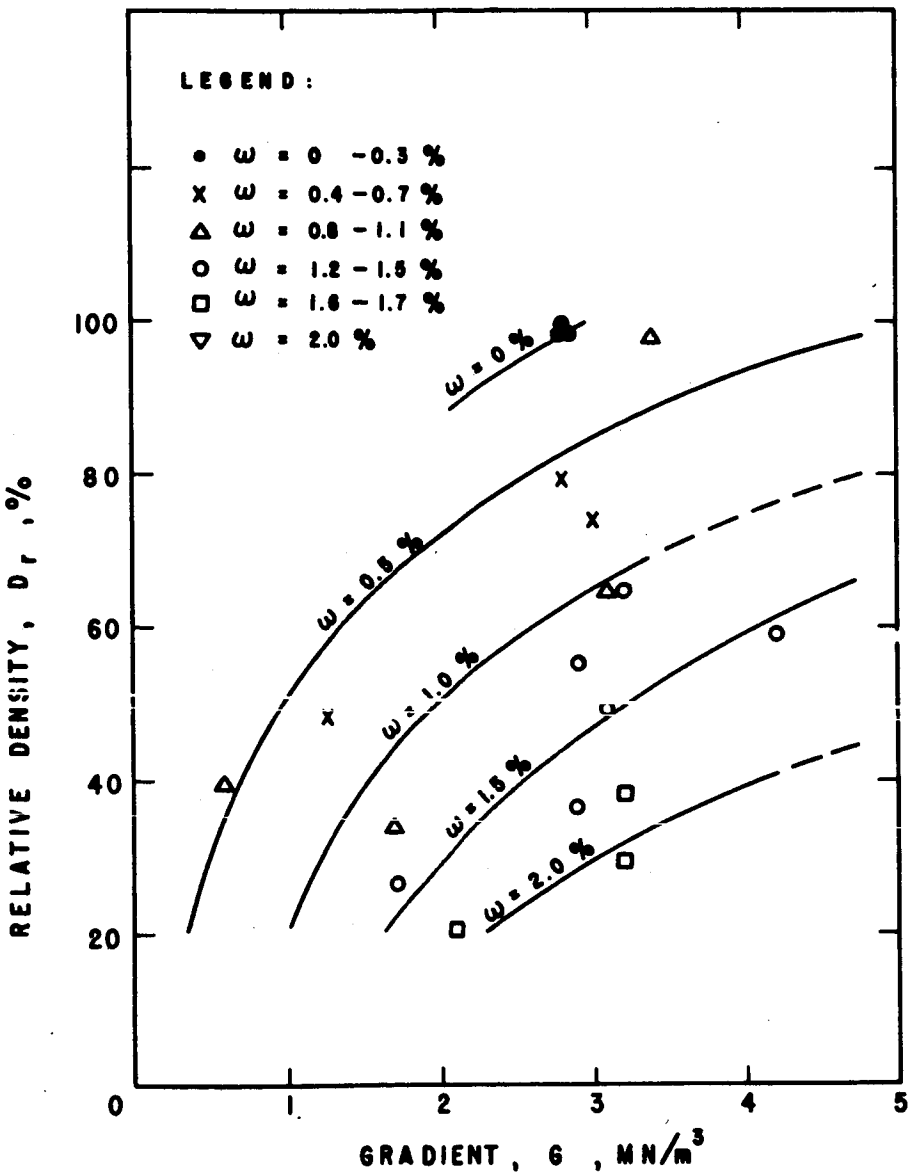

Fig. B-4. Relation between relative density, D_r, gradient, G, and moisture content, ω.

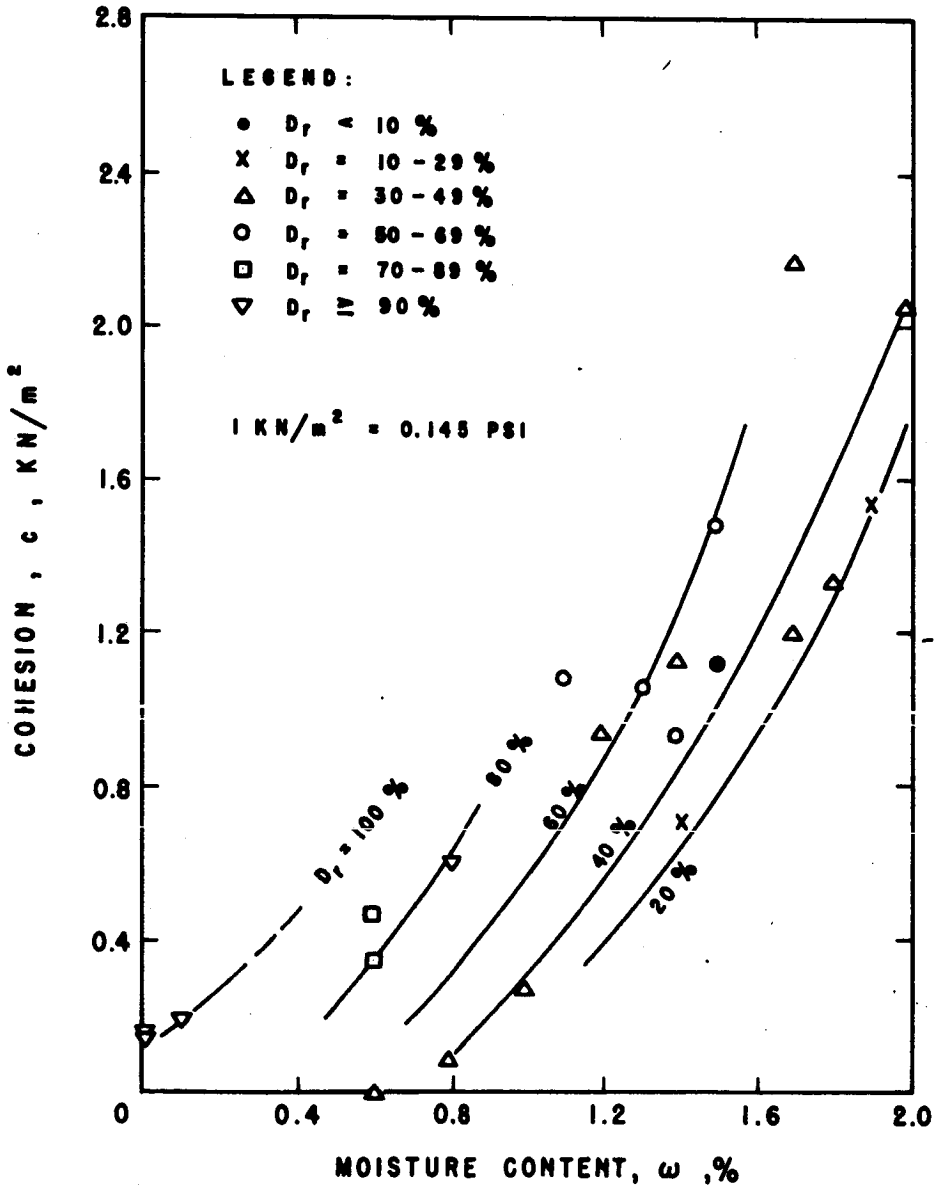

Fig. B-5. Relation between cohesion, c, moisture content, ω, and relative density, D_r.

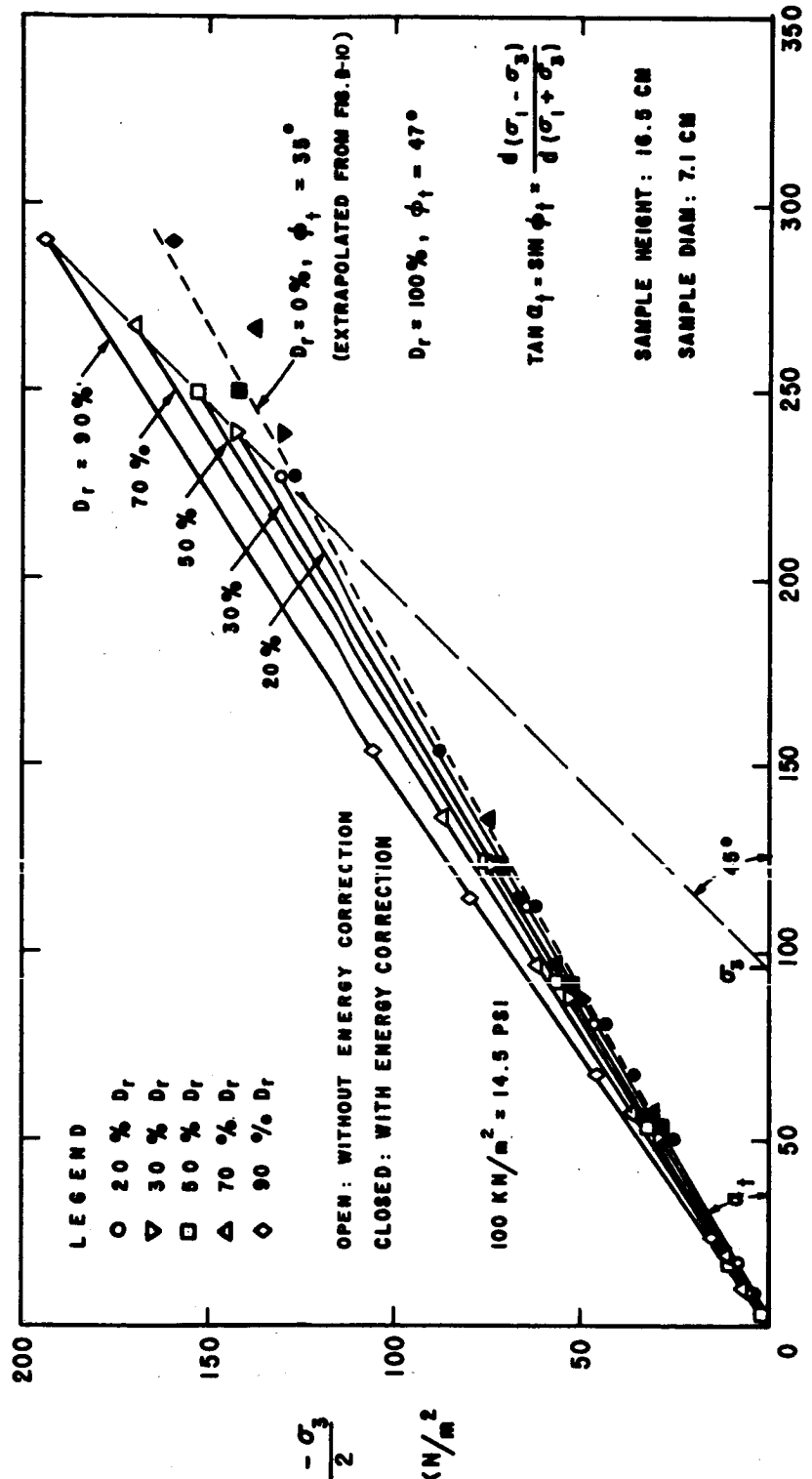

Fig. B-6. Results of vacuum triaxial tests.

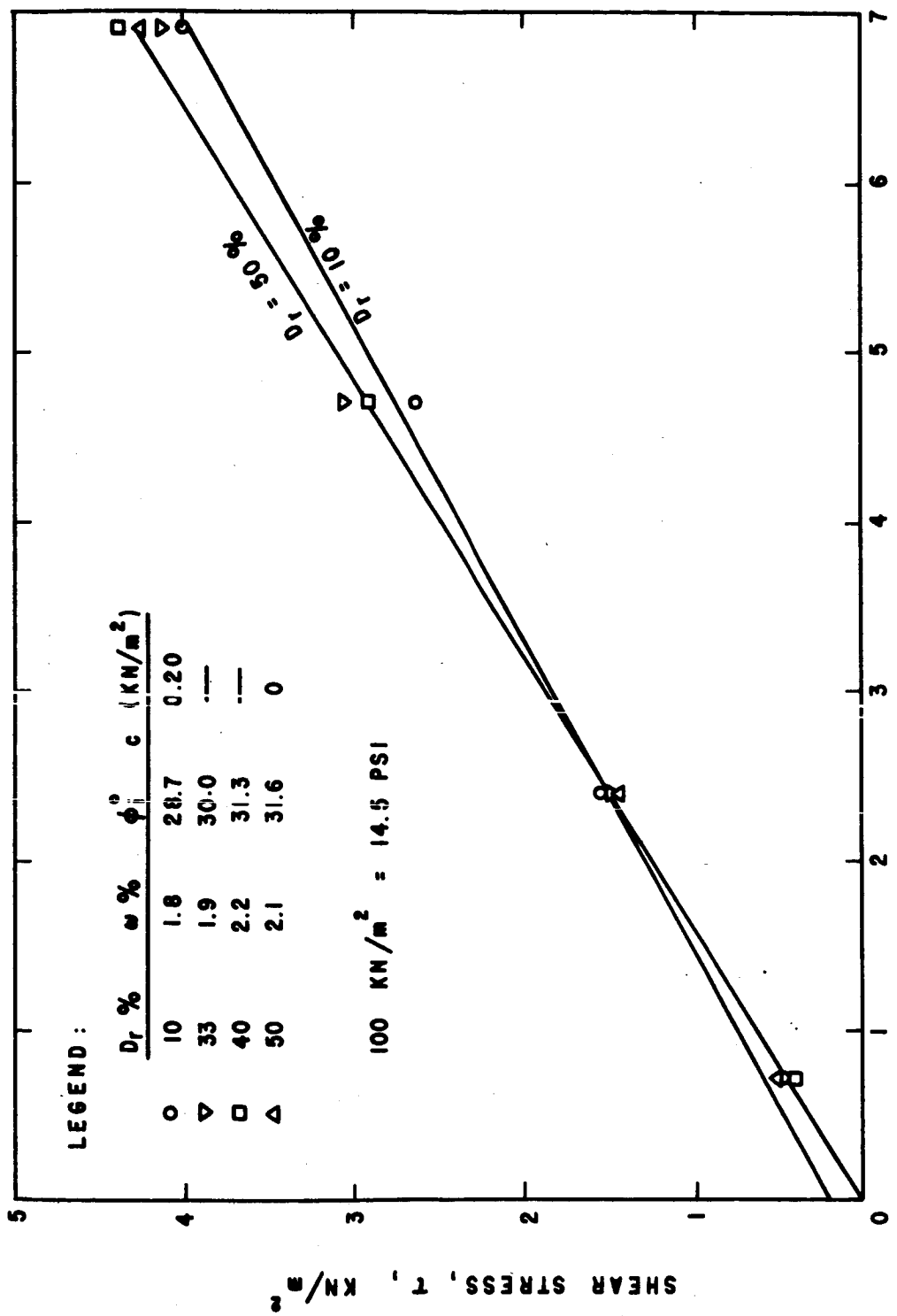

Fig. B-7. Results of in situ shear tests on wet sand.

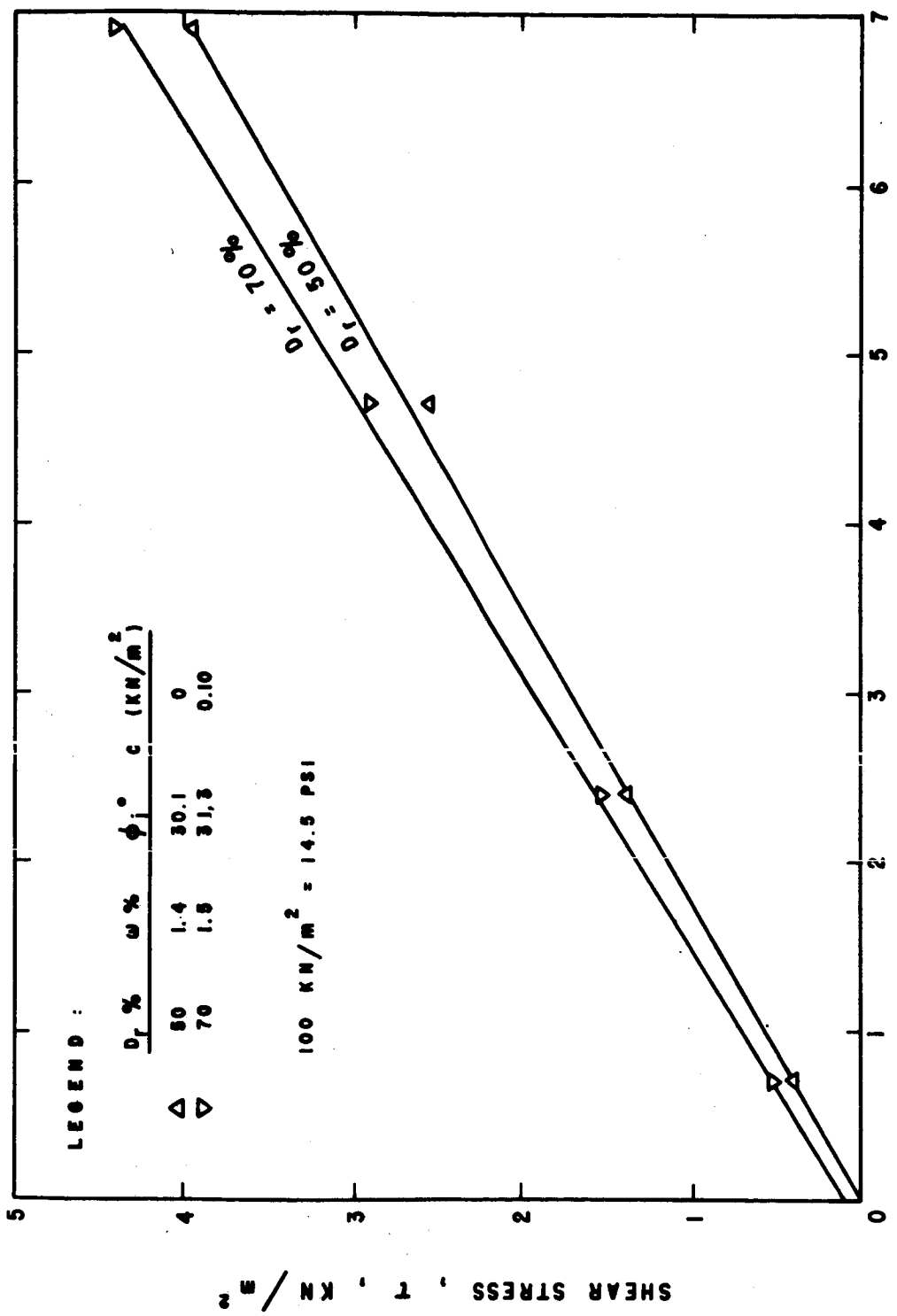

Fig. B-8. Results of in situ shear tests on wet sand.

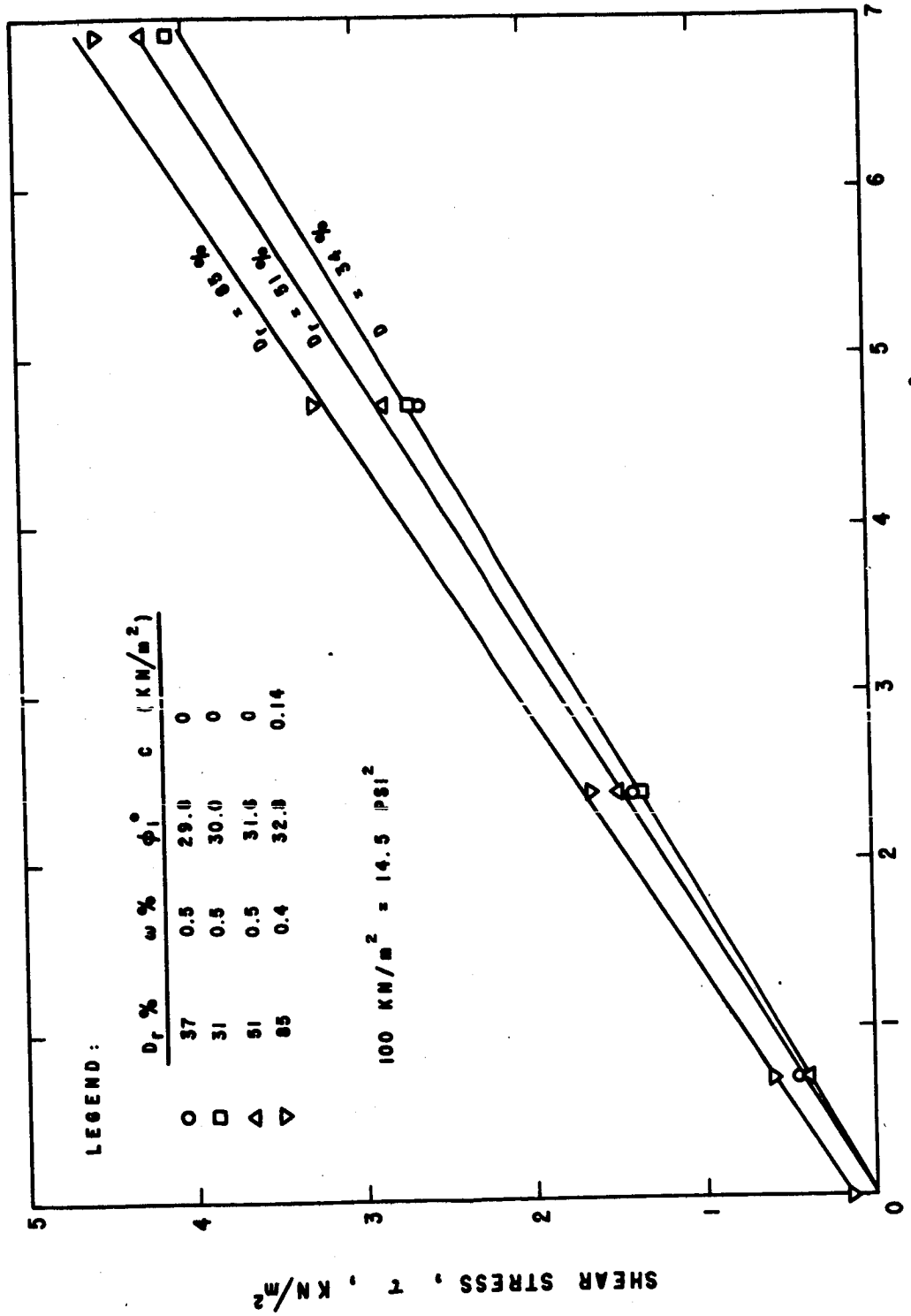

Fig. B-9. Results of in situ shear tests on air-dry sand.

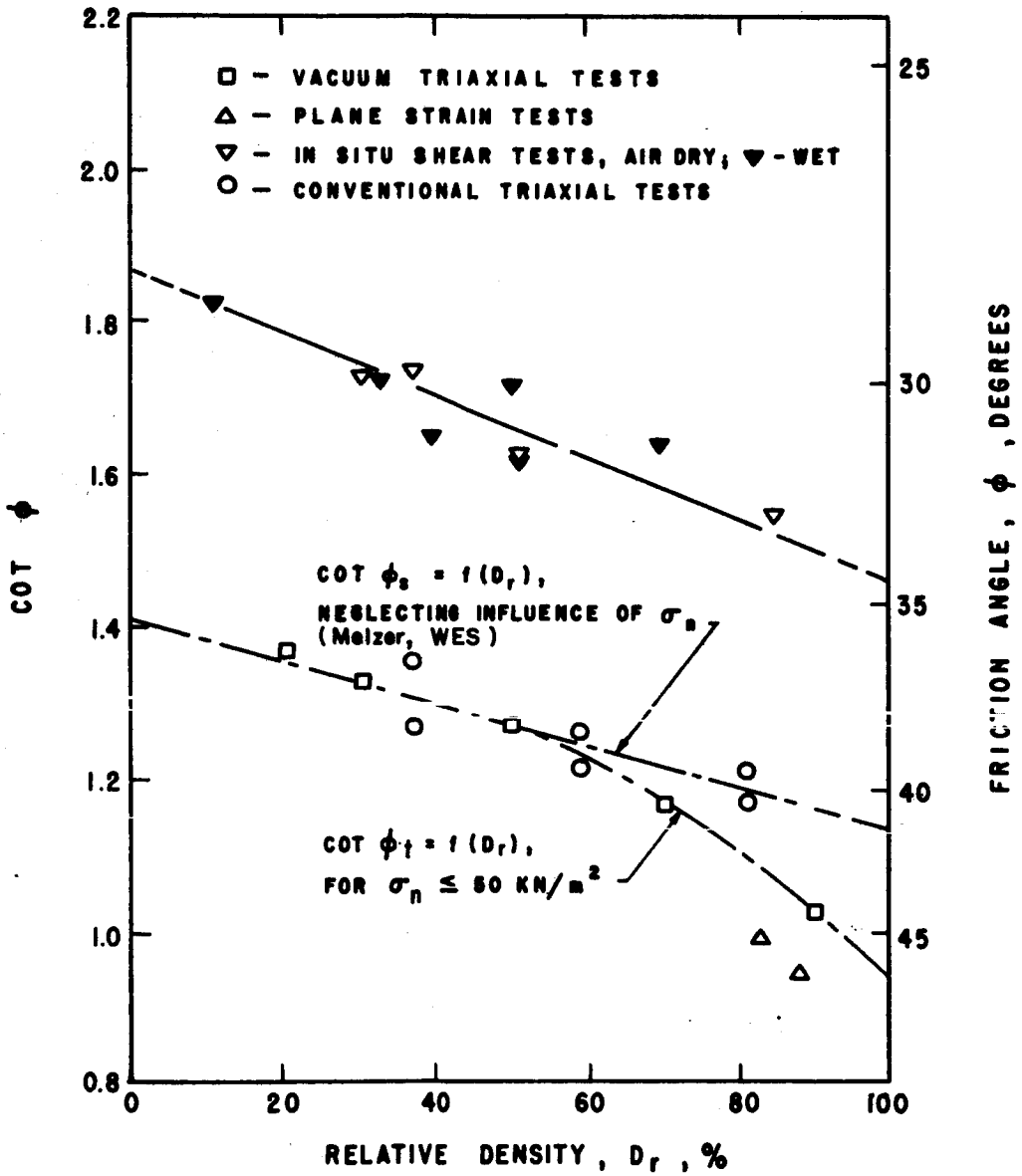

Fig. B-10. Relation between relative density and friction angle.

Appendix C. PRESSURE CELL DATA

This appendix contains the pressure cell data obtained from testing the instrumented spherical wheel at WES. The design of the wheel and the gages, as well as the testing procedure, was described in Chapter 4.

As the wheel rolled through the soil, pressures registered by the gages were automatically recorded on the oscillographs presented in Figures C-1 through C-5. These oscillographs provided the basic data for the pressure contour diagrams presented in Figures 4-7, 4-9, 4-11, 4-13, and 4-15.

In addition, the signals from the gages were fed into a computer, which selected certain points and filtered out the 60-cycle disturbances (small wiggles) shown on the oscillographs. These data are presented in Tables C-1 through C-5.

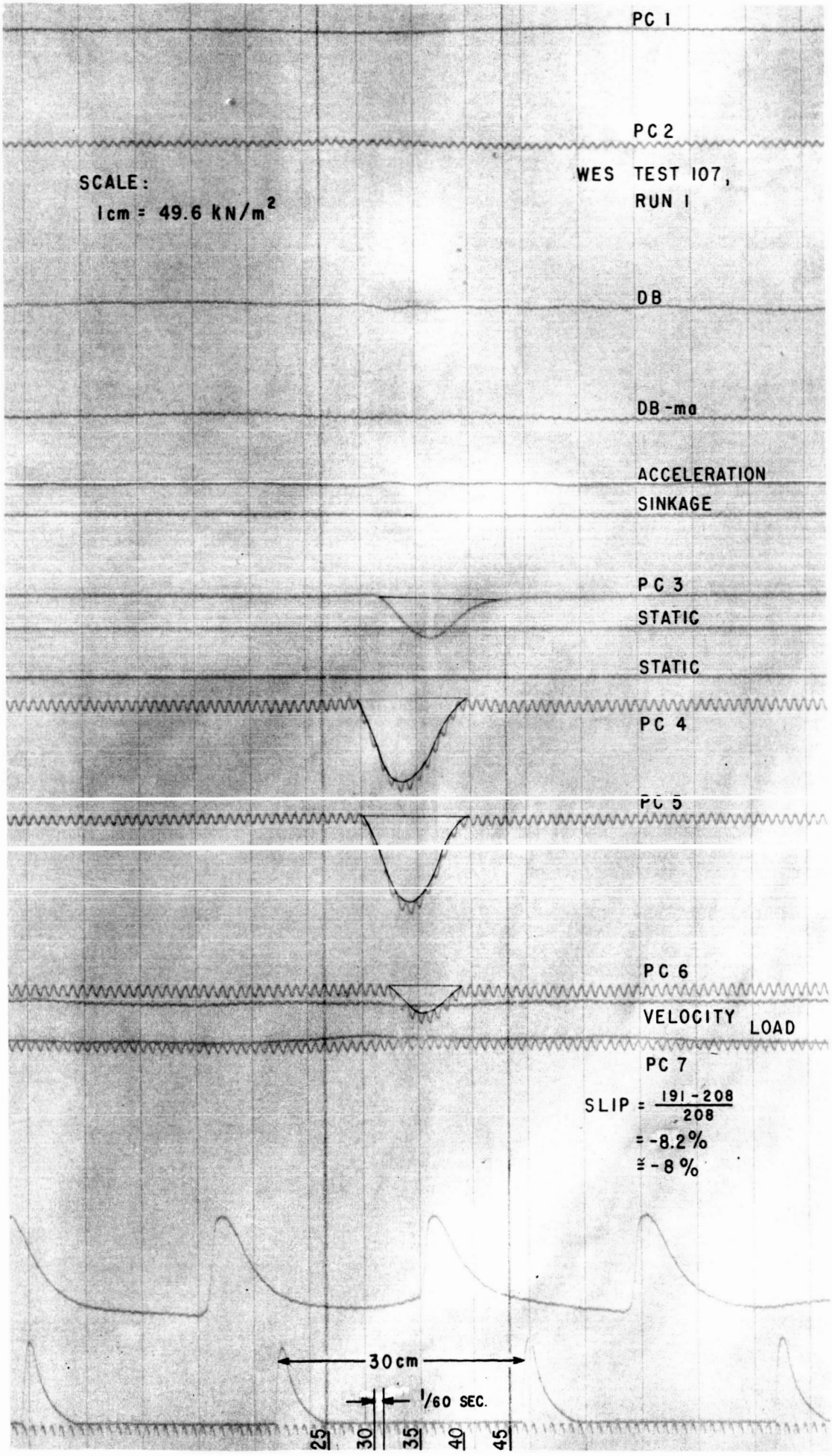

Fig. C-1. Oscillograph, wheel load = 635 newtons.

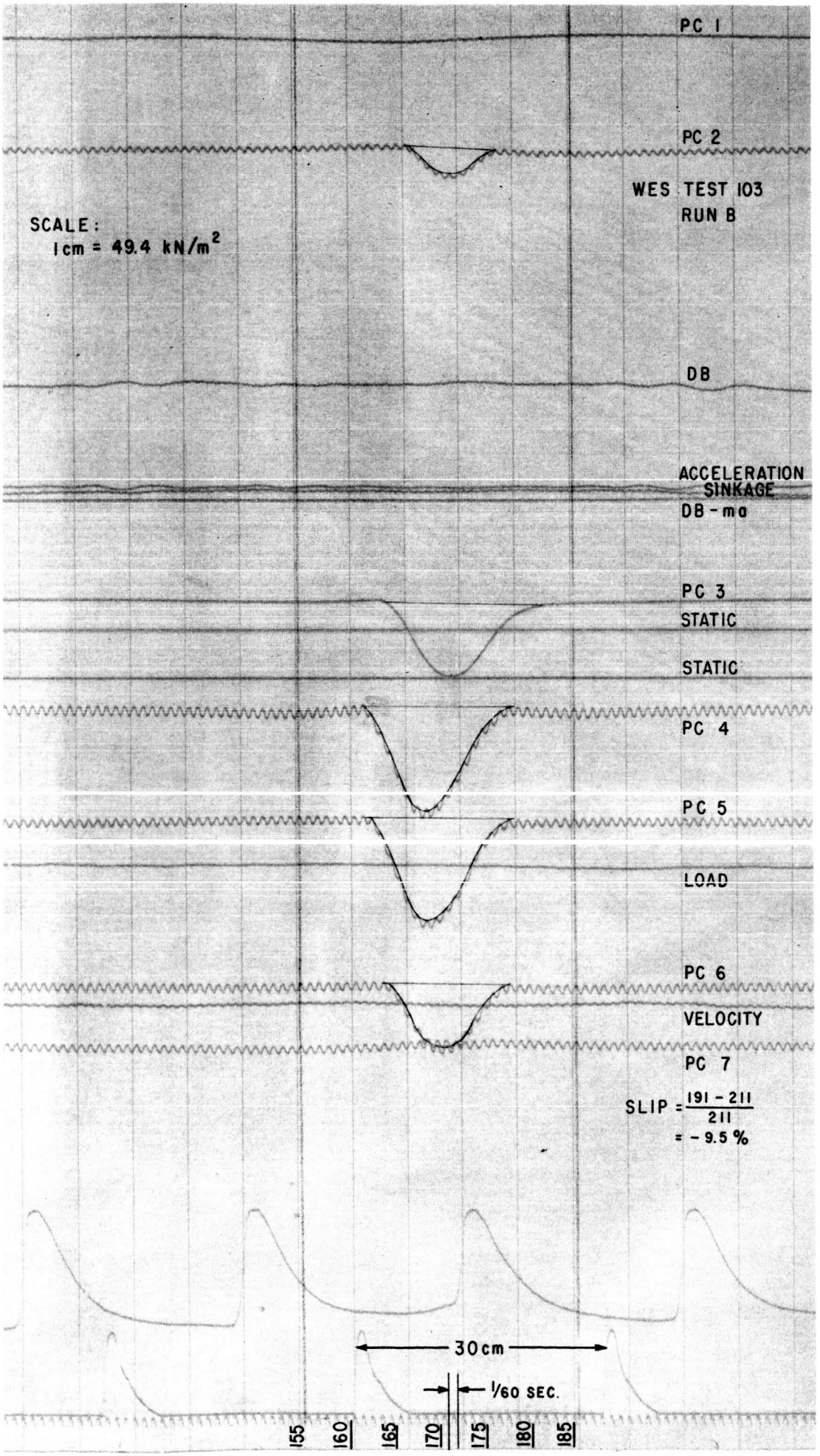

Fig. C-2. Oscillograph, wheel load = 1241 newtons.

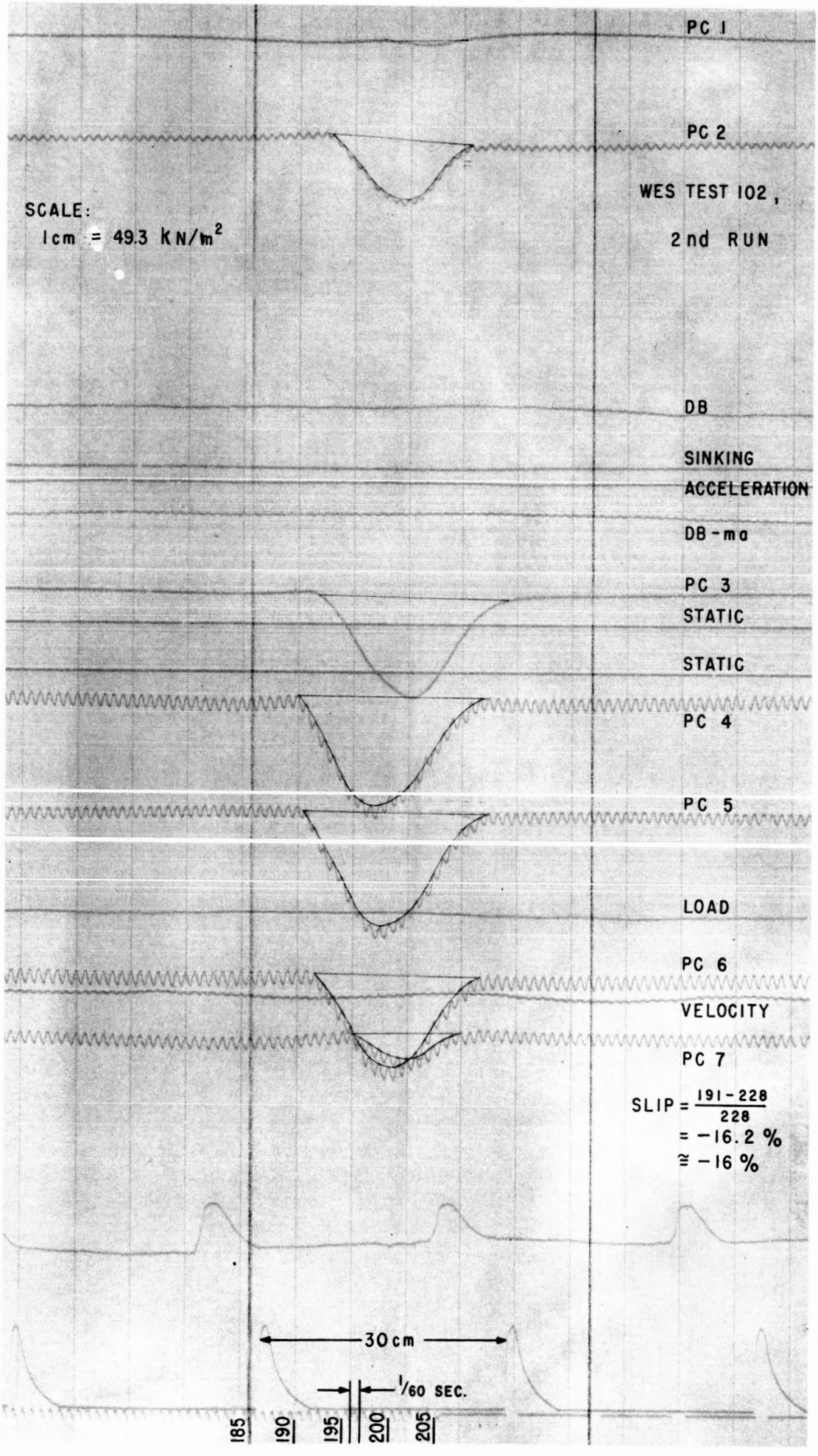

Fig. C-3. Oscillograph, wheel load = 2100 newtons.

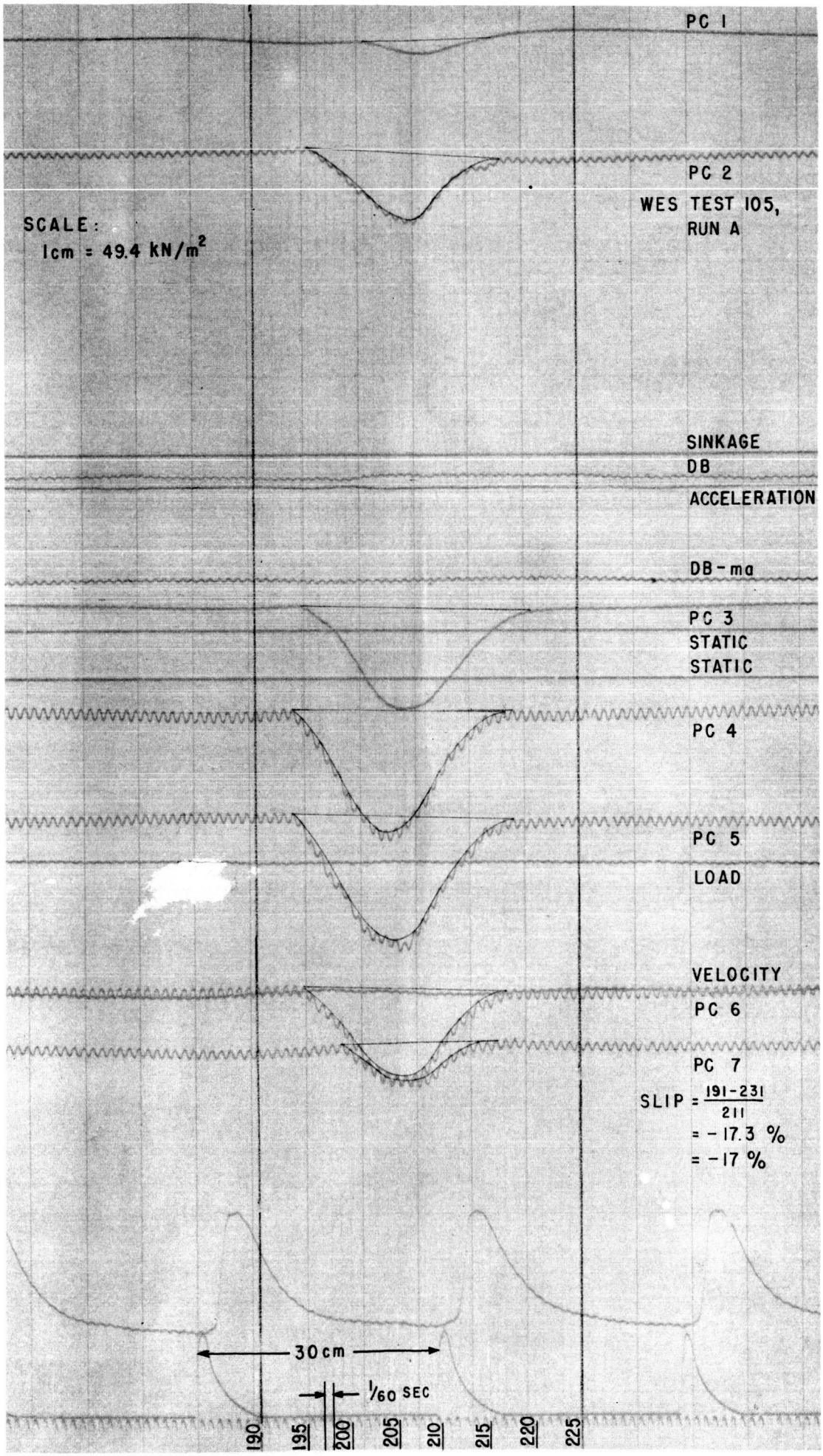

Fig. C-4. Oscillograph, wheel load = 2503 newtons.

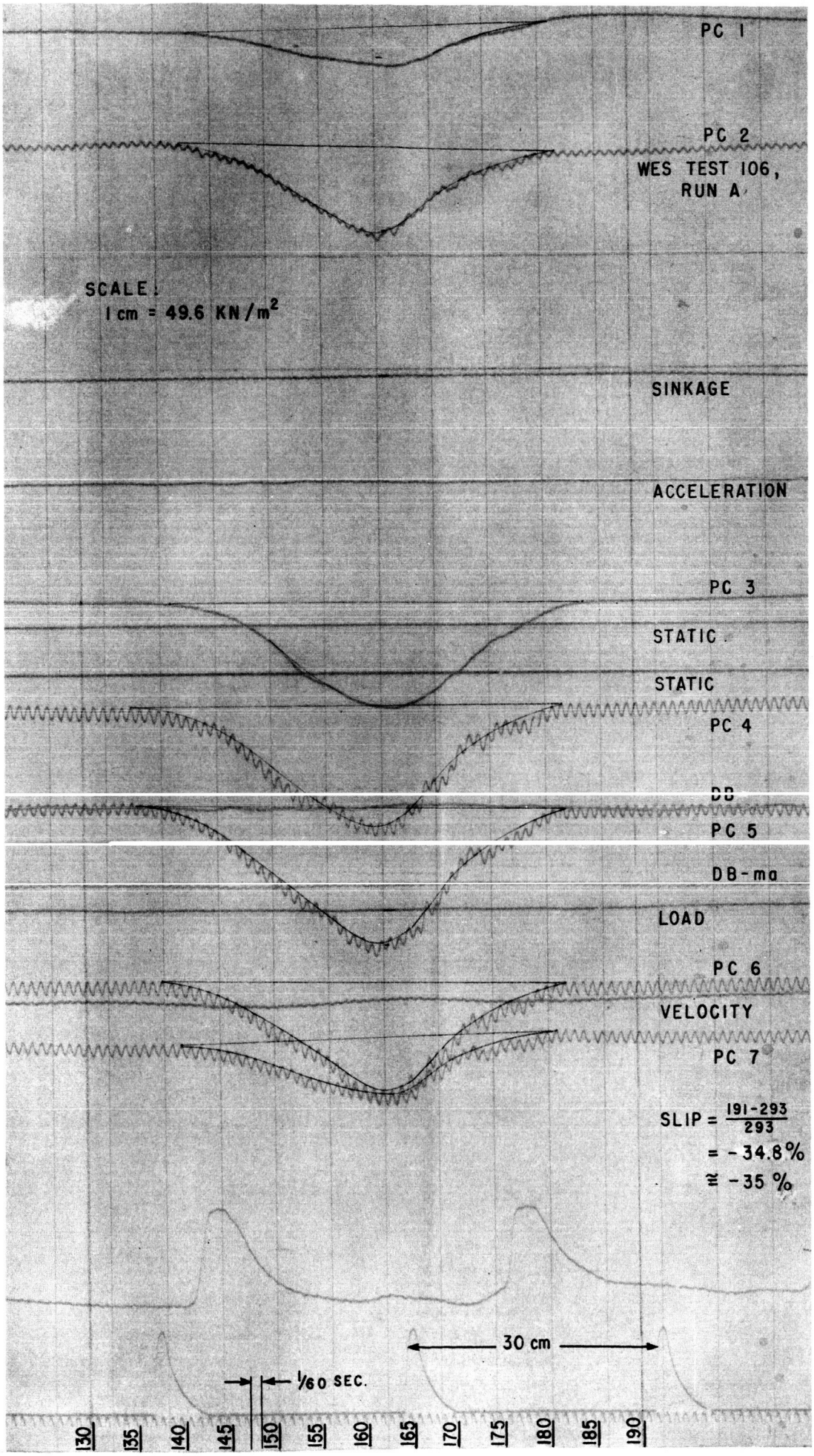

Fig. C-5. Oscillograph, wheel load = 4275 newtons.

Computer-Selected Filtered Data

Table C-1

Wheel Load = 635 newtons

Approximate Averages for Controlled Parameters

DB-ma N	Accel. g	Sinkage cm	Velocity m/sec
78.5	0.011	0.95	0.674

Pressure

	Pressure Cells						
Location	PC 1	PC 2	PC 3	PC 4	PC 5	PC 6	PC 7
125	0.00	0.00	1.05	-.25	-.12	2.22	0.00
	0.00	0.00	.81	.23	-.24	2.43	0.00
	0.00	0.00	.71	4.71	2.29	2.53	0.00
	0.00	0.00	2.69	13.63	8.44	2.53	0.00
	0.00	0.00	7.26	25.62	20.51	2.85	0.00
130	0.00	0.00	14.99	39.73	35.35	4.65	-.21
	-.15	0.00	24.47	52.90	50.19	8.35	-.21
	-.15	0.00	34.78	60.77	63.35	12.79	-.43
	-.15	0.00	41.34	62.54	70.47	17.66	-.54
	-.30	0.00	43.70	58.31	69.02	21.57	-.65
135	-.45	.19	40.75	49.02	60.93	22.63	-.54
	-.60	.38	33.14	37.50	48.63	20.51	-.87
	-.60	.58	23.30	25.04	34.15	15.97	-.87
	-.60	.77	15.10	14.45	20.37	11.31	-1.08
	-.60	.97	8.19	6.70	11.32	6.98	-1.30
140	-.60	.97	3.86	2.11	5.06	4.33	-1.52
	-.75	1.16	2.22	0.00	3.62	3.17	-1.30
	-.75	1.55	1.87	.11	2.65	3.38	-1.08
	-.75	2.13	2.69	.47	3.25	3.38	-.76
	-1.05	2.71	3.04	.70	2.77	4.23	-.43
145	-1.36	2.31	3.39	1.05	2.89	4.33	-.10

Explanation:

Location as identified on lower edge of oscillograph
Db-ma = Drawbar pull corrected for carriage inertia
N = newtons
All pressures are in kilo newtons meter^2 (kN/m^2).

Table C-2

Wheel Load = 1241 newtons

Approximate Averages for Controlled Parameters

DB-ma	Accel	Sinkage	Velocity
N	g	cm	m/sec
205	0.015	1.55	0.670

Pressure

	Pressure Cells						
Location	PC 1	PC 2	PC 3	PC 4	PC 5	PC 6	PC 7
155	1.83	1.84	6.19	6.80	6.57	3.87	6.50
	1.99	1.35	6.30	6.56	5.23	3.22	5.95
	2.60	1.06	6.07	5.72	5.23	2.68	5.51
	2.60	.48	5.34	4.89	4.02	2.25	4.85
	2.60	.29	5.25	4.29	3.77	1.93	4.19
160	2.44	.09	4.79	5.84	4.75	1.93	3.74
	2.60	.09	5.60	11.21	9.74	2.04	3.30
	1.99	.09	10.51	20.64	16.32	3.01	2.86
	1.83	.09	19.62	34.12	30.21	6.45	2.31
	1.22	.09	32.36	50.82	47.03	13.01	1.87
165	1.53	1.26	47.20	67.28	64.57	21.62	1.43
	1.53	3.88	61.69	79.93	78.71	32.59	1.32
	1.22	7.95	72.43	88.04	89.67	43.35	1.10
	1.07	12.81	77.81	90.43	91.62	50.34	1.21
	.91	17.66	78.16	86.61	87.97	54.32	1.10
170	.30	20.96	73.83	78.26	79.44	54.00	1.43
	0.00	21.45	64.95	66.45	67.50	48.94	1.43
	0.00	19.41	53.27	52.61	53.61	41.09	1.32
	0.00	15.53	40.54	39.01	41.18	31.95	.99
	-.15	11.35	28.03	26.96	28.26	22.37	.88
175	-.15	7.47	17.75	17.41	17.42	14.41	.44
	-.30	5.24	11.09	11.21	12.79	9.46	.33
	-.30	4.17	7.36	7.87	9.13	6.34	.33
	-.61	4.27	5.72	6.20	8.28	5.37	.44
	-.91	4.65	5.72	5.96	8.89	5.05	.66
180	-1.07	5.14	5.95	6.20	9.50	5.16	.77
	-1.37	5.33	6.19	6.20	8.65	4.73	.88
	-1.53	5.53	6.19	6.56	9.01	4.62	.99
	-1.53	6.01	6.54	6.68	6.33	4.94	1.21
	-1.53	5.72	6.89	6.80	5.23	5.37	1.65
185	-1.53	5.82	7.00	6.56	5.72	5.37	1.87

Table C-3

Wheel Load = 2100 newtons

Approximate Averages for Controlled Parameters

DB-ma	Accel	Sinkage	Velocity
N	g	cm	m/sec
520	0.014	2.44	0.678

Pressure

Location	Pressure Cells						
	PC 1	PC 2	PC 3	PC 4	PC 5	PC 6	PC 7
185	2.44	-4.68	.95	.96	.99	.21	2.75
	2.60	-5.08	.83	2.89	1.74	.21	2.31
	2.90	-6.05	3.47	8.07	6.11	0.00	1.76
	2.44	-6.23	9.22	16.50	13.98	2.49	1.10
	2.29	-5.88	18.09	28.07	25.47	7.04	.55
190	2.14	-3.29	30.06	43.50	39.33	14.52	.33
	1.99	1.19	46.24	58.56	55.56	24.92	.11
	1.68	8.07	62.17	72.17	70.30	38.58	.66
	1.37	16.55	75.35	83.62	85.03	51.15	2.42
	1.37	25.63	86.37	91.45	95.15	64.15	5.07
195	1.68	33.91	95.47	94.11	102.39	73.58	8.60
	2.29	40.99	100.50	93.99	104.89	79.76	12.57
	3.52	45.98	101.94	91.21	104.52	81.17	16.21
	4.89	48.57	100.74	85.67	98.90	80.84	18.63
	5.51	47.97	94.99	77.12	91.03	74.45	19.30
200	5.20	43.98	84.09	67.72	81.16	65.67	17.75
	4.28	33.91	65.04	51.57	63.31	49.85	14.44
	2.75	23.74	44.92	35.78	44.58	35.43	10.80
	.91	13.36	25.39	21.20	27.59	20.69	7.72
	0.00	4.48	9.46	9.64	13.48	9.21	4.41
205	-1.22	-3.09	-2.39	-.24	1.62	.32	2.09
	-1.68	-4.38	-5.75	-2.04	-.74	-1.19	1.32
	-1.68	-5.08	-5.75	-2.77	-.49	-1.84	.66

Table C-4

Wheel Load = 2503 newtons

Approximate Averages for Controlled Parameters

DB-ma N	Accel g	Sinkage cm	Velocity m/sec
723	0.0	3.21	0.687

Pressure

Location	Pressure Cells						
	PC 1	PC 2	PC 3	PC 4	PC 5	PC 6	PC 7
190	2.25	1.94	7.50	2.32	-4.89	0.00	5.97
	2.25	1.94	7.50	2.32	-4.89	0.00	5.97
	3.76	1.94	7.50	2.32	-4.89	0.00	4.89
	3.76	1.45	6.92	2.32	-4.89	0.00	4.89
	3.76	0.00	6.92	2.32	-4.28	0.00	4.89
195	3.76	0.00	6.34	7.54	0.00	0.00	3.80
	[illegible]	[illegible]	[illegible]	[illegible]	[illegible]	4.74	3.80
	4.51	2.42	17.88	25.55	26.93	13.18	2.71
	4.51	10.67	23.08	42.97	44.69	21.10	2.71
	4.51	14.56	32.89	54.58	54.48	27.43	1.08
200	4.51	21.84	43.85	74.33	65.50	38.51	3.26
	4.51	33.00	56.54	85.36	85.09	49.59	9.78
	5.26	36.88	70.97	94.07	94.27	63.30	13.04
	5.26	42.71	83.09	106.27	99.17	73.33	20.65
	7.52	53.87	91.74	109.17	104.07	77.02	28.26
205	9.78	58.72	95.78	108.01	108.97	82.83	30.43
	[illegible]	61.15	96.93	102.78	111.41	81.77	35.32
	[illegible]	63.58	95.78	92.33	102.23	81.77	34.78
	[illegible]	59.70	92.90	84.20	89.38	71.22	32.06
	[illegible]	52.41	89.43	69.10	75.91	63.30	28.26
210	13.54	44.16	79.62	56.91	61.83	48.01	17.93
	11.28	33.97	69.91	41.81	52.03	38.51	10.86
	9.02	25.72	61.16	33.10	39.79	28.48	5.97
	6.01	19.41	50.77	24.97	32.44	23.21	2.71
	3.76	16.98	41.54	17.42	18.36	14.77	0.00
215	2.25	16.98	34.62	9.87	9.79	13.18	0.00
	0.00	14.56	27.11	7.54	7.34	8.44	0.00
	0.00	10.67	20.77	5.22	3.67	5.80	-2.17
	-2.25	9.70	16.15	5.22	0.00	4.74	-2.17
	-3.76	10.67	13.27	5.80	0.00	4.74	-1.08
220	-3.76	9.70	12.11	5.80	0.00	4.74	0.00
	-5.26	9.70	10.96	5.80	0.00	4.74	0.00
	-5.26	9.70	9.80	5.80	0.00	4.74	0.00
	-6.01	9.70	9.70	5.80	0.00	4.74	0.00
	-5.01	9.70	8.65	3.48	0.00	4.74	0.00
225	-5.26	9.70	8.65	5.22	0.00	3.69	0.00

Table C-5

Wheel Load = 4275 newtons

Approximate Averages for Controlled Parameters

DB-ma	Accel	Sinkage	Velocity
N	g	cm	m/sec
1850	0.025	5.72	0.665

Pressure

	Pressure Cells						
Location	PC-1	PC 2	PC 3	PC 4	PC 5	PC 6	PC 7
130	-6.77	1.05	10.45	8.97	-1.43	4.42	6.83
	-6.47	1.15	10.10	9.31	-2.15	4.42	6.83
	-6.01	1.05	9.77	9.43	-1.91	4.00	7.04
	-5.71	.76	10.22	9.77	-2.63	4.10	7.04
	-5.41	.67	10.22	10.35	-1.67	4.21	7.04
	-5.11	.76	10.56	10.71	-1.19	4.63	6.83
	-5.11	.76	11.36	11.61	-.71	5.26	6.93
	-5.11	1.05	11.94	12.38	-.23	6.00	7.26
	-4.66	2.01	12.86	14.26	1.67	6.73	7.69
	-4.06	3.06	14.53	16.22	3.95	8.21	8.34
140	-3.00	4.60	16.76	18.29	5.75	9.68	8.99
	-1.95	6.42	18.93	20.13	9.82	11.68	9.97
	-1.05	8.63	22.16	22.66	14.37	14.42	11.06
	-.30	10.83	25.60	26.11	20.00	18.00	12.68
	.75	13.04	29.85	30.48	25.99	21.15	14.20
	1.65	15.34	35.37	35.89	32.58	25.36	16.37
	2.85	18.02	41.22	43.13	39.05	30.52	18.54
	4.21	21.09	47.20	50.96	45.76	35.68	21.36
	6.77	25.79	56.34	59.58	53.43	41.47	24.07
	9.02	31.16	66.60	67.52	61.82	47.78	27.32
150	11.41	37.21	74.64	74.77	69.60	53.68	30.57
	13.54	43.06	82.22	81.33	75.95	58.73	34.15
	15.34	49.29	88.88	85.35	82.42	64.10	37.40

Table C-5. (Cont'd)

Location	Pressure Cells						
	PC 1	PC 2	PC 3	PC 4	PC 5	PC 6	PC 7
	16.10	53.99	92.21	88.46	88.17	69.05	40.22
	17.45	58.59	95.08	92.02	92.97	74.31	42.18
	18.66	63.10	98.53	95.82	98.00	80.63	43.58
	19.56	67.61	101.97	99.04	104.23	86.42	45.21
	20.31	71.16	104.35	103.64	110.34	92.00	46.73
	22.72	75.09	105.99	106.40	113.33	96.52	47.81
	23.32	77.29	107.03	108.13	114.65	99.36	49.44
160	23.47	78.54	105.99	108.13	115.97	99.68	50.52
	23.17	77.77	103.01	105.71	114.65	98.21	50.63
	22.12	75.28	100.02	102.61	111.42	96.42	48.46
	19.11	70.58	95.31	95.59	105.55	90.31	44.67
	16.10	65.02	89.46	88.46	99.56	83.78	39.90
	12.33	58.02	82.34	81.33	90.45	77.47	35.13
	8.72	51.50	76.25	74.08	80.03	70.52	29.06
	6.16	46.32	69.59	63.38	67.57	60.73	23.63
	3.16	41.04	61.67	55.79	57.50	53.36	19.51
	1.20	36.15	53.97	48.31	48.40	47.15	16.48
170	-1.05	32.99	46.74	40.83	41.09	40.84	13.33
	-2.40	29.53	41.34	34.16	36.30	35.47	11.27
	-4.06	26.46	36.06	30.59	32.34	31.68	9.54
	-5.56	24.35	32.50	28.13	29.11	30.10	8.67
	-6.77	23.01	28.36	25.65	25.51	26.73	7.15
	-7.97	20.23	25.49	23.00	21.20	22.63	5.31
	-9.78	17.70	20.78	20.36	16.05	19.36	3.57
	-11.73	16.39	16.53	17.43	11.38	16.52	2.49
	-13.54	14.09	13.66	14.72	7.54	13.05	1.30
	-15.34	12.46	11.36	11.61	3.83	10.73	.21
180	-16.25	11.79	10.10	9.77	2.27	9.78	0.00
	-16.25	11.02	9.27	9.43	1.07	9.26	0.00
	-17.00	10.74	9.53	9.20	1.07	8.94	0.00
	-17.45	10.74	9.27	9.20	1.19	8.63	0.00
	-17.75	10.74	10.22	9.20	1.67	8.52	0.00
	-17.75	10.35	10.45	9.09	1.07	8.42	0.00
	-17.60	10.35	10.45	8.28	1.19	8.10	0.00
	-17.60	10.16	10.79	8.05	1.19	8.10	0.00
	-17.15	9.37	10.68	7.82	.95	7.99	0.00
	-17.30	9.78	10.22	7.47	.23	7.89	0.00
190	-17.30	9.68	10.22	7.24	-.23	8.00	0.00

Appendix D. TRACK DATA

Table D-1. Track data.

Car	Slope α°	Sphere	Rolled	$\frac{\gamma_r}{\gamma_s}$	w (cm)	$\frac{w}{D}$ -	dist. to x-sect (cm)	V_r (cc/cm +)	V_w (cc/cm -)	ΔV (cc/cm)	V_t (cc/cm)	$\frac{\Delta V}{V_t}$
1	10	all	no									
γ_s =	15	A	no	2.500								
1.472		B	no	1.450								
		C	short	1.170								
		D	yes	0.713	6.60	0.515	30	1.76	0.88	+0.88	2.64	+0.333
		E	yes	0.353								
		1a	no	1.260								
		3a	no	1.200								
		4	no	1.220								
γ_s =	20	A	no	2.490								
1.485		B	no	1.445								
		C	yes	1.165	8.85	0.710	15	3.28	3.38	-0.10	6.66	-0.015
		D	yes	0.707	5.60	0.453	30	1.10	0.64	+0.46	1.74	+0.264
		1a	yes	1.255	5.20	0.726	30	1.47	1.05	+0.42	2.52	+0.167
		3a	no	1.190								
		4	no	1.210								
	25	A	no									
		B	yes		11.80	0.970	30	3.92	5.14	-1.22	9.06	-0.135
		C	yes		10.50	0.875	30	2.45	3.14	-0.69	5.59	-0123
		D	yes		8.70	0.720	30	1.40	1.64	-0.24	3.04	-0.079

Table D-1. Track data.

Car	Slope α°	Sphere	Rolled	$\frac{\gamma_r}{\gamma_s}$	w (cm)	$\frac{r}{D}$	dist. to x-sect (cm)	V_r (cc/cm +)	V_w (cc/cm -)	ΔV (cc/cm)	V_t (cc/cm)	$\frac{\Delta V}{V_t}$
1 (Cont'd)	25	1a	yes		7.20	1.010	30	1.32	1.57	-0.25	2.89	-0.086
		3a	yes		16.90	0.970	30	8.70	11.00	-2.30	19.70	-0.117
		4	short		25.00	0.985	30	17.40	31.40	-14.00	48.80	-0.287
2	10	E	no									
γ_s =	15	E	yes	0.358	6.40	0.633	30	0.32	1.42	-1.10	1.74	-0.633
1.453		D	no									
	20	A,B,1a	no									
		E	yes	0.358	6.80	0.666	30	0.95	1.15	-0.20	2.10	-0.095
	25	C,1a,3a,4	no									
		E	yes	0.358	7.60	0.632	30	0.98	1.08	-0.10	2.06	-0.049
		D	yes	0.722	9.90	0.820	30	2.70	2.86	-0.16	5.56	-0.029
	30	A	no									
		all other	yes									
3	10	A,B,C	no									
γ_s =		D	yes	0.650	4.40	0.864	30	0.47	0.37	+0.10	0.84	+0.119
1.618		E	yes	0.320	4.10	0.840	30	0.29	0.10	+0.19	0.39	+0.487
		1a,3a,4	no									
	15	A	no	2.28								

Table D-1. Track data.

Car	Slope α°	Sphere	Rolled	$\frac{\gamma_r}{\gamma_s}$	w (cm)	$\frac{w}{D}$	dist. to x-sect (cm)	V_r $\left(\frac{cc/cm}{+}\right)$	V_w $\left(\frac{cc/cm}{-}\right)$	ΔV cc/cm	V_t cc/cm	$\frac{\Delta V}{V_t}$
3 (Cont'd)	15	B	yes	1.32	6.05	0.500	45	1.54	0.59	+0.95	2.13	+0.446
		C	yes	1.07	5.15	0.425	45	0.75	0.37	+0.38	1.12	+0.339
		D	yes	0.65	4.50	0.372	45	0.43	0.18	+0.25	0.61	+0.410
		E	yes	0.322	3.50	0.290	45	0.17	0.20	-0.03	0.37	-0.081
		1a	yes	1.15	3.30	0.461	45	0.42	0.07	+0.35	0.49	+0.715
		3a	yes	1.09	7.50	0.431	45	2.41	0.91	+1.50	3.32	+0.451
		4	yes	1.11	11.00	0.435	45	5.70	1.81	+3.89	7.51	+0.518
	20	A	yes		8.30	0.687	45	3.78	1.05	+2.73	4.83	+0.565
		B	yes		5.80	0.480	45	1.32	0.34	+0.98	1.66	+0.590
		C	yes		5.00	0.414	45	0.81	0.27	+0.54	1.08	+0.500
		D	yes		4.30	0.356	45	0.40	0.16	+0.24	0.56	+0.429
		E	yes		3.35	0.277	45	0.25	0.15	+0.10	0.40	+0.250
		1a	yes		3.30	0.461	45	0.39	0.10	+0.29	0.49	+0.590
		3a	yes		7.20	0.414	45	2.19	0.59	+1.60	2.78	+0.575
		4	yes		11.40	0.450	30	8.33	1.71	+6.62	10.04	+0.657
	25	A	yes		8.50	0.704	60	2.87	0.56	+2.31	3.43	+0.672
		C	yes		4.85	0.402	60	0.54	0.22	+0.32	0.76	+0.422
		E	yes		4.65	0.385	60	0.28	0.14	+0.14	0.42	+0.333

Table D-1. Track data.

Car	Slope α°	Sphere	Rolled	$\frac{\gamma_r}{\gamma_s}$	w (cm)	$\frac{w}{D}$	dist. to x-sect (cm)	V_r (cc/cm +)	V_w cc/cm -	ΔV (cc/cm)	V_t (cc/cm)	$\frac{\Delta V}{V_t}$
4	10	A	yes	2.51	4.40	0.3 4	45	0.62	0.22	+0.40	0.84	+0.477
γ_s =		B	yes	1.46	3.65	0.3 1	45	0.42	0.07	+0.35	0.49	+0.714
1.473		D	yes	0.71	2.26	0.1 7	45	0.05	0.03	+0.02	0.08	+0.250
		E	yes	0.35	1.35	0.1 3	45	0.00	0.04	-0.04	0.04	-1.000
		1a	yes	1.26	1.15	0.1 1	45	0.00	0.03	-0.03	0.03	-1.000
		3a	yes	1.20	5.47	0.3 4	45	0.40	0.39	+0.01	0.79	+0.013
		4	yes	1.22	9.20	0.3 3	45	1.96	1.47	+0.49	3.43	+0.143
	20	A	yes		5.39	0.4 6	45	0.54	0.89	-0.35	1.43	-0.245
		C	yes	1.17	3.57	0.2 8	45	0.12	0.23	-0.11	0.35	-0.314
		D	yes		2.60	0.2 5	45	0.02	0.15	-0.13	0.17	-0.765
		E	yes		2.15	0.1 9	45	0.00	0.14	-0.14	0.14	-1.000
		1a	yes		1.81	0.2 3	45	0.02	0.12	-0.10	0.14	-0.714
		3a	yes		5.74	0.3 0	45	0.41	0.61	-0.20	1.02	-0.196
		4	yes		10.20	0.4 3	45	3.30	1.82	+1.48	5.12	+0.289
	25	A	yes		5.55	0.4 9	45	1.51	0.91	+0.60	2.42	+0.248
		B	yes		4.51	0.3 1	45	0.49	0.29	+0.20	0.78	+0.256
		C	yes		3.92	0.3 7	45	0.58	0.51	+0.07	1.09	+0.064
		E	yes		1.77	0.1 7	45	0.00	0.15	-0.15	0.15	-1.000
		1a	yes		1.53	0.2 3	45	0.07	0.05	+0.02	0.12	+0.167
		3a	yes		6.20	0.3 6	45	1.27	0.49	+0.78	1.76	+0.443

Table D-1. Track data.

Car	Slope α°	Sphere	Rolled	$\frac{\gamma_r}{\gamma_s}$	w (cm)	$\frac{w}{l}$	dist. to x-sect (cm)	V_r (cc/cm +)	V_w (cc/cm -)	ΔV (cc/cm)	V_t (cc/cm)	$\frac{\Delta V}{V_t}$
4 (Cont'd)	25	4	yes		11.50	0.454	45	4.63	1.82	+2.81	6.45	+0.435
	35	A	yes		5.65	0.467	45	2.39	0.43	+1.96	2.82	+0.695
		B	yes		4.18	0.344	45	0.23	0.54	-0.31	0.77	-0.403
		C	yes		3.89	0.324	45	0.56	0.43	+0.13	0.99	+0.132
		E	yes		1.77	0.147	45	0.09	0.31	-0.22	0.40	-0.550
		1a	yes		1.73	0.142	45					
		3a	yes		6.07	0. 49	45	1.02	0.37	+0.65	1.39	+0.468
		4	yes		10.80	0. 27	45	4.78	1.59	+3.19	6.37	+0.500
5	10	A,B,C,D	no									
		E	short		4.80	0. 98	30	0.00	2.41	-2.41	2.41	-1.000
γ_s = 1.245		1a,3a,4	no									
	20	A,B	no									
		C	no		7.85	0. 50	30	0.10	9.36	-9.26	9.46	-0.980
		D	yes	0.84	6.20	0. 14	30	0.00	6.36	-6.36	6.36	-1.000
		E	yes		4.55	0. 77	30	0.00	2.55	-2.55	2.55	-1.000
		1a	yes		3.94	0. 50	30	0.00	2.50	-2.50	2.50	-1.000
		3a	no		13.50	0. 76	30	3.00	28.00	-25.00	31.00	-0.806
		4	no									

Table D-1. Track data.

Car	Slope α°	Sphere	Rolled	$\frac{\gamma_r}{\gamma_s}$	w (cm)	$\frac{w}{D}$	dist. to x-sect (cm)	V_r (cc/cm +)	V_w (cc/cm -)	ΔV (cc/cm)	V_t (cc/cm)	$\frac{\Delta V}{V_t}$
5 (Cont'd)	25	A	no	2.97	10.30	0.350	30	3.19	17.33	-14.14	20.52	-0.688
		B	yes	1.72	8.60	0.712	30	0.86	9.80	-8.94	10.66	-0.838
		C	yes	1.39	7.90	0.655	30	0.86	8.52	-7.66	9.38	-0.815
		E	yes	0.42	4.10	0.840	60	0.02	1.07	-1.05	1.09	-0.961
		1a	yes	1.50	3.72	0.620	30	0.10	1.80	-1.70	1.90	-0.896
		3a	yes	1.42	12.15	0.700	30	2.88	20.60	-17.72	23.48	-0.755
		4	yes	1.44	21.20	0.837	30	15.40	53.80	-38.40	69.20	-0.556
	35	A	yes		10.70	0.886	30	11.10	19.70	-8.60	30.80	-0.279
		C	yes		7.35	0.610	30	2.89	3.67	-0.78	6.56	-0.119
		E	yes		4.30	0.856	30	0.10	1.03	-0.93	1.13	-0.823
		1a	yes		3.50	0.890	30	0.28	0.86	-0.58	1.14	-0.558
		3a	yes		13.00	0.748	30	7.04	19.30	-12.26	26.34	-0.465
		4	yes		21.20	0.837	30	26.50	60.50	-34.00	87.00	-0.390

Table D-1. Track data.

Car	Slope $\alpha°$	Sphere	Rolled	$\frac{\gamma_r}{\gamma_s}$	w (cm)	$\frac{w}{D}$	dist. to x-sect (cm)	V_r (cc/cm +)	V_w (cc/cm -)	ΔV (cc/cm)	V_t (cc/cm)	$\frac{\Delta V}{V_t}$
6	25	1a	yes	1.50	4.50	0.328	150	1.18	1.35	-0.17	2.53	-0.067
γ_s =		4	with push	1.44	20.26	0.800	150	32.40	32.90	-0.50	65.30	-0.008
1.245		3a	with push	1.42	14.35	0.625	150	4.16	23.15	-18.99	27.31	-0.695
7	25	B	yes	1.67	10.50	0.870	150	5.42	6.80	-1.38	12.22	-0.113
γ_s =		C	yes	1.35	8.50	0.704	150	1.44	3.82	-2.38	4.26	-0.560
1.280		D	yes	0.82	7.70	0.638	180	1.84	2.38	-0.54	4.22	-0.128
		E	yes	0.41	4.50	0.373	210	0.32	1.08	-0.76	1.40	-0.543
8	20	A	yes	2.48	5.63	0.467	90	1.40	0.69	+0.71	2.09	+0.340
γ_s =		C	yes	1.16	5.00	0.415	90	0.61	0.53	+0.08	1.14	+0.070
1.491		E	yes	0.35	2.83	0.235	90	0.13	0.08	+0.05	0.21	+0.238
		1a	yes	1.25	2.26	0.316	90	0.26	0.07	+0.19	0.33	+0.576
9	20	3a	yes	1.23	6.08	0.350	90	0.49	0.82	-0.33	1.31	-0.252
γ_s =		4	yes	1.25	11.67	0.461	90	3.38	2.84	+0.54	6.22	+0.087
1.436												